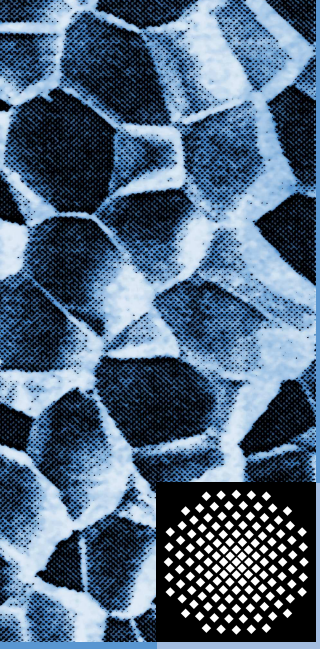

Universität Stuttgart
Germany

Institut für Mechanik (Bauwesen)
Lehrstuhl für Kontinuumsmechanik
Prof. Dr.-Ing. Dr. h. c. W. Ehlers

Parallel Simulation of Volume-Coupled Multi-Field Problems with Special Application to Soil Dynamics

Maik Schenke

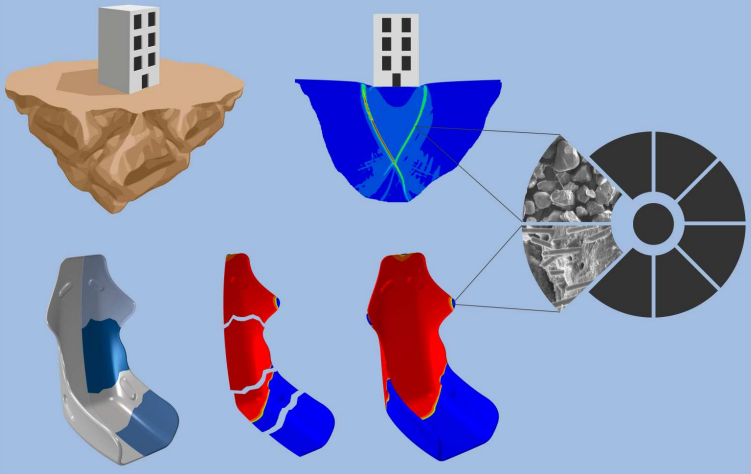

Report No.: II-32 (2017)

Parallel Simulation of Volume-Coupled Multi-Field Problems with Special Application to Soil Dynamics

Von der Fakultät Bau- und Umweltingenieurwissenschaften
der Universität Stuttgart zur Erlangung der Würde
eines Doktor-Ingenieurs (Dr.-Ing.)
genehmigte Abhandlung

vorgelegt von

Maik Schenke, M. Sc.

aus
Gera

Hauptberichter:	Prof. Dr.-Ing. Dr. h. c. Wolfgang Ehlers
Mitberichter:	Prof. Dr.-Ing. Bernd Markert

Tag der mündlichen Prüfung: 30. 06. 2017

Institut für Mechanik (Bauwesen) der Universität Stuttgart
Lehrstuhl für Kontinuumsmechanik, Prof. Dr.-Ing. Dr. h. c. W. Ehlers
2017

Report No. II-32
Institut für Mechanik (Bauwesen)
Lehrstuhl für Kontinuumsmechanik
Universität Stuttgart, Germany, 2017

Editor:
Prof. Dr.-Ing. Dr. h. c. W. Ehlers

Institut für Mechanik (Bauwesen)
Lehrstuhl für Kontinuumsmechanik
Universität Stuttgart
Pfaffenwaldring 7
70569 Stuttgart, Germany

ISBN 978 – 3 – 937399 – 32 – 4
(D 93 – Dissertation, Universität Stuttgart)

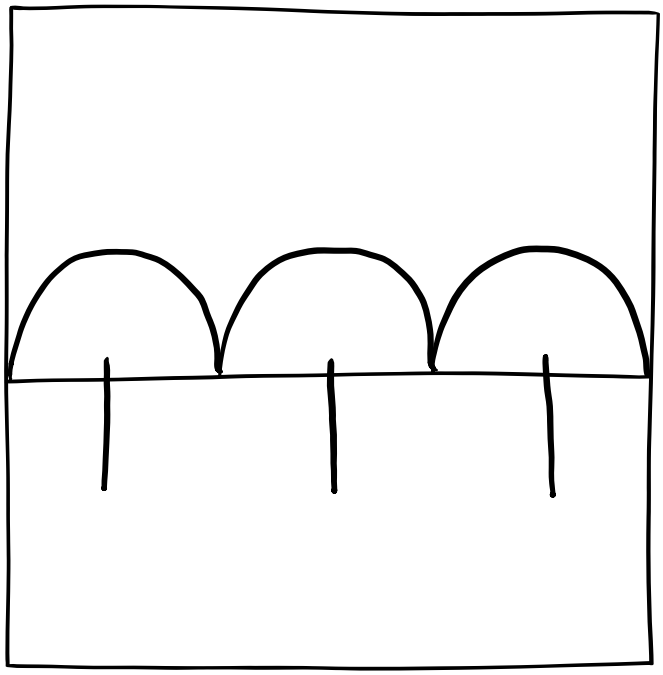

DROODLE*

*The *portmanteau*, i. e. the linguistic blend of words, of *doodle* and *riddle* describes a minimal cartoon featuring rather abstract pictorial elements. The inappropriate choice of perspective prevents a clear catch of the scene and stimulates the creativity of the beholder leaving room for various (mis)interpretations.

Acknowledgements

The work presented in this doctoral thesis was developed during my profession as an assistant lecturer and research assistant at the Institute of Applied Mechanics (Civil Engineering) Chair of Continuum Mechanics, at the University of Stuttgart. At this point, I want to take the opportunity to gratefully acknowledge numerous people who contributed in various ways to complete this work.

First of all, I would like to thank my supervisor Professor Wolfgang Ehlers for giving me the opportunity to prepare my thesis at his institute under his constant scientific support. Without his broad expertise this dissertation would certainly not have been possible. Besides my advisor, I am also grateful to Professor Bernd Markert not only for being the co-supervisor of my thesis, but also for his comprehensive help during the application for the extension of the fundings for the research project GeoTech. Moreover, I would like to thank all my former and current colleagues for this truly outstanding atmosphere, creating a pleasant and efficient working environment and for their true partnership, the willingness to face new challenges together and the always open and warm conversations and the time we spend apart from work. In this regards, I would like to thank my proof readers Sami Bidier, Said Jamei (Seyedmohammad Zinatbakhsh) and Arndt Wagner. Especially, I also want to thank master craftsman Ralf Plonus for his assistance and support, not only for carrying out the various necessary experiments, but also for his aid in the many non-work-related craft problems. Finally, I want to thank my family for giving me the freedom to follow my own path.

Stuttgart, Juni 2017 Maik Schenke

Contents

Deutschsprachige Zusammenfassung

Motivation

Zur Lösung vieler ingenieur- und naturwissenschaftlichen Problemstellungen sind numerische Simulationen ein wichtiges Hilfsmittel. Sie dienen beispielsweise der Wettervorhersage in der Meteorologie oder der Strukturanalyse und Strukturoptimierung im Maschinenbau. In vielen Aufgabenstellungen kann das untersuchte Problem, aufgrund seiner starken Wechselwirkung mit den angrenzenden Systemen, nicht losgelöst betrachtet werden, so dass eine gesamtheitliche Betrachtungsweise notwendig wird. Diese Systeme werden in der Literatur als gekoppelte Probleme bezeichnet. Beispielweise kann das aus der Luftfahrt bekannte Instabilitätsphänomen des aeroelastischen Flatterns auf eine gegenseitige Wechselwirkung zwischen einer elastischen Struktur, z. B. einem Flügel, und der Luftumströmung zurückgeführt werden. Bei näherer Betrachtungsweise lässt sich die Fluid-Struktur-Interaktion wie folgt erklären. Die fluidumströmte Struktur ändert aufgrund der resultierend Druckverteilung ihre Geometrie und zwingt somit die Fluidpartikel auf neue Bahnlinien, wodurch sich wiederum eine neue Druckverteilung entlang der Struktur ausbildet. Entspricht die Frequenz des Zyklus der Eigenfrequenz der Struktur, gerät das System in Resonanz, die zu großen Deformationen und zum kompletten Versagen der Struktur führen kann. Andere Beispiele für gekoppelte Probleme sind z. B. die Thermoelastizität, d. h. die Kopplung zwischen thermischen Einflüssen und mechanischer Deformation, die Interaktion zwischen einem porösen Festkörper und der Porenfluidströmung oder der permanente Knochenauf- und abbau bei Säugetieren aufgrund externer Stimuli in Verbindung mit dem Stoffwechsel.

Die gekoppelten Probleme werden neben anderen Klassifizierungsverfahren in oberflächengekoppelte und volumengekoppelte Probleme unterteilt. Während bei ersteren die Interaktion der verschiedenen Subsysteme über eine gemeinsame Grenzfläche stattfindet, wie z. B. in der Fluid-Struktur-Interaktion, kann bei letzteren keine klare Gebietstrennung identifiziert werden. Hier ist die Kopplung zwischen den koexistierenden physikalischen Feldern intrinsischer Natur, wie z. B. in thermomechanischen Problemen. In vielen Fällen ist die Art der Kopplung von der bei der Modellierung betrachteten Grössenskala abhängig. Beispielsweise lässt sich ein mikrostrukturell oberflächengekoppeltes Problem, z. B. die Porenraumdurchströmung eines porösen Körpers, mittels einer geeigneten Homogenisierungstechnik auf ein volumengekoppeltes Problem auf der Makroskala überführen. Ein makroskopischer Modellierungsansatz ist in vielen Anwendungsbereichen, beispielsweise bei komplexen Mikrostrukturgeometrien, von Vorteil. Typische Beispiele hierfür sind granulare Materialien, wie z. B. Sande oder Pulver, oder biologische Gewebe, wie z. B. Knochen, Knorpel oder Haut.

Aufgrund der Komplexität der betrachteten Probleme sind zur effizienten Lösung der zugrunde liegenden Gleichungen parallele Lösungsstrategien von Vorteil. Hierbei wird das Gesamtproblem in kleinere Teilprobleme zerlegt, die gleichzeitig auf verschiedenen Rechnern oder Prozessoren gelöst werden. Um die Vorteile dieses Lösungsverfahrens bestmöglich

nutzen zu können, sind erhebliche Anstrengungen zunächst für die initiale Entwicklung und Umsetzung eines effizienten Lösungsverfahrens sowie anschließend für dessen kontinuierliche Weiterentwicklung notwendig.

Zielsetzung und Stand der Technik

Die Idee, aufwändige Aufgaben simultan auf verschiedenen Rechnern gleichzeitig zu bearbeiten, wurde bereits in den 1950er-Jahren entwickelt. Sie erlangte aber erst in den letzten Jahrzehnten an Wichtigkeit, da die bisher üblichen Vorgehensweisen zur Performancesteigerung, wie z. B. die Erhöhung des Prozessortaktes, heutzutage an die Grenzen der Thermodynamik und der Quantenphysik stoßen. Gegenwärtig sind deshalb parallele Lösungsstrategien von großem Interesse und Schwerpunkt zahlreicher Publikationen, siehe z. B. Babuška & Elman [11], Ferreira & Rolim [74], Patra *et al.* [154], Wieners [203] oder Bastian *et al.* [12], wobei aktuell auch die Performancesteigerung durch Auslagern von Berechnungen auf Grafikkarten in aktueller Literatur untersucht wird, siehe z. B. Tian *et al.* [183] oder Göddeke [83]. Die Entwicklung und Implementierung effizienter Algorithmen, und insbesondere deren Weiterentwicklung im Einklang mit der sich ständig weiterentwickelnden Computertechnologie, ist zeitaufwändig und oft nicht Gegenstand eines Forschungsvorhabens. Dies führt dazu, dass ein bereits entwickeltes Verfahren veraltet ist und daher nicht mehr für die Lösung der zunehmend komplexer werdenden Problemstellung geeignet ist. Dies gilt insbesondere mit Blick auf die industrielle Anwendung.

Die vorliegende Monographie beschreibt einen Ansatz zur Kosimulation numerischer Probleme zwischen dem kommerziellen auf der Finite-Elemente-Methode (FEM) basierenden Programmpaket Abaqus und dem für die Forschung entwickelten Löser PANDAS. Die Entwicklung von PANDAS wurde 1992 an der TU Darmstadt begonnen und seit 1995 am Institut für Mechanik (Bauwesen), Lehrstuhl für Kontinuumsmechanik, der Universität Stuttgart fortgeführt, siehe Ehlers & Ellsiepen [63]. Der Schwerpunkt beim Programmentwurf lag insbesondere auf der Lösung volumengekoppelter Probleme. In Analogie zu dem Vorgehen von Ammann [6], der eine Kopplung zum Programm M++[2] beschrieb, basiert der hier beschriebene Kosimulationsansatz im Wesentlichen auf der benutzerdefinierbaren Elementroutine UEL von Abaqus. Die Aufgabe der Subroutine, nämlich die Berechnung der Materialantwort auf Elementebene, wird hier von PANDAS übernommen. Durch die Entwicklung einer allgemeinen Schnittstelle können die Materialmodelle von PANDAS direkt, ohne eine langwierige und fehleranfällige Reimplementierung, in eine für die industrielle Anwendung wichtige Simulationsumgebung überführt werden. Hierbei kann direkt auf die umfangreiche Materialmodellbibliothek von PANDAS zurückgegriffen werden. Zusätzlich wird mit PANDAS eine benutzerfreundliche Umgebung zur Umsetzung eigener Materialbeschreibungen bereitgestellt. Die Kopplung wurde zum einen weitgehend automatisiert, so dass der manuelle Eingriff seitens des Benutzers minimiert wird, und zum anderen bleiben die parallelen Lösungsstrategien von Abaqus uneingeschränkt erhalten. Zur Illustration der Anwendungsmöglichkeiten der Abaqus-PANDAS-Kopplung wird diese exemplarisch zur Simulation verschiedener volumengekoppelter Mehrfeldprobleme herangezogen.

[2] Meshes, Multigrid and more [202].

Basis für die Modellbildung ist die makroskopische Theorie der Porösen Medien (TPM), siehe de Boer [21] oder Ehlers [59]. Die TPM ist als theoretisches Grundgerüst vielseitig einsetzbar und war bereits Grundlage zahlreicher Berechnungsmodelle zur Bearbeitung verschiedenster Problemstellungen. Anwendung findet sie beispielsweise in der Bodenmechanik, siehe z. B. Graf [85], Avci [10] oder Bluhm *et al.* [20], der Biomechanik, siehe z. B. in Karajan [111], Krause [117], Wagner [196] oder Ricken *et al.* [163], oder der allgemeinen Mechanik, siehe z. B. in Markert [136] oder Acartürk [1].

In der vorliegenden Arbeit wird die entwickelte Kosimulationsstrategie, stellvertretend für die zahlreichen Anwendungsmöglichkeiten, zur Lösung ausgewählter volumengekoppelter Mehrfeldprobleme aus den Bereichen Bodenmechanik und Mehrphasenströmung verwendet. Als bodenmechanisches Anwendungsbeispiel wird die Tragfähigkeit eines flüssigkeitgesättigten granularen Materials unter quasi-statischen und dynamischen zyklischen Belastungen untersucht. Weiterhin werden mehrphasige Strömungsprozesse, wie sie z. B. im Produktionsprozess von faserverstärkten Kunststoffen auftreten, numerisch simuliert. Im sogenannten Vaccum-Assisted-Resin-Transfer-Moulding (VARTM), wird ein zunächst trockenes (gasgesättigtes) Fasergewebe kontinuierlich mit Harz getränkt, wobei für die praktische Anwendung insbesondere die Zeit bis zur vollständigen Sättigung und der sich einstellende Faservolumenanteil im fertigen Bauteil von großem Interesse sind. Weiterhin werden die Effizienz und die parallele Skalierbarkeit des vorgeschlagenen Kosimulationsansatzes untersucht.

Gliederung der Arbeit

Nach einer kurzen Einführung in die Problemstellung in Kapitel 1, wird in Kapitel 2 die der Modellbildung zugrunde liegende Theorie, d. h. die TPM, mit ihren elementaren Konzepten kurz zusammengefasst. Diese wird anschließend im Kapitel 3 für die Modellbildung herangezogen. Aufgrund der Vielfältigkeit der angestrebten Simulationsbeispiele, welche zwei- und dreiphasige Modelle unter quasi-statischen als auch dynamischen Belastungen umfasst, wird zunächst ein allgemeineres, dynamisches, Dreiphasenmodell, bestehend aus einem inkompressiblen Festkörper und einem inkompressiblen Porenfluid sowie einem kompressiblen Porengas, aufgebaut. Hierbei wird besondere Aufmerksamkeit auf die Beschreibung des elastisch-plastischen Festkörpers im Hinblick auf das spezielle Verhalten granularer Materialien unter zyklischen Belastungen gelegt. Hierfür werden sowohl ein isotropes als auch ein kombiniertes isotropes-kinematisches Verfestigungsmodell umgesetzt. Das allgemeine Modell wird anschließend mittels diverser Annahmen vereinfacht und auf spezielle Anwendungsbeispiele zugeschnitten. Durch die Spezialisierung ergeben sich ein zweiphasiges dynamisches und ein dreiphasiges quasi-statisches Modell. In Kapitel 4 werden die räumliche und zeitliche Diskretisierung der zugrunde liegenden Gleichungen behandelt. Für die räumliche Diskretisierung eines in dieser Arbeit im Allgemeinen semi-infiniten Halbraums wird dieser zunächst in ein Nah- und in ein Fernfeld unterteilt. Anschließend werden die Feldvariablen mittels der FEM bzw. der Infinite-Element-Methode (IEM) approximiert. Das Verfahren wird zunächst allgemein beschrieben und danach auf die zugrunde liegenden Stoffmodelle angewandt. Mit Rücksicht auf die zu erwartenden Phänome aufgrund der dynamischen Belastung, wie z. B. beim Problem der Wellenaus-

breitung, wird am FEM-IEM-Übergang zusätzlich eine energieabsorbierende Schicht zur Unterdrückung von Wellenreflektionen eingeführt. Die Wahl des Zeitdiskretisierungsverfahrens berücksichtigt die effiziente Lösung des zugrunde liegenden Problems. In diesem Zusammenhang wird neben dem impliziten Verfahren nach Hilber, Hughes und Taylor (HHT) [101] auch die Anwendbarkeit von expliziten Verfahren, wie z. B. das explizite zentrale Differenzenverfahren, zur Beschreibung dynamischer volumengekoppelter Probleme diskutiert. Quasi-statische Problemstellungen werden mit dem impliziten Euler-Verfahren diskretisiert. Kapitel 5 ist der parallelen Lösungsstrategie gewidmet. Nach einer kurzen Einführung, welche die Beschreibung der wichtigsten Begriffe, Rechnerarchitekturen sowie Programmiermodelle umfasst, wird der Abaqus-PANDAS-Kosimulationsansatz beschrieben und mittels Benchmarks auf dessen Effizienz und parallele Skalierbarkeit hin untersucht. In Kapitel 6 werden die Anwendungsmöglichkeiten diskutiert. Zunächst werden Parameterstudien vorangestellt, welche zum einen die parallele Skalierbarkeit der verwendeten expliziten und impliziten Zeitintegrationsverfahren sowie zum anderen die Eignung der gewählten Fernfeldbeschreibung für die Simulation dynamischer Problemstellungen untersuchen. Anschließend werden die vorgeschlagenen Modelle zur Beschreibung granularer Materialien für die Analyse der Baugrundstabilität herangezogen. Hierbei werden zunächst die Antworten des rein isotropen sowie des kombinierten isotropen-kinematischen Verfestigungsmodells mit den experimentellen Beobachtungen an quasi-statischen, zyklischen Triaxialversuchen verglichen. Anschließend wird die Eignung des zweiphasigen, dynamischen Bodenmodells mit isotrop verfestigendem Festkörper zum Abbilden von Bodenverflüssigungseffekten, wie sie z. B. während Erdbeben oder während des Setzens von Rüttelinjektionspfählen auftreten, untersucht. Das quasi-statische Dreiphasenmodell wird zur Beschreibung des VARTM-Verfahrens benutzt. Hierbei ist zum einen die Wechselwirkung zwischen Fasergewebe und Porenfluiden und zum anderen die Anwendungsmöglichkeit des vorgestellten Kosimulationsansatzes im Hinblick auf die industrielle Anwendung von Interesse. Abschließend werden weiterführende Arbeiten in Kapitel 7 diskutiert. Hierbei wird auf die Erweiterung der Stoffmodelle und Verbesserungen im Kosimulationsansatz eingegangen. Im Anhang A werden ergänzende Informationen zur Modellbildung bereitgestellt. Darüber hinaus werden zum einen das Verfahren zur Identifikation der Stoffmodellparameter des Korngerüstes und und zum anderen die Ergebnisse der Parameteroptimierung in den Anhängen B und C dargestellt. Die sich im VARTM-Verfahren einstellende Mehrphasenströmung wird in Anhang D in die konvektiven und diffusiven Strömungsanteile zerlegt.

List of acronyms

Acronym	*Description*
CAE (in Abaqus CAE)	complete Abaqus environment
CPU	central processing unit
CSL	critical-state line
FE	finite element
FEA	finite-element analysis
FEM	finite-element method
GPU	graphics processing unit
HHT	Hilber-Hughes-Taylor
HPC	high-performance computing
HRZ	Hinton-Rock-Zienkiewicz
HTV	Hoffmann-Tanner-Voinov
IBVP	initial-boundary-value problem
IEEE	Institute of Electrical and Electronics Engineers
IH	isotropic-hardening (model)
IKH	isotropic-kinematic-hardening (model)
IE	infinite element
LRTM	light resin transfer moulding
ODE	ordinary differential equation
PDE	partial differential equation
REV	representative elementary volume
RSL	row-sum lumping
RTM	resin transfer moulding
TPM	Theory of Porous Media
UEL	user-defined element (subroutine name)
VARTM	vacuum-assisted resin transfer moulding
VDB	viscous-damped boundary
XFEM	extended finite-element method

Chapter 1:
Introduction and Overview

1.1 Motivation

Numerical simulations are widely used in many engineering disciplines. For instance, they serve the weather forcast in meteorology, or the optimisation and the validation of a given design in structural engineering. Many encountered problems cannot be treated individually, as the behaviour of the system of interest may be strongly influenced by its interactions with the surrounding environment. Consequently, a solution requires a holistic consideration of the entire problem. These problems are commonly encompassed by the term coupled problem. To give an example, a common instability phenomenon in aerospace engineering, denoted as aeroelastic fluttering, can be traced back to the coupling between the deformable aircraft wing and the circulating air flow. In particular, the pressure distribution resulting from the air flow dictates a change in the wing geometry, which in turn enforces new path lines and, therefore, a new pressure distribution. Depending on the frequency of the load cycle, the resulting oscillation may correspond to the natural frequency of the wing and, therefore, cause significant wing displacement up to the collapse of the entire structure. Another typical example is the thermoelastic coupling. Herein, the (local or global) changes in body temperature result in density variations and, therefore, in a specific deformation and stress patterns. Other examples are the pore-fluid-solid-skeleton interaction in porous materials, or the steady augmentation and resorption of bone structures of mammals as a consequence of external stimuli and metabolism.

Among other classification schemes, see, e. g., Markert [137] or Zinatbakhsh [220] for an overview, coupled problems can be distinguished into surface-coupled and volume-coupled problems. In surface-coupled problems, adjoining subdomains governed by different physical models are linked together via a common interface, for instance, in fluid-structure-interaction problems, where a fluid-mechanical and a solid-mechanical problem are treated simultaneously. In contrast, in volume-coupled problems, a distinct domain-coupling interface cannot be identified. Instead, the coexisting physical fields exhibit intrinsic interacting properties, for instance, in thermomechanical problems. However, the type of physical coupling may depend on the considered length scale. For instance, the micro-structural surface-coupled problem in porous materials (pore-fluid-solid-skeleton interaction) can be recast into a macroscopically volume-coupled problem by employing a suitable homogenisation technique. In this regard, it is often convenient in many applications to proceed from a macroscopic modelling approach, for instance, if the underlying microstructure exhibits a complex geometry or is characterised by its randomly distributed variations. Typical examples are granular materials, e. g. soils or powders, or biological tissues, e. g. bone, cartilage or skin.

The resulting mathematical models, typically developed in industrial or academic research

projects, are complex and, therefore, require significant computational efforts in order to solve the underlying problem, especially in industrial application scenarios. To cope with that, parallel solution strategies are often exploited. Herein, the overall problem is decomposed into smaller subproblems, which are then solved simultaneously on different processing units, e. g. processor or computer. However, to fully exploit the advantage of the parallel solution strategy, significant efforts need to be made in order to design a fast and efficient solution algorithm.

1.2 Objectives and state of the art

In order to keep pace with the increasing complexity of numerical models, especially, when dealing with coupled problems, previously successful performance-enhancement technologies, such as frequency scaling, nowadays approach fundamental barriers of thermodynamics and quantum physics. Consequently, the design of parallel-capable and efficient applications to solve complex and large-scale problems is of particular interest and, therefore, in the scope of many authors, see, e. g., Babuška & Elman [11], Ferreira & Rolim [74], Patra *et al.* [154], Wieners [203] or Bastian *et al.* [12], while the efficiency enhancement via graphics-processing-unit (GPU) computing is investigated additionally in more recent publications, see, e. g., Tian *et al.* [183] or Göddeke [83]. However, the development of an efficient solution strategy, its implementation and the gradual improvements necessary to keep pace with the permanent technological advancements in computer technology is often time consuming and in many situations not in the line of the underlying research interest. Consequently, the once developed code is often outdated and its capabilities are stretched to its limits, when it comes to the simulation of the newly arising complex problems, in particular, when having industrial applications in mind.

Hence, the present monograph introduces a co-simulation approach incorporating the commercial software package Abaqus, which provides the parallel solution framework based on the finite-element method (FEM), and the research code PANDAS[1], which is a numerical solver, initially developed at the TU Darmstadt and today continued at the Institute of Applied Mechanics (CE), Chair of Continuum Mechanics, at the University of Stuttgart, see Ehlers & Ellsiepen [63]. PANDAS is in particular designed to solve volume-coupled problems. Following the approach proposed by Ammann [6], where a coupling to M++[2] has been established, the co-simulation approach used in this monograph proceeds from a general coupling based on the user-defined element (UEL) subroutine of Abaqus, which functionality, i. e. the element-wise computation of the material response, is redirected by the corresponding PANDAS subroutines instead. Consequently, this strategy, on the one hand, allows for a straightforward transfer of the material models developed within industrial or academic research projects into a simulation environment relevant for practical applications without the need of the often time-consuming and failure-prone reimplementation. On the other hand, it provides a user-friendly programming environment for user-definable material models with an arbitrary number of degrees of freedom in compar-

[1] **P**orous media **A**daptive **N**on-linear finite-element solver based on **D**ifferential **A**lgebraic **S**ystems, www.get-pandas.com

[2] Meshes, Multigrid and more, see [202].

ison to the native UEL subroutine. Furthermore, the coupling exhibits minimal-invasive properties with respect to the definition of the initial-boundary-value problem (IBVP) of interest in Abaqus and exploits its parallel solution capabilities to solve large-scale problems on high-performance computing (HPC) clusters.

Addressing the simulation of volume-coupled multi-field problems, the present monograph proceeds from the macroscopic Theory of Porous Media (TPM) as the underlying modelling framework. The origins of the TPM can be traced back to the works of Truesdell & Toupin [189], Bowen [24] and Truesdell [187], from which it has been evolved up to its current state, see, e. g., de Boer [21] or Ehlers [59]. The TPM has been successfully applied to a wide range of problems, for instance, from biomechanical engineering, e. g. in Karajan [111], Krause [117], Wagner [196] or Ricken *et al.* [163], or geomechanics, e. g. in Graf [85], Avci [10] or Bluhm *et al.* [20], or mechanical engineering, e. g. in Markert [136] or Acartürk [1]. Recent investigations concern the treatment of discontinuities, such as cracks, via the extended finite-element method (XFEM), see, e. g., Rempler [161], or phase field modelling, see, e. g., Provatas & Elder [158] or Ambati *et al.* [3] for an overview.

In order to reveal the possibilities but also the limitations of the presented co-simulation approach against the background of a parallel solution strategy, the parallel scalability of the implicit and explicit time-stepping schemes of Abaqus/Standard and Abaqus/Explicit, respectively, are elaborated. Additionally, the efficiency of the numerical treatment of a particular unbound-domain treatment, which is often necessary in dynamic problems, is assessed. Following this, the co-simulation approach is exemplary applied to soil mechanical problems, in particular, focusing on soils under cyclic loading conditions, and to a multiphasic flow process. In the latter, the resin impregnation of dry fibre fabric, which is an important step in the manufacturing process of fibre-reinforced plastics (FRP), is addressed.

Parametric studies in porous-media dynamics

Addressing the numerical investigation of dynamic processes, it is more efficient to proceed from an explicit time-integration scheme as, in contrast to implicit methods, the solution is found straightforwardly without the time-consuming need to iteratively solve a system of nonlinear algebraic equations. In this regard, a comparison of the computational efficiency and the parallel scalability of the presented co-simulation approach with respect to the implicit and explicit time-marching schemes of Abaqus/Implicit and Abaqus/Explicit, respectively, is addressed in the parametric study.

When investigating problems under rapidly changing loading conditions, specific attention needs to be paid to the approximation of the real problem by a suitable IBVP. In this regard, the semi-infinite half-space is split into a near-field, which is, in general, the domain of interest, and a far-field. However, truncating the semi-infinite half-space at the near field, which is often sufficient in quasi-static simulations, introduces artificial boundaries at which, in a dynamic analysis, the incoming waves are reflected into the domain of interest. To suppress the wave reflections, several methods have been proposed in the literature, see, e. g., von Estorff & Firuziaan [71], Schanz [171] or Basu [13]. For the purpose of this monograph, the approach proposed in Haeggblad & Nordgren [91] is used.

In particular, addressing its application to porous-media dynamics, the modifications of Wunderlich *et al.* [207] and Heider *et al.* [99] have been incorporated. Herein, following the original idea of Lysmer & Kuhlemeyer [133], an energy-absorbing layer composed of viscously damped dashpots is introduced at the interface between the near and the far field. To evaluate the efficiency of the utilised procedure, several parametric studies are carried out.

Soil mechanics

A soil is an aggregate of several mutual interacting components. In particular, it consists of the soil grains composing the solid scaffold and of one or more pore fluids, e. g. pore liquid or pore gas, occupying the intergranular pore space. Due to their granular structure, soils cannot be classified as solids or fluids, as their macroscopically observed state (solid- or fluid-like) strongly relies upon the loading conditions and the mutual interactions between the individual constituents. For instance, common failure scenarios, such as slope instabilities or soil liquefactions, see Figure 1.1, can be traced back to an excess of pore pressure due to, for instance, a heavy rain-fall event. The rise in the pore pressure degrades the intergranular normal contact forces and, consequently, the intergranular frictional forces, and, therefore, the load-bearing capacity of the overall soil compound.

Figure 1.1: *Pictures of soil instabilities: Buried segment of a highway (left)*[3] *due to a landslide, Taiwan 2010, and structural overturning (right)*[4] *as a result of a liquefied foundation soil followed the Niigata earthquake, Japan 1964.*

The simulation of soil failures is addressed in a vast number of literature, proceeding either from quasi-static loading conditions, see, e. g., Li [130], Ferrari *et al.* [73] or Ehlers *et al.* [62], or dynamic loading conditions, see, e. g., Lin & Borja [132], Popescu *et al.* [156] or Heider *et al.* [98]. In the related literature, see, e. g., Castro [36], the soil instabilities are commonly summarised by the term *soil liquefaction*. However, due to the complex physical processes governing the failure, no further classification system, see, e. g., Robertson [164] and Whitman [199], appears to be entirely satisfactory for all possible failure mechanisms, see, e. g., Rauch [160] for an extensive discussion. Nevertheless, it is commonly accepted to distinguish soil liquefaction, according to Castro & Poulos [37], into *flow liquefaction* and *cyclic mobility*. Flow liquefaction addresses an instability phenomenon under quasi-static or dynamic loading conditions, and is associated with loose soils with a low shear strength.

[3] `http://www.weatherwizkids.com`

[4] `https://en.wikipedia.org/wiki/1964_Niigata_earthquake`

Herein, the intergranular frictional forces are reduced dramatically by an increasing pore pressure until the residual shear strength cannot sustain static equilibrium anymore. In contrast, the term cyclic mobility is associated with medium-dense to dense soils under cyclic loading conditions. It refers to a limited plastic deformation under cyclic loading conditions, where, however, the overall stability of the granular assembly is maintained.

Aiming at the description of liquefaction phenomena in fluid-saturated granular media, there are several models available, see e. g. Prévost [157] or Zienkiewicz & Bettes [214] for an overview, from which most are based on the phenomenological and somehow ad hoc formulated *Biot*'s theory [18], however, proceeding from different approaches in order to describe the solid-skeleton behaviour. In this regard, special attention needs to be paid to the description of the contractant (densification) and dilatant (loosening) behaviour of the granular assembly under pure shear deformations as a consequence of the micro-structural grain motions, such as grain sliding and grain rolling. Depending on the initial density, the soil exhibits a macroscopically contractant (loose soil) or dilatant behaviour (dense soil) under shear loading, where in the latter, although the dilatant regime is more pronounced, the deformation behaviour is preceded by a slight contractant property at first. However, experimental observations have revealed that with ongoing shear deformation, independent of the initial soil state (loose or dense), the soil reaches a critical state from which on no further volumetric changes occur, see Casagrande [35]. This observation motivated the development of so-called critical-state-line (CSL) models, see, e. g., Manzari & Dafalias [135], Roscoe & Burland [165] or Schofield & Wroth [174]. In this regard, some are associated with the Cam-Clay-based descriptions, see, e. g., Manzari & Dafalias [135] or Roscoe & Burland [165], and others with the hypoplasticity framework, see, e. g., Wichtmann *et al.* [200]. Furthermore, it is also worth to mention the more phenomenological approaches, e. g. from Zienkiewicz *et al.* [216] or Zienkiewicz *et al.* [215], which employ a direct stress-strain relation that distinguishes between loading and unloading stages. In order to describe the hardening (and softening) behaviour of granular media, isotropic and/or kinematic hardening models are commonly used. While the isotropic hardening model addresses an alteration of the shape of the yield surface, the kinematic hardening model translates and/or rotates the yield surface within the principal stress space through a so-called kinematic back-stress tensor and/or a rotation tensor, respectively. Moreover, in order to mimic the nonlinear (or softening) material properties, two hardening concepts can be distinguished. On the one hand, there are the so-called multiple-yield-surface models, which have been introduced in the scope of kinematic hardening by Iwan [108] and Mróz [145]. Herein, various nested yield surfaces are defined, where each subdomain is associated with constant hardening parameters. Upon loading, the individual hardening regimes are gradually activated and the hardening behaviour accumulates. These models suffer from their piece-wise linear hardening properties. In particular, in order to approximate the nonlinear material behaviour, a large number of nested yield surfaces and, in turn, a significant number of material parameters is necessary. On the other hand, there are nonlinear hardening models, which already propose a nonlinear relationship, in case of isotropic hardening, for the evolution of the yield-surface parameters, see, e. g., Ehlers & Avci [61], or, in case of kinematic hardening, for the kinematic back-stress tensor, see, e. g., Armstrong & Frederick [8], or the evolution of the rotation tensor, see, e. g., Lade & Inel [124], respectively. A comparison between the multiple-yield-surface and the non-

linear hardening models can be found in Meggiolaro *et al.* [142], however, merely in the scope of kinematic hardening.

For the purpose of this monograph, the description of the multi-constituent soil proceeds from the thermodynamically consistent TPM as a suitable modelling approach. Herein, the overall soil is described as an immiscible mixture composed of the soil grains and the percolating pore fluid. Depending on the intended application, the latter is either described as an incompressible pore liquid or treated as mixture composed of the incompressible pore water and the compressible pore gas. The description of the solid skeleton is based on the approach of Ehlers & Avci [61]. They proposed an elasto-(visco)plastic formulation incorporating an isotropic hardening model and a stress-dependent failure surface, where the model has been validated through a simulation of small-scale slope-failure experiments. Subsequently, the solid-skeleton model was incorporated into a dynamic biphasic formulation by Heider *et al.* [98] and Ehlers & Schenke [67] to cope with dynamic loading conditions and related phenomena therein. For the purpose of this monograph, the model will be further enhanced through a kinematic hardening model to overcome its shortcomings under cyclic but quasi-static loading conditions.

Fibre-reinforced plastics

Fibre-reinforced plastics (FRP), often also denoted as fibre-reinforced polymers, are composite materials made of a polymer matrix and enhancing fibres. In particular, the fibres are commonly made of glass, carbon or aramid and add strength and stiffness to the compound. The polymer matrix is usually made of polyester, vinyl-ester or epoxy resins and, on the one hand, protects the fibres against notches, cuts and environmental influences and, on the other hand, adds a support against fibre instabilities, such as buckling. FRP are increasingly being considered as a substitute for traditional engineering materials, such as metals or alloys. In comparison, they are non-corrosive, exhibit a higher ratio between strength/stiffness to density and allow for the production of geometrically complex-shaped structures. Moreover, as the material and structure are made in a single production step, the material can be specifically tailored to the performance requirements, for instance, through the design of weak spots, which create natural and light-weight hinges or joints. Due to the holistic production of material and structure, the knowledge of the exact production process is vital for the product quality and to reduce the production costs through, for instance, the minimisation of the number of production rejects. Consequently, the simulation of the resin-impregnation process, which is an important step in the course of production, is of great interest in industry, see Black [19]. The monograph concerns the simulation of multiphasic flow processes in general, however, exemplarily applied to the so-called vacuum-assisted resin transfer moulding (VARTM)[5], which is a variation of the resin-transfer moulding (RTM).

The RTM has been initially developed for the large-batch production of complex-shaped structures made of thermosetting polymers or elastomers within tight dimensional tolerances. Later on, the process has been adopted to the manufacturing of FRP. The

[5] In the related literature the process is often also denoted as vacuum-assisted resin infusion (VARI), light-RTM (LRTM) process or vacuum moulding.

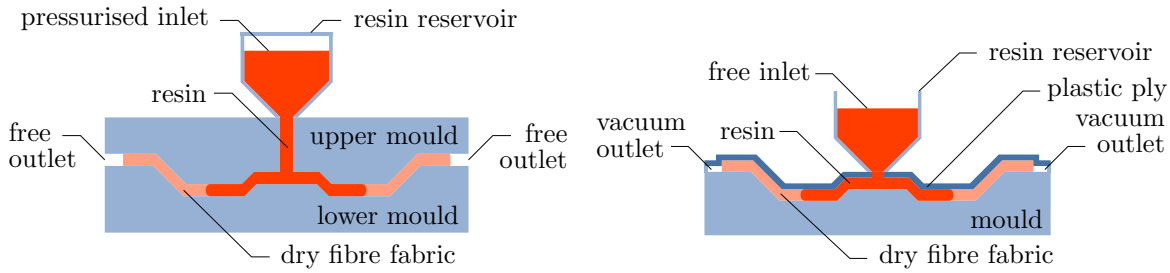

Figure 1.2: *Schematic sketch of resin transfer moulding (RTM) (left) and vacuum-assisted resin transfer moulding VARTM) (right).*

RTM procedure is schematically depicted in Figure 1.2 (left). After placing the dry (fully gas-saturated) fibre fabric in a rigid two-pieced mould, the mould is closed and a resin reservoir is attached to the inlet. Subsequently, the inlet is subjected to an excess pressure, thereby giving rise to a pressure gradient between the inlet and the free (subjected to the ambient pressure) outlet. Consequently, a resin flow is initiated, which gradually impregnates the fabric. Finally, the whole part is cured by keeping the whole mould at a specific resin-dependent curing temperature. A major drawback of the RTM procedure is that it operates with high-cost toolings through its requirement for a two-pieced mould, which is in particular expensive when producing large structures. To overcome this shortcoming, the RTM process has been adopted to the VARTM procedure. Herein, its salient difference in comparision to the RTM is that, on the one hand, the upper mould is replaced by a flexible vacuum bag, see Figure 1.2 (right) and, on the other hand, that the resin is drawn into the preform through a vacuum rather than pumped via an excess of pressure. In particular, after placing the dry fabric in the rigid lower moulding part, the setup is hermetically sealed with the plastic ply, and a vacuum is applied, thereby compacting the fibre fabric through the atmospheric pressure. Subsequently, an open (subjected to the ambient pressure) reservoir resin is attached to the inlet. Similar to the RTM process, the resulting pressure gradient between the open inlet and the outlet gives rise the resin flow, which gradually impregnates the dry fibre fabric. Once the fabric is fully saturated, the whole setup is kept at a specific temperature level in order to cure the resin. In contrast to the RTM process, the use of a single-pieced mould does not entirely ensure the part geometry. In particular, due to the flexibility of the covering plastic ply, the part thickness and especially the fibre content per unit volume, which is of particular interest for a structural engineer, strongly depends on the process variables, such as the injection pressure.

The numerical simulation of the VARTM process, and the RTM process in general, is addressed in a vast number of literature, see Song [180] for an overview. The solution procedure, which is usually based on the Richards transport equation, see Richards [162], as the governing equation. Moreover, in order to deal with the moving-flow-front problem, a solution strategy comprising the finite-element method and the method of control volumes (FE-CV), e. g., see Bruschke & Advani [32] or Trochu *et al.* [186], is exploited. Herein, the field variables are solved with the help of the FE mesh, whereas the control volumes are used to track the flow front by subsequently filling the control volumes adjacent to the flow front. A major drawback of this strategy is the fact that the allowable time increment is constrained by the time needed to completely saturate the control

volume, before the algorithm can advance to the next element. In contrast, more recent developments, such as described in the work of Klunker *et al.* [114], proceed from a mixture-based modelling approach. Therein, the pore space is simultaneously occupied by the ambient air and the resin, which allows for a continuous transition of the resin saturation from fully saturated, over a partially saturated, towards the unsaturated state. For the purpose of this monograph, the underlying model additionally accounts for the fibre-pore-fluid interaction through the multiphasic modelling approach based on the TPM.

1.3 Outline of the thesis

To begin with, **Chapter 2** briefly summarises the TPM as the underlying modelling framework, thereby concerning its basic concepts, the mixture kinematics and the governing balance relations.

Subsequently, **Chapter 3** applies the given concept to setup specific material models. In particular, having the simulation of various application scenarios in mind, the previously introduced modelling concept will be exploited to initially set up a more general dynamic triphasic model, which is composed of an elasto-plastic solid, an incompressible pore liquid and a compressible pore gas. The description of the solid skeleton incorporates either an isotropic or a mixed isotropic-kinematic hardening model. Subsequently, the general formulation is condensed to yield more specific models, which are individually tailored to particular application scenarios, viz. the dynamic biphasic models exhibiting an elasto-plastic scaffold and the quasi-static triphasic model following a linear-elastic solid skeleton description.

Chapter 4 covers the numerical treatment, in particular, the spatial and temporal discretisation methods. The spatial discretisation is carried out via the finite-element method (FEM), where the procedure is, at first, briefly reviewed in a more general setting, but is subsequently applied to the actual governing material models, thereby considering a different treatment for the near and for the far field. In a next step, the temporal discretisation and the underlying solution strategies are presented, thereby, with respect to the nature of the underlying process and for the sake of an efficient solution procedure, exploiting implicit and explicit time-advancement schemes.

Addressing the parallel solution strategy, **Chapter 5** starts with a short introduction into parallel computing covering the basic terminology, computer architectures and programming models, followed by a detailed description of the Abaqus/PANDAS co-simulation approach. Finally, its performance in sequential and parallel execution is investigated through the computation of a benchmark problem.

The possibilities, but also the limitations of the numerical models and the co-simulation-solution strategy are elaborated in detail in **Chapter 6**. In particular, at first, several parametric studies concern the parallel scalability and the viability of the unbound-domain treatment. Subsequently, the simulation of granular materials under (dynamic and quasi-static) cyclic loading conditions and, finally, the investigation of multiphasic flow process by means of the VARTM procedure is addressed.

Finally, future aspects are addressed in **Chapter 7**, therein particularly focusing on the enhancements related, on the one hand, to the numerical models and, on the other hand, to the co-simulation approach.

The preceded elaborations are further supplemented by the explanations given in the appendix. In particular, the derivation process of the material models is complemented by **Appendix A**. Moreover, the identification procedure and the resulting material parameters of the isotropic hardening soil model, and the adjustments made for the mixed isotropic-kinematic hardening model are summarised in **Appendix B** and **Appendix C**, respectively. In **Appendix D** the convective and diffusive contributions in the multiphasic flow process are identified.

Chapter 2:
Fundamentals of the Theory of Porous Media

As outlined before, many natural or engineered multi-field materials exhibit, in general, a complex and heterogeneous micro-structure, which is additionally often not known in detail. Consequently, it is often convenient to proceed from a macroscopic modelling approach without the loss of a particular physical process within the real system. In this regard, the macroscopic Theory of Porous Media (TPM) is exploited as a suitable modelling framework for the purpose of this monograph. Its origins can be traced back to the Theory of Mixtures (TM), see, e. g., Truesdell & Toupin [189] or Bowen [24]. The TPM was developed on the basis of general thermodynamic considerations and, subsequently, extended by the concept of volume fractions in Mills [144] and Bowen [25, 26]. Since then, the TPM was continuously evolved to its current state by de Boer [21] and Ehlers [54, 59] and many others.

The present chapter briefly outlines basic concepts and findings of the TPM in order to provide the necessary theoretical background. For a more detailed insight, the interested reader is referred to the above mentioned related literature and references therein.

2.1 Homogenisation and the concept of volume fractions

Within the macroscopic TPM approach, the overall porous material φ is treated in the sense of an immiscible mixture of various interacting constituents φ^α, i. e. $\varphi = \bigcup_\beta \varphi^\alpha$, which are treated to be homogeneously distributed within a representative elementary volume (REV) $\mathrm{d}v$ by virtually carrying out a homogenisation process, see Figure 2.1.

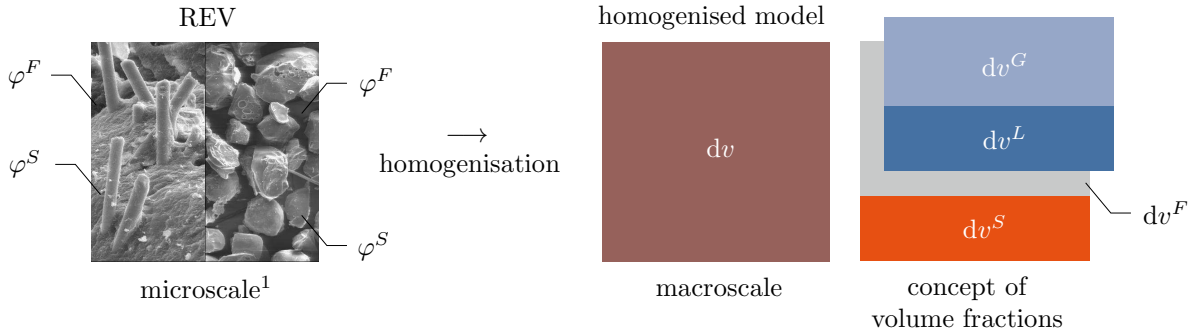

Figure 2.1: *Illustration of the virtual homogenisation and the concept of volume fractions by means of triphasic material, i. e. $\alpha \in \{S, L, G\}$ and $\beta \in \{L, G\}$.*

[1]The microscale pictures of a glass-fibre reinforced plastic (left) and a sand (right) have been captured at the Institute of Material Engineering and Joining Technology (Institut für Material- und Fügetechnik)

In general, the overall porous aggregate is composed of the solid skeleton ($\alpha = S$), which might be the granular assembly in a soil or the molecule chains of a polymer, and of the pore fluid ($\alpha = F$), which can be again a mixture of various interacting constituents φ^β, i. e. $\varphi^F = \bigcup_\beta \varphi^\beta$, for instance, composed of a pore liquid ($\beta = L$) and a pore gas ($\beta = G$). The composition of the bulk volume element is defined through the respective volume fractions $n^\alpha = \mathrm{d}v^\alpha/\mathrm{d}v$, where $\mathrm{d}v^\alpha$ is the partial volume of the constituent φ^α within the REV. In an analogous way, the pore-fluid saturation s^β is defined as the ratio of the partial volume $\mathrm{d}v^\beta$ of the pore-fluid component to the partial volume $\mathrm{d}v^F$ of the overall pore fluid, i. e. $s^\beta = \mathrm{d}v^\beta/\mathrm{d}v^F$. The REV and the pore space can be arbitrarily composed of the individual constituents as long as their respective volume fractions n^α and saturations s^β satisfy the saturation conditions

$$\sum_\alpha n^\alpha = n^S + n^F = 1 \qquad \text{and} \qquad \sum_\beta s^\beta = 1\,, \tag{2.1}$$

respectively, where the individual volume fractions of the pore-fluid constituents compose the volume fraction of the overall pore fluid, i. e.

$$n^F = \sum_\beta n^\beta = \sum_\beta s^\beta n^F\,. \tag{2.2}$$

Following this, two density functions are defined. The material (realistic or effective) density $\rho^{\alpha R} = \mathrm{d}m^\alpha/\mathrm{d}v^\alpha$ relates the local mass $\mathrm{d}m^\alpha$ to its volume $\mathrm{d}v^\alpha$, while the partial (global or bulk) density $\rho^\alpha = \mathrm{d}m^\alpha/\mathrm{d}v$ is associated with the bulk volume. Moreover, both density definitions are related to each other through $\rho^\alpha = n^\alpha \rho^{\alpha R}$. Assuming a materially incompressible material, the realistic density of the solid remains constant under the isothermal conditions, i. e. $\rho^{\alpha R} = \text{const.}$, while the bulk density can still change through a changing volume fraction n^α. Additionally, the density ρ of the overall aggregate (mixture density) is obtained via

$$\rho = \sum_\alpha \rho^\alpha\,. \tag{2.3}$$

2.2 Motion of the constituents

In the framework of the TPM, the individual constituents φ^α are treated as superimposed continua, where each spatial point is simultaneously occupied by material points of any constituent. Each is moving according to its own motion function $\mathbf{x} = \boldsymbol{\chi}_\alpha(\mathbf{X}_\alpha, t)$, which relates any material point in its initial configuration $\mathbf{X}_\alpha$ at $t = t_0$, to a spatial point $\mathbf{x}$ in the current configuration $t > t_0$, see Figure 2.2.

The requirement that the individual motion functions are unique claims for the existence of a unique inverse motion function $\boldsymbol{\chi}_\alpha^{-1}$, which, in turn, requires the existence of a non-singular Jacobian determinant, i. e. $J_\alpha := \det(\partial\boldsymbol{\chi}_\alpha/\partial\mathbf{X}_\alpha) \neq 0$. Following this, independent velocity and acceleration fields either expressed within the Lagrangean setting,

$$\overset{\prime}{\mathbf{x}}_\alpha = \frac{\partial\boldsymbol{\chi}_\alpha(\mathbf{X}_\alpha, t)}{\partial t} = \overset{\prime}{\mathbf{x}}_\alpha(\mathbf{X}_\alpha, t) \qquad \text{and} \qquad \overset{\prime\prime}{\mathbf{x}}_\alpha = \frac{\partial^2\boldsymbol{\chi}_\alpha(\mathbf{X}_\alpha, t)}{\partial t^2} = \overset{\prime\prime}{\mathbf{x}}_\alpha(\mathbf{X}_\alpha, t), \tag{2.4}$$

at the *Otto von Guericke* University of Magdeburg, Germany using a scanning electron microscope (SEM).

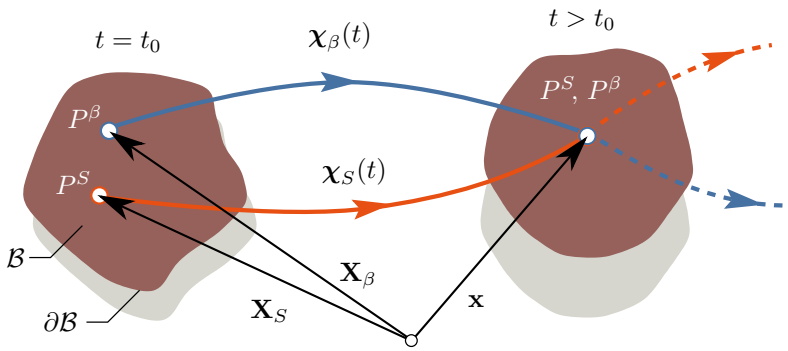

Figure 2.2: *Motion of a material point P^S of the solid skeleton and of a material point P^β of a pore-fluid constituent φ^β.*

or, with the aid of the inverse motion function, within the Eulerian description,

$$\overset{\prime}{\mathbf{x}}_\alpha = \frac{\partial \boldsymbol{\chi}_\alpha(\mathbf{x}_\alpha, t)}{\partial t} = \overset{\prime}{\mathbf{x}}_\alpha(\mathbf{X}_\alpha, t) \qquad \text{and} \qquad \overset{\prime\prime}{\mathbf{x}}_\alpha = \frac{\partial^2 \boldsymbol{\chi}_\alpha(\mathbf{x}_\alpha, t)}{\partial t^2} = \overset{\prime\prime}{\mathbf{x}}_\alpha(\mathbf{x}_\alpha, t)\,. \tag{2.5}$$

Note that in the latter case, the time derivatives with respect to the motion of the constituent φ^α need to account for the local and non-local temporal changes. In particular, besides the temporal change of the spatial field variable at a fixed spatial position (local contribution), additionally, the so-called convective part (non-local contribution), as a consequence of the motion of φ^α through the spatially distributed field, needs to be considered. In this regard, the so-called material time derivative is introduced. It is the total time derivative of an arbitrary, steady and sufficiently differentiable, scalar or vectorial field, Υ or $\boldsymbol{\Upsilon}$, following the motion of the individual constituent φ^α (left column) or the barycentric velocity of the overall aggregate (right column):

$$\begin{aligned}
(\Upsilon)'_\alpha(\mathbf{x}, t) &= \frac{\mathrm{d}_\alpha \Upsilon}{\mathrm{d}t} = \frac{\partial \Upsilon}{\partial t} + \operatorname{grad}\Upsilon \cdot \overset{\prime}{\mathbf{x}}_\alpha\,, & \dot{\Upsilon}(\mathbf{x}, t) &= \frac{\mathrm{d}\Upsilon}{\mathrm{d}t} = \frac{\partial \Upsilon}{\partial t} + \operatorname{grad}\Upsilon \cdot \dot{\mathbf{x}}\,, \\
(\boldsymbol{\Upsilon})'_\alpha(\mathbf{x}, t) &= \frac{\mathrm{d}_\alpha \boldsymbol{\Upsilon}}{\mathrm{d}t} = \frac{\partial \boldsymbol{\Upsilon}}{\partial t} + (\operatorname{grad}\boldsymbol{\Upsilon})\,\overset{\prime}{\mathbf{x}}_\alpha\,, & \dot{\boldsymbol{\Upsilon}}(\mathbf{x}, t) &= \frac{\mathrm{d}\boldsymbol{\Upsilon}}{\mathrm{d}t} = \frac{\partial \boldsymbol{\Upsilon}}{\partial t} + (\operatorname{grad}\boldsymbol{\Upsilon})\,\dot{\mathbf{x}}\,.
\end{aligned} \tag{2.6}$$

Therein, $\dot{\mathbf{x}}$ denotes the barycentric velocity of the overall aggregate, which is given by

$$\dot{\mathbf{x}} = \frac{1}{\rho}\sum_\alpha \rho^\alpha \overset{\prime}{\mathbf{x}}_\alpha\,, \tag{2.7}$$

and $\operatorname{grad}(\cdot) = \partial(\cdot)/\partial\mathbf{x}$ is the gradient with respect to the actual configuration.

Addressing the simulation of solid materials, the solid motion is conveniently expressed in the Lagrangean description through the solid displacement

$$\mathbf{u}_S = \mathbf{x}_S - \mathbf{X}_S\,, \qquad (\mathbf{u}_S)'_S = \mathbf{v}_S = \overset{\prime}{\mathbf{x}}_S\,, \qquad (\mathbf{u}_S)''_S = (\mathbf{v}_S)'_S = \overset{\prime\prime}{\mathbf{x}}_S\,, \tag{2.8}$$

and the motion of the pore-fluid constituent φ^β in the Eulerian setting relative to the solid motion. In this regard, in analogy to the definition of the material time derivative, see (2.6), the fluid-particle acceleration exhibits a convective contribution, which is defined relative to the deforming solid skeleton given by

$$(\mathbf{v}_\beta)'_S = (\mathbf{v}_\beta)'_\beta - (\operatorname{grad}\mathbf{v}_\beta)\,\mathbf{w}_\beta\,, \qquad \text{where} \qquad \mathbf{w}_\beta = \mathbf{v}_\beta - \mathbf{v}_S\,. \tag{2.9}$$

Therein, $\mathbf{v}_\beta$ denotes the velocity of a pore-fluid particle of φ^β and $\mathbf{w}_\beta$ the respective seepage velocity.

Additionally, the so-called diffusion velocity of a particle of φ^α, which is its relative velocity with respect to the barycentric velocity of the overall aggregate,

$$\mathbf{d}_\alpha = \overset{\prime}{\mathbf{x}}_\alpha - \dot{\mathbf{x}}\,, \qquad \text{where} \qquad \sum_\alpha \rho^\alpha\,\mathbf{d}_\alpha = \underbrace{\sum_\alpha \rho^\alpha \overset{\prime}{\mathbf{x}}_\alpha}_{\rho\,\dot{\mathbf{x}}} - \dot{\mathbf{x}} \underbrace{\sum_\alpha \rho^\alpha}_{\rho} = \mathbf{0}\,, \tag{2.10}$$

is introduced. Therein, by inserting $(2.10)_1$ into $(2.10)_2$, and by further incorporating (2.7) and (2.3), it can be concluded that the sum of the diffusive mass flows vanishes.

2.2.1 Deformation, strain and stress measures

The present section provides the definitions of the underlying strain and stress measures. However, with respect to the scope of this monograph, only a minimal set of the respective measures is introduced. A more comprehensive overview on strain and stress measures is provided in the related textbooks, see, for instance, Holzapfel [104] in the general continuum-mechanical setting, or Ehlers [54] within the scope of the TPM.

Deformation and strain measures

The description of the deformation is based on the material deformation gradient $\mathbf{F}_\alpha$ and its inverse $\mathbf{F}_\alpha^{-1}$ given by

$$\mathbf{F}_\alpha = \frac{\partial \mathbf{x}}{\partial \mathbf{X}_\alpha} = \mathrm{Grad}_\alpha\,\mathbf{x} \qquad \text{and} \qquad \mathbf{F}_\alpha^{-1} = \frac{\partial \mathbf{X}_\alpha}{\partial \mathbf{x}} = \mathrm{grad}\,\mathbf{X}_\alpha\,, \tag{2.11}$$

where $\mathrm{Grad}_\alpha\,(\,\cdot\,)$ and $\mathrm{grad}\,(\,\cdot\,)$ denote the gradient with respect to the reference configuration of φ^α and to the current configuration, respectively. Note that in the initial (undeformed) state, the deformation gradient tensor is equal to the identity tensor, i. e. $\mathbf{F}_\alpha(t = t_0) = \mathrm{Grad}_\alpha\,\mathbf{X}_\alpha = \mathbf{I}$, where the relation $\det \mathbf{F}_\alpha(t_0) = \det \mathbf{I} = 1$ holds. From the above introduced relations together with the definition of the solid displacement (2.8), one can deduce

$$\mathbf{F}_S = \frac{\partial(\mathbf{u}_S + \mathbf{X}_S)}{\partial \mathbf{X}_S} = \mathrm{Grad}_S\,\mathbf{u}_S + \mathbf{I} \qquad \text{and} \qquad \mathbf{F}_S^{-1} = \frac{\partial(\mathbf{x} - \mathbf{u}_S)}{\partial \mathbf{x}} = \mathbf{I} - \mathrm{grad}\,\mathbf{u}_S\,, \tag{2.12}$$

respectively.

The two-field deformation tensor $\mathbf{F}_\alpha$ can be used to map a line element $\mathrm{d}\mathbf{X}_\alpha$ in the reference configuration to its representative $\mathrm{d}\mathbf{x}$ in the actual configuration and vice versa via

$$\mathrm{d}\mathbf{x} = \mathbf{F}_\alpha\,\mathrm{d}\mathbf{X}_\alpha \qquad \text{and} \qquad \mathrm{d}\mathbf{X}_\alpha = \mathbf{F}_\alpha^{-1}\,\mathrm{d}\mathbf{x}\,. \tag{2.13}$$

Based on this transformation, the right ($\mathbf{C}_\alpha$) and left ($\mathbf{B}_\alpha$) Cauchy-Green deformation tensors are given by

$$\begin{aligned} \mathrm{d}\mathbf{x}\cdot\mathrm{d}\mathbf{x} &= \mathrm{d}\mathbf{X}_\alpha\cdot(\mathbf{F}_\alpha^T\,\mathbf{F}_\alpha)\,\mathrm{d}\mathbf{X}_\alpha =: \mathrm{d}\mathbf{X}_\alpha\cdot\mathbf{C}_\alpha\,\mathrm{d}\mathbf{X}_\alpha\,, \qquad \text{where} \quad \mathbf{C}_\alpha = \mathbf{F}_\alpha^T\,\mathbf{F}_\alpha\,, \\ \mathrm{d}\mathbf{X}_\alpha\cdot\mathrm{d}\mathbf{X}_\alpha &= \mathrm{d}\mathbf{x}\cdot(\mathbf{F}_\alpha^{T-1}\,\mathbf{F}_\alpha^{-1})\,\mathrm{d}\mathbf{x} =: \mathrm{d}\mathbf{x}\cdot\mathbf{B}_\alpha^{-1}\,\mathrm{d}\mathbf{x}\,, \qquad \text{where} \quad \mathbf{B}_\alpha = \mathbf{F}_\alpha\,\mathbf{F}_\alpha^T\,. \end{aligned} \tag{2.14}$$

To capture the deformation of a non-rigid solid skeleton, dimensionless strain measures are introduced. In particular, among other definitions, see, e. g., Holzapfel [104], they are commonly computed via the squared difference of a line element between the current and the reference configuration, i. e.

$$\begin{aligned} \mathrm{d}\mathbf{x}\cdot\mathrm{d}\mathbf{x} - \mathrm{d}\mathbf{X}_\alpha\cdot\mathrm{d}\mathbf{X}_\alpha &= \mathrm{d}\mathbf{X}_\alpha\cdot(\mathbf{C}_\alpha-\mathbf{I})\,\mathrm{d}\mathbf{X}_\alpha =: \mathrm{d}\mathbf{X}_\alpha\cdot 2\,\mathbf{E}_\alpha\,\mathrm{d}\mathbf{X}_\alpha\,,\\ \mathrm{d}\mathbf{x}\cdot\mathrm{d}\mathbf{x} - \mathrm{d}\mathbf{X}_\alpha\cdot\mathrm{d}\mathbf{X}_\alpha &= \mathrm{d}\mathbf{x}\cdot(\mathbf{I}-\mathbf{B}_\alpha^{-1})\,\mathrm{d}\mathbf{x} \quad =: \mathrm{d}\mathbf{x}\cdot 2\,\mathbf{A}_\alpha\,\mathrm{d}\mathbf{x}\,, \end{aligned} \tag{2.15}$$

where, consequently, the Green-Lagrangean $\mathbf{E}_\alpha$ and the Almansian $\mathbf{A}_\alpha$ strain tensors are given by

$$\mathbf{E}_\alpha = \frac{1}{2}(\mathbf{C}_\alpha-\mathbf{I})\,, \qquad \mathbf{A}_\alpha = \frac{1}{2}(\mathbf{I}-\mathbf{B}_\alpha^{-1}) \qquad \text{with} \qquad \mathbf{A}_\alpha = \mathbf{F}_\alpha^{T-1}\mathbf{E}_\alpha\mathbf{F}_\alpha^{-1}\,. \tag{2.16}$$

With these definitions at hand, the corresponding Green-Lagrangean and the Almansian strain tensors of the solid skeleton ($\alpha = S$), $\mathbf{E}_S$ and $\mathbf{A}_S$, are given by, see, e. g., Ehlers [54],

$$\begin{aligned} \mathbf{E}_S &= \tfrac{1}{2}(\mathrm{Grad}_S\,\mathbf{u}_S + \mathrm{Grad}_S^T\,\mathbf{u}_S + \mathrm{Grad}_S^T\,\mathbf{u}_S\,\mathrm{Grad}_S\,\mathbf{u}_S)\,,\\ \mathbf{A}_S &= \tfrac{1}{2}(\mathrm{grad}_S\,\mathbf{u}_S + \mathrm{grad}_S^T\,\mathbf{u}_S - \mathrm{grad}_S^T\,\mathbf{u}_S\,\mathrm{grad}_S\,\mathbf{u}_S)\,. \end{aligned} \tag{2.17}$$

Deformation and strain rates

In order to describe deformation and strain rates, the material time derivative of the deformation gradient, proceeding from the Lagrangean setting, is given by

$$(\mathbf{F}_\alpha)'_\alpha = \frac{\mathrm{d}_\alpha}{\mathrm{d}t}\,\mathbf{F}_\alpha = \frac{\partial \overset{\prime}{\mathbf{x}}_\alpha(\mathbf{X}_\alpha,t)}{\partial\mathbf{X}_\alpha} = \mathrm{Grad}_\alpha\,\overset{\prime}{\mathbf{x}}_\alpha\,, \tag{2.18}$$

whereas, proceeding from the Eulerian description, the material time derivative is given through

$$(\mathbf{F}_\alpha)'_\alpha = \frac{\mathrm{d}_\alpha}{\mathrm{d}t}\,\mathbf{F}_\alpha = \frac{\partial \overset{\prime}{\mathbf{x}}_\alpha(\mathbf{x},t)}{\partial\mathbf{X}_\alpha} = \frac{\partial \overset{\prime}{\mathbf{x}}_\alpha}{\partial\mathbf{x}}\frac{\partial\mathbf{x}}{\partial\mathbf{X}_\alpha} =: \mathbf{L}_\alpha\mathbf{F}_\alpha\,. \tag{2.19}$$

In the latter,

$$\mathbf{L}_\alpha = \frac{\partial \overset{\prime}{\mathbf{x}}_\alpha(\mathbf{x},t)}{\partial\mathbf{x}} = \mathrm{grad}\,\overset{\prime}{\mathbf{x}}_\alpha = (\mathbf{F}_\alpha)'_\alpha\mathbf{F}_\alpha^{-1} \tag{2.20}$$

is known as the spatial velocity gradient of φ^α. For further applications, it is useful, to split $\mathbf{L}_\alpha$ into a symmetric deformation velocity $\mathbf{D}_\alpha = \mathbf{D}_\alpha^T$ and a skew-symmetric spin tensor $\mathbf{W}_\alpha = -\mathbf{W}_\alpha^T$ through

$$\mathbf{L}_\alpha = \mathbf{D}_\alpha + \mathbf{W}_\alpha \quad \text{with} \quad \mathbf{D}_\alpha = \tfrac{1}{2}(\mathbf{L}_\alpha + \mathbf{L}_\alpha^T) \quad \text{and} \quad \mathbf{W}_\alpha = \tfrac{1}{2}(\mathbf{L}_\alpha - \mathbf{L}_\alpha^T)\,. \tag{2.21}$$

Subsequently, with the help of the material time derivative of the right Cauchy-Green deformation tensor

$$(\mathbf{C}_\alpha)'_\alpha = (\mathbf{F}_\alpha^T\mathbf{F}_\alpha)'_\alpha = 2\,\mathbf{F}_\alpha^T\mathbf{D}_\alpha\mathbf{F}_\alpha\,, \tag{2.22}$$

the rate of the Green-Lagrangean strain tensor is given by

$$(\mathbf{E}_\alpha)'_\alpha = \tfrac{1}{2}(\mathbf{C}_\alpha)'_\alpha = \mathbf{F}_\alpha^T\mathbf{D}_\alpha\mathbf{F}_\alpha\,. \tag{2.23}$$

Stress measures

In general, any deformation imposed on a body $\mathcal{B}$, either directly by an externally applied deformation or implicitly by an externally applied load, causes stresses inside the body to counteract the deformations. The stress is defined as the force per unit area, which immediately leads to its mathematical definition. In particular, addressing multiphasic materials in the framework of the TPM, the partial Cauchy stress tensors $\mathbf{T}^\alpha$ of the constituent φ^α can be introduced using Cauchys theorem, as

$$\mathbf{t}^\alpha(\mathbf{x}, \mathbf{n}, t) = \mathbf{T}^\alpha(\mathbf{x}, t)\, \mathbf{n}\,. \tag{2.24}$$

Therein, $\mathbf{t}^\alpha(\mathbf{x}, \mathbf{n}, t)$ denotes the surface traction vector, which comprises all contact forces acting on a fictitious cutting plane defined by the outward-oriented unit surface normal vector $\mathbf{n}$ of the current configuration. In this connection, the partial Cauchy stress is understood as the true stress, as therein the actual incremental surface force $\mathrm{d}\mathbf{k}^\alpha$ is related to the current area element $\mathrm{d}a$, via

$$\mathrm{d}\mathbf{k}^\alpha = \mathbf{t}^\alpha \mathrm{d}a = (\mathbf{T}^\alpha\, \mathbf{n})\mathrm{d}a = \mathbf{T}^\alpha(\, \mathbf{n}\, \mathrm{d}a) = \mathbf{T}^\alpha\, \mathrm{d}\mathbf{a}\,. \tag{2.25}$$

Therein, $\mathrm{d}\mathbf{a} = \mathbf{n}\, \mathrm{d}a$ denotes the oriented surface element. In this connection, addressing large deformations, i. e. the geometrically non-linear case, it is often convenient to introduce further stress measurements. Common measures are the volume-weighted Kirchoff stress $\boldsymbol{\tau}^\alpha$ and the first and second Piola-Kirchhoff stress tensors, $\mathbf{P}^\alpha$ and $\mathbf{S}^\alpha$, where in the former, only the area element and in the latter both the area element and the force vector are given in the reference configuration. Following Ehlers [54], they are defined by

$$\begin{aligned} \boldsymbol{\tau}^\alpha &= (\det \mathbf{F}_\alpha)\, \mathbf{T}^\alpha\,, \\ \mathbf{P}^\alpha &= (\det \mathbf{F}_\alpha)\, \mathbf{T}^\alpha\, \mathbf{F}_\alpha^{T-1}\,, \\ \mathbf{S}^\alpha &= (\det \mathbf{F}_\alpha)\, \mathbf{F}_\alpha^{-1}\, \mathbf{T}^\alpha\, \mathbf{F}_\alpha^{T-1}\,. \end{aligned} \tag{2.26}$$

2.3 Balance relations

In continuum mechanics, the balance relations are fundamental material-independent conservation laws of physical quantities. Based on the balanced physical quantity, they can be distinguished into mechanical balance relations, consisting of the balance of mass, momentum and moment of momentum, and thermodynamical conservation laws, composed of the energy and entropy balance. Basically, the balance laws state that the change of a physical quantity (mass, momentum, moment of momentum, energy or entropy) is conducted by actions from the vicinity (near-field actions), e. g. contact forces, the long range (far-field actions), e. g. gravitational forces, and the production of the quantity from the interior.

Within the framework of the TPM and in analogy to the mechanics of singlephasic materials, the same balance laws need to be fulfilled, which, however, in the context of multifield materials, need to be adopted by accounting for Truesdell's metaphysical principles of mixture theories, see Truesdell [187]:

1. *All properties of the mixture must be mathematical consequences of properties of the constituents.*
2. *So as to describe the motion of a constituent, we may in imagination isolate it from the rest of the mixture, provided we allow properly for the actions of the other constituents upon it.*
3. *The motion of the mixture is governed by the same equations as is a single body.*

According to theses statements, each constituent can be described independently by individual motion functions and balance equations, where the latter are then denoted as the partial balance relations in the following, as long as one accounts for the possible interactions, which are carried out through the production terms. Moreover, the balance relations of the overall mixture exhibits the same structure as the balance law of a singlephasic material.

In general, when balancing a certain physical quantity, one has to define the spatial domain under consideration, which, subsequently, can be classified as either an open or a closed system. In the former, mass can be transferred over the domain boundaries, which, however, is prohibited in the latter[2]. Following this terminology, within the present monograph, the overall aggregate will be understood as a closed system, whereas the concepts of an open system apply to the partial balance laws associated with the individual constituents, thereby allowing for a possible interaction among them.

2.3.1 Mechanical balance laws

The governing mechanical balance laws, in particular, the balance of mass, the balance of linear momentum and the balance of moment of momentum, are described in what follows.

Balance of mass

In the scope of non-relativistic physics[3], the balance of mass states that the mass of a closed system $\mathcal{B}$ is constant. However, in the context of the multiphasic modelling framework, merely the mass of the overall aggregate is constant, while the mass of particular constituents can still change through possible mass-exchange processes among the individual components. Thus, the overall and partial mass balance are given by

$$\frac{\mathrm{d}}{\mathrm{d}t}\int\limits_{\mathcal{B}} \rho \,\mathrm{d}v = 0\,, \qquad \frac{\mathrm{d}_\alpha}{\mathrm{d}t}\int\limits_{\mathcal{B}} \rho^\alpha \,\mathrm{d}v = \int\limits_{\mathcal{B}} \hat{\rho}^\alpha \,\mathrm{d}v\,. \tag{2.27}$$

Therein, ρ and ρ^α are the densities of the overall aggregate and the partial density of φ^α, respectively. Moreover, $\hat{\rho}^\alpha$ denotes the mass production contributing to the realistic

[2]Note that a closed system still allows for an exchange of energy, e. g. via heat or work, over the domain boundaries. Consequently, in thermomechanics, the definition of an isolated system has been introduced, which, additionally, does not allow for an exchange of none of these.

[3]Thereby, also excluding, for instance, chemical reactions, which may act as mass source or mass sink.

density associated with the constituent φ^α, which can used to describe mass-exchange processes among the particular constituents if $\hat{\rho}^\alpha \neq 0$.
The local forms of the overall aggregate and the partial mass balance are

$$\dot{\rho} + \rho \operatorname{div} \dot{\mathbf{x}} = 0 \,, \qquad (\rho^\alpha)'_\alpha + \rho^\alpha \operatorname{div} \overset{\prime}{\mathbf{x}}_\alpha = \hat{\rho}^\alpha \,. \tag{2.28}$$

Therein, $\operatorname{div}(\cdot) = \operatorname{grad}(\cdot) \cdot \mathbf{I}$ is the divergence operator. According to Truesdell's first metaphysical principle, a comparison of $(2.28)_1$ and $(2.28)_2$ gives

$$\rho = \sum_\alpha \rho^\alpha \,, \qquad \sum_\alpha \hat{\rho}^\alpha = 0 \,. \tag{2.29}$$

Balance of linear momentum

The balance of momentum states that the change of momentum is driven by forces from the vicinity (e. g. contact forces), forces from a distance (e. g. gravitational forces) and by the momentum production. In particular, the temporal change of the overall momentum of the aggregate and of the momentum of the constituent φ^α within a body $\mathcal{B}$ is given by

$$\begin{aligned} \frac{\mathrm{d}}{\mathrm{d}t} \int_{\mathcal{B}} \rho \, \dot{\mathbf{x}} \, \mathrm{d}v &= \int_{\partial\mathcal{B}} \mathbf{T}\mathbf{n} \, \mathrm{d}a + \int_{\mathcal{B}} \rho \, \mathbf{b} \, \mathrm{d}v + \int_{\mathcal{B}} \hat{\mathbf{s}} \, \mathrm{d}v \,, \\ \frac{\mathrm{d}_\alpha}{\mathrm{d}t} \int_{\mathcal{B}} \rho^\alpha \, \overset{\prime}{\mathbf{x}}_\alpha \, \mathrm{d}v &= \int_{\partial\mathcal{B}} \mathbf{T}^\alpha \mathbf{n} \, \mathrm{d}a + \int_{\mathcal{B}} \rho^\alpha \, \mathbf{b}^\alpha \, \mathrm{d}v + \int_{\mathcal{B}} \hat{\mathbf{s}}^\alpha \, \mathrm{d}v \,. \end{aligned} \tag{2.30}$$

Therein, $\mathbf{b}$ and $\mathbf{b}^\alpha$ denote the body forces of the overall aggregate and of the constituent, respectively, both defined per unit volume. Furthermore, $\hat{\mathbf{s}}$ and $\hat{\mathbf{s}}^\alpha$ are the momentum productions of the overall aggregate and the constituent φ^α, respectively, where the former, due to the momentum conserving property of the overall aggregate, $\hat{\mathbf{s}} = \mathbf{0}$ holds.
The local form of the momentum balances of the overall aggregate and of the individual constituent φ^α are given with the help of $(2.28)_1$ and $(2.28)_2$ by

$$\rho \, \ddot{\mathbf{x}} = \operatorname{div} \mathbf{T} + \rho \, \mathbf{b} \,, \qquad \rho^\alpha \, \overset{\prime\prime}{\mathbf{x}}_\alpha = \operatorname{div} \mathbf{T}^\alpha + \rho^\alpha \, \mathbf{b}^\alpha + \hat{\mathbf{p}}^\alpha \,. \tag{2.31}$$

By exploiting Truesdell's first principle, a comparison of $(2.31)_1$ and $(2.31)_2$, identifies the following relations, see de Boer & Ehlers [23]:

$$\begin{aligned} \rho \, \dot{\mathbf{x}} &= \sum_\alpha \rho^\alpha \, \overset{\prime}{\mathbf{x}}_\alpha \,, & \mathbf{T} &= \sum_\alpha (\mathbf{T}^\alpha - \rho^\alpha \, \mathbf{d}_\alpha \otimes \mathbf{d}_\alpha) \,, \\ \rho \, \mathbf{b} &= \sum_\alpha \rho^\alpha \, \mathbf{b}^\alpha \,, & \mathbf{0} &= \sum_\alpha \hat{\mathbf{s}}^\alpha = \sum_\alpha (\hat{\mathbf{p}}^\alpha + \hat{\rho}^\alpha \, \overset{\prime}{\mathbf{x}}_\alpha) \,, \\ \rho \, \ddot{\mathbf{x}} &= \sum_\alpha [\, \rho^\alpha \overset{\prime\prime}{\mathbf{x}}_\alpha - \operatorname{div}(\rho^\alpha \, \mathbf{d}_\alpha \otimes \mathbf{d}_\alpha) + \hat{\rho}^\alpha \overset{\prime}{\mathbf{x}}_\alpha] \,. \end{aligned} \tag{2.32}$$

Therein, $\hat{\mathbf{s}} = \hat{\mathbf{p}}^\alpha + \hat{\rho}^\alpha \, \overset{\prime}{\mathbf{x}}_\alpha$ denotes the momentum production, which is composed of a direct momentum production $\hat{\mathbf{p}}^\alpha$ driven by the interaction between the individual constituents and a second term associated with momentum production due to mass generation, for instance, via mass exchange between the individual constituents.

Balance of angular momentum

In analogy to the balance of linear momentum, the change of angular momentum of a body $\mathcal{B}$ is driven by near- and far-field actions and by a direct production of angular momentum. However, within the present context, one introduces an arbitrary but spatial fixed reference point, which, for the sake of simplicity is located in the origin of the inertial basis system $\{\mathcal{O}, \mathbf{e}_i\}$. The balances of angular momentum for the overall aggregate and the constituent φ^α read

$$\begin{aligned} \frac{\mathrm{d}}{\mathrm{d}t}\int\limits_{\mathcal{B}} \mathbf{x}\times(\rho\,\dot{\mathbf{x}})\,\mathrm{d}v &= \int\limits_{\partial\mathcal{B}} \mathbf{x}\times\mathbf{T}\,\mathrm{d}a + \int\limits_{\mathcal{B}} \mathbf{x}\times(\rho\,\mathbf{b})\,\mathrm{d}v + \int\limits_{\mathcal{B}} \hat{\mathbf{h}}\,\mathrm{d}v\,, \\ \frac{\mathrm{d}_\alpha}{\mathrm{d}t}\int\limits_{\mathcal{B}} \mathbf{x}\times(\rho^\alpha\,\overset{\prime}{\mathbf{x}}_\alpha)\,\mathrm{d}v &= \int\limits_{\partial\mathcal{B}} \mathbf{x}\times\mathbf{T}^\alpha\,\mathrm{d}a + \int\limits_{\mathcal{B}} \mathbf{x}\times(\rho^\alpha\,\mathbf{b}^\alpha)\,\mathrm{d}v + \int\limits_{\mathcal{B}} \hat{\mathbf{h}}^\alpha\,\mathrm{d}v\,. \end{aligned} \tag{2.33}$$

Therein, $\hat{\mathbf{h}}$ and $\hat{\mathbf{h}}^\alpha$ denote the production of angular momentum of the overall aggregate and of the constituent φ^α, respectively, where, in the former, the momentum conserving property of the overall aggregate holds, i. e. $\hat{\mathbf{h}} = \mathbf{0}$.

With the help of the mass and momentum balances of the overall aggregate, $(2.28)_1$ and $(2.31)_1$, and the partial mass and momentum balances of the constituent φ^α, $(2.28)_2$ and $(2.31)_2$, the local forms of the balance of the angular momentum of the overall aggregate and of the individual constituent read

$$\mathbf{0} = \mathbf{I}\times\mathbf{T}\,, \qquad \mathbf{0} = \mathbf{I}\times\mathbf{T}^\alpha + \hat{\mathbf{h}}^\alpha\,. \tag{2.34}$$

Note that from relation $(2.34)_1$ together with the property of the axial vector[4], the symmetry of the overall Cauchy stress can be concluded, i. e. $\mathbf{T} = \mathbf{T}^T$.

By comparing the balance of angular momentum of the aggregate and of the individual constituent, one can identify

$$\mathbf{0} = \sum_\alpha \hat{\mathbf{h}}^\alpha = \sum_\alpha [\hat{\mathbf{m}}^\alpha + \mathbf{x}\times(\hat{\mathbf{p}}^\alpha + \hat{\rho}^\alpha\,\overset{\prime}{\mathbf{x}}_\alpha)]\,. \tag{2.35}$$

Therein, $\hat{\mathbf{m}}^\alpha = \hat{\mathbf{h}}^\alpha - \mathbf{x}\times(\hat{\mathbf{p}}^\alpha + \hat{\rho}^\alpha\,\overset{\prime}{\mathbf{x}}_\alpha)$ corresponds to the direct production of angular momentum of the constituent φ^α. Note that for the case of non-polar materials (*Cauchy-Boltzmann continua*) with symmetric stress tensors on the microscale, a homogenisation procedure shows that the macroscopic stresses have to be symmetric as well, see Ehlers [59] and Hassanizadeh & Gray [95]. Consequently, $\mathbf{T}^\alpha = (\mathbf{T}^\alpha)^T \rightarrow \hat{\mathbf{m}}^\alpha \equiv \mathbf{0}$.

2.3.2 Thermodynamical balance laws

In addition to the previously introduced mechanical balances, the thermodynamical balance laws, in particular, the balances of energy and entropy, are provided. Note that, as

[4]The axial vector $\overset{A}{\mathbf{a}}$ is given by $2\,\overset{A}{\mathbf{a}} = \mathbf{I}\times\mathbf{A} = \overset{3}{\mathbf{E}}\mathbf{A}^T$, where $\overset{3}{\mathbf{E}}$ is the Ricci permuation tensor with the property $\mathbf{a}\times\mathbf{b} = \overset{3}{\mathbf{E}}(\mathbf{a}\otimes\mathbf{b})$.

thermal effects are neglected within the scope of the present monograph, the balance of energy is not utilised by means a of governing balance relation, instead it merely serves the simplification of the entropy balance, which is important for thermodynamically consistent material modelling.

Balance of energy

The balance of energy, also known as the first law of thermodynamics, states that the temporal change of the sum of the internal energy $\mathcal{E}$ and the kinetic energy $\mathcal{K}$ of a body $\mathcal{B}$ is driven by the mechanical power $\mathcal{L}$ and non-mechanical power $\mathcal{Q}$ both applied by the near- and far-field actions. In an abstract representation, the balance of energy reads

$$\frac{\mathrm{d}}{\mathrm{d}t}\left[\,\mathcal{E}(\mathcal{B},t)+\mathcal{K}(\mathcal{B},t)\,\right]=\mathcal{L}(\mathcal{B},t)+\mathcal{Q}(\mathcal{B},t)\,. \tag{2.36}$$

The balance of energy can be given for the overall mixture and the constituent φ^α:

$$\begin{aligned}
&\frac{\mathrm{d}}{\mathrm{d}t}\int_{\mathcal{B}}\rho\,(\varepsilon+\tfrac{1}{2}\,\dot{\mathbf{x}}\cdot\dot{\mathbf{x}})\,\mathrm{d}v=\int_{\partial\mathcal{B}}(\mathbf{T}^T\dot{\mathbf{x}}-\mathbf{q})\cdot\mathbf{n}\,\mathrm{d}a+\int_{\mathcal{B}}\rho\,(\mathbf{b}\cdot\dot{\mathbf{x}}+r)\,\mathrm{d}v+\int_{\mathcal{B}}\hat{e}\,\mathrm{d}v\,,\\
&\frac{\mathrm{d}_\alpha}{\mathrm{d}t}\int_{\mathcal{B}}\rho^\alpha\,(\varepsilon^\alpha+\tfrac{1}{2}\,\overset{\prime}{\mathbf{x}}_\alpha\cdot\overset{\prime}{\mathbf{x}}_\alpha)\,\mathrm{d}v=\int_{\partial\mathcal{B}}[\,(\mathbf{T}^\alpha)^T\overset{\prime}{\mathbf{x}}_\alpha-\mathbf{q}^\alpha\,]\cdot\mathbf{n}\,\mathrm{d}a+\int_{\mathcal{B}}\rho^\alpha\,(\mathbf{b}^\alpha\cdot\overset{\prime}{\mathbf{x}}_\alpha+r^\alpha)\,\mathrm{d}v+\int_{\mathcal{B}}\hat{e}^\alpha\,\mathrm{d}v\,.
\end{aligned} \tag{2.37}$$

Therein, $\mathbf{q}$ and $\mathbf{q}^\alpha$ denote the energy influx, r and r^α the non-mechanical action from the distance, and $\hat{e}$ and $\hat{e}^\alpha$ the energy productions all associated with the overall aggregate and the constituents φ^α, respectively. Note that within the present scope, the overall aggregate is energy conserving, i. e. $\hat{e}=0$.

The local forms of the energy balance of the overall aggregate and and the individual constituent invoking the total and partial mass and momentum balances, respectively, read

$$\begin{aligned}
&\rho\,\dot{\varepsilon}=\mathbf{T}\cdot\mathbf{L}-\operatorname{div}\mathbf{q}+\rho\,r\,, \qquad && \rho^\alpha\,(\varepsilon^\alpha)'_\alpha=\mathbf{T}^\alpha\cdot\mathbf{L}_\alpha-\operatorname{div}\mathbf{q}^\alpha+\rho^\alpha\,r^\alpha+\hat{\varepsilon}^\alpha\,,\\
&&& \text{where}\qquad \hat{e}^\alpha=\hat{\varepsilon}^\alpha+\hat{\mathbf{p}}^\alpha\cdot\overset{\prime}{\mathbf{x}}_\alpha+\hat{\rho}^\alpha\,(\varepsilon^\alpha+\tfrac{1}{2}\,\overset{\prime}{\mathbf{x}}_\alpha\cdot\overset{\prime}{\mathbf{x}}_\alpha)\,.
\end{aligned} \tag{2.38}$$

Therein, the expression of the energy production $\hat{e}^\alpha$ of the constituent φ^α contains (in the order of appearance), contributions from a direct internal energy production, e. g. from a chemical reaction, the direct momentum production and a part related to the mass exchange between the individual constituents.

Through a comparison of the energy balance of the aggregate with the energy balance of

the individual constituents, the following relations can be identified:

$$\begin{aligned}
\varepsilon &= \frac{1}{\rho}\sum_{\alpha}\rho^{\alpha}\left(\varepsilon^{\alpha}+\tfrac{1}{2}\,\mathbf{d}_{\alpha}\cdot\mathbf{d}_{\alpha}\right),\\
\mathbf{q} &= \sum_{\alpha}\left[\,\mathbf{q}^{\alpha}-(\mathbf{T}^{\alpha})^{T}\mathbf{d}_{\alpha}+\rho^{\alpha}\,\varepsilon^{\alpha}\mathbf{d}_{\alpha}+\tfrac{1}{2}\,\rho^{\alpha}\left(\mathbf{d}_{\alpha}\cdot\mathbf{d}_{\alpha}\right)\mathbf{d}_{\alpha}\,\right],\\
r &= \frac{1}{\rho}\sum_{\alpha}\rho^{\alpha}\left(r^{\alpha}+\mathbf{b}^{\alpha}\cdot\mathbf{d}_{\alpha}\right),\\
0 &= \sum_{\alpha}\hat{e}^{\alpha}=\sum_{\alpha}\left[\,\hat{\varepsilon}^{\alpha}+\hat{\mathbf{p}}^{\alpha}\cdot\overset{\prime}{\mathbf{x}}_{\alpha}+\hat{\rho}^{\alpha}\left(\varepsilon+\tfrac{1}{2}\,\overset{\prime}{\mathbf{x}}_{\alpha}\cdot\overset{\prime}{\mathbf{x}}_{\alpha}\right)\right].
\end{aligned}\tag{2.39}$$

Balance of entropy

The balance of entropy states that the temporal change of the entropy $\mathcal{H}$ in a body $\mathcal{B}$ is governed by the external entropy supply $\mathcal{S}_e$ and the internal production of entropy $\mathcal{S}_i$, i. e.

$$\frac{\mathrm{d}}{\mathrm{d}t}\,\mathcal{H}(\mathcal{B},t)=\mathcal{S}_i(\mathcal{B},t)+\mathcal{S}_e(\mathcal{B},t)\,.\tag{2.40}$$

The balance of entropy can be written for the overall aggregate and the individual constituent φ^{α} yielding

$$\begin{aligned}
\frac{\mathrm{d}}{\mathrm{d}t}\int_{\mathcal{B}}\rho\,\eta\,\mathrm{d}v &= -\int_{\partial\mathcal{B}}\frac{\mathbf{q}}{\theta}\cdot\mathbf{n}\,\mathrm{d}a+\int_{\mathcal{B}}\frac{\rho\,r}{\theta}\,\mathrm{d}v+\int_{\mathcal{B}}\hat{\eta}\,\mathrm{d}v\,,\\
\frac{\mathrm{d}_{\alpha}}{\mathrm{d}t}\int_{\mathcal{B}}\rho^{\alpha}\,\eta^{\alpha}\,\mathrm{d}v &= -\int_{\partial\mathcal{B}}\frac{\mathbf{q}^{\alpha}}{\theta^{\alpha}}\cdot\mathbf{n}\,\mathrm{d}a+\int_{\mathcal{B}}\frac{\rho^{\alpha}\,r^{\alpha}}{\theta^{\alpha}}\,\mathrm{d}v+\int_{\mathcal{B}}\hat{\eta}^{\alpha}\,\mathrm{d}v\,.
\end{aligned}\tag{2.41}$$

Therein, η and η^{α} denote the entropy density, θ and θ^{α} the absolute Kelvin's temperature, and $\hat{\eta}$ and $\hat{\eta}^{\alpha}$ the entropy production each associated with the overall mixture and the constituent φ^{α}, respectively. Moreover, note that the relations $\rho\,r/\theta$, $\rho^{\alpha}\,r^{\alpha}/\theta^{\alpha}$, $\mathbf{q}/\theta$ and $\mathbf{q}^{\alpha}/\theta^{\alpha}$ are introduced as *a priori* constitutive assumptions, see Ehlers [54, 58, 60] and references therein.

By incorporating the overall and aggregate mass balances, the local forms of the entropy inequality of the overall aggregate and of the constituents φ^{α}, respectively, read

$$\rho\,\dot{\eta}=-\mathrm{div}\,\frac{\mathbf{q}}{\theta}+\frac{\rho\,r}{\theta}+\hat{\eta}\,,\qquad \rho^{\alpha}\,(\eta^{\alpha})'_{\alpha}=-\mathrm{div}\,\frac{\mathbf{q}^{\alpha}}{\theta^{\alpha}}+\frac{\rho^{\alpha}\,r^{\alpha}}{\theta^{\alpha}}+\hat{\zeta}^{\alpha}\,,\qquad \text{where}\quad \hat{\eta}^{\alpha}=\hat{\zeta}^{\alpha}+\hat{\rho}^{\alpha}\eta^{\alpha}\,.\tag{2.42}$$

Therein, $\hat{\zeta}^{\alpha}$ is the direct entropy production associated with the constituent φ^{α}. Finally, the entropy inequality of the overall aggregate is obtained by *a priory* assuming that the entropy production of the mixture is always equal (fully reversible processes) or larger than zero (dissipative actions), i. e. $\hat{\eta}\geq 0$. Consequently, one obtains

$$\hat{\eta}=\sum_{\alpha}\hat{\eta}^{\alpha}=\sum_{\alpha}\left[\,\rho^{\alpha}(\eta^{\alpha})'_{\alpha}+\hat{\rho}^{\alpha}\eta^{\alpha}+\mathrm{div}\,\frac{\mathbf{q}^{\alpha}}{\theta^{\alpha}}-\frac{\rho^{\alpha}\,r^{\alpha}}{\theta^{\alpha}}\,\right]\geq 0\,.\tag{2.43}$$

With the help of the energy balance and the definition of the Helmholtz free energy $\psi^\alpha := \varepsilon^\alpha - \theta^\alpha \eta^\alpha$, the relation (2.43) can be reformulated and yields the so-called Clausius-Duhem inequality, viz.:

$$\begin{aligned} \sum_\alpha \frac{1}{\theta^\alpha} \Big\{ \mathbf{T}^\alpha \cdot \mathbf{L}_\alpha - \rho^\alpha \left[(\psi^\alpha)'_\alpha + (\theta^\alpha)'_\alpha \eta^\alpha \right] - \hat{\mathbf{p}}^\alpha \cdot \overset{'}{\mathbf{x}}_\alpha - \\ - \hat{\rho^\alpha} (\psi^\alpha + \tfrac{1}{2} \overset{'}{\mathbf{x}}_\alpha \cdot \overset{'}{\mathbf{x}}_\alpha) - \frac{\mathbf{q}^\alpha}{\theta^\alpha} \cdot \operatorname{grad} \theta^\alpha + \hat{e}^\alpha \Big\} \quad \geq \quad 0 \,. \end{aligned} \tag{2.44}$$

Chapter 3:
Constitutive Models

The addressed Abaqus-PANDAS co-simulation approach offers a wide range of application possibilities. In order to illustrate its diversity, selected volume-coupled multi-field problems from different engineering disciplines, in particular, soil mechanics and multiphasic flow processes, are solved as showcases. In this regard, proceeding from the previously discussed TPM modelling framework, the present chapter is dedicated to the derivation of the underlying material models, where, initially, a more general dynamic triphasic model is set up. In particular, the model comprises an elasto-plastic porous scaffold incorporating an isotropic-kinematic hardening model and two pore fluids, namely the incompressible pore liquid and the compressible pore gas, both percolating independently through the pore space. Subsequently, having the efficient solution of a particular physical process in mind, the dynamic triphasic model will be simplified, such that more dedicated models tailored to specific application scenarios are obtained. In particular, the simplification yields the quasi-static triphasic model, which is constrained to slow processes, and the dynamic hybrid model, where the pore space is occupied by an inseparable mixture of pore liquid and pore gas. Note that, from the latter, furthermore the dynamic liquid-saturated model is obtained.

3.1 Dynamic Triphasic Model

The triphasic model consists of the solid skeleton ($\alpha = S$), the materially incompressible pore liquid ($\alpha = L$) and the materially compressible pore gas ($\alpha = G$). In order to simplify the upcoming derivation process, the following modelling constraints are imposed:

Prelimary constraints	
isothermal conditions:	$\theta^\alpha = \theta = \text{const.}$
equal body forces:	$\rho^\alpha \mathbf{b}^\alpha = \rho^\alpha \mathbf{g}$
no mass production/mass exchange:	$\hat{\rho}^\alpha = 0$
incompressible solid/liquid:	$\rho^{SR} = \text{const.}\,,\ \rho^{\mathrm{LR}} = \text{const.}$
compressible gas:	$\rho^{GR} \neq \text{const.}$
small deformations:	$\mathbf{E}_S \approx \mathbf{A}_S$
	$\mathbf{T}^S \approx \boldsymbol{\tau}^S \approx \mathbf{P}^S \approx \mathbf{S}^S$
	$\mathbf{T}^S = (\mathbf{T}^S)^T$

(3.1)

In particular, aiming at the investigation of isothermal processes, the temperature of the individual constituents are assumed to be constant, i. e. $\theta = \theta^\alpha = \text{const.}$ Moreover, the

individual phases are exposed to the same body forces, viz. gravitational acceleration, i. e. $\rho^\alpha \mathbf{b}^\alpha = \rho^\alpha \mathbf{g}$, where $\mathbf{g}$ denotes the gravitational acceleration vector. Furthermore, mass production, and thereby mass-exchange processes between the individual constituents, are prohibited, i. e. $\hat{\rho}^\alpha = 0$. The solid and the liquid constituents are materially incompressible, i. e. the realistic solid and liquid densities, ρ^{SR} and ρ^{LR}, are constant, while the pore gas is treated as materially compressible, i. e. the realistic gas density ρ^{GR} is variable.

The deformation of the solid skeleton is confined to the small-strain regime. Consequently, there is no need to distinguish the strain and stress measures in the different configurations, i. e. $\mathbf{E}_S \approx \mathbf{A}_S$ and $\mathbf{T}^S \approx \boldsymbol{\tau}^S \approx \mathbf{P}^S \approx \mathbf{S}^S$. Moreover, aiming also at the simulation of geomechanical problems, the deformation behaviour of granular assemblies is of especial interest. In particular, the macroscopic behaviour of granular materials is mainly governed by the micro-structural grain motions, e. g., grain sliding and rolling[1]. However, according to Ehlers & Scholz [69], the grain rotations can be neglected when the solid deformation is confined to the small strain regime and therefore, for the purpose of this monograph, the solid skeleton is treated as a non-polar material. In consequence, for the solid skeleton, the partial stress tensor is assumed to be symmetric, i. e. $\mathbf{T}^S = (\mathbf{T}^S)^T$, and only the symmetric part of the strain-rate tensor $\mathbf{L}_S$, viz. $\mathbf{D}_S$, is utilised.

3.1.1 Balance relations

To begin with, the governing balance laws, in particular, the mass and momentum balances, are derived. Additionally, the entropy inequality is evaluated in order to identify constraints for the sake of a thermodynamically consistent modelling procedure.

Balance of mass

In the absence of mass production or mass exchange processes, i. e. $\hat{\rho}^\alpha = 0$, the local mass balance $(2.28)_2$ reads

$$(\rho^\alpha)'_\alpha \; + \; \rho^\alpha \operatorname{div} \overset{\prime}{\mathbf{x}}_\alpha \; = \; 0 \,. \tag{3.2}$$

At first, the attention is drawn to the solid skeleton ($\alpha = S$). With the help of the incompressibility constraint of the solid phase, $\rho^{SR} = \text{const.} \rightarrow (\rho^{SR})'_S = 0$, the solid mass balance can be reformulated to yield the solid volume balance,

$$(\rho^S)'_S + \rho^S \operatorname{div} \overset{\prime}{\mathbf{x}}_S = (n^S \rho^{SR})'_S + \rho^S \operatorname{div} \overset{\prime}{\mathbf{x}}_S = 0 \qquad \longrightarrow \qquad (n^S)'_S + n^S \operatorname{div} \overset{\prime}{\mathbf{x}}_S = 0 \,, \tag{3.3}$$

which can be integrated analytically over time, see, e. g., Wagner [196]:

$$n^S = n^S_{0S} \, (\det \mathbf{F}_S)^{-1} \,. \tag{3.4}$$

By incorporating the small-strain assumption, a linearisation of $\det \mathbf{F}_S$ around the undeformed state is reasonable. Consequently, the solid volume fraction is computed via

$$n^S = n^S_{0S} \, (1 - \operatorname{Div}_S \mathbf{u}_S) \approx n^S_{0S} \, (1 - \operatorname{div} \mathbf{u}_S) \,. \tag{3.5}$$

[1] Therefore, granular materials are generally denoted as micro-polar materials

Therein, n^S_{0S} denotes the solid volume fraction in the reference configuration. Moreover, $\mathrm{Div}_S(\cdot)$ and $\mathrm{div}(\cdot)$ are the divergence operator with respect to the reference and the current configuration, respectively.

Next, the mass balances of the pore-fluid constituents are elaborated. In particular, the partial mass balances (3.2) are rewritten for the pore liquid ($\alpha = L$) and for the pore gas ($\alpha = G$), where the former can be further simplified to a volume balance by incorporating the materially incompressibility of the pore liquid, viz. $\rho^{LR} = \text{const.} \rightarrow (\rho^{LR})'_L = 0$. Subsequently, the volume balance of the pore liquid and the mass balance of the pore gas read

$$(n^L)'_L + n^L \mathrm{div}\,\mathbf{v}_L = 0 \qquad \text{and} \qquad (\rho^G)'_G + \rho^G \mathrm{div}\,\mathbf{v}_G = 0\,, \tag{3.6}$$

respectively, which are reformulated, by utilising the material time derivative $(2.6)_2$,

$$(n^L)'_L \;=\; (n^L)'_S \;+\; \mathrm{grad}\, n^L \cdot \mathbf{w}_L \qquad \text{and} \qquad (\rho^G)'_G \;=\; (\rho^G)'_S \;+\; \mathrm{grad}\, \rho^G \cdot \mathbf{w}_G\,, \tag{3.7}$$

to yield their final forms:

$$\begin{aligned} 0 &= (n^L)'_S + n^L\, \mathrm{div}\,(\mathbf{u}_S)'_S + \mathrm{div}\,(n^L \mathbf{w}_L)\,, \\ 0 &= \underbrace{n^G (\rho^{GR})'_S + \rho^{GR} (n^G)'_S}_{= (\rho^G)'_S = (n^G \rho^{GR})'_S} + n^G \rho^{GR}\, \mathrm{div}\,(\mathbf{u}_S)'_S + \mathrm{div}\,(n^G \rho^{GR}\, \mathbf{w}_G)\,. \end{aligned} \tag{3.8}$$

Balance of momentum

By incorporating the assumption of equal gravitational acceleration, i. e. $\rho^\alpha \mathbf{b}^\alpha = \rho^\alpha \mathbf{g}$, the partial momentum balance $(2.31)_2$ is reformulated to read

$$\rho^\alpha \overset{\prime\prime}{\mathbf{x}}_\alpha = \mathrm{div}\,\mathbf{T}^\alpha + \rho^\alpha\, \mathbf{g} + \hat{\mathbf{p}}^\alpha\,. \tag{3.9}$$

Subsequently, (3.9) is rewritten with respect to the individual constituents, i. e. $\alpha \in \{S, L, G\}$, in order to obtain the particular momentum balances of the solid, the pore liquid and the pore gas,

$$\begin{aligned} \rho^S \overset{\prime\prime}{\mathbf{x}}_S &= \mathrm{div}\,\mathbf{T}^S + \rho^S \mathbf{g} + \hat{\mathbf{p}}^S\,, \\ \rho^L \left[\, (\mathbf{v}_L)'_S + (\mathrm{grad}\,\mathbf{v}_L)\, \mathbf{w}_L \,\right] &= \mathrm{div}\,\mathbf{T}^L + \rho^L \mathbf{g} + \hat{\mathbf{p}}^L\,, \\ \rho^G \left[\, (\mathbf{v}_G)'_S + (\mathrm{grad}\,\mathbf{v}_G)\, \mathbf{w}_G \,\right] &= \mathrm{div}\,\mathbf{T}^G + \rho^L \mathbf{g} + \hat{\mathbf{p}}^G\,, \end{aligned} \tag{3.10}$$

respectively. Note that, therein, the material time derivatives $(2.9)_1$ have been exploited. Instead of proceeding with the respective momentum balance of the individual phases, it is more convenient in most applications to replace the solid momentum balance by the momentum balance of the overall aggregate. It is obtained via a summation of the partial momentum balances and reads

$$\begin{aligned} \rho^S (\mathbf{v}_S)'_S + \rho^L \left[\, (\mathbf{v}_L)'_S + (\mathrm{grad}\,\mathbf{v}_L)\, \mathbf{w}_L \,\right] + \rho^G \left[\, (\mathbf{v}_G)'_S + (\mathrm{grad}\,\mathbf{v}_G)\, \mathbf{w}_G \,\right] = \\ = \mathrm{div}\,(\mathbf{T}^S + \mathbf{T}^L + \mathbf{T}^G) + (\rho^S + \rho^L + \rho^G)\, \mathbf{b}\,, \end{aligned} \tag{3.11}$$

where, according to $(2.32)_4$, the overall aggregate is momentum conserving and, therefore, the sum of the individual direct momentum productions has to vanish, i. e.

$$\hat{\mathbf{p}}^S + \hat{\mathbf{p}}^L + \hat{\mathbf{p}}^G = \mathbf{0}\,. \tag{3.12}$$

Entropy inequality

In contrast to the previously elaborated balance laws, the entropy inequality does not provide an additional governing relation. Instead, it serves for the thermodynamically consistent modelling by providing constraints to be imposed on the constitutive modelling process. In this regard, constrained to isothermal processes, i. e. $\theta = \theta^\alpha = \text{const.} \rightarrow \operatorname{grad}\theta^\alpha = \mathbf{0}, (\theta)'_\alpha = 0$, and neglecting of mass-productions processes, i. e. $\hat{\rho}^\alpha = 0$, the Clausius-Duhem inequality (2.43) recasts to the so-called Clausius-Planck inequality:

$$\mathcal{D}_{\text{int}} = \sum_\alpha \left[\, \mathbf{T}^\alpha \cdot \mathbf{D}_\alpha - \rho^\alpha (\psi^\alpha)'_\alpha - \hat{\mathbf{p}}^\alpha \cdot \overset{\prime}{\mathbf{x}}_\alpha \,\right] \geq 0\,. \tag{3.13}$$

Therein, $\mathcal{D}_{\text{int}}$ represents the internal dissipation of the mechanical energy. For $\mathcal{D}_{\text{int}} = 0$ the process is fully reversible, whereas for $\mathcal{D}_{\text{int}} > 0$ the process is irreversible as a consequence of dissipative actions, such as inelastic deformations of the solid skeleton, or the viscous pore-fluid motion.

For arbitrary processes, the saturation constraint $(2.1)_1$ has to be always fulfilled. Consequently, it needs to be imposed as a side constraint on the thermomechanical problem. In particular, its material time derivative with respect to the motion of the solid skeleton, herein utilising the mass balance of the pore gase and the volume balance of the pore liquid, see Appendix A for details,

$$\begin{aligned} 1 = n^S + n^L + n^G \quad \longrightarrow \quad 0 &= -\left[(n^S)'_S + (n^L)'_S + (n^G)'_S\right] \\ &= n^S \operatorname{div}\mathbf{v}_S + \operatorname{grad} n^L \cdot \mathbf{w}_L + n^L \operatorname{div}\mathbf{v}_L + \\ &\quad + \frac{n^G}{\rho^{GR}} (\rho^{GR})'_G + \operatorname{grad} n^G \cdot \mathbf{w}_G + n^G \operatorname{div}\mathbf{v}_G\,, \end{aligned} \tag{3.14}$$

is multiplied with the yet undetermined Lagrange multiplier $\mathcal{P}$ and added to the entropy inequality (3.13):

$$\begin{aligned} 0 \;\leq\; & \underbrace{(\,\mathbf{T}^S + n^S \mathcal{P}\,\mathbf{I}\,)}_{\mathbf{T}^S_E} \cdot \mathbf{D}_S + \underbrace{(\,\mathbf{T}^L + n^L \mathcal{P}\,\mathbf{I}\,)}_{\mathbf{T}^L_E} \cdot \mathbf{D}_L + \underbrace{(\,\mathbf{T}^G + n^G \mathcal{P}\,\mathbf{I}\,)}_{\mathbf{T}^G_E} \cdot \mathbf{D}_G - \\ & - \left[\,\rho^S (\psi^S)'_S + \rho^L (\psi^L)'_L + \rho^G (\psi^G)'_G\,\right] + \mathcal{P}\,\frac{n^G}{\rho^{GR}}\,(\rho^{GR})'_G - \\ & - \underbrace{(\,\hat{\mathbf{p}}^L - \mathcal{P}\operatorname{grad} n^L\,)}_{\hat{\mathbf{p}}^L_E} \cdot \mathbf{w}_L - \underbrace{(\,\hat{\mathbf{p}}^G - \mathcal{P}\operatorname{grad} n^G\,)}_{\hat{\mathbf{p}}^G_E} \cdot \mathbf{w}_G\,. \end{aligned} \tag{3.15}$$

Herein, proceeding from the symmetry of the strain tensor, the relation $\operatorname{div}(\mathbf{v}_\alpha) = \mathbf{L}_\alpha \cdot \mathbf{I} = \mathbf{D}_\alpha \cdot \mathbf{I}$ has been utilised. Furthermore, the relationships $\hat{\mathbf{p}}^S = -(\hat{\mathbf{p}}^L + \hat{\mathbf{p}}^G)$, see (3.12),

and $\mathbf{w}_\beta = \mathbf{v}_\beta - \mathbf{v}_S$, see $(2.9)_1$, have been exploited. In (3.15), $(\cdot)^\alpha_E$ denote the so-called extra quantities, see Truesdell & Noll [188], and ψ^α are the Helmholtz free energies. As these quantities cannot be evaluated from the balance equations with the knowledge of the initial conditions and the full state of motion, following the principle of *determinism*, suitable constitutive relations for yet undefined response functions

$$\mathcal{R} = \{\, \psi^\alpha\,,\ \mathbf{T}^\alpha_E\,,\ \hat{\mathbf{p}}^\beta_E \,\} \tag{3.16}$$

need to be proposed. Proceeding from the principle of *equipresence*, the response functions $\mathcal{R}(\mathcal{V})$ depend on a set of process variables $\mathcal{V}$, which define the initial and the current state of the aggregate. With respect to multiphasic materials under isothermal conditions, the following set of process variables can be specified, see Ehlers [54, 55]:

$$\mathcal{V} = \{\, n^\alpha,\, \operatorname{grad} n^\alpha,\, \rho^{\alpha R},\, \operatorname{grad} \rho^{\alpha R},\, \mathbf{F}_S,\, \operatorname{grad} \mathbf{F}_S,\, \overset{\prime}{\mathbf{x}}_\beta,\, \operatorname{grad} \overset{\prime}{\mathbf{x}}_\beta,\, \mathbf{X}_\alpha \,\}\,. \tag{3.17}$$

In what follows, the set of process variables is simplified, thereby exploiting the fundamental thermodynamical principles of *equipresence*, *determinism*, *local action*, *frame indifference* and *dissipation*, see, e. g., Truesdell [187], Noll [148] and Coleman & Noll [42]. At first, following the argumentation of Bowen [25, 26], merely actions at the material point P^α and its immediate vicinity are considered and, consequently, the principle of *local actions* is applied. Moreover, assuming the homogeneous distribution of the material quantities in the reference configuration, the dependency of $\mathbf{X}_\alpha$ is eliminated. In order to account for the principle of *frame indifference*, the pore-fluid velocities $\overset{\prime}{\mathbf{x}}_\beta$ are, on the one hand, replaced by the seepage velocities $\mathbf{w}_\beta$, and, on the other hand, by the symmetric part $\mathbf{D}_\beta$ of the velocity gradient. Both are independent of the position of the observer, see Ehlers [54]. Finally, the dependencies of the volume fractions n^α, with $\alpha \in \{S, L, G\}$, on the remaining process variables, i. e. $n^S = n^S(\mathbf{F}_S)$, $n^L = n^L(n^F, s^L)$ and $n^G = n^G(n^F, s^G)$, are exploited. Note that in the latter two, the saturation condition (2.2) has been utilised. The relationship $n^S = n^S(\mathbf{F}_S)$ motivates the elimination of n^S and, consequently, of n^F due to the dependency $n^F = n^F(n^S)$. Subsequently, the saturation condition (2.2), i. e. $s^L = s^L(s^G)$, suggests the drop of either the pore-liquid or the pore-gas saturation from the set of process variables.

In consequence, the following set of process variables is defined:

$$\tilde{\mathcal{V}} = \{s^L,\, \rho^{GR},\, \mathbf{F}_S,\, \mathbf{w}_\beta,\, \mathbf{D}_\beta \}\,. \tag{3.18}$$

Following, the principle of *phase separation*, see Ehlers [53], whereupon each constituent depends on its own process variables, the following dependencies on the Helmholtz free energies can be proposed:

$$\psi^S \,=\, \psi^S(\mathbf{F}_S)\,, \quad \psi^L \,=\, \psi^L(s^L)\,, \quad \psi^G \,=\, \psi^G(\rho^{GR})\,. \tag{3.19}$$

At first, the attention is drawn to the evaluation of the dependency $\psi^S(\mathbf{F}_S)$[2]. To begin with, proceeding from the framework of finite elasto-plasticity, the deformation gradient

[2]Note that the dependency $\psi^S(\mathbf{F}_S)$ can also be expressed in terms of the strain measures, e. g., $\psi^S(\mathbf{E}_S)$ or $\psi^S(\mathbf{A}_S)$, as the deformation gradient $\mathbf{F}_S$ can be, via a polar decomposition, split into a rigid body rotation and a stretch. Herein, the former is invariant with respect to the reference frame of an observer (*principle of frame indifference*), see Ehlers [54], or, in other words, the Helmholtz free energy merely depends on the material stretch, but not on the rigid body motions.

$\mathbf{F}_S$ is multiplicatively decomposed in an elastic part $\mathbf{F}_{Se}$ and a plastic part $\mathbf{F}_{Sp}$, thereby, introducing a stress-free intermediate configuration by virtually cutting the body into finite stress-free pieces, see, e. g., Lee [126], Haupt [96], Ehlers [55]. The multiplicative decomposition of the deformation-gradient tensor results in an additive decomposition of the Green-Lagrangean strain tensor $\mathbf{E}_S$, see Lee [126], which can then, under the assumption of small strains, linearised around the reference configuration to obtain the linearised solid strain tensor $\boldsymbol{\varepsilon}_S$, i. e.

$$\begin{aligned} &\mathbf{E}_S = \tfrac{1}{2}(\mathbf{F}_S^T\,\mathbf{F}_S - \mathbf{I}) \qquad \text{with} \qquad \mathbf{F}_S = \mathbf{F}_{Se}\,\mathbf{F}_{Sp} \\ &\longrightarrow \qquad \boldsymbol{\varepsilon}_S = \boldsymbol{\varepsilon}_{Se} + \boldsymbol{\varepsilon}_{Sp} = \operatorname{lin}(\mathbf{E}_{Se} + \mathbf{E}_{Sp}) = \operatorname{lin}\mathbf{E}_S\,. \end{aligned} \tag{3.20}$$

Therein, $\boldsymbol{\varepsilon}_{Se}$ and $\boldsymbol{\varepsilon}_{Sp}$ denote the linearised elastic and plastic parts, respectively, of the linearised total strain tensor,

$$\boldsymbol{\varepsilon}_S := \tfrac{1}{2}(\operatorname{Grad}_S\mathbf{u}_S + \operatorname{Grad}_S^T\mathbf{u}_S)\,. \tag{3.21}$$

Subsequently, the dependencies of the Helmholtz free energy function of the elasto-plastic solid skeleton are elaborated in more detail. In particular, proceeding from purely elastic loading conditions, e. g. during unloading, the change in the partial Cauchy stresses has to be independent of the previous plastic deformations. Therefore, based on an idea of Green & Naghdi [87], the following additive decomposition of the free energy function is proposed:

$$\psi^S(\boldsymbol{\varepsilon}_{Se}, \boldsymbol{\varepsilon}_{Sp}, \alpha_i) = \psi^{Se}(\boldsymbol{\varepsilon}_{Se}) + \psi^{Sp}(\boldsymbol{\varepsilon}_{Sp}, \alpha_i)\,. \tag{3.22}$$

Herein, $\psi^{Se}(\boldsymbol{\varepsilon}_{Se})$ denotes the elastic contribution, whereas $\psi^{Sp}(\boldsymbol{\varepsilon}_{Sp}, \alpha_i)$ is the plastic part governed by the scalar-valued internal variables α_i, which are associated with isotropic-hardening mechanisms, and by the plastic strain tensor $\boldsymbol{\varepsilon}_{Sp}$, which is related to the kinematic-hardening process, see Ehlers [55]. Note that ψ^{Sp} is only active at the onset of plastic deformations. Carrying out the material time derivatives of the Helmholtz free energies with respect to the corresponding constituents gives

$$\begin{aligned} \rho^S_{0S}(\psi^S)'_S &= \rho^S_{0S}\frac{\partial\psi^{Se}}{\partial\boldsymbol{\varepsilon}_{Se}}\cdot(\boldsymbol{\varepsilon}_{Se})'_S + \rho^S_{0S}\frac{\partial\psi^{Sp}}{\partial\boldsymbol{\varepsilon}_{Sp}}\cdot(\boldsymbol{\varepsilon}_{Sp})'_S + \rho^S_{0S}\frac{\partial\psi^{Sp}}{\partial\alpha_i}(\alpha_i)'_S\,, \\ \rho^L(\psi^L)'_L &= \rho^L\frac{\partial\psi^L}{\partial s^L}(s^L)'_L = \\ &= \rho^L\frac{\partial\psi^L}{\partial s^L}\frac{1}{n^F}[(s^L n^F)'_L - s^L(n^F)'_L] = \\ &= \rho^L\frac{\partial\psi^L}{\partial s^L}\frac{1}{n^F}[(n^L)'_L + s^L(n^S)'_L] = \\ &= -\rho^L\frac{\partial\psi^L}{\partial s^L}\frac{1}{n^F}(n^L\operatorname{div}\mathbf{v}_L + s^L n^S\operatorname{div}\mathbf{v}_S - s^L\operatorname{grad}n^S\cdot\mathbf{w}_L)\,, \\ \rho^G(\psi^G)'_G &= \rho^G\frac{\partial\psi^G}{\partial\rho^{GR}}(\rho^{GR})'_G\,. \end{aligned} \tag{3.23}$$

In $(3.23)_2$, the volume balances of the pore liquid and solid skeleton have been exploited[3]. Subsequently, by incorporating the relation $(\boldsymbol{\varepsilon}_S)'_S = (\boldsymbol{\varepsilon}_{Se})'_S + (\boldsymbol{\varepsilon}_{Sp})'_S$ and the assumption of the symmetry of the strain tensors, which gives $\operatorname{div}(\mathbf{v}_\alpha) = \mathbf{I}\cdot\mathbf{D}_\alpha$, the entropy inequality (3.15) is recast to take the form:

$$\begin{aligned} 0 \;\leq\; & (\underbrace{\boldsymbol{\sigma}^S_E + \frac{\rho^L}{n^F}\frac{\partial\psi^L}{\partial s^L}\, s^L n^S \mathbf{I}}_{\boldsymbol{\sigma}^S_{Em}} - \rho^S_{0S}\frac{\partial\psi^{Se}}{\partial\boldsymbol{\varepsilon}_{Se}})\cdot(\boldsymbol{\varepsilon}_{Se})'_S + (\,\mathcal{P}\,\frac{n^G}{\rho^{GR}} - \rho^G\frac{\partial\psi^G}{\partial\rho^{GR}}\,)\,(\rho^{GR})'_G + \\ & + (\underbrace{\boldsymbol{\sigma}^S_E + \frac{\rho^L}{n^F}\frac{\partial\psi^L}{\partial s^L}\, s^L n^S \mathbf{I}}_{\boldsymbol{\sigma}^S_{Em}} - \rho^S_{0S}\frac{\partial\psi^{Sp}}{\partial\boldsymbol{\varepsilon}_{Sp}})\cdot(\boldsymbol{\varepsilon}_{Sp})'_S \;-\; \rho^S_{0S}\frac{\partial\psi^{Sp}}{\partial\alpha_i}\,(\alpha_i)'_S + \\ & + (\underbrace{\mathbf{T}^L_E + \frac{\rho^L}{n^F}\frac{\partial\psi^L}{\partial s^L}\, n^L\mathbf{I}}_{\mathbf{T}^L_{Em}})\cdot\mathbf{D}_L + \mathbf{T}^G_E\cdot\mathbf{D}_G - \hat{\mathbf{p}}^G_E\cdot\mathbf{w}_G - (\underbrace{\hat{\mathbf{p}}^L_E + \frac{\rho^L}{n^F}\frac{\partial\psi^L}{\partial s^L}s^L\operatorname{grad} n^S}_{\hat{\mathbf{p}}^L_{Em}})\cdot\mathbf{w}_L\,. \end{aligned} \tag{3.24}$$

Therein, the summarised terms of the type $(\cdot)^\alpha_{Em}$ denote the pure mechanical extra quantities. In particular, $\boldsymbol{\sigma}^S_{Em}$ is the geometrical linear elastic solid extra stress tensor, and $\mathbf{T}^L_{Em}$ and $\mathbf{T}^G_E$ are the dissipative friction forces of the viscous pore liquid and of the viscous pore gas, respectively.

Following the evaluation procedure of Coleman & Noll [42], any addend has to satisfy the entropy inequality on its own for arbitrary values of the process variables. In particular, from the former two addends, which are denoted as the equilibrium (reversible) part due to their energy-storing capabilities, one can perceive

$$\begin{aligned} (\,\boldsymbol{\sigma}^S_{Em} - \rho^S_{0S}\frac{\partial\psi^{Se}}{\partial\boldsymbol{\varepsilon}_{Se}}\,)\cdot(\boldsymbol{\varepsilon}_{Se})'_S = 0 \;\;&\longrightarrow\;\; \boldsymbol{\sigma}^S_{Em} = \rho^S_{0S}\frac{\partial\psi^{Se}}{\partial\boldsymbol{\varepsilon}_{Se}} = \frac{\partial\Psi^{Se}}{\partial\boldsymbol{\varepsilon}_{Se}}\,, \\ (\,\mathcal{P}\,\frac{n^G}{\rho^{GR}} - \rho^G\frac{\partial\psi^G}{\partial\rho^{GR}}\,)\,(\rho^{GR})'_G = 0 \;\;&\longrightarrow\;\; \mathcal{P} = (\rho^G)^2\frac{\partial\psi^G}{\partial\rho^{GR}}\,. \end{aligned} \tag{3.25}$$

Therein, Ψ^{Se} denotes the volume-specific Helmholtz free energy function. Moreover, by utilising the definitions of the effective Cauchy stresses, $\boldsymbol{\sigma}^S_E$, $\mathbf{T}^L_E$ and $\mathbf{T}^G_E$, and of the direct momentum productions, $\hat{\mathbf{p}}^G_E$ and $\hat{\mathbf{p}}^L_E$ from (3.15), the following relations can be identified from the entropy inequality (3.24):

$$\begin{aligned} \boldsymbol{\sigma}^S_{Em} &= \mathbf{T}^S + (\mathcal{P} + \frac{\rho^L}{n^F}\frac{\partial\psi^L}{\partial s^L}\, s^L)\, n^S\,\mathbf{I}\,, \\ \mathbf{T}^G_E &= \mathbf{T}^G + n^G\mathcal{P}\,\mathbf{I}\,, & \mathbf{T}^L_{Em} &= \mathbf{T}^L + (\mathcal{P} + \frac{\rho^L}{n^F}\frac{\partial\psi^L}{\partial s^L})\, n^L\,\mathbf{I}\,, \\ \hat{\mathbf{p}}^G_E &= \hat{\mathbf{p}}^G - \mathcal{P}\operatorname{grad} n^G\,, & \hat{\mathbf{p}}^L_{Em} &= \hat{\mathbf{p}}^L - \mathcal{P}\operatorname{grad} n^L + \frac{\rho^L}{n^F}\frac{\partial\psi^L}{\partial s^L}s^L\operatorname{grad} n^S\,. \end{aligned} \tag{3.26}$$

[3] On the one hand, the relation $(n^L)'_L = -\operatorname{div}\mathbf{v}_L$, which proceeds from the volume balance of the pore liquid $(3.6)_1$, has been used. On the other hand, the material time derivative of the solid volume fraction with respect to the pore liquid, viz. $(n^S)'_L = (n^S)'_S + \operatorname{grad} n^S\cdot\mathbf{w}_L$, and, herein, the expression $(n^S)'_S = -\operatorname{div}(\mathbf{v}_S)$, which results from the solid volume balance (3.3), has been utilised.

Therewith, following Ehlers [60], the effective pore-gas pressure p^{GR} and the effective pore-liquid pressure p^{LR} can be identified with the help of $(3.25)_4$:

$$p^{GR} := \mathcal{P} = (\rho^G)^2 \frac{\partial \psi^G}{\partial \rho^{GR}}\,, \qquad p^{LR} := \mathcal{P} + \frac{\rho^L}{n^F}\,\frac{\partial \psi^L}{\partial s^L}\,. \tag{3.27}$$

Subsequently, the prominent Dalton's law,

$$p^{FR} = s^L\, p^{LR} \,+\, s^G\, p^{GR}\,, \tag{3.28}$$

is exploited. It states that the effective pressure of the overall pore-fluid mixture p^{FR} is given by the sum of the partial pore-fluid pressures, $s^\beta\, p^{\beta R}$ with $\beta \in \{L, G\}$. In contrast to the effective pressures of a constituent, which act on the area element of the pore space associated with a particular pore-fluid constituent, the partial pressure is applied on an area element related to the entire pore space and can, therefore, be understood as a pore-space averaged pressure. Subsequently, by utilising $(3.27)_1$,$(3.27)_2$ and the saturation condition[4], Daltons law (3.28) can be recast to read

$$p^{FR} = s^L p^{LR} + s^G p^{GR} = s^L(\mathcal{P} + \frac{\rho^L}{n^F}\,\frac{\partial \psi^L}{\partial s^L}) + (1 - s^L)\mathcal{P} = \mathcal{P} + s^L \frac{\rho^L}{n^F}\,\frac{\partial \psi^L}{\partial s^L}\,. \tag{3.29}$$

A comparison between (3.29) and $(3.26)_1$ reveals the relation for the effective pressure of the pore-fluid mixture:

$$\boldsymbol{\sigma}^S_{Em} = \mathbf{T}^S + \underbrace{(\mathcal{P} + \frac{\rho^L}{n^F}\frac{\partial \psi^L}{\partial s^L}\, s^L)}_{p^{FR}}\, n^S\, \mathbf{I}\,. \tag{3.30}$$

In the next step, the entropy inequality (3.24) is investigated with respect to the dissipative actions. In this regard, the reversible contributions are neglected and the remaining parts are gathered in the dissipation inequality. Again, the individual addends have to fulfil the inequality on their own, i. e. they have to be greater or equal to zero, for arbitrary process variables. The dissipation inequality reads

$$\begin{aligned} \mathcal{D} = \overbrace{(\boldsymbol{\sigma}^S_{Em} - \rho^S_{0S}\,\frac{\partial \psi^{Sp}}{\partial \boldsymbol{\varepsilon}_{Sp}}) \cdot (\boldsymbol{\varepsilon}_{Sp})'_S - \rho^S_{0S}\,\frac{\partial \psi^{Sp}}{\partial \alpha_i}\,(\alpha_i)'_S}^{\mathcal{D}_S \geq 0} + \\ \underbrace{+\,\mathbf{T}^L_{Em}\cdot\mathbf{D}_L - \hat{\mathbf{p}}^L_{Em}\cdot\mathbf{w}_L + \mathbf{T}^G_E\cdot\mathbf{D}_G - \hat{\mathbf{p}}^G_E\cdot\mathbf{w}_G}_{\mathcal{D}_F \geq 0} \geq 0\,. \end{aligned} \tag{3.31}$$

At first, the attention is drawn to the examination of the internal dissipation $\mathcal{D}_S$ associated with the solid skeleton. The following constraints can be deduced:

$$(\boldsymbol{\sigma}^S_{Em} - \rho^S_{0S}\,\frac{\partial \psi^{Sp}}{\partial \boldsymbol{\varepsilon}_{Sp}}) \cdot (\boldsymbol{\varepsilon}_{Sp})'_S \geq 0 \qquad \text{and} \qquad -\,\rho^S_{0S}\,\frac{\partial \psi^{Sp}}{\partial \alpha_i}\,(\alpha_i)'_S \geq 0\,. \tag{3.32}$$

[4] In fact, the saturation condition $(2.1)_2$ is reformulated before usage, i. e. $s^G + s^L = 1 \;\rightarrow\; s^G = 1 - s^L$.

Herefrom, following Ehlers [54], the translation tensor associated with the kinematic hardening, i. e. the back-stress tensor $\mathbf{Y}_E^S$, and, according to Avci [10], the internal stresses $t_i = t_i(\alpha_i)$ related to the isotropic hardening, can be identified:

$$\mathbf{Y}_E^S = \rho_{0S}^S \frac{\partial \psi^{Sp}}{\partial \boldsymbol{\varepsilon}_{Sp}}, \qquad t_i = -\rho_{0S}^S \frac{\partial \psi^{Sp}}{\partial \alpha_i}. \tag{3.33}$$

Consequently, the stress tensor $\overline{\boldsymbol{\sigma}}_{Em}^S$ in the shifted principal stress space is computed via

$$\overline{\boldsymbol{\sigma}}_{Em}^S = \boldsymbol{\sigma}_{Em}^S - \mathbf{Y}_E^S. \tag{3.34}$$

Note that the dissipative properties $\mathcal{D}_S$ are only active during plastic deformation.

Following this, the evaluation of the internal dissipations due to the motion of the pore fluids is addressed. To begin with, the dissipation inequality associated with the pore fluids, $\mathcal{D}_F$ in (3.31), is further simplified. In this regard, it can be shown by carrying out a dimensional analysis, see Ehlers *et al.* [64], that the pore-fluid extras stresses $\mathbf{T}_E^\beta$ can be *a priori* neglected in relation to the corresponding direct momentum productions, i. e.

$$\operatorname{div} \mathbf{T}_E^\beta \ll \hat{\mathbf{p}}_E^\beta \qquad \longrightarrow \qquad \mathbf{T}_E^\beta \approx \mathbf{0}. \tag{3.35}$$

Consequently, the dissipation inequality $\mathcal{D}_F$ simplifies to

$$\mathcal{D}_F = -\hat{\mathbf{p}}_{Em}^L \cdot \mathbf{w}_L - \hat{\mathbf{p}}_E^G \cdot \mathbf{w}_G \geq 0, \tag{3.36}$$

which, consequently, motivates an ansatz for $\hat{\mathbf{p}}_{Em}^L$ and $\hat{\mathbf{p}}_E^G$ to be, for instance, negative proportional to the seepage velocities $\mathbf{w}_\beta$, i. e. $\hat{\mathbf{p}}_{Em}^L \propto (-\mathbf{w}_L)$ and $\hat{\mathbf{p}}_E^G \propto (-\mathbf{w}_G)$.

Following this, the mechanical extra momentum production $\hat{\mathbf{p}}_{Em}^L$, see $(3.26)_5$, can be reformulated exploiting the saturation condition[5] and the product rule,

$$\begin{aligned}
\hat{\mathbf{p}}_{Em}^L &= \hat{\mathbf{p}}^L - \mathcal{P}\operatorname{grad} n^L + \frac{\rho^L}{n^F} \frac{\partial \psi^L}{\partial s^L} s^L \operatorname{grad} n^S = \\
&= \hat{\mathbf{p}}^L - \mathcal{P}\operatorname{grad} n^L + \frac{\rho^L}{n^F} \frac{\partial \psi^L}{\partial s^L} [-s^L \operatorname{grad} n^F] = \\
&= \hat{\mathbf{p}}^L - \mathcal{P}\operatorname{grad} n^L + \frac{\rho^L}{n^F} \frac{\partial \psi^L}{\partial s^L} [\operatorname{grad} (s^L n^F) - n^F \operatorname{grad} s^L] = \\
&= \hat{\mathbf{p}}^L - (\mathcal{P} + \frac{\rho^L}{n^F} \frac{\partial \psi^L}{\partial s^L}) \operatorname{grad} n^L - \frac{\rho^L}{n^F} \frac{\partial \psi^L}{\partial s^L} n^F \operatorname{grad} s^L,
\end{aligned} \tag{3.37}$$

and, finally, a comparison with (3.27) identifies

$$\hat{\mathbf{p}}_{Em}^L = \hat{\mathbf{p}}^L - p^{LR} \operatorname{grad} n^L - \frac{\rho^L}{n^F} \frac{\partial \psi^L}{\partial s^L} n^F \operatorname{grad} s^L. \tag{3.38}$$

[5] In fact, the saturation condition, see $(2.1)_1$, is reformulated, i. e. $n^S + n^F = 1 \longrightarrow n^S = 1 - n^F$, from which relation $\operatorname{grad} n^S = -\operatorname{grad} n^F$ is obtained.

Finally, for the sake of a clear representation, the thermodynamic constraints to be imposed on the constitutive modelling are summarised as follows:

Summarised thermodynamic restrictions

$$
\begin{aligned}
\boldsymbol{\sigma}^S &= -n^S\, p^{FR}\, \mathbf{I} + \boldsymbol{\sigma}^S_{Em}\,, \\
\mathbf{T}^L &= -n^L\, p^{LR}\, \mathbf{I} + \mathbf{T}^L_E \approx -n^L\, p^{LR}\, \mathbf{I} \qquad \text{with} \qquad \mathbf{T}^L_E \approx \mathbf{0}\,, \\
\mathbf{T}^G &= -n^G\, p^{GR}\, \mathbf{I} + \mathbf{T}^G_E \approx -n^G\, p^{GR}\, \mathbf{I} \qquad \text{with} \qquad \mathbf{T}^G_E \approx \mathbf{0}\,, \\
\hat{\mathbf{p}}^L &= p^{LR} \operatorname{grad} n^L + \frac{\rho^L}{n^F}\, \frac{\partial \psi^L}{\partial s^L}\, n^F \operatorname{grad} s^L + \hat{\mathbf{p}}^L_{Em}\,, \\
\hat{\mathbf{p}}^G &= p^{GR} \operatorname{grad} n^G + \hat{\mathbf{p}}^G_E\,.
\end{aligned}
\tag{3.39}
$$

Note that a further evaluation of the term associated with $\operatorname{grad} s^L$ in $(3.39)_4$ requires the identification of the wetting and non-wetting pore fluids which, however, strongly depends on the material pairings and is, therefore, application-specific. In this regard, refer to Section 3.1.3 for the details on the treatment within the partially saturated zone and to Section 6.3 for the particulars in the scope of the VARTM procedure.

3.1.2 Solid skeleton

The present section concerns the description of the solid skeleton, which, having soil-mechanical applications in mind, is considered as an assembly of soil grains. In this regard, the macroscopic behaviour of the entire granular assembly strongly relies on the microstructural grain-to-grain interaction. More precisely, it depends, on the one hand, on the grain geometry, and, on the other hand, on the intergranular frictional forces[6]. If the intergranular force is below a specific threshold, the granular configuration is unchanged and the macroscopic behaviour merely originates from the elasticity of the individual grains. Therefore, the deformation is fully reversible, i. e. purely elastic. In contrast, if the force exceeds the threshold, grain motions, such as grain sliding and rolling, are triggerd, thereby leading to macroscopic plastic deformations. These irreversible deformations are usually accompanied by macroscopic hardening or softening effects. With this in mind, a suitable modelling framework is provided by the elastoplasticity. Herein, the evaluation whether the current stress state yields purely elastic, or elasto-plastic deformations, is made based on the so-called yield criterion F. Herein, the deformation is purely elastic for $F < 0$ and elasto-plastic for $F = 0$. Note that, once plastic deformations are commenced, the load cannot increase any further unless the elastic domain is altered through a suitable hardening law, where the so-called failure surface ultimately bounds all admissible stress states.

For the purpose of this contribution, the experimentally validated solid-skeleton description of Ehlers & Avci [61] is used. In particular, based on comprehensive material tests,

[6] Therefore, granular media are often denoted as so-called frictional materials.

they propsed an elasto-plastic formulation incorporating an isotropic hardening model and a stress-dependent failure surface. Note that the experiments have been carried out merely under quasi-static monotonic loading conditions. Therefore, the model cannot reproduce physical phenomena, which are only observed during (dynamic and quasi-static) cyclic loading conditions. In particular, due to the granular microstructure, the soils exhibit an anisotropic material behaviour, which strongly depends on the preceded loading history, see, e. g., Santamarina *et al.* [167] or Ko & Scott [115]. This anisotropy is of particular importance upon the stress reversal under cyclic loading conditions. In this regard, see, for instance, the experimental results of Arslan [9], where a gradual accumulation of plastic deformations was observed during pure deviatoric and pure isotropic loading. To mimic this particular behaviour of granular matter, kinematic hardening models, which have initially developed to describe metal plasticity, are well suited. A reason for that can be found in the similarities between the dislocation movement in solid materials, e. g. metals, known as the *Bauschinger effect* [16], and the grain motion as well as the grain-to-grain interaction. Through a kinematic hardening model the yield surface is rotated or translated within the principal stress space. An example of the former can be found in Mróz [146], where the yield surface is allowed to tilt over the hydrostatic axis of the principal stress space. In contrast, other authors, for instance Armstrong & Frederick [8] and de Boer & Brauns [22], follow the latter approach, which can be considered as more suitable for granular matter as it, in contrast to the rotational hardening, additionally allows for a plastic strain accumulation during cyclic isotropic compression. In consequence, together with the already utilised isotropic hardening model of Ehlers & Avci [61], the present solid-skeleton description yields a combined isotropic-kinematic hardening model.

Following the elasto-plastic modelling framework, this section comprises the individual model components, in particular, the description within the elastic domain, the yield criterion, the evolution of the plastic strains, the isotropic and the kinematic hardening models, and the stress-dependent failure surface. Note that, for the sake of a clearer representation, the subscript associated with the mechanical part of the solid extra stress, see Expression (3.24), is dropped in the following, i. e. $\boldsymbol{\sigma}^S_E = \boldsymbol{\sigma}^S_{Em}$ and $\overline{\boldsymbol{\sigma}}^S_E = \overline{\boldsymbol{\sigma}}^S_{Em}$.

Elastic domain

Proceeding from the comprehensive experimental investigations, Ehlers & Avci [61] proposed the volume-specific Helmholtz free-energy function

$$\begin{aligned}\Psi^{Se} = \; & \mu^S \, \boldsymbol{\varepsilon}^D_{Se} \cdot \boldsymbol{\varepsilon}^D_{Se} + \\ & + \frac{1}{2}\,(k^S_0 - k^S_1)\,(\varepsilon^V_{Se})^2 \; - \; k^S_1 (\varepsilon^V_{Se\,\mathrm{crit}})^2 \left[\ln\left(\frac{\varepsilon^V_{Se\,\mathrm{crit}} - \varepsilon^V_{Se}}{\varepsilon^V_{Se\,\mathrm{crit}}} \right) + \frac{\varepsilon^V_{Se}}{\varepsilon^V_{Se\,\mathrm{crit}}} \right],\end{aligned} \tag{3.40}$$

from which, with the help of relation $(3.25)_1$, an expression for the elastic stress is deduced:

$$\boldsymbol{\sigma}^S_E := \frac{\partial \Psi^{Se}}{\partial \boldsymbol{\varepsilon}_{Se}} = 2\,\mu^S \, \boldsymbol{\varepsilon}^D_{Se} + \left[k^S_0 + k^S_1 \left(\frac{\varepsilon^V_{Se\,\mathrm{crit}}}{\varepsilon^V_{Se\,\mathrm{crit}} - \varepsilon^V_{Se}} - 1 \right) \right] \varepsilon^V_{Se}\, \mathbf{I}\,. \tag{3.41}$$

Therein, $\varepsilon^V_{Se} = \boldsymbol{\varepsilon}_S \cdot \mathbf{I}$ is the volumetric elastic strain and $\boldsymbol{\varepsilon}^D_{Se} = \boldsymbol{\varepsilon}_{Se} - 1/3\; \varepsilon^V_{Se}\, \mathbf{I}$ denotes the deviatoric elastic strain. Moreover, μ^S is the constant elastic shear modulus, k^S_0 and k^S_1

are the volumetric bulk moduli, and $\varepsilon^V_{Se\,\mathrm{crit}}$ is the critical volumetric strain given by

$$\varepsilon^V_{Se\,\mathrm{crit}} = 1 - \frac{n^S_{\max}}{n^S_P}\,. \tag{3.42}$$

Herein, $n^S_{\max}$ defines the densest packing related to the point of compaction. In this regard, proceeding from the multiplicative decomposition of the solid deformation gradient (3.20), the solidity relation (3.4) can be reformulated to yield

$$n^S = n^S_{0S}(\det \mathbf{F}_p)^{-1}(\det \mathbf{F}_e)^{-1}\,, \tag{3.43}$$

where, confined to the small strain regime, its linearisation is sufficiently accurate. It reads, see Ehlers & Scholz [69],

$$n^S = n^S_{0S}(1-\varepsilon^V_S) = n^S_{0S}(1-\varepsilon^V_{Sp})(1-\varepsilon^V_{Se}) = n^S_p(1-\varepsilon^V_{Se})\,. \tag{3.44}$$

Therein, $n^S_p = n^S_{0S}(1-\varepsilon^V_{Sp})$ denotes the plastic volume fraction formally associated with the locally unloaded stress-free plastic intermediate configuration.

Yield surface

In the related literature, many authors have proposed various yield-surface descriptions, especially tailored to the unique characteristics of granular materials, where the dependency of the allowable shear stress on the hydrostatic stress state is of particular interest. In this regard, proceeding from the prominent Mohr-Coulomb model, see, e. g., Schad [170], and the model of Drucker & Prager [52], further enhancements gave birth to the so-called *Cam-Clay* (Cambridge Clay) models, see Schofield & Wroth [174], and the *cap-models*, see, e. g., Roscoe & Burland [165], Arslan [9], Lade [121] or Vermeer [192].

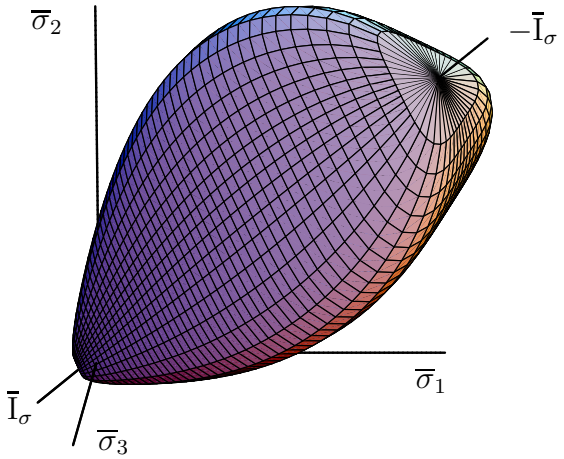

Figure 3.1: *Single-surface yield criterion for cohesive-frictional materials in the principal stress space of* $\overline{\boldsymbol{\sigma}}^S_E$.

For the purpose of this monograph, the description of the yield surface follows the single-surface approach of Ehlers [56], where, in contrast to the above mentioned criteria, the

elastic domain is bounded by a continuously differentiable formulation, see Figure 3.1. From a numerical point of view this is an advantageous property, as the evolution of the plastic strains is uniquely defined (see next paragraph). The single-surface yield criterion reads

$$\begin{aligned} \overline{F} &= \sqrt{\Gamma \overline{\mathrm{II}}_\sigma^D + \frac{1}{2}\alpha \overline{\mathrm{I}}_\sigma^2 + \delta^2 \overline{\mathrm{I}}_\sigma^4} + \beta \overline{\mathrm{I}}_\sigma + \varepsilon + \overline{\mathrm{I}}_\sigma^2 - \kappa = 0\,, \\ \Gamma &= (1 + \gamma \frac{\overline{\mathrm{III}}_\sigma^D}{(\overline{\mathrm{II}}_\sigma^D)^{3/2}})^m. \end{aligned} \tag{3.45}$$

Therein, $\overline{\mathrm{I}}_\sigma$, $\overline{\mathrm{II}}_\sigma^D$ and $\overline{\mathrm{III}}_\sigma^D$ are the first principal invariant of $\overline{\boldsymbol{\sigma}}_E^S$ and the (negative) second and third principal invariants of the effective stress deviator $(\overline{\boldsymbol{\sigma}}_E^S)^D$, all given in the shifted principal stress space. The material parameter sets

$$\mathcal{S}_h = (\delta, \varepsilon, \beta, \alpha, \kappa)^T \quad \text{and} \quad \mathcal{S}_d = (\gamma, m)^T \tag{3.46}$$

define the shape of the yield surface in the hydrostatic ($\mathcal{S}_h$) and deviatoric plane ($\mathcal{S}_d$).

To decide whether the current load increment corresponds to a plastic or neutral loading or an unloading, the *loading criterion*,

$$\frac{\partial \overline{F}}{\partial \overline{\boldsymbol{\sigma}}_E^S} \cdot (\overline{\boldsymbol{\sigma}}_E^S)'_S \quad \begin{cases} > & 0 & : & \text{plastic loading}\,, \\ = & 0 & : & \text{neutral loading}\,, \\ < & 0 & : & \text{unloading}\,, \end{cases} \tag{3.47}$$

needs to be checked. Herein, $\partial \overline{F} / \partial \overline{\boldsymbol{\sigma}}_E^S$ (associated plasticity) denotes the yielding direction and $(\overline{\boldsymbol{\sigma}}_E^S)'_S$ the load increment.

Evolution of the plastic strains

At the onset of plastic deformations, the evolution of the plastic-strain tensor needs to be evaluated. In this regard, the *flow rule*

$$(\boldsymbol{\varepsilon}_{Sp})'_S = \Lambda \frac{\partial \overline{G}}{\partial \overline{\boldsymbol{\sigma}}_E^S} \tag{3.48}$$

is utilised, where Λ is the plastic multiplier and $\overline{G}$ is the plastic potential, which, following the proposal of Mahnkopf [134], is given by

$$\overline{G} = \sqrt{\psi_1 \overline{\mathrm{II}}_\sigma^D + \frac{1}{2}\alpha\, \overline{\mathrm{I}}_\sigma^2 + \delta^2 \overline{\mathrm{I}}_\sigma^4} + \psi_2 \beta\, \overline{\mathrm{I}}_\sigma + \epsilon\, \overline{\mathrm{I}}_\sigma^2\,. \tag{3.49}$$

Therein, ψ_1 and ψ_2 are material parameters, which serve to relate the dilatation angle ν_D, i. e. the ratio between the fractions of the plastic-strain evolution in the deviatoric and hydrostatic direction, respectively, see Figure 3.2, to experimental data.

Herein, supported by the experimental findings of Yamada & Ishihara [210] and Lade & Duncan [123], who revealed that the evolution of the plastic strains is nearly coaxial in the deviatoric stress plane in the principle stress space, the plastic potential is independent of the third stress invariant III_σ^D resulting in a circular cross-sectional shape in the deviatoric plane.

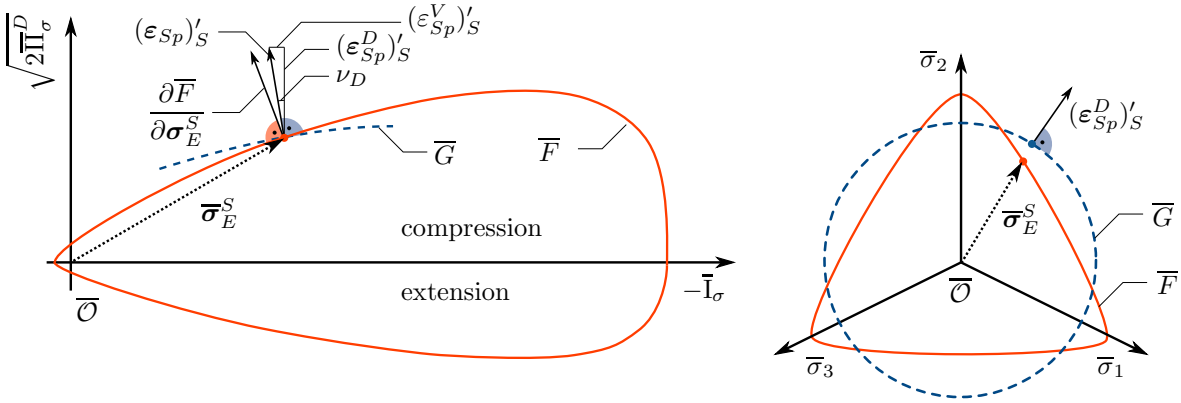

Figure 3.2: *Sketch of the evolution of the plastic flow in the hydrostatic (left) and deviatoric plane (right).*

Remark: Note that, with respect to the scope of granular media, or frictional materials in general, the concept of so-called non-associated plasticity is exploited for the purpose of this monograph. Herein, in contrast to the associated plasticity, the plastic potential is not equal to the yield surface, i. e. $\overline{F} \neq \overline{G}$, as, following the experimental observations of Lade [122], an associated flow rule would overestimate the dilatation angle ν_D. □

Subsequently, the plastic-strain evolutions are found from the dissipation inequality $(3.32)_1$, viz.

$$\overline{\boldsymbol{\sigma}}^S_E \cdot (\boldsymbol{\varepsilon}_{Sp})'_S \geq 0\,. \tag{3.50}$$

Note that, herein, the relations $(3.33)_1$ and (3.34) have been incorporated. In particular, $\boldsymbol{\varepsilon}_{Sp}$ and Λ need to be found in a way to maximise the internal dissipation, which is often referred to as the *principle of maximum plastic dissipation* (PMD), where the constraints imposed by the Karush-Kuhn-Tucker (KKT) conditions, given by

$$\overline{F} \leq 0\,, \qquad \Lambda \geq 0\,, \qquad \Lambda \overline{F} = 0 \tag{3.51}$$

need to be considered. The KKT conditions ensure, firstly, that the stress state satisfies the yield criterion ($\overline{F} \leq 0$), secondly, that the plastic-strain evolution is in direction of $\partial \overline{G} / \partial \overline{\boldsymbol{\sigma}}^S_E$ ($\Lambda \geq 0$) and, lastly, that the former two are satisfied simultaneously ($\Lambda \overline{F} = 0$), which is referred to as the *complementary slackness theorem* in the related literature, see, e. g., Boyd & Vandenberghe [27].

Upon plastic loading, additionally, the so-called *consistency condition*[7],

$$(\overline{F})'_S = \frac{\partial \overline{F}}{\partial \overline{\boldsymbol{\sigma}}^S_E} \cdot (\overline{\boldsymbol{\sigma}}^S_E)'_S + \sum_{p_i} \frac{\partial \overline{F}}{\partial p_i} \cdot (p_i)'_S + \frac{\partial \overline{F}}{\partial \mathbf{Y}^S_E} \cdot (\mathbf{Y}^S_E)'_S = 0\,, \tag{3.52}$$

needs to be satisfied[8], where $p_i \in \{\beta, \delta, \epsilon, \gamma\}$ defines the set of yield-surface parameters to be altered through isotropic hardening. The consistency condition guarantees that the

[7] In order to emphasise that the consistency is only valid upon plastic deformations, it is commonly given through $\Lambda(\overline{F})'_S = 0$ as well.

[8] Instead of the consistency conditions, the so-called predictor-corrector scheme ensures the validity of the stress state during the numerical computation, see Section 4.3.1 for details.

stress point satisfies the yield criterion $(3.51)_1$, i. e. it remains on the yield surface, upon plastic loading.

At the onset of plastic deformations, the plastic strains may accumulate in local areas, often referred to as localisation problem, thereby forming the so-called shear bands, see, e. g., Oka *et al.* [151] or Ehlers *et al.* [65]. It can be observed from experiments that the thickness of the developing shear bands is related to a micro-structural length scale, for instance, the average grain size, see, e. g., Wolf *et al.* [204]. In contrast, in the theoretical description a length scale does not yet exist and, consequently, the shear band will be represented by a singular surface. From a mathematically point of view, the initially *well-posed problem* turns into an *ill-posed problem*. In this regard, according to Hadamard [90], a problem is said to be well-posed if a solution exists, the solution is unique and the solution continuously depends on the initial data. An ill-posed problem fails to satisfy at least one of these three criteria. To cope with that, it needs to be regularised, in particular, with respect to the given plasticity framework, an internal length scale needs to be introduced, which limits the shear-band thickness. An investigation of different regularisation methods, applied to the elasto-plastic problems within the scope of soil mechanics, is provided in Ammann [6]. In this regard, the present problem is regularised by introducing a rate-dependent elasto-viscoplasticity model, which implicitly introduces an internal length scale to limit the shear-band thickness. In particular, the overstress concept of Perzyna [155] is introduced:

$$\Lambda = \frac{1}{\eta}\Big\langle \frac{\overline{F}}{\sigma_0} \Big\rangle^r \qquad \text{or} \qquad \Lambda\eta \Big\langle \sigma_0 \Big\rangle^r = \Big\langle \overline{F} \Big\rangle^r . \tag{3.53}$$

Therein, $\langle\, \cdot \,\rangle$ are the Macaulay brackets, η is the relaxation time (viscosity parameter), σ_0 the reference stress and r the viscoplastic exponent. Note that for $r = 1$ and $\eta = 0$, relation (3.53) reassembles the elasto-plastic formulation. Therefore, it is preferred to set η to very small values, viz. $\eta \to 0$. The influence of the relaxation time on the shear-band thickness is extensively discussed in Ammann [6].

Isotropic and kinematic hardening

Any macroscopic plastic deformation of a granular assembly is accompanied by hardening or softening effects. They can be described through isotropic or kinematic hardening models. In particular, an isotropic hardening model alters the shape of the yield surface, e. g. via expansion or shrinkage, from its initial state F_0 towards $\widetilde{F}$ through a variation of the yield surface parameters, see Figure 3.3[9]. On the other hand, the kinematic hardening model shifts the yield locus from its initial position $\mathcal{O}$ towards $\overline{\mathcal{O}}$ via the back-stress tensor $\mathbf{Y}_E^S$, see relation (3.34),

$$\boldsymbol{\sigma}_E^S = \overline{\boldsymbol{\sigma}}_E^S + \mathbf{Y}_E^S . \tag{3.54}$$

For the purpose of this monograph, both hardening concepts are united to yield a mixed isotropic-kinematic hardening (IKH) model.

[9] Herein, stress tensors are interpreted as vectors in the principal stress space.

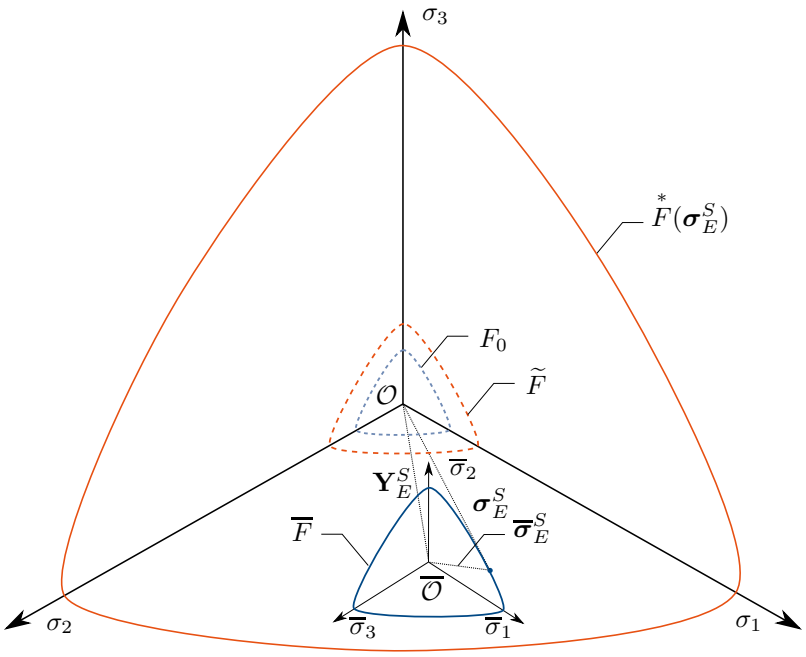

Figure 3.3: *Sketch of the combined isotropic-kinematic hardening concept and the failure surface.*

Any hardening model needs to ensure that the current stress state is admissible. In particular, it has to satisfy the yield criterion, i. e. $\overline{F} = \overline{F}(p_i) \leq 0$, and, in addition, the failure criterion

$$\overset{*}{F} = F\big(\overset{*}{p}_i\big) \leq 0 \tag{3.55}$$

as the ultimate loading boundary, where $\overset{*}{p}_i \in \{\overset{*}{\alpha}, \overset{*}{\beta}, \overset{*}{\delta}, \overset{*}{\epsilon}, \overset{*}{\gamma}\}$ denotes the set of material parameters governing the shape of the failure surface.

In order to ensure the admissibility of the computed stress state, the usual predictor-corrector scheme, see Simo & Taylor [179], is used. Herein, a preliminary overstress is computed based on the current strain increment (predictor step), which is, subsequently, checked whether the current increment is elastic ($F < 0$) or elasto-plastic ($F \geq 0$). In case of plasticity, the governing equations of the plasticity model are solved such that the resulting stress state lies on the yield surface ($F = 0$) (plastic corrector step), where, in the scope of the IHK model, the shape of the yield surface is adjusted (isotropic hardening) and its yield locus is shifted through the principal stress space (kinematic hardening) simultaneously. During kinematic hardening the translation direction is of particular interest. In this regard, Mróz [146] proposed an approach based on the geometric requirement that the tangential plane on the yield surface, which is associated with the current stress state, has to correspond to a tangential plane on the failure surface, thereby defining a second stress state on the failure surface. The evolution of the plastic strain is then governed by the vector defined through the current stress state and the second stress state leading to neither an associated nor a plastic-potential-driven non-associated flow rule. Note that the approach of Mróz [146] prevents an intersection of the yield and failure surfaces.

The current model also proceeds from a stress-projection method, but in contrast to Mróz [146], following a non-associated flow rule exploiting a plastic potential. In particular, the projection is carried out utilising the current stress state $\boldsymbol{\sigma}_E^S$ and the normalised flow direction $\mathbf{N}$, which proceeds from the plastic potential (3.49). The projected stress state $\overset{*}{\boldsymbol{\sigma}}{}_E^S$, which lies on the failure surface, is then found with the help of the scaling factor ζ, see Figure 3.3. In particular, following the concept of the volumetric and deviatoric splitting, the projection is carried out independently along the hydrostatic and the deviatoric direction via

$$(\overset{*}{\boldsymbol{\sigma}}{}_E^S)^V = \boldsymbol{\sigma}_E^S + \zeta^V \mathbf{N}^V\,, \qquad (\overset{*}{\boldsymbol{\sigma}}{}_E^S)^D = \boldsymbol{\sigma}_E^S + \zeta^D \mathbf{N}^D\,, \tag{3.56}$$

where the projected stress tensors $(\overset{*}{\boldsymbol{\sigma}}{}_E^S)^V$ and $(\overset{*}{\boldsymbol{\sigma}}{}_E^S)^D$, the scalar multipliers ζ^V and ζ^D and the normalised projection directions $\mathbf{N}^V$ and $\mathbf{N}^D$ are the corresponding contributions in the hydrostatic and deviatoric direction, respectively. The projection directions are computed through

$$\begin{aligned} \mathbf{N}^V &= \frac{1}{3}\operatorname{sgn}(G^V)\mathbf{I} \qquad \text{with} \quad G^V = \frac{\partial \overline{G}}{\partial \overline{\boldsymbol{\sigma}}_E^S} \cdot \mathbf{I}\,, \\ \mathbf{N}^D &= \frac{1}{\|\mathbf{G}^D\|}\mathbf{G}^D \qquad \text{with} \quad \mathbf{G}^D = \frac{\partial \overline{G}}{\partial \overline{\boldsymbol{\sigma}}_E^S} - \frac{1}{3}\left(\frac{\partial \overline{G}}{\partial \overline{\boldsymbol{\sigma}}_E^S} \cdot \mathbf{I}\right)\mathbf{I}\,, \end{aligned} \tag{3.57}$$

where $\operatorname{sgn}(\cdot) = (\cdot)/\|\cdot\|$ denotes the signum function with $\|(\cdot)\| = \sqrt{((\cdot)\cdot(\cdot))}$ being the Euklidian norm. Exploiting the relations $(3.56)_1$ and $(3.56)_2$, ζ^V and ζ^D can be computed[10] through the requirement that the projected stresses have to lie on the failure surface, i. e.

$$\overset{*}{F}\big(\zeta^V\big) \overset{!}{=} 0 \qquad \text{and} \qquad \overset{*}{F}\big(\zeta^D\big) \overset{!}{=} 0\,. \tag{3.58}$$

Consequently, the presented formulation always ensures the admissibility of the resulting stress state. To make this point more clear, lets assume an invalid stress state, i. e. where the current stress point lies outside the domain bound by the failure surface. In this case, at the onset of plastic deformations, the scaling factor ζ will be negative and the plastic strain increment, will be in the opposite direction, thereby leading to a softening material behaviour.

Next, the isotropic and kinematic hardening laws are addressed. In this regard, concerning the isotropic hardening, suitable evolution laws for the parameter subset p_i of the yield surface $\overline{F}$ have been proposed by Ehlers *et al.* [66], viz.

$$\begin{aligned} &(p_i)'_S = (p_i^V)'_S + (p_i^D)'_S = (\overset{*}{p}_i - p_i)\big[\, C_{pi}^V\, (\varepsilon_{Sp}^V)'_S + C_{pi}^D\, \|(\boldsymbol{\varepsilon}_{Sp}^D)'_S\|\,\big] \\ &\text{with} \qquad p_i(t=0) = p_{i0}\,, \end{aligned} \tag{3.59}$$

[10] Note that under pure hydrostatic or deviatoric loading, the contributions of the plastic flow in the deviatoric or hydrostatic direction, respectively, are not uniquely defined due to $\|\mathbf{G}^D\| = 0$ and $G^V = 0$, respectively. Consequently, arbitrary projection directions $\mathbf{N}^D$ and $\mathbf{N}^V$ are defined in this case in order to keep the formulation computable. In this case, the scaling factors, ζ^V and ζ^D, do not contribute to the hardening, see (3.60).

which, however, are adopted to match the present mixed isotropic-kinematic hardening concept and yield

$$\begin{aligned} (p_i)'_S &= (p_i^V)'_S + (p_i^D)'_S = \zeta^V C_{pi}^V (\varepsilon_{Sp}^V)'_S + \zeta^D C_{pi}^D \|(\boldsymbol{\varepsilon}_{Sp}^D)'_S\| \\ \text{with} \qquad & p_i(t=0) = p_{i0}\,. \end{aligned} \tag{3.60}$$

Therein, the evolution equation $(p_i)'_S$ for the parameters p_i is separated into volumetric and deviatoric parts, $(p_i^V)'_S$ and $(p_i^D)'_S$, which are driven by the corresponding plastic strain rates, $(\varepsilon_{Sp}^V)'_S$ and $(\varepsilon_{Sp}^D)'_S$, together with the volumetric and the deviatoric evolution constants, C_{pi}^V and C_{pi}^D. Moreover, p_{i0} denotes the initial values of the parameters p_i. Evidently, the deviatoric part only governs plastic hardening, whereas the volumetric part $(p_i^V)'_S$ can take positive or negative values and, therefore, describes both hardening and softening processes.

The evolution of the kinematic back-stress tensor $\mathbf{Y}_E^S$ is based on the approach of Armstrong & Frederick [8]. However, it has been modified to match the present framework:

$$\begin{aligned} (\mathbf{Y}_E^S)'_S = \zeta^V (C_0^V - C_1^V |\mathrm{Y}_E^{SV}|)(\varepsilon_{Sp}^V)'_S\,\mathbf{I} + \\ + \zeta^D [\, C_0^D (\boldsymbol{\varepsilon}_{Sp}^D)'_S - C_1^D \|(\boldsymbol{\varepsilon}_{Sp}^D)'_S\| \mathbf{Y}_E^{SD}\,]\,. \end{aligned} \tag{3.61}$$

Therein, $(\mathbf{Y}_E^S)'_S$ denotes the rate of the kinematic back-stress tensor. Furthermore, $\mathrm{Y}_E^{SV} = \mathrm{Y}_E^S \cdot \mathbf{I}$ and $\mathbf{Y}_E^{SD} = \mathbf{Y}_E^S - 1/3\,\mathrm{Y}_E^{SV}\mathbf{I}$ denote the volumetric and the deviatoric part of the back-stress tensor, and $|(\cdot)|$ is the absolute value of $(\cdot)$. Moreover, C_0^V and C_1^V, and C_0^D and C_1^D are the volumetric and the deviatoric evolution constants, respectively. In contrast, to other authors, see e. g., de Boer & Brauns [22], who proposed a linear kinematic hardening model, the nonlinear extension in (3.61) is vital for an adequate representation of the cyclic loading behaviour. The differences between the linear kinematic and the Armstrong & Frederick (AF) hardening model is schematically illustrated in Figure 3.4.

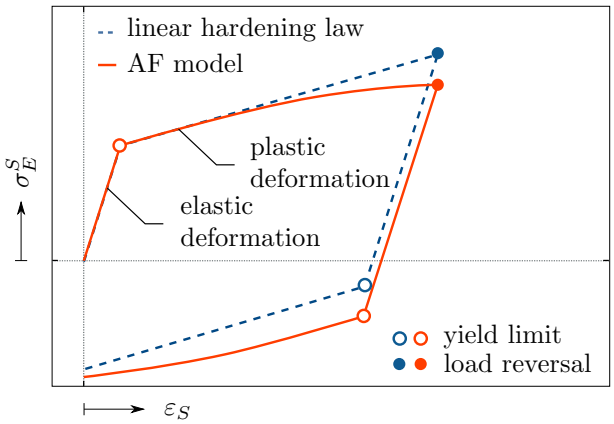

Figure 3.4: *Comparison between a linear kinematic hardening law and the model of Armstrong and Frederick.*

In particular, at the onset of yielding the nonlinear part is initially inactive, but, with ongoing (monotonic) loading, it becomes more and more pronounced, thereby slowing

down the rate of the back-stress tensor. Upon load reversal, the back-stress tensor and its rate have opposite directions and, therefore, the additional term increases the stress rate. For more details on the AF model, the interested reader is referred, for instance, to the work of Jirásek & Bažant [109], Chaboche [38, 39] or Ohno & Wang [150], where the latter three in particular focus on its further extension, however, merely with respect to metal plasticity.

A suitable model for the description of granular media needs to account for the contractant and dilatant properties of the granular assembly, which are within the current setting driven through the plastic potential. In consequence, the used hardening models adapt, in addition to the yield surface, the plastic potential and, therefore, the direction of the plastic flow as well. The impact on the plastic strain increment related to the isotropic and the kinematic hardening model and is qualitatively sketched in Figure 3.5 (left) and Figure 3.5 (right), respectively. Herein, both hardening models are subjected to the same loading scenario starting with an isotropic compression to reach the stress state A and followed up by a pure deviatoric load from A to C. At first, the attention is drawn to the pure isotropic hardening model. Herein, the evolution of the volumetric contribution of the plastic strain increment gradually changes from a contractant behaviour at A towards a dilatant behaviour at C, see Figure 3.5 (left). In contrast, in case of the kinematic hardening model, the volumetric part in the plastic strain increment merely exhibits contractant and isochoric properties, see Figure 3.5 (right). Consequently, only the isotropic hardening part in the combined isotropic-kinematic hardening model mimics the commonly observed contract-dilatant property of granular matter under pure shear deformation.

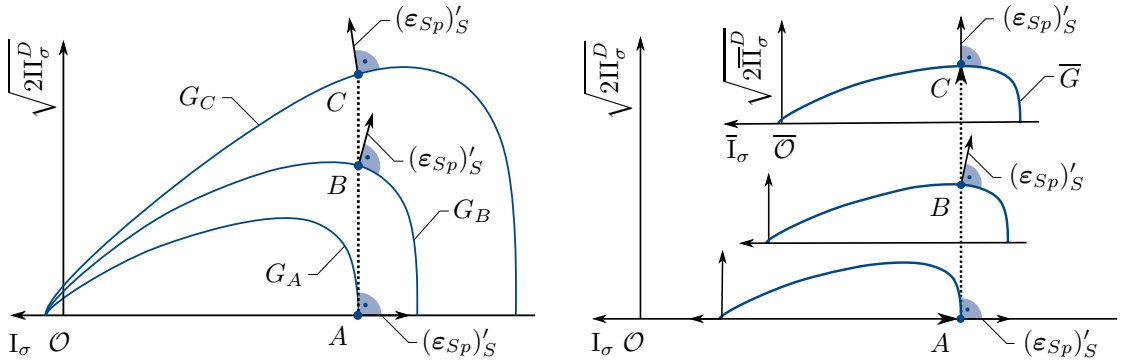

Figure 3.5: *Comparison of the evolution of the plastic strains in case of pure isotropic (left) and pure kinematic hardening (right).*

Stress-dependent failure surface

The comprehensive experimental investigations under monotonic quasi-static loading conditions carried out by Ehlers & Avci [61] have revealed that the failure surface is not constant, but depends on the hydrostatic stress state, i. e. on the confining pressure I_σ. In particular, different confining pressures lead to slightly different granular configurations and, consequently, to discriminative grain movements upon loading. Therefore, at failure the granular configuration and consequently, the corresponding stress states are different.

Following the approach of Ehlers & Avci [61], the evolution of the stress-dependent failure surface is conducted via

$$\overset{*}{\epsilon}(\mathrm{I}_\sigma) = \overset{*}{\epsilon}_0(1 + \overset{*}{C}_\epsilon\, \mathrm{I}_\sigma) \qquad \text{with} \qquad \overset{*}{\epsilon} \geq \overset{*}{\epsilon}_{lim}\,, \tag{3.62}$$

Therein, $\overset{*}{C}_\epsilon$ is a constant evolution parameter of the failure surface, while $\overset{*}{\epsilon}_0$ theoretically defines the failure surface for the unloaded virgin material, which is adjusted as small as possible but large enough for the smallest confining pressure used in a triaxial experiment. The failure-surface limit is defined given by $\overset{*}{\epsilon}_{lim}$.

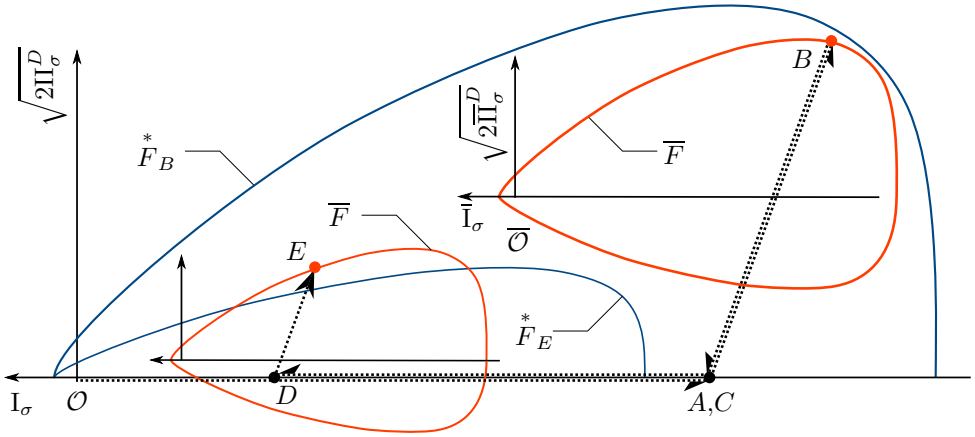

Figure 3.6: *Schematic sketch of a possible loading scenario illustrating the impact of the variable failure surface on the hardening behaviour.*

Next, the behaviour of the plasticity model and, in particular, its interplay with the stress-dependent failure surface is elaborated in terms of a loading, unloading and reloading cycle. For this purpose, a loading scenario as depicted in Figure 3.6 is considered. Therein, $\overset{*}{F}_B$ and $\overset{*}{F}_E$ denote the failure surfaces associated with stress states B and E, respectively. In the considered load case, a soil specimen is initially subjected to a hydrostatic compression and a subsequent triaxial load (load path: $\mathcal{O}$-A-B). Next, the specimen is unloaded and the hydrostatic stress level is reduced (load path: B-C-D). Finally, the specimen is reloaded again but starting at a lower hydrostatic stress state (load path: $D - E$). Following this loading scenario, the stress path $\mathcal{O}$-A-B causes a consolidation and, thereby a specific load-path-related granular configuration, which is represented through a shift and an expansion of the elastic domain through the kinematic and isotropic hardening models. A similar behaviour can be observed during the unloading stage B-C-D, however, associated with a shrinkage (isotropic hardening) and a shift to the left (kinematic hardening) of the elastic domain. Note that, again, a load-path-related granular configuration is established, which initially remains intact in the subsequent reload D-E if the load increment is purely elastic, i. e. the yield criterion is not violated. Once the applied load exceeds the yield limit, plastic deformations are commenced and the granular assembly rearranges such that granular configuration and the current hydrostatic stress state match. This behaviour is represent in the plasticity model through a return of the computed stress state onto the failure surface. For a more detailed discussion of the interplay between the stress-dependent failure surface and the material

hardening, the interested reader is referred to [61]. Note that, herein, the interplay is only discussed with respect to an isotropic hardening model.

Model summary

To sum up the previous elaborations, two different formulations, each composed of set of ordinary differential equations (ODE), governing the solid-skeleton behaviour either related to the mixed isotropic-kinematic or the pure isotropic hardening model. In particular, the mixed isotropic-kinematic hardening (IKH) model comprises the equations (3.48), (3.53), (3.60), (3.61), $(3.58)_1$ and $(3.58)_2$ and reads

$$\boldsymbol{\mathcal{L}}_{\mathrm{IKH}} = \begin{bmatrix} (\boldsymbol{\varepsilon}_{Sp})'_S \\ 0 \\ (p_i)'_S \\ (\mathbf{Y}_E^S)'_S \\ 0 \\ 0 \end{bmatrix} - \begin{bmatrix} \Lambda \dfrac{\partial \overline{G}}{\partial \overline{\boldsymbol{\sigma}}_E^S} \\ \Lambda - \dfrac{1}{\eta} \left\langle \dfrac{\overline{F}}{\sigma_0} \right\rangle \\ \zeta^V C_{pi}^V \, (\varepsilon_{Sp}^V)'_S + \zeta^D C_{pi}^D \| (\boldsymbol{\varepsilon}_{Sp}^D)'_S \| \\ \zeta^V (C_0^V - C_1^V |\mathrm{Y}_E^{SV}|)(\varepsilon_{Sp}^V)'_S \, \mathbf{I} + \zeta^D [C_0^D \dot{\boldsymbol{\varepsilon}}_p^D - C_1^D \| (\boldsymbol{\varepsilon}_{Sp}^D)'_S \| \mathbf{Y}_E^{SD}] \\ \overset{*}{F} \left(\zeta^V \right) \\ \overset{*}{F} \left(\zeta^D \right) \end{bmatrix} = \mathbf{0} \,. \tag{3.63}$$

The purely isotropic-hardening (IH) model, composed of the relations (3.48), (3.53) and (3.59) is summarised as

$$\boldsymbol{\mathcal{L}}_{\mathrm{IH}} = \begin{bmatrix} (\boldsymbol{\varepsilon}_{Sp})'_S \\ 0 \\ (p_i)'_S \end{bmatrix} - \begin{bmatrix} \Lambda \dfrac{\partial \overline{G}}{\partial \overline{\boldsymbol{\sigma}}_E^S} \\ \Lambda - \dfrac{1}{\eta} \left\langle \dfrac{\overline{F}}{\sigma_0} \right\rangle \\ (\overset{*}{p_i} - p_i) [\, C_{pi}^V \, (\varepsilon_{Sp}^V)'_S + C_{pi}^D \, \| (\boldsymbol{\varepsilon}_{Sp}^D)'_S \| \,] \end{bmatrix} = \mathbf{0} \,. \tag{3.64}$$

Note that, alternatively, $(3.64)_2$ may be solved for Λ and inserted into $(3.64)_1$, in order to reduce the number of ODE within the local system on the one hand and to allow for explicit time-discretisation schemes on the other hand.

3.1.3 Pore fluids

The present section encompasses the description of the individual pore fluids, in particular, of the materially incompressible pore liquid ($\beta = L$) and the materially compressible pore gas ($\beta = G$), and their mutual interactions. In this regard, within the scope of partially saturated porous media, the fully liquid- and gas-saturated domain, where solely one of the pore fluids is mobile, are separated by an interfacial area denoted as the partially saturated domain, see Figure 3.7.

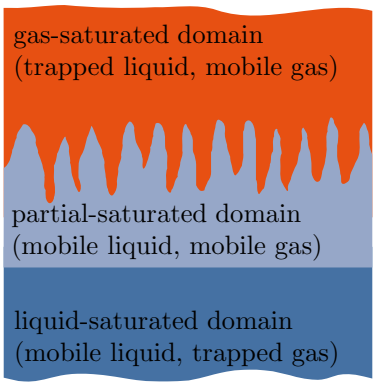

Figure 3.7: *Saturation states in a partially saturated porous material.*

Pore-fluid flow

In what follows, a constitutive relations for the extra momentum productions associated with the pore liquid and the pore gas, $\hat{\mathbf{p}}^L_{Em}$ and $\hat{\mathbf{p}}^G_E$, are proposed. Note that, herein, for the sake of convenience, the notation $\hat{\mathbf{p}}^L_E = \hat{\mathbf{p}}^L_{Em}$ is used. With respect to a thermodynamic consistent modelling approach, suitable relations have to satisfy the dissipation inequality (3.36) of the pore-fluid. Therefore, the respective constitutive relations have to fulfil $-\hat{\mathbf{p}}^L_{Em} \cdot \mathbf{w}_L \geq 0$ and $-\hat{\mathbf{p}}^G_E \cdot \mathbf{w}_G \geq 0$. In this regard, assuming isotropic lingering flow conditions at low Reynolds numbers, which is a valid assumption in the case of low permeabilities, the entire percolation process is appropriately described by a linear filter law. In this connection, following the approach of Ehlers [60], the extra momentum production of the pore fluids are introduced via

$$\hat{\mathbf{p}}^\beta_E = -(n^\beta)^2\, \gamma^{\beta R} (\mathbf{K}^\beta_r)^{-1}\, \mathbf{w}_\beta \tag{3.65}$$

with $\beta \in \{L, G\}$. Therein, $\gamma^{\beta R}$ is the specific weight of φ^β and $\mathbf{K}^\beta_r$ is the relative permeability tensor, which, in general, depends on the pore-fluid saturation s^β and the pore space $n^F = 1 - n^S$ and is, therefore, given by

$$\mathbf{K}^\beta_r = \kappa^\beta_r(s^\beta)\mathbf{K}^\beta(n^S)\,. \tag{3.66}$$

Therein, $\kappa^\beta_r(s^\beta) \in [0, 1]$ denotes the scalar saturation-dependent relative permeability, which is of particular importance in the partially saturated domain (see subsequent paragraph). Assuming isotropic permeability conditions, (3.66) can be reformulated such that

$$\mathbf{K}^\beta_r = \kappa^\beta_r(s^\beta) K^\beta(n^S)\mathbf{I}\,, \tag{3.67}$$

where $K^\beta(n^S)$ is the Darcy permeability, which can be expressed in terms of the specific fluid weight $\gamma^{\beta R}$ and the dynamic pore-fluid viscosity $\mu^{\beta R}$:

$$K^\beta(n^S) = \frac{\gamma^{\beta R}}{\mu^{\beta R}} K^S(n^S)\,. \tag{3.68}$$

Therein, $K^S(n^S)$ is the fluid-property-independent and deformation-dependent intrinsic permeability, which is, for the purpose of this monograph, treated as constant constrained to the small-strain regime, i. e. $K^S := K^S_{0S}$, with K^S_{0S} as the initial intrinsic permeability.

Finally, the momentum balances of the pore liquid and of the pore gas, $(3.10)_2$ and $(3.10)_3$, respectively, can be solved for the corresponding filter velocities, thereby further incorporating (3.65), (3.67) and (3.68), to reassemble a Darcy-like[11] filter law:

$$\begin{aligned} n^L \mathbf{w}_L &= -\frac{\kappa_r^L}{\mu^{LR}} K_{0S}^S \left[\operatorname{grad} p^{LR} - \rho^{LR} \mathbf{g} - \frac{\rho^L}{n^F} \frac{\partial \psi^L}{\partial s^L} n^F \operatorname{grad} s^L \right], \\ n^G \mathbf{w}_G &= -\frac{\kappa_r^G}{\mu^{GR}} K_{0S}^S \left[\operatorname{grad} p^{GR} - \rho^{GR} \mathbf{g} \right]. \end{aligned} \tag{3.69}$$

Therein, $n^L \mathbf{w}_L$ and $n^G \mathbf{w}_G$ denote the so-called filter velocities, which correspond to the seepage velocities, however averaged over the surface area of the REV.

Partially saturated zone

In contrast to the fully liquid- and gas-saturated domains, both pore fluids are mobile in the partially saturated zone. Herein, the motion of the individual fluids is governed by an interplay between the pore liquid, the pore gas and the solid skeleton. In the related literature, see, e. g., Fredlund & Rahardjo [78] or Bear [17], the so-called capillary pressure is defined as the difference between the pressure of the wetting ($\beta = W$) and the non-wetting pore fluid ($\beta = NW$). The fluid with an acute wetting (or contact) angle ω is denoted as the wetting fluid, see Figure 3.8. The wetting angle is a result of unbalanced

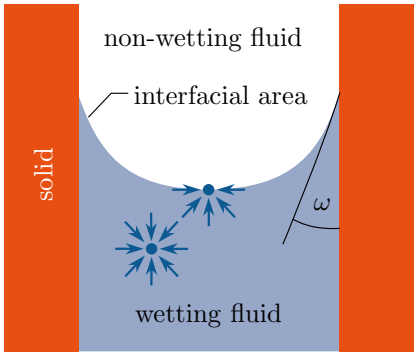

Figure 3.8: *Illustration of the wetting and non-wetting fluids on the microstructure.*

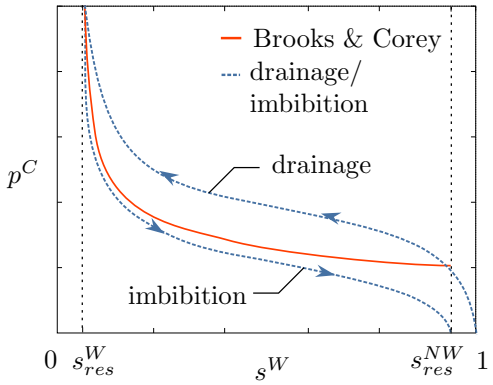

Figure 3.9: *Sketch of the typical drainage and imbibition behaviour of porous material and curve plot of the Brooks & Corey [31] relation.*

intermolecular forces. In particular, inside the fluid each molecule is neighboured with a molecule of the same type, thereby balancing the attractive and repulsive forces in all directions. In contrast, the molecules at the interfacial area may exhibit a net force acting in a particular direction, where the material pairing governs the resultant force. To be more precise, as the molecules of the wetting fluid are more attracted to the solid molecules rather than to the molecules of the non-wetting fluid, the former wets the solid, thereby displacing the latter.

[11] In the relation proposed by Darcy [48], the filter velocity merely depends on applied pressure gradient.

As a result, a pressure drop denoted as the capillary-pressure drop p^C, see the Young-Laplace equation in [212], across the interface from the non-wetting towards wetting fluid can be observed:

$$p^W + p^C = p^{NW} \qquad \longrightarrow \qquad p^C := p^{NW} - p^W \,. \tag{3.70}$$

Based on this definition together with the knowledge of the wetting and non-wetting fluids, a relation for the capillary pressure can be established. In particular, proceeding, for instance, from the assumption of the pore liquid being the wetting and the pore gas being the non-wetting fluid, i. e. $p^W = p^{LR}$ and $p^{NW} = p^{GR}$, and by further incorporating $(3.27)_1$ and $(3.27)_2$, the capillary pressure is given by

$$p^C = p^{GR} - p^{LR} = \mathcal{P} - (\mathcal{P} + \frac{\rho^L}{n^F}\frac{\partial \psi^L}{\partial s^L}) = -s^L \rho^{LR} \frac{\partial \psi^L}{\partial s^L} \,. \tag{3.71}$$

Consequently, a more general relation without a distinct choice of the wetting and non-wetting fluids proceeds from $(3.70)_2$ and reads

$$p^C = p^{NW} - p^W = -s^W \rho^{WR} \frac{\partial \psi^W}{\partial s^W} \,. \tag{3.72}$$

Note that, as the decision of the wetting and non-wetting parts is a constitutive choice depending on the material pairings and, in turn, is related to the particular application scenario, the matter is kept in a more general setting at this stage by utilising the superscripts W and NW rather than the particular pore-fluid identifiers.

In most imbibition or drainage processes, it is common knowledge, see, e. g., Helmig [100], that the generally irregular and complex-shaped pore space cannot be fully saturated or desaturated, respectively, with one of the mobile pore fluids, see Figure 3.9. Therefore, a relation between the saturation and the so-called effective saturation s^W_{eff} is established,

$$s^W_{eff} := \frac{s^W - s^W_{res}}{1 - s^W_{res} - s^{NW}_{res}} \,, \tag{3.73}$$

where s^W_{res} and s^{NW}_{res} denote the residual saturations of the wetting and non-wetting pore fluids, respectively. The effective saturation can be related to the capillary pressure through the relation of Brooks & Corey [31]:

$$s^W_{eff}(p^C) = \left(\frac{p^D}{p^C}\right)^{\lambda} \qquad \text{or} \qquad p^C(s^W_{eff}) = p^D \left(s^W_{eff}\right)^{-\frac{1}{\lambda}} \,. \tag{3.74}$$

Therein, p^D is the bubbling or entry pressure and λ is a parameter related to the pore-size distribution. In this regards, Figure 3.9 illustrates the difference between a typical drainage and imbibition process, starting from the initially wetting-fluid-saturated state, and the capillary-pressure-saturation relation of Brooks & Corey. As depicted, the relation of Brooks & Corey fails, like, for instance, the commonly used law of van Genuchten [81][12], to mimic the hysteretic behaviour during the drainage and the subsequent imbibition. This flaw can be traced back to the fact that both curves are composed of pairs of

[12] An empirical relation between the parameters of van Genuchten and the Brooks & Corey law has been proposed in Lenhard *et al.* [127].

values associated with the thermodynamic equilibrium, i. e. the established saturation for a prescribed capillary pressure, and are, therefore, merely a rather coarse approximation of actual drainage or imbibition processes, respectively. With respect to the thermodynamically consistent modelling approach, a Helmholtz free-energy function φ^L can be constructed, in such a way that relation (3.74) can be recovered with the help of (3.72), see Graf [85].

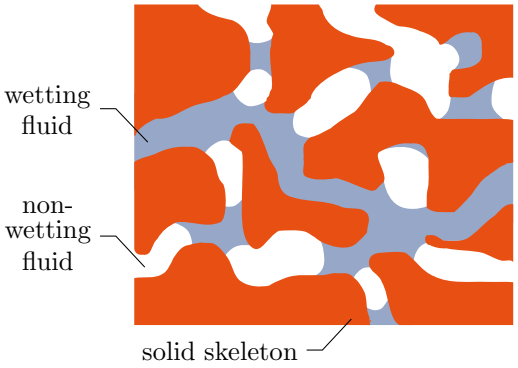

Figure 3.10: *Sketch of a partially saturated porous microstructure.*

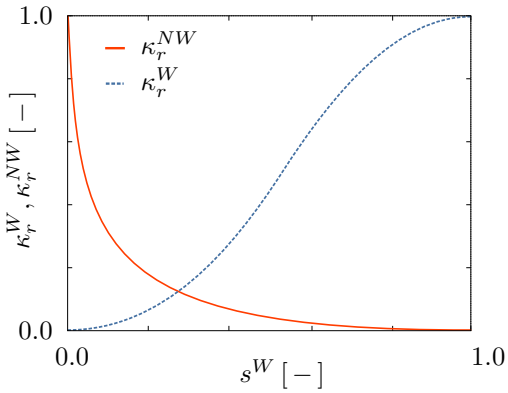

Figure 3.11: *Principle sketch of the relative-permeability factors of the wetting κ_r^W and non-wetting fluid κ_r^{NW}.*

In order to allow for any of the pore-fluids to percolate through the pore space, a least amount of interconnected pore-fluid particles is necessary, see Figure 3.10. Consequently, with respect to the macroscopic modelling approach, the respective permeabilities depend on the saturation level within the partially saturated domain. In particular, if the saturation of any of the pore fluids falls below a certain threshold, the microstructure is treated as impermeable with respect to the corresponding pore fluid. Suitable relations for the relative-permeability factors associated with the wetting and the non-wetting fluid are provided by Brooks & Corey [31]:

$$\kappa_r^W = (s_{eff}^W)^{\frac{2+3\lambda}{\lambda}} \qquad \text{and} \qquad \kappa_r^{NW} = (1 - s_{eff}^W)^2 (1 - (s_{eff}^W)^{\frac{2+\lambda}{\lambda}}) \,. \tag{3.75}$$

A graphical representation of the respective formulations is provided in Figure 3.11.

Pore gas

In order to complete the constitutive description, a relation between the realistic density ρ^{GR} of the materially compressible pore gas and the respective pore pressure p^{GR} needs to be provided. In this connection and with respect to a thermodynamic-consistent modelling approach, a suitable Helmholtz free-energy function can be proposed:

$$\psi^G(\rho^{GR}, \theta) = R^G \theta \ln \rho^{GR} + g(\theta) \,. \tag{3.76}$$

Subsequently, the well-known ideal gas law after Boyle and Mariotte, see, e. g., Gerthsen & Meschede [82], is reassembled by exploiting relation (3.25):

$$\rho^{GR} = \frac{p^{GR}}{R^G \, \theta} \,. \tag{3.77}$$

Therein, θ is the absolute Kelvin temperature of the gas constituent and R^G denotes its specific gas constant.

3.2 Dedicated models

With the previously discussed constitutive relations at hand, an adequate set of yet undetermined independent field variables can be, for instance, composed of the soil displacement $\mathbf{u}_S$, the pore-liquid and pore-gas velocities, $\mathbf{v}_L$ and $\mathbf{v}_G$, and the effective pore pressures of the pore liquid and the pore gas, p^{LR} and p^{GR}, i. e.

$$\mathbf{y} = [\,\mathbf{u}_S,\, \mathbf{v}_L,\, \mathbf{v}_G,\, p^{LR},\, p^{GR}\,]^T\,. \tag{3.78}$$

The unknown field variables are computed from the set of coupled PDE comprised of the momentum balances of the overall aggregate (3.11), the pore liquid $(3.10)_2$ and the pore gas $(3.10)_3$, and of the pore-liquid volume balance $(3.8)_1$ and the pore-gas mass balance $(3.8)_2$:

$$\begin{aligned}
\rho^S\,(\mathbf{v}_S)'_S + \rho^L(\mathbf{v}_L)'_L + \rho^G(\mathbf{v}_G)'_G &= \operatorname{div}(\mathbf{T}^S + \mathbf{T}^L + \mathbf{T}^G) + \rho\,\mathbf{b} + \mathbf{0}\,,\\
\rho^L\,(\mathbf{v}_L)'_L &= \operatorname{div}\mathbf{T}^L + \rho^L\mathbf{g} + \hat{\mathbf{p}}^L\,,\\
\rho^G\,(\mathbf{v}_G)'_G &= \operatorname{div}\mathbf{T}^G + \rho^L\mathbf{g} + \hat{\mathbf{p}}^G\,,\\
0 &= (n^L)'_S + n^L \operatorname{div}(\mathbf{u}_S)'_S + \operatorname{div}(n^L\mathbf{w}_L)\,,\\
0 &= (\rho^G)'_S + \rho^G \operatorname{div}(\mathbf{u}_S)'_S + \operatorname{div}(\rho^G\,\mathbf{w}_G)\,.
\end{aligned} \tag{3.79}$$

With respect to the efficient solution of a given problem, it is often more reasonable to proceed with a simplified but dedicated material model. In this regard, proceeding from the more general dynamic triphasic model, the following sections are devoted to the derivation of simplified material models, which are tailored to specific application scenarios. In this regard, in what follows a quasi-static triphasic model, which is constrained to slow processes, and dynamic biphasic models, are derived, where in the latter the pore space is solely occupied by a single pore fluid, which is either governed by a materially incompressible pore liquid yielding the dynamic liquid-saturated model or by an inseparable mixture of materially compressible pore gas and materially incompressible pore liquid resulting in the dynamic hybrid model.

3.2.1 Quasi-static triphasic model

In many application scenarios, such as multiphasic flow processes or slope failures, the assumption of quasi-static conditions (slow processes) is, with respect to the governing physical processes, a reasonable simplification. Herein, it is assumed that the inertia effects can be neglected, i. e. $\overset{\prime\prime}{\mathbf{x}}_\alpha = \mathbf{0}$, and, therefore, the set of independent field variables[13]

[13] Note that, depending on the indented application, other sets of primary variables might be suitable as well. Refer to Section 6.3 for details with respect to the addressed multiphasic flow process.

can be reduced to

$$\mathbf{y} = [\,\mathbf{u}_S,\, p^{LR},\, p^{GR}\,]^T\,. \tag{3.80}$$

Consequently, the number of governing PDE can be reduced as well by dropping the momentum balances of the pore-liquid constituents, viz. $(3.79)_2$ and $(3.79)_3$. To allow for further simplifications, the Relation $(2.32)_5$,

$$\rho\,\ddot{\mathbf{x}} = \sum_\alpha [\,\rho^\alpha \mathbf{x}''_\alpha - \operatorname{div}(\rho^\alpha\,\mathbf{d}_\alpha \otimes \mathbf{d}_\alpha) + \hat{\rho}^\alpha \mathbf{x}'_\alpha]\,, \tag{3.81}$$

is exploited. In particular, the absence of mass-production processes associated with the individual constituents, i. e. $\hat{\rho}^\alpha = 0$, and the negligence of the inertia terms reformulates Expression (3.81) to yield

$$\rho\,\ddot{\mathbf{x}} = \sum_\alpha [-\operatorname{div}(\rho^\alpha\,\mathbf{d}_\alpha \otimes \mathbf{d}_\alpha)]\,. \tag{3.82}$$

Moreover, proceeding form the constraint to quasi-static conditions, the velocities of the individual constituents are low and do not exhibit any abrupt spatial changes. In consequence, on the one hand, the spatial gradients of the diffusion velocities vanish. On the other hand, the realistic density of the materially compressible pore gas, is assumed, in addition to the realistic densities of the solid and the pore liquid, to be spatially constant as well. Consequently, the divergence term vanishes and, therefore, Expression (3.82) reveals $\rho\,\ddot{\mathbf{x}} = \mathbf{0}$. Following this, the set of governing PDE composed of the momentum balance of the overall aggregate $(3.79)_1$, the volume balance of the materially incompressible pore liquid $(3.79)_4$ and the mass balance of the materially compressible pore gas $(3.79)_5$, see also Ehlers [60], reads

$$\begin{aligned}
\mathbf{0} &= \operatorname{div}\mathbf{T} + \rho\,\mathbf{b}\,,\\
0 &= (n^L)'_S + n^L \operatorname{div}(\mathbf{u}_S)'_S + \operatorname{div}(n^L \mathbf{w}_L)\,,\\
0 &= (n^G \rho^{GR})'_S + n^G \rho^{GR} \operatorname{div}(\mathbf{u}_S)'_S + \operatorname{div}(n^G \rho^{GR}\,\mathbf{w}_G)\,.
\end{aligned} \tag{3.83}$$

Herein, the filter velocities, $n^L\mathbf{w}_L$ and $n^G\mathbf{w}_G$, are found from $(3.69)_1$ and $(3.69)_2$, respectively, and the simplified overall Cauchy stress tensor reads

$$\mathbf{T} = \sum_\alpha [\mathbf{T}^\alpha - \rho^\alpha\,(\mathbf{d}_\alpha \otimes \mathbf{d}_\alpha)] \;\longrightarrow\; \mathbf{T} = \sum_\alpha \mathbf{T}^\alpha \qquad \text{with} \qquad \alpha \in \{S, L, G\}\,. \tag{3.84}$$

3.2.2 Dynamic biphasic models

In many dynamic problems, depending on the frequency of the excitation, it is often reasonable to assume that one or more constituents obey the same motion function and are, consequently, driven by the same velocity and acceleration fields. In this connection, proceeding from the dynamic triphasic model (3.79), by imposing the assumption that both pore fluids follow the same motion function, the so-called dynamic biphasic hybrid model is obtained, which, in turn, comprises the cases of the fully liquid- and the fully gas-saturated pore space as well.

Dynamic hybrid model

In the dynamic hybrid model, the overall pore fluid is treated as an inseparable mixture of the materially incompressible pore liquid and the materially compressible pore gas. Basically the derivation process follows the assumptions and procedure described in Mahnkopf [134], who, however, proceeded from the quasi-static case. A dynamic formulation was already proposed in Heider [97]. However, for the sake of a complete presentation, the corresponding formulation is briefly summarised.

The hybrid model proceeds from the assumption that the motion of both pore fluids is governed by the same motion function and, therefore, φ^L and φ^G follow the same velocity field, in particular, the barycentric velocity of the pore-fluid mixture φ^F, and have the same material time derivative, i. e.

$$\mathbf{v}_L = \mathbf{v}_G \equiv \mathbf{v}_F \qquad \text{and} \qquad (\cdot)'_L = (\cdot)'_G \equiv (\cdot)'_F \,. \tag{3.85}$$

In consequence, the independent field variables are the solid displacement $\mathbf{u}_S$, the velocity $\mathbf{v}_F$ and the pressure p^{FR} of the pore-fluid mixture,

$$\mathbf{y} = [\, \mathbf{u}_S,\, \mathbf{v}_F,\, p^{FR} \,]^T \,. \tag{3.86}$$

They are computed utilising the momentum balances of the overall aggregate and the pore-fluid mixture, and from the mass balance of the pore-fluid mixture. Their respective formulations are given in the following.

To begin with, the momentum balance of the pore-fluid mixture proceeds from a summation of the of pore-liquid $(3.79)_1$ and pore-gas momentum $(3.79)_2$ balance:

$$\underbrace{\rho^L (\mathbf{v}_L)'_L + \rho^G (\mathbf{v}_G)'_G}_{\rho^F (\mathbf{v}_F)'_F} = \operatorname{div} (\underbrace{\mathbf{T}^L + \mathbf{T}^G}_{\mathbf{T}^F}) + (\underbrace{\rho^L + \rho^G}_{\rho^F}) \, \mathbf{b} + \underbrace{\hat{\mathbf{p}}^L + \hat{\mathbf{p}}^G}_{\hat{\mathbf{p}}^F} \,. \tag{3.87}$$

Therein, $\rho^F = n^F \rho^{FR}(p^{FR})$ denotes the partial density of the pore-fluid mixture as a function of the pore-fluid-mixture pressure p^{FR} and $\mathbf{T}^F$ is the Cauchy stress associated with the pore-fluid mixture. Moreover, the direct momentum production of the pore-fluid mixture $\hat{\mathbf{p}}^F$ is found through a summation of the corresponding contributions of the pore liquid $(3.39)_4$ and the pore gas $(3.39)_5$, where, as before, the capillary-pressure-driven contribution is neglected,

$$\begin{aligned}
\hat{\mathbf{p}}^F &= \hat{\mathbf{p}}^L + \hat{\mathbf{p}}^G = \\
&= p^{LR} \operatorname{grad} n^L + \hat{\mathbf{p}}^L_{Em} + p^{GR} \operatorname{grad} n^G + \hat{\mathbf{p}}^G_E = \\
&= p^{LR} (n^F \operatorname{grad} s^L + s^L \operatorname{grad} n^F) + p^{GR} (n^F \operatorname{grad} s^G + s^G \operatorname{grad} n^F) + \hat{\mathbf{p}}^L_{Em} + \hat{\mathbf{p}}^G_E = \\
&= \underbrace{(p^{LR} s^L + p^{GR} s^G)}_{p^{FR}} \operatorname{grad} n^F + p^{LR} n^F \underbrace{(\operatorname{grad} s^L + \operatorname{grad} s^G)}_{\operatorname{grad} (s^L + s^G) = \mathbf{0}} + \underbrace{\hat{\mathbf{p}}^L_{Em} + \hat{\mathbf{p}}^G_E}_{\hat{\mathbf{p}}^F_E} = \\
&= p^{FR} \operatorname{grad} n^F + \hat{\mathbf{p}}^F_E \,.
\end{aligned} \tag{3.88}$$

Herein, the extra momentum production of the pore-fluid mixture $\hat{\mathbf{p}}_E^F$ is found from a constitutive ansatz similar to $(3.69)_2$, viz.

$$\hat{\mathbf{p}}_E^F = -\frac{(n^F)^2\,\mu^{FR}}{K_{0S}^S}\,\mathbf{w}_F\,. \tag{3.89}$$

Note that the governing material parameters, in particular, the dynamic viscosity μ^{FR} and the specific weight γ^{FR} of the pore-fluid mixture, are not a direct consequence of the properties of the respective pore-fluid component, at least within the given modelling framework. Consequently, the Darcy-like filter law reads

$$n^F\,\mathbf{w}_F = -\frac{K_{0S}^S}{\mu^{FR}}\Big[\operatorname{grad} p^{FR} - \rho^{FR}\,\mathbf{g}\Big]\,. \tag{3.90}$$

Subsequently, the momentum balance of the overall mixture is obtained in a similar way. In particular, a summation of the momentum balances of the solid, the pore liquid and the pore gas gives

$$\begin{aligned}\rho^S(\mathbf{v}_S)'_S + \underbrace{\rho^L(\mathbf{v}_L)'_L + \rho^G(\mathbf{v}_G)'_G}_{:=\,\rho^F(\mathbf{v}_F)'_F} &= \operatorname{div}\big[\,\underbrace{\mathbf{T}^S + \mathbf{T}^L + \mathbf{T}^G)}_{\mathbf{T}}\,\big] + \\ &\quad + (\rho^S + \underbrace{\rho^L + \rho^G}_{\rho^F})\,\mathbf{b} + \underbrace{\hat{\mathbf{p}}^S + \hat{\mathbf{p}}^L + \hat{\mathbf{p}}^G}_{=\,\mathbf{0}}\,.\end{aligned} \tag{3.91}$$

Herein, ρ^F denotes the partial density of the pore-fluid mixture.

The mass balance of the pore-fluid mixture, which is found through a summation of the pore-liquid volume balance $(3.79)_4$ multiplied with the realistic liquid density ρ^{LR} and the pore-gas mass balance $(3.79)_5$, reads

$$(\underbrace{n^L\rho^{LR} + n^G\rho^{GR}}_{:=\,n^F\rho^{FR}})'_S + (\underbrace{n^L\rho^{LR} + n^G\rho^{GR}}_{:=\,n^F\rho^{FR}})\operatorname{div}(\mathbf{u}_S)'_S + \operatorname{div}(\underbrace{n^L\rho^{LR}\,\mathbf{w}_L + n^G\rho^{GR}\,\mathbf{w}_G}_{:=\,n^F\rho^{FR}\mathbf{w}_F})\,, \tag{3.92}$$

where $\mathbf{w}_F$ denotes the seepage velocity of the pore-fluid mixture,

$$\mathbf{w}_F = \mathbf{v}_\beta - \mathbf{v}_S \qquad \text{with} \qquad \mathbf{v}_\beta \equiv \mathbf{v}_F\,. \tag{3.93}$$

In order to complete the description, a constitutive relation for the pressure-dependent pore-fluid density $\rho^{FR}(p^{FR})$ needs to be identified. In this connection, following the procedure described in Mahnkopf [134], the partial mass balances $(2.28)_2$ can be rewritten for the pore liquid $(\beta = L)$ and the pore gas $(\beta = G)$, thereby incorporating the assumption of negligible mass-transfer processes, i. e. $\hat{\rho}^\alpha = 0$:

$$\left.\begin{aligned}(\rho^L)'_F + \rho^L\operatorname{div}\mathbf{v}_F &= 0\\ (\rho^G)'_F + \rho^G\operatorname{div}\mathbf{v}_F &= 0\end{aligned}\right\} \;\rightarrow\; \frac{(\rho^L)'_F}{\rho^L} = \frac{(\rho^G)'_F}{\rho^G}\,. \tag{3.94}$$

An analytical integration results in a constant ratio between ρ^L and ρ^G given by

$$\rho^L = C\,\rho^G \qquad \text{where} \qquad C = \left.\frac{n^L\rho^{LR}}{n^G\rho^{GR}}\right|_{t=t_0} = \frac{n_0^L\rho^{LR}}{n_0^G\rho_0^{GR}}\,. \tag{3.95}$$

Therein, the integration constant C is not a material but a structural parameter conducting the composition of the pore-fluid mixture. Moreover, n_0^L and n_0^G denote the initial volume fractions of the pore liquid and the pore gas, respectively, and ρ_0^{GR} is the initial gas density associated with initial gas pressure p_0.

Finally, the expression of the pressure-dependent pore-fluid density is obtained by recasting (3.95), with the help of the mixture density, $n^F \rho^{FR} = n^L \rho^{LR} + n^G \rho^{GR}$, the saturation condition of the pore-fluid mixture, $n^F = n^G + n^L$, and the ideal gas law (3.77). It reads

$$\rho^{FR}(p^{FR}) = \rho^{LR} \frac{1 + C}{C + \frac{\rho^{LR}}{\rho^{GR}(p^{FR})}} \qquad \text{with} \qquad \rho^{GR}(p^{FR}) = \frac{p^{FR} + p_0}{R^G \, \theta} \,. \tag{3.96}$$

Therein, p_0 is the initial pressure of the gaseous phase, R^G is the specific gas constant, and θ is the absolute temperature.

To sum up, the governing balance laws of the dynamic biphasic hybrid model read

$$\begin{aligned} n^S \rho^{SR} \, (\mathbf{v}_S)'_S + n^F \rho^{FR} \, (\mathbf{v}_F)'_F &= \operatorname{div} (\, \mathbf{T}^S + \mathbf{T}^F \,) + \rho \, \mathbf{b} \,, \\ n^F \rho^{FR} (\mathbf{v}_F)'_F &= \operatorname{div} \mathbf{T}^F + n^F \rho^{FR} \mathbf{g} + \hat{\mathbf{p}}^F \,, \\ 0 &= (n^F \rho^{FR})'_F + n^F \rho^{FR} \operatorname{div} (\mathbf{u}_S)'_S + \operatorname{div} (n^F \rho^{FR} \, \mathbf{w}_F) \,. \end{aligned} \tag{3.97}$$

Therein, ρ^{FR} denotes the pressure-dependent realistic density of the pore-fluid mixture for which the expression initially provided in Mahnkopf [134] is used. Note that $(3.96)_1$ also comprises the case of a fully gas-saturated pore space by setting $n_0^L = 0$ yielding $C = 0$ and, thus, $\rho^{FR} = \rho^{GR}$. In contrast, the case of a fully liquid-saturated pore space is obtained by setting $n_0^G = 0$ resulting in $C \to \infty$ and, herewith, by exploiting the rule of de l'Hôspital [129], $\rho^{FR} = \rho^{LR}$.

Dynamic liquid-saturated model

The underlying equations of the dynamic liquid-saturated model can be deduced proceeding either from the dynamic biphasic hybrid model (3.97) or the dynamic triphasic model (3.79). For the purpose of this monograph, the former is exploited. In particular, it is assumed that the the pore space is fully occupied with the pore liquid, i. e. $n^F = n^L$ and $n_0^G = 0$. Consequently, proceeding from the fully liquid-saturated pore space, $n_0^G = 0$, the mixture constant goes to infinity, i. e. $C \to \infty$. In consequence, the density of the pore-fluid mixture becomes equal to the pore-liquid density by applying the rule of de l'Hôspital [129], i. e. $\rho^{FR} = \rho^{LR}$. Additionally, the pore-liquid motion is governed through the velocity of the pore-fluid mixture, i. e. $\mathbf{v}_L \equiv \mathbf{v}_F$ and the corresponding material time derivative $(\cdot)'_F \equiv (\cdot)'_L$. Following this, by furthermore incorporating the incompressibility constraint of the pore liquid, the underlying balance laws, in particular, the momentum balance of

the overall mixture, and the momentum and volume balance of the pore liquid, read

$$\begin{aligned} n^S \rho^{SR} \, (\mathbf{v}_S)'_S + n^L \rho^{LR} \, (\mathbf{v}_L)'_L &= \operatorname{div} (\, \mathbf{T}^S + \mathbf{T}^L \,) + \rho \, \mathbf{b} \, , \\ n^L \rho^{LR} (\mathbf{v}_L)'_L &= \operatorname{div} \mathbf{T}^L + n^L \rho^{LR} \mathbf{g} + \hat{\mathbf{p}}^L \, , \\ 0 &= (n^L)'_S + n^L \operatorname{div} \mathbf{v}_S + \operatorname{div} (n^L \, \mathbf{w}_L) \, . \end{aligned} \tag{3.98}$$

Therein, it can be seen that the volume balance of the pore liquid does not exhibit a dependency on the pore-liquid pressure, which leads to a singular matrix when exploiting a numerical solution procedure, see Markert *et al.* [138]. To cope with that, $(3.98)_3$ needs to be reformulated, such that the volume balance of the overall aggregate is utilised instead. By adding the volume balance of the solid to the volume balance of the pore liquid, the volume balance of the aggregate is obtained:

$$\begin{aligned} 0 &= (n^L)'_S + n^L \operatorname{div} \mathbf{v}_S + \operatorname{div} (n^L \, \mathbf{w}_L) + (n^S)'_S + n^S \operatorname{div} \mathbf{v}_S \, , \\ \longrightarrow \quad 0 &= \underbrace{(n^L + n^S)'_S}_{=0} + \underbrace{(n^L + n^S)}_{=1} \operatorname{div} \mathbf{v}_S + \operatorname{div} (n^L \, \mathbf{w}_L) \, , \\ \longrightarrow \quad 0 &= \operatorname{div} (\mathbf{v}_S + n^L \, \mathbf{w}_L) \, . \end{aligned} \tag{3.99}$$

In a subsequent step, the expression $n^L \, \mathbf{w}_L$ is replaced by the Darcy-like filter law (3.69) to yield the final form of the governing set of PDE:

$$\begin{aligned} n^S \rho^{SR} \, (\mathbf{v}_S)'_S + n^L \rho^{LR} \, (\mathbf{v}_L)'_L &= \operatorname{div} (\, \mathbf{T}^S + \mathbf{T}^L \,] + \rho \, \mathbf{b} \, , \\ n^L \rho^{LR} (\mathbf{v}_L)'_L &= \operatorname{div} \mathbf{T}^L + n^L \rho^{LR} \mathbf{g} + \hat{\mathbf{p}}^L \, , \\ 0 &= \operatorname{div} \left[\mathbf{v}_S - \frac{K^S_{0S}}{\mu^{LR}} \, (\operatorname{grad} p^{LR} - \rho^{LR} \, \mathbf{g}) \right] \, . \end{aligned} \tag{3.100}$$

Chapter 4:
Numerical Treatment

Due to the complexity of the governing partial differential equations (PDE), analytical solutions are not possible for arbitrary problems but only for very specific problems incorporating various assumptions and simplifications. Consequently, to solve arbitrary IBVP, numerical solution strategies have to be exploited. A survey on commonly used methods can be found, e. g., in Larsson & Thomée [125] or Evans *et al.* [72]. In general, the numerical solution procedure proceeds from a piecewise approximation in time and space of the space- and time-continuous field functions of the underlying PDE on the nodes of a grid-like pattern, thereby transferring the initial set of coupled PDE to a set of coupled algebraic equations.

For the purpose of this monograph, the solution domain is spatially discretised through the FEM. Herein, the overall domain of interest is divided into smaller, but finite, non-overlapping subdomains, denoted as the finite elements (FE), wherein the unknown field variables are approximated through suitable ansatz (shape, basis or trial) functions. However, as in general the domain of interest is merely an excerpt of the infinite halfspace, artificial boundaries are introduced, which may have a significant influence on the solution. To cope with that, the solution domain is extended towards infinity through infinite elements (IE), thereby, on the one hand, introducing a decaying property, which tends to zero at infinity, to the approximating ansatz functions of the field variables and, on the other hand, maintaining the grid-like structure of the discrete solution domain. However, addressing the simulation of dynamic multi-field problems, in particular, the wave propagation in a porous material, the domain-extension approach does not provide a sufficiently accurate solution, see Heider [97], as the pore pressure does not tend to zero at infinity, thereby leading to spurious wave reflections at the artificial domain boundaries. To cope with that, several methods are proposed in the related literature, where, for the purpose of this monograph, additionally, an energy-absorbing layer is introduced at the FE-IE interface, to allow for a proper unbounded domain treatment. Subsequently, the spatially discretised problem is discretised in time exploiting different implicit and explicit time-integration schemes, which are chosen with respect to an efficient solution strategy of the underlying problem.

4.1 Spatial Discretisation

Concerning the spatial discretisation, the FEM has been proven to be a suitable framework for various problems in science and engineering and is, therefore, in the scope of numerous literature, see, e. g., Bathe [15], Braess [28], Huebner *et al.* [106] and Zienkiewicz & Taylor [217, 218] for a general introduction, or, for a more particulars of its application within the porous-media framework, e. g., Ellsiepen [70] and Lewis & Schrefler [128]. To begin with, the basic idea of the FEM is introduced in a more general setting and, subsequently,

applied to specific underlying problems which are in the scope of the present monograph. The underlying set of partial differential equations can be summarised via

$$\mathfrak{G}\mathbf{y}(\mathbf{x},t) - \boldsymbol{f}(\mathbf{x},t) = \mathbf{0} \qquad \text{where} \qquad \forall\,\mathbf{x} \in \Omega\,,\ \forall\, t \in [\,t_0, T\,]\,. \tag{4.1}$$

Therein, $\mathbf{y}(\mathbf{x},t)$ denotes a vector gathering the space- and time-dependent unknown field variables, $\mathfrak{G}$ is some differential operator, containing spatial and temporal derivatives, and $\boldsymbol{f}(\mathbf{x},t)$ is a known space- and time-dependent vector-valued function. The problem is defined within the temporal interval $t \in [\,t_0, T\,]$ and within the spatial domain Ω, where the latter is bounded by the boundary Γ, which can be further decomposed into either Dirichlet (D) or Neumann (N) boundaries, acting on Γ^{D} or Γ^{N}, respectively,

$$\Gamma = \Gamma^{\mathrm{D}} \cup \Gamma^{\mathrm{N}} \qquad \text{with} \qquad \Gamma^{\mathrm{D}} \cap \Gamma^{\mathrm{N}} = \emptyset\,. \tag{4.2}$$

A feasible solution for $\mathbf{y}(\mathbf{x},t)$ has to satisfy relation (4.1) at any time t and at any spatial point $\mathbf{x}$. This requirement is considered as a strong restriction and, therefore, (4.1) is denoted as the strong form of the given problem. However, as it is often impossible to find a closed form solution, this constraint is relaxed and the FEM seeks an approximate solution $\mathbf{y}^h(\mathbf{x},t)$, such that the approximation error

$$\boldsymbol{\mathcal{R}}\big(\mathbf{y}^h(\mathbf{x},t)\big) = \mathfrak{G}\,\mathbf{y}^h(\mathbf{x},t) - \boldsymbol{f}(\mathbf{x},t)\,, \tag{4.3}$$

averaged over the solution domain Ω, is minimised:

$$\min_{\mathbf{y}^h(\mathbf{x},t)} \int_\Omega \boldsymbol{\mathcal{R}}\big(\mathbf{y}^h(\mathbf{x},t)\big)\,\mathrm{d}\Omega\,. \tag{4.4}$$

Note that, with respect to the FEM, the overall spatial domain Ω is assembled from non-overlapping individual subdomains associated with the finite elements, $\Omega = \cup_e \Omega_e$. The optimisation problem (4.4) is then solved by the *method of weighted residuals*. Herein, the approximation error, which is weighted through a multiplication with a weighting functions $\mathbf{w}$, therefore often denoted as *error distribution principle*, see Huebner *et al.* [106], has to vanish over the spatial domain:

$$\mathcal{F}^h = \mathcal{F}(\mathbf{y}^h(\mathbf{x},t)) := \int_\Omega \boldsymbol{\mathcal{R}}\big(\mathbf{y}^h(\mathbf{x},t)\big) \cdot \mathbf{w}\,\mathrm{d}\Omega \stackrel{!}{=} 0\,. \tag{4.5}$$

Therein, the choice of the weighting function governs the type of the used scheme, where the different methods, such as the *collocation method* or the *method of least squares*, see, e. g., Finlayson [75], are collectively referred to as Petrov-Galerkin methods. However, within the FE framework, it is common practise to follow the Bubnov-Galerkin approach, where the same functions are used for the spatial approximation and the spatial weighting, i. e. $\mathbf{w} = \delta\mathbf{y}^h$. In this regard, the latter are denoted as test functions[1].

[1] Within the scope of the variational Bubnov-Galerkin approach, a solution $\mathfrak{u}$ solves the optimisation problem $\mathfrak{R}(\mathfrak{u})$, if an infinitesimal perturbation $\delta\mathfrak{u}$ applied on the problem satisfies the condition $\delta\mathfrak{u}\,\mathfrak{R}(\mathfrak{u}) = 0$, i. e. it is stationary. In particular, $\delta\mathfrak{u}$ tests $\mathfrak{R}(\mathfrak{u})$ for the stationary condition and is, therefore, denoted as test function.

To ensure the solution of the problem, the trial and test functions have to be chosen from the standard Sobolev space $\mathcal{H}^1(\Omega)$, thereby accounting for the square-integrability requirement, see Ellsiepen [70],

$$\begin{array}{rcl} \mathcal{S}_{\mathbf{y}}(t) & = & \{\, \mathbf{y} \in \mathcal{H}^1(\Omega)^d : \mathbf{y}(\mathbf{x},\, t) = \bar{\mathbf{y}}(\mathbf{x},\, t) \text{ on } \Gamma^{\mathrm{D}} \,\}\,, \\ \mathcal{T}_{\mathbf{y}} & = & \{\, \delta\mathbf{y} \in \mathcal{H}^1(\Omega)^d : \delta\mathbf{y}(\mathbf{x}) = \mathbf{0} \text{ on } \Gamma^{\mathrm{D}} \,\}\,, \end{array} \tag{4.6}$$

where $d \in \{1, 2, 3\}$ denotes the spatial dimension of the problem. In particular, the ansatz functions approximating the field variables have to satisfy the Dirichlet boundary conditions on the Dirichlet boundaries, $\mathbf{y}(\mathbf{x},\, t) = \bar{\mathbf{y}}(\mathbf{x},\, t)$, whereas the test functions have to vanish on the Dirichlet boundaries, $\delta\mathbf{y}(\mathbf{x}) = \mathbf{0}$. Note that different ansatz functions are used for the approximation of the field variables in the near field (domain of interest) and the far field (extension towards infinity). More details are provided in the respective sections 4.1.2 and 4.1.3.

Subsequently, following the Bubnov-Galerkin approach, the field variables $\mathbf{y}(\mathbf{x}, t)$ and the corresponding test function $\delta\mathbf{y}(\mathbf{x})$ are approximated via

$$\begin{aligned} \mathbf{y}(\mathbf{x}, t) \approx \mathbf{y}^h(\mathbf{x}, t) &= \overline{\mathbf{y}}^h(\mathbf{x}, t) + \sum_{i=1}^{N} \boldsymbol{\phi}^i(\mathbf{x})\, \boldsymbol{y}^i(t)\,, \\ \delta\mathbf{y}(\mathbf{x}) \approx \delta\mathbf{y}^h &= \sum_{i=1}^{N} \boldsymbol{\phi}^i(\mathbf{x})\, \delta\boldsymbol{y}^i\,, \end{aligned} \tag{4.7}$$

where $(\cdot)^h$ denotes the spatial approximation of the respective quantity. Moreover, $\overline{\mathbf{y}}^h(\mathbf{x}, t)$ is the solution on the Dirichlet boundaries exactly satisfying the Dirichlet boundary conditions, $\boldsymbol{\phi}^i(\mathbf{x})$ is a matrix collecting the space-dependent ansatz functions. The ansatz functions are associated with the D time-dependent nodal degrees of freedom gathered in the vector of nodal unknowns and test functions, $\boldsymbol{y}^i(t) = [\mathsf{y}_1^i, \ldots, \mathsf{y}_D^i]^T$ and $\delta\boldsymbol{y}^i = [\delta\mathsf{y}_1^i, \ldots, \delta\mathsf{y}_{\mathrm{D}}^i]^T$, both associated with the i-th node of the N-noded FE mesh.

Finally, the spatially discretised problem, which has to be solved within the FE framework, can be summarised as

$$\boxed{\text{find} \quad \boldsymbol{y}(t) \quad \text{such that} \quad \mathcal{F}^h(\boldsymbol{y}(t)) = \mathbf{0} \quad \forall\, t \in [\, t_0, T\,]\,.} \tag{4.8}$$

In particular, the nodal degrees of freedom $\boldsymbol{y}(t) = [\boldsymbol{y}^1(t), \ldots, \boldsymbol{y}^{\mathrm{N}}(t)]$ need to be tuned in such a way that the domain-averaged spatial approximation error vanishes at any time t within the simulated time interval $[\, t_0,\, T\,]$.

In what follows, the previously discussed procedure is applied to the spatial discretisation of the underlying material models. In particular, the quasi-static triphasic model and the dynamic biphasic models are considered, where the governing strong forms are initially transferred to the weak forms and, subsequently, the unknown field variables are approximated in space using suitable ansatz functions. This process transforms the space-continuous problem into a spatially discretised problem. In this connection, recall that the field variables within the near field Ω^{FE} are approximated via the ansatz function of

the finite elements, whereas infinite-element approximations are used for their extension towards infinity (far field) Ω^{IE}. Consequently, the overall spatial domain assembles from the near and far field, i. e. $\Omega = \Omega^{\mathrm{FE}} \cup \Omega^{\mathrm{IE}}$.

4.1.1 Weak forms

As elucidated before, following the Bubnov-Galerkin approach, the weak forms are obtained by multiplying the underlying strong forms with suitable test functions followed by an integration over the spatial solution domain Ω, thereby integrating by parts and exploiting the Gaussian theorem. For the purpose of this monograph, the weak forms of the quasi-static triphasic model and the dynamic hybrid and liquid-saturated model are provided here.

Quasi-static triphasic model

The quasi-static triphasic model will be used to simulate multiphasic flow processes. Consequently, the collocation of the set of independent field variables, is, on the one hand, governed by the robustness and efficiency of the solution procedure, see, e. g., Wu & Forsyth [206] or Helmig [100] and, on the other hand, constrained by the knowledge of the underlying initial and boundary conditions of the intended application scenario. In this regard, having the simulation of multiphasic flow processes in mind, a feasible set of primary variables is composed of the solid displacement $\mathbf{u}_S$, the pore-liquid saturation s^L and the pore-liquid pressure p^{LR}.

Subsequently, the underlying strong forms, i. e. the momentum balance of the overall aggregate $(3.83)_1$ (MM), the volume balance of the pore liquid $(3.83)_2$ (VL) and the mass balance of the pore gas $(3.83)_3$ (MG), are transferred to their corresponding weak forms $\mathcal{G}_{\mathrm{MM}}$, $\mathcal{G}_{\mathrm{VL}}$ and $\mathcal{G}_{\mathrm{MG}}$:

$$
\begin{aligned}
\mathcal{G}_{\mathrm{MM}} &\equiv \int_{\Omega} (\boldsymbol{\sigma}^S_{Em} - p^{FR}\mathbf{I}) \cdot \operatorname{grad} \delta\mathbf{u}_S \,\mathrm{d}v - \int_{\Omega} \rho\, \boldsymbol{g} \cdot \delta\mathbf{u}_S \,\mathrm{d}v - \int_{\Gamma^N_t} \bar{\mathbf{t}} \cdot \delta\mathbf{u}_S \,\mathrm{d}a\,, \\
\mathcal{G}_{\mathrm{VL}} &\equiv \int_{\Omega} [\,(n^L)'_S + n^L \operatorname{div} (\mathbf{u}_S)'_S\,]\, \delta s^L \,\mathrm{d}v - \int_{\Omega} n^L\, \mathbf{w}_L \cdot \operatorname{grad} \delta s^L \,\mathrm{d}v + \\
&\quad + \int_{\Gamma^N_v} \bar{v}^L \delta s^L \,\mathrm{d}a\,, \\
\mathcal{G}_{\mathrm{MG}} &\equiv \int_{\Omega} [\, n^G(\rho^{GR})'_S + \rho^{GR}(n^G)'_S + n^G\rho^{GR} \operatorname{div} (\mathbf{u}_S)'_S\,]\, \delta p^{LR} \mathrm{d}v - \\
&\quad - \int_{\Omega} n^G \rho^{GR}\, \mathbf{w}_G \cdot \operatorname{grad} \delta p^{LR} \,\mathrm{d}v + \int_{\Gamma^{\mathrm{N}}_m} \bar{m}^G \delta p^{LR} \,\mathrm{d}a\,.
\end{aligned}
\tag{4.9}
$$

Therein, $\bar{\mathbf{t}} := (\boldsymbol{\sigma}^S_{Em} - p^{FR}\,\mathbf{I})\,\mathbf{n}$ is the external load vector, $\bar{v}^L = n^L \mathbf{w}_L \cdot \mathbf{n}$ denotes the efflux of the pore liquid and $\bar{m}^G = n^G \rho^{GR} \mathbf{w}_G \cdot \mathbf{n}$ is the efflux of the pore gas, all acting on the

Neumann boundaries Γ_t^{N}, Γ_v^{N} and Γ_m^{N}, respectively. Moreover, $\mathbf{n}$ is the outward-oriented unit normal vector on the surface of the corresponding Neumann boundary, and $\delta\mathbf{u}_S$, δs^L and δp^{LR} are the test function related to the primary variables. Subsequently, the coupled problem governing the quasi-static triphasic model is summarised as

$$\boldsymbol{\mathcal{G}}(\mathbf{y}, \mathbf{y}'_S) = [\, \mathcal{G}_{\mathrm{MM}},\, \mathcal{G}_{\mathrm{VL}},\, \mathcal{G}_{\mathrm{MG}} \,]^T = \mathbf{0}\,. \tag{4.10}$$

Dynamic hybrid model

The set of primary variables of the dynamic hybrid model is composed of the solid displacement $\mathbf{u}_S$, the pore-fluid velocity, $\mathbf{v}_F$ and the pressure of the pore-fluid mixture p^{FR}, i. e. $\mathbf{y} = [\, \mathbf{u}_S, \mathbf{v}_F, p^{FR} \,]^T$. Proceeding from the strong forms, in particular, the momentum balances of the overall aggregate $(3.97)_1$, and the momentum and mass balance of the pore-fluid mixture, $(3.97)_2$ and $(3.97)_3$, the underlying weak forms $\mathcal{G}_{\mathrm{MM}}$, $\mathcal{G}_{\mathrm{MF}}$ and $\mathcal{G}_{\mathrm{MP}}$ read

$$\begin{aligned}
\mathcal{G}_{\mathrm{MM}} \;\equiv\; & \int_\Omega \{\rho^S (\mathbf{v}_S)'_S + \rho^F [(\mathbf{v}_F)'_S + \operatorname{grad} \mathbf{v}_F\, \mathbf{w}_F] - (\rho^S + \rho^F)\mathbf{b}\} \cdot \delta\mathbf{u}_S \,\mathrm{d}v + \\
& + \int_\Omega (\boldsymbol{\sigma}^S_{Em} - p^{FR}\,\mathbf{I}) \cdot \operatorname{grad} \delta\mathbf{u}_S \,\mathrm{d}v - \int_{\Gamma^{\mathrm{N}}_{\mathbf{t}}} \overline{\mathbf{t}} \cdot \delta\mathbf{u}_S \,\mathrm{d}a\,, \\
\mathcal{G}_{\mathrm{MF}} \;\equiv\; & \int_\Omega [\rho^F (\mathbf{v}_F)'_S + (\operatorname{grad} \mathbf{v}_F)\, \mathbf{w}_F - \mathbf{b}] \cdot \delta\mathbf{v}_F \,\mathrm{d}v + \int_\Omega (-n^F p^{FR}) \operatorname{div} \delta\mathbf{v}_F \,\mathrm{d}v \\
& + \int_\Omega [\frac{(n^F)^2 \mu^{FR}}{K^S_{0S}} \mathbf{w}_F - p^{FR} \operatorname{grad} n^F] \cdot \delta\mathbf{v}_F \,\mathrm{d}v - \int_{\Gamma^{\mathrm{N}}_{\mathbf{t}^F}} \overline{\mathbf{t}}^F \cdot \delta\mathbf{v}_F \,\mathrm{d}a\,, \\
\mathcal{G}_{\mathrm{MP}} \;\equiv\; & -\int_\Omega (n^F \rho^{FR} \mathbf{w}_F) \cdot \operatorname{grad} \delta p^{FR} \,\mathrm{d}v + \int_\Omega [(\rho^{FR} n^F)'_S + \rho^{FR} n^F \operatorname{div} \mathbf{v}_S\,]\, \delta p^{FR} \,\mathrm{d}v \\
& + \int_{\Gamma^{\mathrm{N}}_v} \overline{m}\, \delta p^{FR} \,\mathrm{d}a\,.
\end{aligned} \tag{4.11}$$

Therein, $\overline{\mathbf{t}} = (\boldsymbol{\sigma}^S_{Em} - p^{FR}\,\mathbf{I})\,\mathbf{n}$ and $\overline{\mathbf{t}}^F = -n^F p^{FR}\,\mathbf{n}$ denote the external loading vectors acting on the Neumann boundaries $\Gamma^{\mathrm{N}}_{\mathbf{t}}$ and $\Gamma^{\mathrm{N}}_{\mathbf{t}^F}$ of the overall aggregate and the pore fluid, respectively, and $\overline{m} = \rho^{FR} n^F \mathbf{w}_F \cdot \mathbf{n}$ is the mass efflux draining through the Neumann boundary Γ^{N}_v with $\mathbf{n}$ as the outward-oriented unit surface normal. Furthermore, $\delta\mathbf{u}_S$, $\delta\mathbf{v}^F$ and δp^{FR} are the corresponding test functions.

Subsequently, the overall coupled problem governing the dynamic biphasic hybrid model can be summarised as

$$\boldsymbol{\mathcal{G}}(\mathbf{y}, \mathbf{y}'_S, \mathbf{y}''_S) = [\, \mathcal{G}_{\mathrm{MM}},\, \mathcal{G}_{\mathrm{VL}},\, \mathcal{G}_{\mathrm{MF}} \,]^T = \mathbf{0}\,. \tag{4.12}$$

Dynamic liquid-saturated model

The set of primary variables of the dynamic liquid-saturated model is collocated by the solid displacement $\mathbf{u}_S$, the pore-liquid velocity, $\mathbf{v}_L$ and the pressure of the pore liquid p^{LR}, i. e. $\mathbf{y} = [\,\mathbf{u}_S, \mathbf{v}_L, p^{LR}\,]^T$. Proceeding from the strong forms, in particular, the momentum balance of the overall aggregate $(3.100)_1$, and the momentum and volume balance of the pore liquid, $(3.100)_2$ and $(3.100)_3$, the underlying weak forms $\mathcal{G}_{\mathrm{MM}}$, $\mathcal{G}_{\mathrm{ML}}$ and $\mathcal{G}_{\mathrm{VL}}$ read

$$
\begin{aligned}
\mathcal{G}_{\mathrm{MM}} &\equiv \int_{\Omega} \{\rho^S (\mathbf{v}_S)'_S + \rho^F [(\mathbf{v}_F)'_S + (\operatorname{grad} \mathbf{v}_F)\, \mathbf{w}_F] - (\rho^S + \rho^F)\mathbf{b}\} \cdot \delta\mathbf{u}_S \, \mathrm{d}v + \\
&+ \int_{\Omega} (\boldsymbol{\sigma}^S_{Em} - p^{FR}\, \mathbf{I}) \cdot \operatorname{grad} \delta\mathbf{u}_S \, \mathrm{d}v - \int_{\Gamma^{\mathrm{N}}_{\mathbf{t}}} \overline{\mathbf{t}} \cdot \delta\mathbf{u}_S \, \mathrm{d}a \,, \\
\mathcal{G}_{\mathrm{ML}} &\equiv \int_{\Omega} [\rho^L (\mathbf{v}_L)'_S + (\operatorname{grad} \mathbf{v}_L)\, \mathbf{w}_L - \mathbf{b}] \cdot \delta\mathbf{v}_L \, \mathrm{d}v + \int_{\Omega} (-n^L p^{LR}) \operatorname{div} \delta\mathbf{v}_L \, \mathrm{d}v \\
&+ \int_{\Omega} [\frac{(n^L)^2 \mu^{LR}}{K^S_{0S}} \mathbf{w}_L - p^{LR} \operatorname{grad} n^L] \cdot \delta\mathbf{v}_L \, \mathrm{d}v - \int_{\Gamma^{\mathrm{N}}_{\mathbf{t}^L}} \overline{\mathbf{t}}^L \cdot \delta\mathbf{v}_L \, \mathrm{d}a \,, \\
\mathcal{G}_{\mathrm{VL}} &\equiv \int_{\Omega} \delta p^{LR} \operatorname{div} \mathbf{v}_S \, \mathrm{d}v + \int_{\Omega} \operatorname{grad} \delta p^{LR} \cdot [\frac{K^S_{0S}}{\mu^{LR}} (\operatorname{grad} p^{LR} - \rho^{LR}\, \mathbf{g})] \, \mathrm{d}v \\
&+ \int_{\Gamma^{\mathrm{N}}_{v}} \overline{v}\, \delta p^{LR} \, \mathrm{d}a \,.
\end{aligned}
\tag{4.13}
$$

Therein, $\overline{\mathbf{t}} = (\boldsymbol{\sigma}^S_{Em} - p^{LR}\, \mathbf{I})\, \mathbf{n}$ and $\overline{\mathbf{t}}^L = -n^L p^{LR}\, \mathbf{n}$ denote the external loading vectors acting on the Neumann boundaries $\Gamma^{\mathrm{N}}_{\mathbf{t}}$ and $\Gamma^{\mathrm{N}}_{\mathbf{t}^L}$ of the overall aggregate and the pore fluid, respectively, and $\overline{v} = n^L \mathbf{w}_L \cdot \mathbf{n}$ is the volume efflux draining through the Neumann boundary Γ^{N}_{v} with $\mathbf{n}$ as the outward-oriented unit surface normal. Furthermore, $\delta\mathbf{u}_S$, $\delta\mathbf{v}_L$ and δp^{LR} are the corresponding test functions.

Subsequently, the overall coupled problem governing the dynamic biphasic hybrid model can be summarised as

$$
\boldsymbol{\mathcal{G}}(\mathbf{y}, \mathbf{y}'_S, \mathbf{y}''_S) = [\,\mathcal{G}_{\mathrm{MM}},\, \mathcal{G}_{\mathrm{ML}},\, \mathcal{G}_{\mathrm{VL}}\,]^T = \mathbf{0} \,. \tag{4.14}
$$

4.1.2 Finite-element approximation

With the previously discussed weak forms at hand, the spatial discretisation of the near field is carried out via the FEM, thereby subdividing the continuous domain Ω^{FE} into small but finite subregions Ω^{FE}_e, i. e. $\Omega^{\mathrm{FE}} = \cup_e \Omega^{\mathrm{FE}}_e$, in which the unknown field variables

and the test functions are approximated by suitable trial and test functions, see (4.7):

$$\begin{aligned} \mathbf{y}(\mathbf{x},t) \;\approx\; \mathbf{y}^h(\mathbf{x},t) \;&=\; \overline{\mathbf{y}}^h(\mathbf{x},t) \;+\; \sum_{i=1}^{N} \boldsymbol{\phi}^i_{\mathrm{FE}}(\mathbf{x})\, \boldsymbol{y}^i(t)\,, \\ \delta\mathbf{y}(\mathbf{x}) \;\approx\; \delta\mathbf{y}^h \;&=\; \sum_{i=1}^{N} \boldsymbol{\phi}^i_{\mathrm{FE}}(\mathbf{x})\, \delta\boldsymbol{y}^i\,. \end{aligned} \tag{4.15}$$

Therein, $\mathbf{y}$ and $\delta\mathbf{y}$ are vectors gathering the primary variables and the respective test functions, which are approximated within the finite-element domain through the ansatz function summarised in the matrix $\boldsymbol{\phi}^i_{\mathrm{FE}}$. Furthermore, $\boldsymbol{y}^i$ and $\delta\boldsymbol{y}^i$ denote vectors concentrating the respective nodal values of the associated primary variables of the FE mesh. Moreover, $(\cdot)^h$ denotes the spatially approximated quantity. Note that, with respect to the various problems considered for the purpose of this monograph, the composition of $\mathbf{y}$ and $\delta\mathbf{y}$ and, consequently, of $\boldsymbol{\phi}^i_{\mathrm{FE}}$, $\boldsymbol{y}^i$ and $\delta\boldsymbol{y}^i$ alters according to the problem under consideration, see Section 4.1.1. For the particular formulations of the commonly used ansatz functions refer, for instance, to Zienkiewicz & Taylor [217, 218]. However, in order to achieve stable results, the choice of the trial and ansatz functions are constrained by the so-called *inf-sup* condition (Ladyshenskaja-Babuška-Brezzi (LBB) condition), see Brezzi & Fortin [30]. In particular, proceeding from polynomial-type functions, the order of the polynomial approximating the solid displacements have to be of one order higher than the approximating polynom of the remaining field variables, such as the pore-fluid velocities or the pore pressure. Consequently, quadratic ansatz functions for the solid displacement and linear ansatz functions for the remaining field variables are utilised. In consequence, Taylor-Hood elements are used for the spatial approximation.

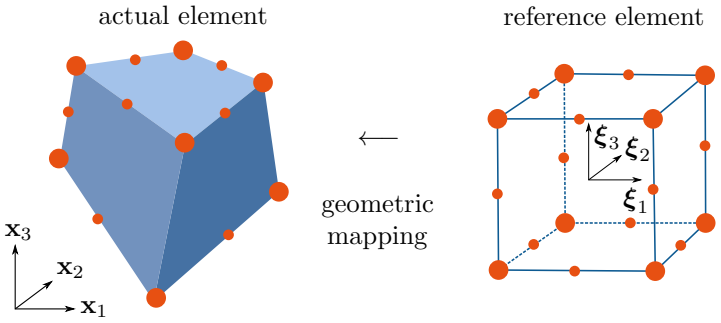

Figure 4.1: *Sketch of the geometry transformation between the actual and the reference finite elements.*

In this connection, since the element-wise decomposition of Ω^{FE} generally leads to irregular-shaped finite elements, the ansatz functions are, for the sake of convenience, defined within a so-called unit reference element, see Figure 4.1. Consequently, a suitable geometric mapping between the actual element, defined with respect to the global coordinate system $\mathbf{x}$, and the reference element, which is given within a local coordinate system $\boldsymbol{\xi}$ is carried out via

$$\mathbf{x}(\boldsymbol{\xi}) = \sum_{i=1}^{N_e} \boldsymbol{\phi}^i_{\mathrm{FE,geo}}(\boldsymbol{\xi})\, \mathbf{x}^i(t)\,. \tag{4.16}$$

Therein, N_e denotes the number of nodes of a single element with the global coordinates $\mathbf{x}^i$, and $\boldsymbol{\phi}^i_{\mathrm{FE,geo}}$ are the shape functions used for the geometric approximation of the element shape, where, following the *isoparametric concept*, the shape functions coincide with the ansatz functions used for the solid displacements, i. e. $\boldsymbol{\phi}^i_{\mathrm{FE,geo}} \equiv \boldsymbol{\phi}^i_{\mathbf{u}_S}$.

Subsequently, the integrals in the weak formulations can be reformulated with respect to the local coordinate system and are approximated by the Gauss quadrature rule,

$$\int_{\Omega_e^{\mathrm{FE}}} \underbrace{\boldsymbol{\mathcal{R}}(\mathbf{x}) \cdot \delta\mathbf{y}}_{f(\mathbf{x})} \,\mathrm{d}v = \int_{\Omega_e^{\mathrm{FE}}} f(\boldsymbol{\xi})\, J_e(\boldsymbol{\xi})\,\mathrm{d}v_\xi \overset{\text{Gauss}}{\approx} \sum_{k=1}^{N_g} f(\boldsymbol{\xi}_k)\, J_e(\boldsymbol{\xi}_k)\, w_k \,, \tag{4.17}$$

$$\text{where} \qquad J_e(\boldsymbol{\xi}) := \left| \det\left(\frac{\mathrm{d}\mathbf{x}(\boldsymbol{\xi})}{\mathrm{d}\boldsymbol{\xi}} \right) \right| .$$

Therein, Ω_e^{FE} denotes the spatial domain of a single finite element, $\mathrm{d}v_\xi$ is an infinitesimal volume in the reference element and $J_e(\boldsymbol{\xi})$ is the so-called Jacobi determinant, which is responsible for mapping of the volume of the reference element to the actual finite element. Moreover, N_g is the number of Gauss points and w_k denotes the weights associated with the Gauss integration points $\boldsymbol{\xi}_k$.

4.1.3 Infinite-element approximation

To cope with the extension towards infinity in an infinite space or semi-infinite halfspace, infinite elements (IE) are exploited. Similar to the approximation of the field variables and the respective test functions via ansatz functions within the finite elements, the approximation within the infinite domain Ω^{IE} is conducted through shape functions as well by

$$\begin{aligned} \mathbf{y}(\mathbf{x},t) \;\approx\; \mathbf{y}^h(\mathbf{x},t) \;&=\; \overline{\mathbf{y}}^h(\mathbf{x},t) \;+\; \sum_{i=1}^{N} \boldsymbol{\phi}^i_{\mathrm{IE}}(\mathbf{x})\, \boldsymbol{y}^i(t) \,, \\ \delta\mathbf{y}(\mathbf{x}) \;\approx\; \delta\mathbf{y}^h \;&=\; \sum_{i=1}^{N} \boldsymbol{\phi}^i_{\mathrm{IE}}(\mathbf{x})\, \delta\boldsymbol{y}^i \,, \end{aligned} \tag{4.18}$$

where $\boldsymbol{\phi}^i_{\mathrm{IE}}$ denotes a matrix collocating the respective ansatz functions within the infinite-element domain. In particular, addressing the simulation of coupled problems, the composition of $\boldsymbol{\phi}^i_{\mathrm{IE}}$ depends on the investigated problem and, more specifically, on the property of the approximated field variable at infinity. As the ansatz functions of the infinite elements are designed such that they exhibit a decaying characteristic towards infinity, the associated field variable vanishes at infinity as well, see Marques & Owen [139] for suitable formulations. This property, however, may not be suitable for every field. For instance, in the case of the dynamic liquid-saturated model, the solid displacement and liquid velocities are zero at infinity, while the pore-liquid pressure does not vanish. In particular, due to the incompressibility of the pore liquid, which, consequently, leads to infinite wave-propagation velocities, the pore pressure is instantaneously propagated towards infinity.

In order to cover the unboundedness of the geometric domain, the geometry-mapping functions, which are responsible for the mapping between the reference and the actual

element and are gathered in $\phi^i_{\mathrm{IE,geo}}$, extend towards infinity as well, see Figure 4.2. Note

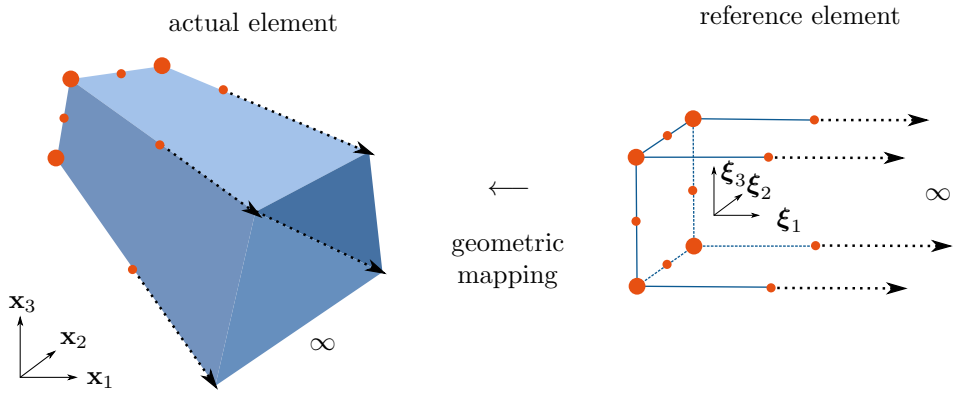

Figure 4.2: *Sketch of the geometry transformation between the actual and the reference infinite elements.*

that the evaluation of the integrals of the weak forms is carried out as in the FE approach. In particular, their computation in the reference element is done via the Gauss quadrature rule, see (4.16) with $\phi^i_{\mathrm{FE,geo}} \equiv \phi^i_{\mathrm{IE,geo}}$, and their subsequent transfer to the actual element. Consequently, this IE procedure entails only minor modifications in most FE codes.

4.2 Unbound-domain treatment

In contrast to quasi-static problems, where the truncation of the infinite half-space at the near field often does not affect the numerical investigation, the trimmed spatial domain may significantly alter the simulation results of a dynamic problem, for instance, when incoming waves are reflected back into the domain of interest at the introduced artificial boundaries. In order to overcome this problem, several methods have been proposed in the literature. These methods can be generally classified into

- the **coupled finite-element-boundary-element methods (FEM-BEM)**, where the near field is discretised with the FEM and the far-field response is captured using the boundary-element method (BEM), see, e. g., von Estorff & Firuziaan [71] and Yazdchi *et al.* [211],
- the **coupled finite-element-infinite-element methods (FEM-IEM)**, in which the FEM discretises the near field and the IEM extends towards infinity, see, e. g., Khalili *et al.* [112] and Schanz [171], and
- the **absorbing boundary condition (ABC) schemes**, such as the method of perfectly matched layers (PML), where an unphysical wave absorbing layer is placed at the near-field-far-field intersection and basically prevents wave reflections back to the near domain, see, e. g., Basu & Chopra [14], Basu [13] and Oskooi *et al.* [152] for details.

Note that in the ABC schemes, the governing equations are solved in the frequency instead of the time domain, see, e. g., Li [131] and Aneiros [7] and references therein. Therefore, the implementation into FE-based codes is a rather complex procedure. For the purpose

of this monograph, the approach initially proposed in Haeggblad & Nordgren [91] and further extended towards the application of porous media by Wunderlich *et al.* [207] and Heider *et al.* [99] will be used. Therein, the near and the far field are spatially discretised using finite elements (FE) and infinite elements (IE), respectively. Additionally, following the idea of Lysmer & Kuhlemeyer [133], an energy-absorbing layer composed of viscous damped dashpots is introduced at the FE-IE interface Γ_{I}, which is also often denoted as viscous damped boundary (VDB), see Figure 4.3.

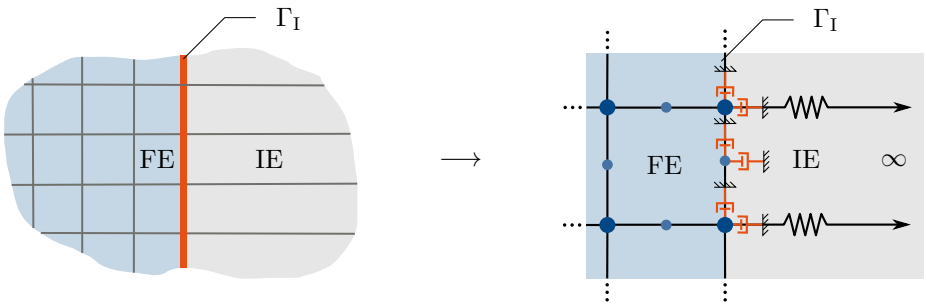

Figure 4.3: *Sketch of the unbound-domain treatment.*

According to Heider *et al.* [99], the governing weak form of the unbound-domain treatment is composed of a quasi-static linear elastic porous solid and a viscous-damped part and reads

$$\underbrace{\int_{\Omega} (\boldsymbol{\sigma}^{S}_{Em} - p^{FR}\,\mathbf{I}) \cdot \operatorname{grad} \delta\mathbf{u}_S \,\mathrm{d}\Omega - \int_{\Omega} \rho\,\mathbf{b} \cdot \delta\mathbf{u}_S \,\mathrm{d}\Omega}_{\text{quasi-static part}} + \underbrace{\int_{\Gamma_{\mathrm{I}}} \mathbf{r} \cdot \delta\mathbf{u}_S \,\mathrm{d}\Gamma}_{\text{visous-damped part}} = 0\,, \tag{4.19}$$

$$\text{where} \qquad \mathbf{r} = \mathbf{P}^{T} \begin{bmatrix} a\rho c_p & 0 \\ 0 & b\rho c_s \\ 0 & b\rho c_s \end{bmatrix} \mathbf{P}(\mathbf{u}_S)'_S\,.$$

Therein, ρ denotes the density of the overall aggregate, see expression (2.3), Ω denotes the volume of the infinite element, Γ_I the area of the FE-IE interface and $\mathbf{P}$ a projection matrix relating the global solid velocity components to the local coordinate system (normal and shear direction) on Γ_{I}. Furthermore, $\mathbf{r}$ represents an area-weighted three-dimensional force vector containing the nodal contributions of the dashpots to the nodes associated with the area at the FE-IE interface. The force vector depends on the compression- and shear-wave velocities, see Heider *et al.* [99],

$$c_p = \sqrt{(2\mu_S + \lambda_S)/\rho} \qquad \text{and} \qquad c_s = \sqrt{\mu_S/\rho} \tag{4.20}$$

respectively, and on the dimensionless compression- and shear-wave damping coefficients a and b. In this connection, Lysmer & Kuhlemeyer [133] proposed $a = b = 1$, which gives the best energy absorption if the wave-propagation direction is normal to the FE-IE interface, whereas White *et al.* [198] computed their respective values based on the requirement to achieve maximum energy-dissipation over different wave incidence angles, viz.

$$a = \frac{8}{15\pi}(5 + 2c - 2c^2)\,, \qquad b = \frac{8}{15\pi}(3 + 2c)\,, \qquad \text{where} \qquad c = \sqrt{\mu^S/(\lambda^S + 2\mu^S)}\,. \tag{4.21}$$

A numerical study of the damping parameters is addressed in Chapters 6.

4.3 Temporal discretisation and solution method

In what follows, the temporal discretisation of the coupled problem and its related solution method, which is strongly connected to the underlying time-marching scheme, is addressed. The semi-discretised system can be summarised as:

$$\boldsymbol{\mathcal{F}}^h(t,\, \boldsymbol{y},\, \dot{\boldsymbol{y}},\, \ddot{\boldsymbol{y}},\, \boldsymbol{q},\, \dot{\boldsymbol{q}}) = \left[\begin{array}{c} \boldsymbol{\mathcal{G}}^h(t,\, \boldsymbol{y},\, \dot{\boldsymbol{y}},\, \ddot{\boldsymbol{y}},\, \boldsymbol{q}) \\ \boldsymbol{\mathcal{L}}^h(t,\, \boldsymbol{q},\, \dot{\boldsymbol{q}},\, \boldsymbol{y}) \end{array}\right] = \boldsymbol{\mathcal{R}}^h \approx \boldsymbol{0}\,. \tag{4.22}$$

Therein, the functionals $\boldsymbol{\mathcal{G}}^h$ and $\boldsymbol{\mathcal{L}}^h$ comprise the spatially discretised coupled balance relations proceeding from the FE method (global system), and the governing equations of the elasto-plastic solid skeleton (local system), respectively, where the latter either follows the pure isotropic ($\boldsymbol{\mathcal{L}}^h = \boldsymbol{\mathcal{L}}^h_{\mathrm{IH}}$) or the mixed isotropic-kinematic hardening model ($\boldsymbol{\mathcal{L}}^h = \boldsymbol{\mathcal{L}}^h_{\mathrm{IKH}}$). Moreover, $\boldsymbol{y}$ and $\boldsymbol{q}$ denote vectors gathering the unknowns at the nodes and the Gauss points of the FE mesh, where their respective collocation depends on the model under consideration. Note that, for the sake of a clear representation, the abbreviations $\dot{(\cdot)} = (\cdot)'_S$ and $\ddot{(\cdot)} = (\cdot)''_S$ representing the first and second time derivative with respect to the solid skeleton have been used. Note that for the quasi-static problems, the inertia terms are neglected and, therefore, the acceleration terms vanish, i. e. $\ddot{\boldsymbol{y}} = \boldsymbol{0}$. Moreover, it is assumed that in the following, the system is solved sufficiently accurate and, therefore, the spatial approximation error is assumed to be zero, i. e. $\boldsymbol{\mathcal{R}}^h \approx \boldsymbol{0}$.

Furthermore, the semi-discrete problem will be, with respect to the intended application, discretised in time using either implicit or explicit time-integration schemes, thereby having the implementation into Abaqus/Standard (implicit time-integration schemes) and Abaqus/Explicit (explicit time-integration schemes) in mind, where both provide algorithms for quasi-static and dynamic problems. In an implicit procedure, the underlying balance laws are evaluated at the new unknown state. Thus, in each time step, a system of algebraic equations needs to be solved, such that the solution satisfies the governing balance relations at the new state, a process, which is, specially for large system, very time consuming. In contrast, in an explicit scheme, it is assumed that the current solution satisfies the balance laws at the known state, which is, in general, merely true when proceeding from the initial state. Consequently, each temporal increment introduces a small numerical error, which accumulates over the simulated time span.

For quasi-static problems, the negligence of the acceleration terms degrades the governing PDE system (4.22) to be of first order in time. In this regard, suitable time-marching schemes are collected in the class of the Runge-Kutta methods, see, e. g., Hairer *et al.* [93] or Hairer & Wanner [94], comprising simultaneously implicit and explicit time-advancing methods, where the implicit methods are, due to their unconditional stability, often favourable for slow (quasi-static) processes. In contrast, the stability of the explicit schemes is constrained by the prominent CFL condition named after Courant-Friedrichs-Lewy, see Courant *et al.* [45], which governs the maximum allowable time increment. Consequently, explicit methods are more suitable for rapid processes, as small time increments are anyway necessary in order to resolve the transient response of the system,

see the Nyquist-Shannon sampling theorem, e. g., in Shannon [175]. However, explicit strategies are not applicable for the dynamic fluid-saturated model following a monolithic solution strategy[2], as the material incompressibility of the pore liquid leads to algebraic constraint, see, e. g., Heider [97] or Markert *et al.* [138], or Section 4.3.2 for more details. To cope with this, one either proceeds from an implicit method, such as the implicit Hilber-Hughes-Taylor (HHT) method, see Hilber *et al.* [101], or has to exploit a staggered solution strategy[3], such as the so-called fractional-step method, see, e. g., Markert *et al.* [138].

4.3.1 Implicit methods

In what follows, the utilised implicit temporal discretisation schemes and the respective solution procedure are briefly summarised. In particular, the backward (implicit) Euler method is applied to quasi-static problems, i. e. the quasi-static triphasic model and the elasto-plastic solid skeleton, whereas the implicit Hilber-Hughes-Taylor scheme temporally discretises the dynamic biphasic models.

Backward-Euler time-integration scheme

Addressing the simulation of quasi-static processes, where the inertia terms are neglected, i. e. $\ddot{\boldsymbol{y}}_{n+1} \equiv \boldsymbol{0}$, the unconditionally stable backward (implicit) Euler scheme, which belongs to the class of diagonally implicit Runge-Kutta methods (DIRK), see, e. g., Ellsiepen [70], is utilised. Herein, the primary and the internal-state variables $\boldsymbol{y}_{n+1}$ and $\boldsymbol{q}_{n+1}$ at the new (unknown) time t_{n+1}, are advanced proceeding from the known values $\boldsymbol{y}_n$ and $\boldsymbol{q}_n$ at time t_n by means of a Taylor-series-like expansion truncated after the linear terms. In particular, in contrast to the actual Taylor-series expansion, which computes the derivatives at the known state at t_n, herein, the derivatives are evaluated at the unknown state at t_{n+1} yielding

$$\begin{aligned} \boldsymbol{y}_{n+1} &= \boldsymbol{y}_n + \Delta t\, \dot{\boldsymbol{y}}_{n+1} \qquad \text{with} \qquad \dot{\boldsymbol{y}}_{n+1} = \frac{1}{\Delta t}(\boldsymbol{y}_{n+1} - \boldsymbol{y}_n)\,, \\ \boldsymbol{q}_{n+1} &= \boldsymbol{q}_n + \Delta t\, \dot{\boldsymbol{q}}_{n+1} \qquad \text{with} \qquad \dot{\boldsymbol{q}}_{n+1} = \frac{1}{\Delta t}(\boldsymbol{q}_{n+1} - \boldsymbol{q}_n)\,, \end{aligned} \tag{4.23}$$

where $\Delta t = t_{n+1} - t_n$ denotes the time increment. Consequently, with respect to the implicit nature of the backward Euler method, (4.22) is evaluated at t_{n+1}, where $\dot{\boldsymbol{y}}_{n+1}$ and $\dot{\boldsymbol{q}}_{n+1}$ are substituted by $(4.23)_1$ and $(4.23)_2$, respectively, and yields

$$\boldsymbol{\mathcal{F}}^h_{n+1} = \boldsymbol{\mathcal{F}}^h(t_{n+1},\, \boldsymbol{y}_{n+1},\, \boldsymbol{q}_{n+1}) = \begin{bmatrix} \boldsymbol{\mathcal{G}}^h(\boldsymbol{y}_{n+1},\, \boldsymbol{q}_{n+1}) \\ \boldsymbol{\mathcal{L}}^h(\boldsymbol{y}_{n+1},\, \boldsymbol{q}_{n+1}) \end{bmatrix} \overset{!}{=} \boldsymbol{0}\,. \tag{4.24}$$

This system of algebraic equations needs to be solved for the unknowns $\boldsymbol{y}_{n+1}$ and $\boldsymbol{q}_{n+1}$.

[2] Within a monolithic solution strategy, the actual coupled problem is treated as a single entity and, therefore, the whole coupled problem is advanced in time using the same time-integration scheme with the same time-step size, see, e. g., Zinatbakhsh [220].

[3] In contrast to monolithic schemes, the individual subproblems of the overall coupled problem can be advanced in time using different time-integration schemes with different time-step sizes, see, e. g., Zinatbakhsh [220].

Hilber-Hughes-Taylor time-integration scheme

The dynamic fluid-saturated model is adequately discretised by the implicit Hilber-Hughes-Taylor (HHT) method [101], which is a generalisation of Newmark's method [147], but with a straightforward control of the numerical damping via the scheme parameters. Following the implicit HHT procedure, the global system $(4.22)_1$ is recast to

$$\begin{aligned} \boldsymbol{\mathcal{G}}^h_{n+1} &= \boldsymbol{M}\ddot{\boldsymbol{y}}_{n+1} + (1+\alpha)(\,\boldsymbol{r}_{n+1} - \boldsymbol{f}_{n+1}) - \alpha(\,\boldsymbol{r}_n - \boldsymbol{f}_n) \stackrel{!}{=} \boldsymbol{0} \\ \text{with} \qquad \boldsymbol{y}_{n+1} &= \boldsymbol{y}_n + \Delta t\,\dot{\boldsymbol{y}}_n + \Delta t^2\big((\frac{1}{2}-\beta)\,\ddot{\boldsymbol{y}}_n + \beta\,\ddot{\boldsymbol{y}}_{n+1}\big)\,, \\ \dot{\boldsymbol{y}}_{n+1} &= \dot{\boldsymbol{y}}_n + \Delta t\,\big((1-\gamma)\,\ddot{\boldsymbol{y}}_n + \gamma\,\ddot{\boldsymbol{y}}_{n+1}\big)\,. \end{aligned} \tag{4.25}$$

Therein, $\boldsymbol{r}_{n+1} = \boldsymbol{r}(t_{n+1}, \boldsymbol{y}_{n+1}, \dot{\boldsymbol{y}}_{n+1}, \boldsymbol{q}_{n+1})$ and $\boldsymbol{r}_n = \boldsymbol{r}(t_n, \boldsymbol{y}_n, \dot{\boldsymbol{y}}_n, \boldsymbol{q}_n)$ denote the quasi-static response of the system at the new (unknown) state at t_{n+1}, and at the previous (known) state at t_n, respectively. Moreover, $\boldsymbol{M} = \partial\boldsymbol{\mathcal{G}}^h_{n+1}/\partial\ddot{\boldsymbol{y}}_{n+1}$ is the mass matrix and is governed by the constituent densities and, therefore, may depend on the primary variables. The parameter α controls the numerical damping by governing the parameters β and γ via

$$\beta = \frac{1}{4}(1-\alpha)^2 \qquad \text{and} \qquad \gamma = \frac{1}{2}(1-\alpha)\,, \tag{4.26}$$

which are inherit from Newmarks method. A suitable choice of the parameter α ranges from $\alpha = -1/3$ (significant damping) to $\alpha = 0$ (no damping), where, in the latter, the trapezoidal rule ($\beta = 1/4$, $\gamma = 1/2$) is obtained. Note that a value of $\alpha = -0.05$ is in general considered as a good choice, as the inevitably time-stepping-induced high-frequency noise is quickly removed without a significant effect on the low-frequency response of the system.

To proceed[4], $(4.25)_2$ and $(4.25)_3$ are reformulated, see Kuhl [118], such that

$$\begin{aligned} \dot{\boldsymbol{y}}_{n+1} &= \frac{\gamma}{\beta\Delta t}(\boldsymbol{y}_{n+1} - \boldsymbol{y}_n) - (\frac{\gamma}{\beta} - 1)\dot{\boldsymbol{y}}_n - (\frac{\gamma}{2\beta} - 1)\Delta t\ddot{\boldsymbol{y}}_n\,, \\ \ddot{\boldsymbol{y}}_{n+1} &= \frac{1}{\beta\Delta t^2}(\boldsymbol{y}_{n+1} - \boldsymbol{y}_n) - \frac{1}{\beta\Delta t}\dot{\boldsymbol{y}}_n - (\frac{1}{2\beta} - 1)\ddot{\boldsymbol{y}}_n\,, \end{aligned} \tag{4.27}$$

and are inserted into $(4.25)_1$. Subsequently, by further applying the backward-Euler procedure to the local system $\boldsymbol{\mathcal{L}}^h_{n+1}$, (4.22) can be recast into a system of algebraic equations, viz.

$$\boldsymbol{\mathcal{F}}^h_{n+1} = \boldsymbol{\mathcal{F}}^h(t_{n+1},\, \boldsymbol{y}_{n+1},\, \boldsymbol{q}_{n+1}) = \left[\begin{array}{c} \boldsymbol{\mathcal{G}}^h(\boldsymbol{y}_{n+1},\, \boldsymbol{q}_{n+1}) \\ \boldsymbol{\mathcal{L}}^h(\boldsymbol{y}_{n+1},\, \boldsymbol{q}_{n+1}) \end{array}\right] \stackrel{!}{=} \boldsymbol{0}\,, \tag{4.28}$$

which then is solved for the unknowns $\boldsymbol{y}_{n+1}$ and $\boldsymbol{q}_{n+1}$.

[4] Alternatively, one may also proceed with $\ddot{\boldsymbol{y}}_{n+1}$ as the unknown of the system of algebraic equations. However, confined to the framework of Abaqus/Standard and for the purpose of this monograph, $\boldsymbol{y}_{n+1}$ is used as the primary unknown.

Solution method

Subsequently, the nonlinear systems of algebraic equations, (4.28) and (4.24), are iteratively solved for the unknowns $\boldsymbol{y}_{n+1}$ and $\boldsymbol{q}_{n+1}$. Herein, the iterative Newton-Raphson method is exploited. Note that, in order to obtain an efficient solution strategy, the actual coupled systems (4.24) and (4.28) are solved in the same decoupled manner by exploiting the block-structured nature through a generalisation of the block Gauß-Seidel-Newton method, which is also known as multilevel or, in this particular case, as the two-stage Newton method. In particular, this solution procedure results in two nested Newton iterations, where at each global iteration step, to find the solution to the global system, the local system is iteratively solved for the internal state variables $\boldsymbol{q}_{n+1}$ at each Gauss integration point with frozen global variables $\boldsymbol{y}_{n+1}$,

$$\boldsymbol{\mathcal{L}}^h(\boldsymbol{y}_{n+1},\, \boldsymbol{q}_{n+1}) = \boldsymbol{0} \qquad \longrightarrow \qquad \boldsymbol{q}_{n+1} = \boldsymbol{q}_{n+1}(\boldsymbol{y}_{n+1})\,. \tag{4.29}$$

As usual within the framework of elasto-plasticity, the solution of the local system is found via the commonly used *predictor-corrector scheme*, see Simo & Taylor [179]. Herein, initially an elastic trial stress is computed proceeding from the global strain tensor $\boldsymbol{\varepsilon}_{S,n+1} = \boldsymbol{\varepsilon}_S(\boldsymbol{y}_{n+1})$ (predictor step), which is subsequently checked whether the increment is purely elastic ($F < 0$) or elastic-plastic ($F \geq 0$). In a pure elastic step the internal variables do not evolve, whereas in case of an elastic-plastic step, the local system is solved for the internal variables $\boldsymbol{q}_{n+1}$ such that the resulting stress state lies on the yield surface (plastic corrector step), i. e. $F = 0$.

Assuming that the solution $\boldsymbol{q}_{n+1}$ is sufficiently accurate, the derivative of $\boldsymbol{\mathcal{L}}^h(\boldsymbol{y}_{n+1},\, \boldsymbol{q}_{n+1})$ with respect to $\boldsymbol{y}_{n+1}$ has to vanish as well:

$$\frac{\mathrm{d}\boldsymbol{\mathcal{L}}^h_{n+1}}{\mathrm{d}\boldsymbol{y}_{n+1}} = \frac{\partial \boldsymbol{\mathcal{L}}^h_{n+1}}{\partial \boldsymbol{y}_{n+1}} + \frac{\partial \boldsymbol{\mathcal{L}}^h_{n+1}}{\partial \boldsymbol{q}_{n+1}} \frac{\partial \boldsymbol{q}_{n+1}}{\partial \boldsymbol{y}_{n+1}} \approx \boldsymbol{0} \qquad \longrightarrow \qquad \frac{\partial \boldsymbol{q}_{n+1}}{\partial \boldsymbol{y}_{n+1}} = -\left[\frac{\partial \boldsymbol{\mathcal{L}}^h_{n+1}}{\partial \boldsymbol{q}_{n+1}}\right]^{-1} \frac{\partial \boldsymbol{\mathcal{L}}^h_{n+1}}{\partial \boldsymbol{y}_{n+1}}\,. \tag{4.30}$$

Note that, herein, the derivative $\mathrm{d}\boldsymbol{\mathcal{L}}^h_{n+1}/\mathrm{d}\boldsymbol{y}_{n+1}$ accounts for the implicit dependencies between the global and local variables through the algorithmically consistent linearisation, which was initially proposed by Simo & Taylor [178], see also Wriggers [205] or Simo & Hughes [177].

With the solution of the internal-state variables at hand, the next iteration in the global Newton iteration to find the solution to the global system is computed by solving

$$\boldsymbol{J}_{\boldsymbol{\mathcal{G}}_{n+1}}\, \boldsymbol{y}_{n+1} = \boldsymbol{\mathcal{G}}^h_{n+1}\,. \tag{4.31}$$

Herein, $\boldsymbol{J}_{\boldsymbol{\mathcal{G}}_{n+1}}$ denotes the so-called Jacobian matrix and is obtained via algorithmically consistent linearisation of the global system, viz.

$$\boldsymbol{J}_{\boldsymbol{\mathcal{G}}_{n+1}} = \frac{\mathrm{d}\boldsymbol{\mathcal{G}}^h_{n+1}}{\mathrm{d}\boldsymbol{y}_{n+1}} = \frac{\partial \boldsymbol{\mathcal{G}}^h_{n+1}}{\partial \boldsymbol{y}_{n+1}} + \frac{\partial \boldsymbol{\mathcal{G}}^h_{n+1}}{\partial \dot{\boldsymbol{y}}_{n+1}} \frac{\partial \dot{\boldsymbol{y}}_{n+1}}{\partial \boldsymbol{y}_{n+1}} + \frac{\partial \boldsymbol{\mathcal{G}}^h_{n+1}}{\partial \ddot{\boldsymbol{y}}_{n+1}} \frac{\partial \ddot{\boldsymbol{y}}_{n+1}}{\partial \boldsymbol{y}_{n+1}} + \frac{\partial \boldsymbol{\mathcal{G}}^h_{n+1}}{\partial \boldsymbol{q}_{n+1}} \frac{\partial \boldsymbol{q}_{n+1}}{\partial \boldsymbol{y}_{n+1}}\,, \tag{4.32}$$

where the derivative $\partial \boldsymbol{q}_{n+1}/\partial \boldsymbol{y}_{n+1}$ is computed with the help of $(4.30)_2$.

Proceeding from the HHT time-marching scheme, the Jacobian matrix is given by

$$\begin{aligned} \boldsymbol{J}_{\boldsymbol{\mathcal{G}}_{n+1}} &= \frac{1}{\beta\Delta t^2}\boldsymbol{M}_{n+1} + (1+\alpha)\Big(\boldsymbol{K}_{n+1} + \frac{\gamma}{\beta\Delta t}\boldsymbol{C}_{n+1}\Big) + \frac{\partial \boldsymbol{\mathcal{G}}^h_{n+1}}{\partial \boldsymbol{q}_{n+1}}\frac{\partial \boldsymbol{q}_{n+1}}{\partial \boldsymbol{y}_{n+1}} \\ \text{with} \qquad \boldsymbol{K}_{\mathrm{n+1}} &= \frac{\partial \boldsymbol{\mathcal{G}}^{\mathrm{h}}_{\mathrm{n+1}}}{\partial \boldsymbol{y}_{\mathrm{n+1}}}\,,\ \boldsymbol{C}_{\mathrm{n+1}} = \frac{\partial \boldsymbol{\mathcal{G}}^{\mathrm{h}}_{\mathrm{n+1}}}{\partial \dot{\boldsymbol{y}}_{\mathrm{n+1}}}\,,\ \boldsymbol{M}_{\mathrm{n+1}} = \frac{\partial \boldsymbol{\mathcal{G}}^{\mathrm{h}}_{\mathrm{n+1}}}{\partial \ddot{\boldsymbol{y}}_{\mathrm{n+1}}}\,. \end{aligned} \tag{4.33}$$

Therein, $\boldsymbol{K}_{n+1}$, $\boldsymbol{C}_{n+1}$ and $\boldsymbol{M}_{n+1}$ denote the linearised stiffness, damping and mass matrices, respectively, associated with the current Newton increment, which are continuously updated throughout the iterative procedure. In case of the backward Euler method, where the partial derivatives with respect to the accelerations vanish, i. e. $\partial \boldsymbol{\mathcal{G}}^h_{n+1}/\partial \ddot{\boldsymbol{y}}_{n+1} = \boldsymbol{0}$, the Jacobian matrix is computed via

$$\boldsymbol{J}_{\boldsymbol{\mathcal{G}}_{n+1}} = \boldsymbol{K}_{n+1} + \frac{1}{\Delta t}\boldsymbol{C}_{n+1} + \frac{\partial \boldsymbol{\mathcal{G}}^h_{n+1}}{\partial \boldsymbol{q}_{n+1}}\frac{\partial \boldsymbol{q}_{n+1}}{\partial \boldsymbol{y}_{n+1}}\,. \tag{4.34}$$

To sum up, the solution procedure results in two nested Newton iterations, where at each global iteration step, the nonlinear local system is iteratively solved for the internal variables at each Gauss integration point with frozen global variables, where each iteration stops, as soon as a certain convergence criterion is met, e. g. $\|\boldsymbol{\mathcal{L}}^h_{n+1}\| < \epsilon_{\mathcal{L}}$ and $\|\boldsymbol{\mathcal{G}}^h_{n+1}\| < \epsilon_{\mathcal{G}}$, with $\epsilon_{\mathcal{L}}$ and $\epsilon_{\mathcal{G}}$ being the admissible numerical error of the local and the global system, respectively.

4.3.2 Explicit schemes

For an efficient solution of dynamic problems, such as the dynamic biphasic model, solution strategies based on explicit time-integration schemes are commonly preferred. Note that, when aiming for the solution of a dynamic elasto-plastic problem, it is vital for the efficiency of the overall solution procedure to apply an explicit discretisation scheme to the elasto-plastic model as well, although this is not mandatory from a technical point of view. However, as the explicit procedure is merely applied to elastic problems for the purpose of this monograph, explicit time-marching schemes for the elasto-plastic local system are not further elaborated. Nevertheless, an interested reader may refer, for instance, to the work of Vrh *et al.* [195] for the treatment of elasto-plastic models within an explicit framework.

Before addressing the temporal discretisation procedure, their application possibilities with respect to the dynamic hybrid model and the dynamic liquid-saturated model are elaborated. In this connection, the attention is firstly drawn to the dynamic hybrid model incorporating a materially compressible pore fluid. The spatial-discrete problem can be summarised as

$$\boldsymbol{\mathcal{G}}^h = \underbrace{\begin{bmatrix} \boldsymbol{M}_{11} & \boldsymbol{M}_{12} & \boldsymbol{0} \\ \boldsymbol{0} & \boldsymbol{M}_{22} & \boldsymbol{0} \\ \boldsymbol{0} & \boldsymbol{0} & \boldsymbol{0} \end{bmatrix}}_{\boldsymbol{M}} \ddot{\boldsymbol{y}} + \underbrace{\begin{bmatrix} \boldsymbol{C}_{11} & \boldsymbol{C}_{12} & \boldsymbol{0} \\ \boldsymbol{C}_{21} & \boldsymbol{C}_{22} & \boldsymbol{0} \\ \boldsymbol{C}_{31} & \boldsymbol{C}_{32} & \boldsymbol{C}_{33} \end{bmatrix}}_{\boldsymbol{C}} \dot{\boldsymbol{y}} + \underbrace{\begin{bmatrix} \boldsymbol{K}_{11} & \boldsymbol{0} & \boldsymbol{K}_{13} \\ \boldsymbol{K}_{21} & \boldsymbol{0} & \boldsymbol{K}_{23} \\ \boldsymbol{K}_{31} & \boldsymbol{0} & \boldsymbol{K}_{33} \end{bmatrix}}_{\boldsymbol{K}} \boldsymbol{y} - \boldsymbol{f} = \boldsymbol{0}, \tag{4.35}$$

where the temporal order of the fluid momentum balance is upgraded from one to two by exploiting the relation $\mathbf{v}_F = (\mathbf{u}_F)'_S$. Herein, $\mathbf{v}_F$ and $\mathbf{u}_F$ denote vectors gathering the nodal values of the pore-fluid velocities and the fictitious pore-fluid displacements, respectively. Moreover, $\boldsymbol{f}$ denotes a vector gathering the external loads applied on the Neumann boundaries, and $\boldsymbol{M}$, $\boldsymbol{C}$ and $\boldsymbol{K}$ are the overall mass, damping and stiffness matrices, which are divided into coupling (highlighted) and non-coupling terms.

From this representation, it can be concluded that monolithic explicit time-integration schemes are not feasible for the dynamic hybrid model[5], as the singular submatrix $\boldsymbol{M}_{33} = \boldsymbol{0}$ results in a non-invertible overall mass matrix $\boldsymbol{M}$. In consequence, the coupled problem (4.35) will be decomposed, such that the Block-Jacobi solution procedure, see, e. g., Matthies *et al.* [140] or Matthies & Steindorf [141], is obtained. The resulting solution

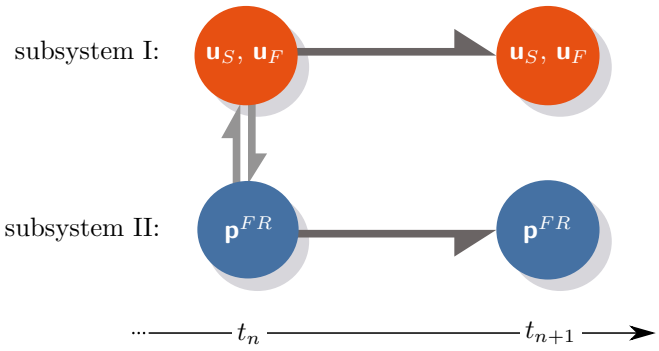

Figure 4.4: *Sketch of the decoupled Block-Jacobian solution scheme to advance the primary variables from t_n to t_{n+1} exemplary applied to the dynamic hybrid model.*

strategy is qualitatively sketched in Figure 4.4. Herein, the primary variables are advanced independently from a given state at time t_n to the new state at t_{n+1} with the individual subsystems, where the other field variables are kept constant. Note that this procedure introduces a numerical error, which is minimised if the number of subsystems is reduced, see Zinatbakhsh [220]. The decomposition results in the subsystems $\mathcal{G}^h_{\mathrm{I}} = \mathcal{G}^h_{MM} \cup \mathcal{G}^h_{MF}$ (filled box) and $\mathcal{G}^h_{\mathrm{II}} = \mathcal{G}^h_{MP}$ (framed box), viz.

$$\boldsymbol{\mathcal{G}}^h = \begin{bmatrix} \mathcal{G}^h_{\mathrm{I}} \\ \mathcal{G}^h_{\mathrm{II}} \end{bmatrix} = \begin{bmatrix} \boldsymbol{M}_{11} & \boldsymbol{M}_{12} & \boldsymbol{0} \\ \boldsymbol{0} & \boldsymbol{M}_{22} & \boldsymbol{0} \\ \boldsymbol{0} & \boldsymbol{0} & \boxed{\boldsymbol{0}} \end{bmatrix} \ddot{\boldsymbol{y}} + \begin{bmatrix} \boldsymbol{C}_{11} & \boldsymbol{C}_{12} & \boldsymbol{0} \\ \boldsymbol{C}_{21} & \boldsymbol{C}_{22} & \boldsymbol{0} \\ \boldsymbol{C}_{31} & \boldsymbol{C}_{32} & \boxed{\boldsymbol{C}_{33}} \end{bmatrix} \dot{\boldsymbol{y}} + \begin{bmatrix} \boldsymbol{K}_{11} & \boldsymbol{0} & \boldsymbol{K}_{13} \\ \boldsymbol{K}_{21} & \boldsymbol{0} & \boldsymbol{K}_{23} \\ \boldsymbol{K}_{31} & \boldsymbol{0} & \boxed{\boldsymbol{K}_{33}} \end{bmatrix} \boldsymbol{y} - \boldsymbol{f} = \boldsymbol{0}\,, \tag{4.36}$$

which can be given in the following more compact representation:

$$\begin{aligned} \mathcal{G}^h_{\mathrm{I}} &= \boldsymbol{M}_{\mathrm{I}}\,\ddot{\boldsymbol{y}}_{\mathrm{I}} + \boldsymbol{r}_{\mathrm{I}}(\dot{\boldsymbol{y}}_{\mathrm{I}}, \boldsymbol{y}_{\mathrm{I}}, \boldsymbol{y}_{\mathrm{II}}, \boldsymbol{q}) - \boldsymbol{f}_{\mathrm{I}} = \boldsymbol{0}\,, \\ \mathcal{G}^h_{\mathrm{II}} &= \boldsymbol{C}_{\mathrm{II}}\,\dot{\boldsymbol{y}}_{\mathrm{II}} + \boldsymbol{r}_{\mathrm{II}}(\boldsymbol{y}_{\mathrm{II}}, \dot{\boldsymbol{y}}_{\mathrm{I}}, \boldsymbol{y}_{\mathrm{I}}, \boldsymbol{q}) - \boldsymbol{f}_{\mathrm{II}} = \boldsymbol{0}\,. \end{aligned} \tag{4.37}$$

Therein, $\boldsymbol{r}_{\mathrm{I}}$ and $\boldsymbol{r}_{\mathrm{II}}$ are the quasi-static and the static residual vectors of the subsystems I and II, respectively, depending on the vectors of the nodal unknowns $\boldsymbol{y}_{\mathrm{I}} = [\mathbf{u}_S, \mathbf{u}_F]^T$

[5] Note that in case of the fluid-saturated biphasic model, the incompressibility of the pore liquid further leads to a singular submatrix $\boldsymbol{C}_{33} = \boldsymbol{0}$ and, thus, to a non-invertible damping matrix $\boldsymbol{C}$. Consequently, monolithic explicit time-marching schemes are not applicable for the liquid-saturated biphasic model, see Markert *et al.* [138].

and $\boldsymbol{y}_{\mathrm{II}} = \mathbf{p}^{FR}$ and their respective temporal derivatives. Furthermore, $\boldsymbol{f}_{\mathrm{I}}$ and $\boldsymbol{f}_{\mathrm{II}}$ are the Neumann force vectors of the corresponding subsystems, $\boldsymbol{M}_{\mathrm{I}}$ is the mass matrix of the subsystem I, and $\boldsymbol{C}_{\mathrm{II}} = \boldsymbol{C}_{33}$ denotes the capacitance matrix of the subsystem II. In the next step, the temporal discretisation of the semi-discrete decoupled system (4.37) is carried out. In particular, subsystem I is discretised using the central-difference method, whereas the forward (explicit) Euler method is used for the discretisation of subsystem II.

Central-difference time-integration scheme

The subproblem I will be discretised in time exploiting the explicit central-difference scheme, which was initially described by Sheppard [176]. Herein, the subsystem will be advanced in time proceeding from the known state at t_n to the unknown state t_{n+1} via a linear extrapolation of the velocities and accelerations,

$$\begin{aligned} &\boldsymbol{M}\ddot{\boldsymbol{y}}_{\mathrm{I},n} + \boldsymbol{r}(\boldsymbol{y}_{\mathrm{I},n}, \dot{\boldsymbol{y}}_{\mathrm{I},n}, \boldsymbol{q}_n) - \boldsymbol{f}_{\mathrm{I},n} = \mathbf{0} \\ &\text{with} \qquad \dot{\boldsymbol{y}}_{\mathrm{I},n} \approx \dot{\boldsymbol{y}}_{\mathrm{I},n-\frac{1}{2}} = \frac{1}{\Delta t}(\boldsymbol{y}_{\mathrm{I},n} - \boldsymbol{y}_{\mathrm{I},n-1})\,,\ \dot{\boldsymbol{y}}_{\mathrm{I},n+\frac{1}{2}} = \frac{1}{\Delta t}(\boldsymbol{y}_{\mathrm{I},n+1} - \boldsymbol{y}_{\mathrm{I},n}) \\ &\qquad\qquad \ddot{\boldsymbol{y}}_{\mathrm{I},n} = \frac{1}{\Delta t}(\ddot{\boldsymbol{y}}_{\mathrm{I},n+\frac{1}{2}} - \ddot{\boldsymbol{y}}_{\mathrm{I},n-\frac{1}{2}}) = \frac{1}{\Delta t^2}(\boldsymbol{y}_{\mathrm{I},n+1} - 2\,\boldsymbol{y}_{\mathrm{I},n} + \boldsymbol{y}_{\mathrm{I},n-1})\,. \end{aligned} \tag{4.38}$$

Therein, the velocities at the intermediate steps are computed via $\dot{\boldsymbol{y}}_{\mathrm{I}}(t_{n-\frac{1}{2}}) = \dot{\boldsymbol{y}}_{\mathrm{I},n-\frac{1}{2}}$ and $\ddot{\boldsymbol{y}}_{\mathrm{I}}(t_{n+\frac{1}{2}}) = \ddot{\boldsymbol{y}}_{\mathrm{I},n+\frac{1}{2}}$, where it is common practice to consider the former as an approximation for the velocity vector $\dot{\boldsymbol{y}}_{\mathrm{I},n}$.

Forward-Euler time-integration scheme

Following the explicit (forward) Euler method, the subsystem II will be advanced from the known state at t_n to the unknown state t_{n+1}, through a Taylor-series expansion truncated after the linear term. Consequently, the discrete form of the subproblem II reads

$$\boldsymbol{C}\dot{\boldsymbol{y}}_{\mathrm{II},n} + \boldsymbol{r}(\boldsymbol{y}_{\mathrm{II},n}, \boldsymbol{q}_n) - \boldsymbol{f}_{\mathrm{II},n} = \mathbf{0} \qquad \text{with} \qquad \dot{\boldsymbol{y}}_{\mathrm{II},n} = \frac{1}{\Delta t}(\boldsymbol{y}_{\mathrm{II},n+1} - \boldsymbol{y}_{\mathrm{II},n})\,. \tag{4.39}$$

Solution method

Proceeding from the previously introduced approximations for the velocities and accelerations of the subsystem I, $\dot{\boldsymbol{y}}_{\mathrm{I},n} = \dot{\boldsymbol{y}}_{\mathrm{I},n}(\boldsymbol{y}_{\mathrm{I},n}, \boldsymbol{y}_{\mathrm{I,n-1}})$ and $\ddot{\boldsymbol{y}}_{\mathrm{I},n} = \ddot{\boldsymbol{y}}_{\mathrm{I},n}(\boldsymbol{y}_{\mathrm{I},n+1}, \boldsymbol{y}_{\mathrm{I},n}, \boldsymbol{y}_{\mathrm{I},n-1})$, and for the velocities of the subsystem II, $\dot{\boldsymbol{y}}_{\mathrm{II},n} = \dot{\boldsymbol{y}}_{\mathrm{II},n}(\boldsymbol{y}_{\mathrm{II},n+1}, \boldsymbol{y}_{\mathrm{II,n}})$, (4.37) can be recast to yield

$$\begin{aligned} \boldsymbol{\mathcal{G}}^h_{\mathrm{I}} &= \frac{1}{\Delta t^2}\boldsymbol{M}_{\mathrm{I}}\,\boldsymbol{y}_{\mathrm{I},n+1} + \boldsymbol{r}_{\mathrm{I}}(\boldsymbol{y}_{\mathrm{I},n}, \boldsymbol{y}_{\mathrm{I},n-1}, \boldsymbol{y}_{\mathrm{II},n}, \boldsymbol{q}_n) - \boldsymbol{f}_{\mathrm{I}} = \mathbf{0}\,, \\ \boldsymbol{\mathcal{G}}^h_{\mathrm{II}} &= \frac{1}{\Delta t}\boldsymbol{C}_{\mathrm{II}}\,\boldsymbol{y}_{\mathrm{II},n+1} + \boldsymbol{r}_{\mathrm{II}}(\boldsymbol{y}_{\mathrm{II},n}, \boldsymbol{y}_{\mathrm{I},n}, \boldsymbol{y}_{\mathrm{I},n-1}, \boldsymbol{q}_n) - \boldsymbol{f}_{\mathrm{II}} = \mathbf{0}\,, \end{aligned} \tag{4.40}$$

which can be solved for the unknowns $\boldsymbol{y}_{\mathrm{I},n+1}$ and $\boldsymbol{y}_{\mathrm{II},n+1}$. So far, the explicit procedure does not gain any advantage in comparison to an implicit procedure, as the nodal unknowns

need to be evaluated through an inversion of the mass and the capacitance matrices, This is, although both matrices are sparsely populated, still an expensive task from a computational point of view. To cope with that, the set of coupled algebraic equations needs to be decoupled through a matrix lumping procedure, which is vital for the efficiency of the explicit procedures. Herein, the matrix is diagonalised such that a straightforward identification of the nodal unknowns is possible. Note that, thereby, one introduces, on the one hand, dissipative properties of stiffness matrix form, see Zienkiewicz *et al.* [219], which helps to quickly remove the inevitably time-stepping-induced high-frequency noise, but, on the other hand, also a small inaccuracy, see, e. g., Tracy [185] or Huebner *et al.* [106].

A very common and efficient lumping procedure is the method of row-sum lumping (RSL), where all components A_{ij} of a matrix $\mathbf{A}$ are concentrated to the diagonal element of row i via

$$\widetilde{\mathbf{A}} = \operatorname{diag}(\widetilde{A}_i) \qquad \text{with} \qquad \widetilde{A}_i = \sum_{j=1}^{m} A_{ij} \qquad i = 1, 2, ..., m\,. \tag{4.41}$$

Therein, m denotes the number of columns (equal to the number of rows), which corresponds to the degrees of freedom of the FE mesh. In this connection, it is important to point out that the RSL method cannot be applied to elements with quadratic ansatz functions, as the row sum yields negative diagonal terms, see Cook [44] or Bathe [15]. To cope with that, alternative lumping techniques, such as the procedure after Hinton, Rock & Zienkiewicz (HRZ) [102], or the nodal-quadrature method of Fried & Malkus [79] can be applied.

With respect to the given problem, the RSL method is applied to the mass matrix $\boldsymbol{M}_{\mathrm{I}}$ of subproblem I and to the capacitance matrix $\boldsymbol{C}_{\mathrm{II}}$ of subproblem II, yielding the corresponding diagonalised forms $\widetilde{\boldsymbol{M}}_{\mathrm{I}}$ and $\widetilde{\boldsymbol{C}}_{\mathrm{II}}$, respectively. With the diagonalised matrices at hand, the nodal unknowns $(\boldsymbol{y}_{\mathrm{I},n+1})$ and $(\boldsymbol{y}_{\mathrm{II},n+1})$ can be identified straightforwardly by solving

$$\begin{aligned} \boldsymbol{\mathcal{G}}_{\mathrm{I}}^{h} &= \frac{1}{\Delta t^2}\widetilde{\boldsymbol{M}}_{\mathrm{I}}\,\boldsymbol{y}_{\mathrm{I},n+1} + \boldsymbol{r}_{\mathrm{I}}(\boldsymbol{y}_{\mathrm{I},n}, \boldsymbol{y}_{\mathrm{I},n-1}, \boldsymbol{y}_{\mathrm{II},n}, \boldsymbol{q}_n) - \boldsymbol{f}_{\mathrm{I}} = \boldsymbol{0}\,, \\ \boldsymbol{\mathcal{G}}_{\mathrm{II}}^{h} &= \frac{1}{\Delta t}\widetilde{\boldsymbol{C}}_{\mathrm{II}}\,\boldsymbol{y}_{\mathrm{II},n+1} + \boldsymbol{r}_{\mathrm{II}}(\boldsymbol{y}_{\mathrm{II},n}, \boldsymbol{y}_{\mathrm{I},n}, \boldsymbol{y}_{\mathrm{I},n-1}, \boldsymbol{q}_n) - \boldsymbol{f}_{\mathrm{II}} = \boldsymbol{0}\,. \end{aligned} \tag{4.42}$$

In a subsequent step, the unknown velocities and displacements of the individual subsystem can be computed.

Chapter 5:
Parallel solution procedure

The present chapter gives an insight into the solution procedure of the previously discussed strongly coupled problems. The material models are, at first, implemented into the research code PANDAS, which serves as a convenient tool during the material-model development and/or enhancement stage. However, its capabilities in terms of the complexity and the size of the underlying numerical model are stretched to the limits when it comes to the simulation of problems relevant for industrial applications. To cope with that, the present monograph introduces a general interface between PANDAS and the commercial FEA package Abaqus, thereby extending the material-model library of Abaqus with the previously set up or enhanced material descriptions of PANDAS. Consequently, the coupling allows for a straighforward transfer of the outcome of research projects into a simulation environment utilised in the industry, thereby also exploiting the parallel-capable solution framework of Abaqus in order to analyse large-scale problems on high-performance computing clusters.

In this regard, the present chapter begins with an introduction into parallel computing, spanning from the related terminology, over computer architectures towards parallel programming models. However, as the first section merely serves as a brief summary, the interested reader is referred to related literature, such as Grama *et al.* [86], Hager & Wellein [92], Brawer [29], Xavier & Iyengar [208] or Sasikumar *et al.* [168], for a more comprehensive insight. Subsequently, a detailed description of the coupling procedure, performance benchmarks and a discussion of its possibilities and limitations are provided.

5.1 Introduction to parallel computing

In order to keep pace with the increasing complexity of numerical models, faster computers are necessary. However, classical machines based on the von Neumann architecture, see Godfrey & Hendry [84], von Neuman [194], which perform operations in a sequential manner, hit the wall when it comes to the handling of complex and/or data-intensive problems. Thus, in order to overcome these limits the possibilities of parallel computing were discussed. already in the late 1950s. A few years later, computer engineers gave birth to the first parallel-capable computers, affiliating only a few central processing units (CPU) to a single computing network at the beginning, which were continuously extended towards the massive parallel supercomputers, gathering tens of thousands processing units, as we have them nowadays. Nevertheless, despite obvious performance enhancements compared to sequential-operating computers, it took decades for parallel computers to enter the mass market, mainly due to a lack of convenient programming models for parallel computing. Nowadays, the previously successful performance-enhancement technologies, such as frequency scaling and transistor-size reduction, approach fundamental barriers given by the laws of thermodynamics and quantum physics. Consequently, parallel-capable

computing devices get more and more prominent, especially through the development of power-efficient multi-core CPU, where multiple independently working processing units are combined into a single processor.

5.1.1 Basic terminology

Parallel computing is based on the principle that a problem can be hierarchically decomposed into smaller but more specific subproblems, see Figure 5.1. In particular, a *process*, which can be considered as an abstract representation of the problem, i. e. the computer programme, can be fragmented into several *tasks*[1], which, in turn, are an assembly of several *instructions*[2] to be executed within a quantum[3]. Several tasks can be, not necessarily in chronological succession, affiliated to form a so-called *thread*, which in the case of multiple coexisting threads residing in a single process yields a so-called multithreaded process. In this connection, it is important to remark that a process is associated with its own hardware resources (e. g. memory), whereas threads share the same resources, when assigned to the same process.

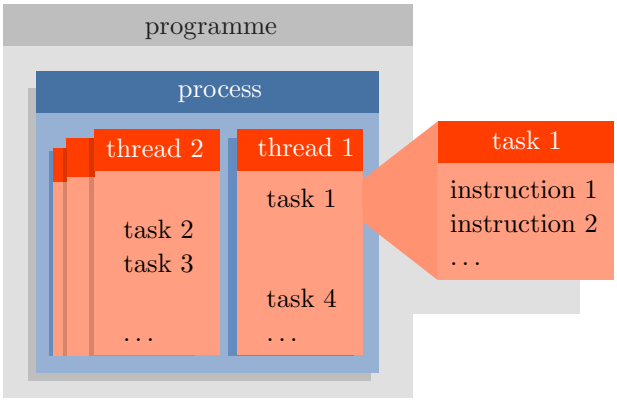

Figure 5.1: *Schematic workflow of a sequential multithreaded process or programme.*

In parallel computing, the individual threads are then executed simultaneously on different physical processing units, e. g. on a single-core CPU or on a particular processing unit of a multi-core CPU, which requires the individual threads to be independent, or in the related terminology, to be *concurrent*. However, the term multithreading is not necessarily associated with parallel computing as multiple threads can still be executed sequentially on a single processing unit, where, however, no performance enhancement can be observed.

[1] In computer science, the term *task* is often used in a diffuse manner. On the one hand, it refers to as a part of a process, in particular, a number of operations loaded in memory, which is the case within the present contribution, and, on the other hand, as a synonym for the process itself.

[2] An instruction is a primitive operation provided by the processors instruction set containing definitions of very basic operations related to, for instance, arithmetics (e. g. `add` or `subtract`), boolean operations (e. g. `and` or `not`), data handling (e. g. `load` or `store`) or flow control (e. g. `goto` or `if`) Fischer & Hofer [76].

[3] A quantum is the time interval (approx. 10 to 30 ms) in which the individual instructions of a instruction sequence are executed by the processor before the pending instruction sequences, which also include previously uncompleted instruction queues, are rescheduled.

On the contrary, a small loss can be measured due to necessary context switching[4] between the different threads.

Similar to the threads of a multithreaded process, an application can create multiple simultaneously operating processes as well, which, in turn, can fork multiple threads running in parallel, see Figure 5.2.

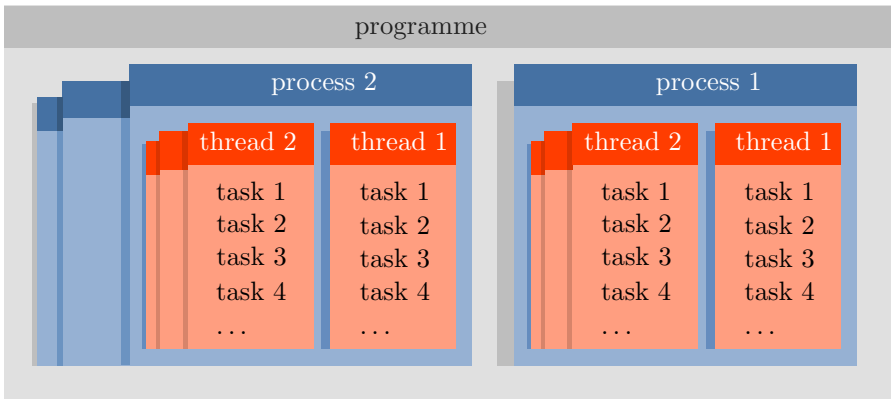

Figure 5.2: *Parallel multithreading within multiple parallel processes.*

In general, in contrast to sequential processing, the concurrency of operations (within tasks or processes) in parallel computing, gives rise to an additional level of complexity and, thus, to various parallel-computing-exclusive programme failure scenarios. The most common ones are, in particular, *dead-lock* and *live-lock* scenarios, which refer to a blocked programme flow, and *data races* and *race conditions*, which address a non-deterministic programme output. In a dead-lock scenario, the overall programme progress is blocked as at least two competing operations on concurrent threads or processes are all in a pending state waiting for the other one to finish, and thus neither ever will. In contrast, a live lock refers to a blocking state where the competing operations are still continuously changing their state and are, thus, considered as living. The second set refers to a non-deterministic programme output. In particular, a data race describes a situation in which operations assigned to different threads or processes, alter the data at the same memory location. Consequently, as the chronological order of the operations is not defined, the result of the parallel-executed task is undefined as well. Similarly, in a race condition, the programme flow path, which is assumed to be governed by the content of a specific memory location, e. g. the value of a variable, is undetermined.

5.1.2 Computer architecture

In order to best exploit the capabilities of the parallel-capable machines, specifically tailored programmes are necessary. However, the diversity of possible machine architectures, makes it often difficult and time consuming to design a programme according to the specific hardware needs. Thus, it is auxiliary to pool different hardware designs, from a programming point of view, to similar architectures, which then exploit the same (abstract)

[4] At a context switch, the processing of the current instruction set is suspended and, instead, another instruction set is started or resumed.

programming model. In this connection, Flynn [77] introduced in 1972 a classification of hardware architectures, which is also known as *Flynn's Taxonomy*. It is based on the concurrency of instruction streams[5], which are defined as a set of instructions that compose the task, and the available data streams, which are defined as a set of data the instructions work on. According to Flynn [77], four categories are identified:

- **SISD** (single instruction stream, single data stream): one processor executes instructions sequentially on a single data block, which represents the classical von Neumann computer (single-core processors), see Godfrey & Hendry [84] or von Neuman [194].
- **SIMD** (single instruction, multiple data streams): multiple processors execute the same instructions in parallel on the same data block exploiting so-called vector processors.
- **MISD** (multiple instruction streams, single data stream): multiple processors execute different instructions from an instruction pool on the same data (rarely used), which is usually used for fault tolerance, e. g. Space Shuttle flight control computer.
- **MIMD** (multiple instruction streams, multiple data streams): multiple processors execute different instructions on different data blocks.

Since nowadays most computers follow the MIMD architecture, further classifications of the latter were necessary assigning architectures to the categories of *single programme multiple data streams* (SPMD) and *multiple programmes multiple data streams* (MPMD). In the latter, autonomous processors operate, at least to some extent, on two independent programmes, for instance, in a master-slave setup. Therein, a master programme controls the tasks and distributes these to the slave programmes which, in turn, accomplish the actual task and return the results to the master programme. In contrast, in SPMD different instances of the same programme are executed on different processor units. It is the most common style of parallel-computer architecture and, therefore, the underlying hardware for the purpose of this monograph.

Figure 5.3: *Contrasting juxtaposition of SMP (left) and DMM (right) architecture.*

In this regard, with respect to the parallel programming model, the SPMD systems are further classified according to their memory organisation, in particular, into distributed-memory machines (DMM) and shared-memory machines (SMM)[6]. In SMM, the individual

[5]Instructions are said to be concurrent, if multiple instructions can be executed in an overlapping time interval without affecting the outcome of the operations, which is the necessary design property of an operation to be executed safely in parallel.

[6]Further classifications based on the memory access distinguish between unified memory access (UMA) and non-uniform memory access (NUMA). Therein, the architecture is distinguished according to their memory-access time, in particular, if it does (NUMA) or does not (UMA) depend on the accessing processing unit.

cores or CPU share the same memory address space, see Figure 5.3 (left), whereas, in a DMM actual independent computers, denoted as a compute node in the high-performance computing (HPC) terminology, are connected via the network interconnection to build the overall computing cluster, see Figure 5.3 (right). In the latter, a direct access of the memory of a different node is not possible.

To sum up, on a SMM a fast communication through the shared memory address space is possible, which, however, also limits the software parallelisation to shared-memory hardware architectures, whereas DMM suffers from slow node-to-node communication through the network interconnect. In this connection, so-called hybrid machines try to comprise the best of both architectures. Herein, several SMM are interconnected via the network to compose the overall computing cluster, see Figure 5.4, thereby, allowing fast communication within a compute node with large scattering on the distributed system. Nowadays, all modern HPC clusters are hybrid systems.

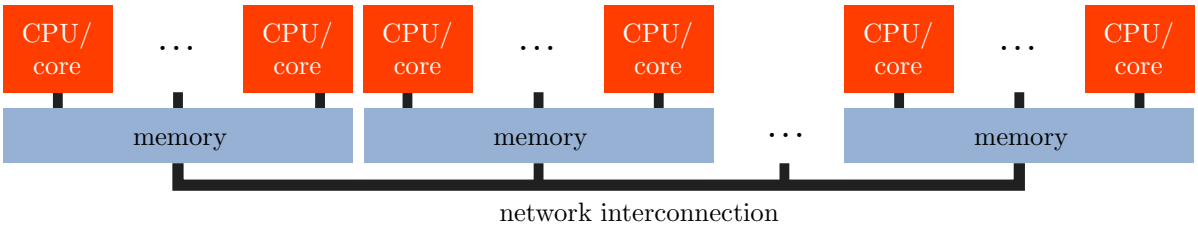

Figure 5.4: *Schematic representation of a hybrid architecture combining SMM and DMM design.*

5.1.3 Parallel performance measurements

When performing tasks in parallel, the performance improvement in comparison to a sequential execution is usually of particular interest. In this regard, the so-called parallel-speedup and parallel-efficiency factors measure the enhancement, in terms of runtime reduction for a given complexity or, vice verse, the allowable change in problem complexity for a targeted simulation time. Thus, for a particular application, with the parallel-speedup factor at hand, the allowable problem complexity or the analysis time can be estimated. Nevertheless, it is important to note that, depending on the governing problem, a change in the problem complexity[7] may lead to different solution procedures, and, thus, the evaluated speedup factor is not meaningful anymore. Consequently, for the purpose of this monograph the parallel speedup factor is considered as a runtime-reduction and not as a problem-complexity multiplier.

The parallel speedup factor and the parallel efficiency, see Rauber & Rünger [159], are given by

$$S_p(n) = \frac{T_1(n)}{T_p(n)} \qquad \text{where} \qquad S_p(n) \leq \mathrm{p}\,, \tag{5.1}$$

[7]For instance, in a FEM-based simulation, the problem complexity is strongly connected with the number of elements in the numerical model. However, a finer mesh resolution may trigger different local phenomena, which did not appear in case of the coarse mesh.

and

$$E_p(n) = \frac{S_p(n)}{\mathrm{p}} = \frac{T_1(n)}{\mathrm{p}\, T_p(n)}\,. \tag{5.2}$$

respectively. Therein, $T_s(n)$ is the run time of the best available sequential implementation to solve a specific problem of complexity n, which, however, may not represent the theoretically fastest possible algorithm as it may be difficult to be determined or implemented. Moreover, $T_p(n)$ denotes the execution time of the parallel algorithm using p processors. It can be concluded from the inequality constraint in equation $(5.1)_2$, that the best parallel speedup is equal to the number of used processors, which, however, can never be achieved in practical applications as parallel execution requires, at least, a minimum of process and/or thread communication. Additionally, not all tasks of a programme can be performed in parallel. Some may require sequential execution, which degrades the parallel speedup even more.

In this connection, Amdahl [4] introduced in 1967 the well-known *Amdahls law*, also known as *Amdahl argument*, which has initially been designed to find the maximum expected improvement of a system, when only parts of the system are enhanced. However nowaday, this statement is strongly connected to parallel computing as it servers as a measurement of the parallel design of a programme. Herein, a comparison between the practically achieved and the theoretically possible performance enhancements serves as a fundamental limit of the performance improvement through parallel computing. It states that if a fraction f $(0 \leq f \leq 1)$ of a parallel programme has to be executed sequentially, the overall runtime is decomposed into a sequential part, $f\, T_1(n)$, and a parallel part with p processor $(1-f)\, T_1/p$, respectively, the speedup factor is given by

$$S_p(n) = \frac{T_1(n)}{f\, T_s(n) + \frac{1-f}{\mathrm{p}} T_1(n)} = \frac{1}{f + \frac{1-f}{\mathrm{p}}}\,. \tag{5.3}$$

Consequently, even with an infinite number of processors, i. e. $p \to \infty$, the parallel speedup is limited to $1/f$ and, therefore, is often more fruitful in massive parallel computing to increase the number of parallel-executable tasks, rather than fine-tune already parallelised tasks. Nevertheless, as far as is known by the author, *Amdahls law* is a purely theoretical concept and cannot be used to predict the parallel speedup, as the ratio f is in general not known.

5.1.4 Programming models for parallel computing

With the advent of parallel hardware and software technologies, users are faced with the challenge to choose a programming paradigm[8] best suited for the underlying computer architecture. In this regard, in the related literature, see, e. g., Gebali [80] and Rauber & Rünger [159], different hierarchical levels of parallelism are identified, depending on the level in hardware or software on which operations can be carried out in parallel before a communication or synchronisation is necessary. This classification covers the range from

[8] A programming paradigm is a fundamental style of computer programming, which defines the way how structure and elements of computer programmes are build, such as object-oriented or procedural programming, see, e. g., Tucker & Noonan [190].

the fine-grained bit[9] level, over the medium-grained instruction level, up to the coarse-grained thread and process level. Depending on the governing parallel programming model and the used programming language, different levels of parallelism are addressable by the programmer[10]. In contrast, commonly used high-level programming languages[11], such as C, C++ or FORTRAN, operate on the coarse-grained thread and process level. Herein, particular programming techniques are necessary in order enable a thread- or process-based parallelisation, which, however, can be combined in order to achieve a hybrid thread- and process-based parallelisation.

From a programming point of view, the crucial task in the parallelisation of a programme is its decomposition into smaller parallel-executable tasks such that the idle time of the hardware is minimised. However, the more computations are performed within a task, i. e. the more coarse-grained the parallelisation is, the higher is the probability of a idling task, which has to wait for another thread or process be finished at first. In contrast, the more fine-grained the parallelisation is, the higher is the communication overhead. Thus, it is the programmers responsibility to balance the load on the hardware, in order to keep all processing units (CPU, cores or machines) running permanently in the best case.

In this connection, in a first step, the parallelisable tasks and the underlying computer architecture need to be identified. In order to get an optimal parallel efficiency, one has to exploit parallel programming models, which are especially tailored to a specific class of machines, i. e., for the purpose of this monograph, shared- and distributed-memory machines, see Section 5.1.2. In particular, a *thread-based parallelisation*, where the programme flow path is forked into several independently working concurrent threads, scattered to different execution units (CPU or a core within a CPU), thereby using the mandatory shared-memory address space for the communication and synchronisation. Consequently, the term *shared-memory parallelisation* is related to a thread-based parallelisation. In contrast, on distributed-memory machines, several instances of the same programme are executed inside different processes, which are usually, but not necessarily, assigned to the different computing nodes, thereby using explicit process-to-process synchronisation and communication methods via, for instance, the prominent message-passing interface (MPI), see, e. g., Message Passing Interface Forum [143].

Thread-based parallelisation

As was mentioned before, in a thread-based parallelisation, the programme workflow is forked into different, but independently working threads. In this connection, nowadays, two actually unrelated standards for the thread managment are established, in particular, the Portable Operating System Interface for Unix (POSIX), see, e. g., Buttlar *et al.* [34] or Butenhof [33], and the Open Multi-Processing (OpenMP), see, e. g., Chapman *et al.*

[9] A bit is defined as the smallest storable information unit being either 0 or 1.

[10] Most fine-grained parallelisms, e. g. on the bit or instruction level, are usually not addressable by the programmer, as they are built-in to the hardware.

[11] The level of programming language does not, as often misunderstood, refer to its complexity, but to its hardware abstraction level. For instance, a programme written on a low-level programmining language, e. g. Assembler, contains much more hardware-specific commands, than a high-level programming language, such as C.

[41] or Chandra *et al.* [40].

POSIX, which is nowadays commonly referred to as *Pthreads*, is a family of compatibility standards specified by the IEEE[12]. It is a programming model, which is on a very low hardware-abstraction level, and, therefore, needs the programmers attention to the detail, which in turn pays off with a very fine-grained thread control.

In contrast, **OpenMP**, which is managed by the nonprofit technology consortium OpenMP Architecture Review Board (OpenMP ARB) and which is represented by group of major computer hardware and software vendors, is on a much higher hardware-abstraction level. Hence, it provides a better portability to different hardwares, but suffers from a lack of detailed thread control. However, it provides programmers a simple and flexible interface for developing parallel applications for platforms ranging from the standard desktop computer to HPC clusters. In comparison, OpenMP excels Pthreads in terms of distribution as it is easier to handle and provides sufficient thread control to build programmes with a good performance.

It is important to note that thread-parallelised applications are, in general, prone to data races and race conditions, see Section 5.1.1, as different threads may alter the content at the same memory address at the same time.

MPI-based parallelisation

The message-passing interface MPI is a standard for the inter-process communication in parallel applications and is available for several high-level programming languages. Note that the MPI standard solely defines the programming interfaces of the subroutines, such as subroutine names and arguments, and its particular implementation, e. g. PMPI from IBM, is vendor-dependent and are, therefore, in general not compatible.

The MPI-defined operations are distinguished according to their process-interaction behaviour. In particular, they are classified from a process-local point of view as *blocking operations* or *non-blocking operations*, and, from a global perspective, as *synchronous communication* or *asynchronous communication*. In this regard, an operation is said to be a blocking operation, if, once the command has been deployed, control is not returned to the calling process until the operation has been (successfully or unsuccessfully) completed, thereby, unlocking the associated resources, such as memory, for subsequent usage[13]. In contrast, in a non-blocking operation, control is immediately returned to the calling process once the command has been deployed, but not necessarily completed, thereby allowing access to the associated resources[14]. As was mentioned before, the global-viewpoint equivalent to blocking and non-blocking operations are synchronous and asynchronous

[12]The **I**nstitute of **E**lectrical and **E**lectronics **E**ngineers, which was founded in 1963, is the largest association of technical professionals from electrical and electronic engineering, telecommunications, computer engineering and allied disciplines.

[13]In a blocking communication, which is composed of a paired send and receive operation deployed on different processes, all associated resources, e. g. message buffer, are locked and the sending process is idle until the receiver has confirmed the transmission.

[14]In a non-blocking communication, the associated messages buffer is unlocked and can be modified once the send command has been issued, although the transmission has not yet been confirmed by the receiving process.

communication. In particular, a synchronous communication is only successful if both, the sending and receiving process, completed the respective send and receive operations. In contrast, similar to a non-blocking operation, an asynchronous communication does not require a matching command (e. g. send and receive) to be deployed in order to finish its counterpart (e. g. the receive command of a send operation).

A collection of some selected point-to-point-communication procedures[15] defined within the MPI standard are given below. A more comprehensive collection is found in the MPI standard [143] and a more related details on the particular subroutines can be found, for instance, in Gropp *et al.* [89] and Pacheco [153].

- `MPI_Init()` sets up the MPI-execution environment
- `MPI_Send()`/`MPI_Isend()` initiates an blocking/synchronous and non-blocking/asynchronous message transmission, respectively
- `MPI_Recv()`/`MPI_Irecv()` initiates an blocking/synchronous and non-blocking/asynchronous receive operation, respectively
- `MPI_Wait()` idles the sending or receiving process in an non-blocking/asynchronous operation until the communication has been completed
- `MPI_Probe()` checks if a message with a specific message-identifier tag is available (blocking)
- `MPI_Test()` checks if a specific non-blocking operation has been completed
- `MPI_Finalize()` terminates the MPI-execution environment

In these connections, it is important to point out that blocking operations are prone to deadlock scenarios, whereas non-blocking operations are vulnerable to race conditions and data races.

5.2 Parallelisation in FEM

In parallel-executed application, the crucial point to obtain the best overall performance is to distribute the workload such that the idle time and the inter-process communication of the individual threads and/or processes are minimised. In the related taxonomy, this scattering is called *load balancing*. In the scope of FE simulations, the most work-intensive tasks, which need be scattered, are, in particular, the evaluations of the element-wise contributions to the overall system of equations and, additionally, in an implicit procedure, its solution. In this connection, the optimal load balancing[16] with respect to the FEM is of great interest and, therefore, addressed in a vast number of literature, see, e. g., Cybenko [46] and Walshaw *et al.* [197], or Xu & Lau [209] for an overview. In particular, in FE-based

[15] In contrast, collective communication and synchronisation functions are defined within the MPI standard as well, and allow for a scattered communication to broadcast to all processes used from a particular application.

[16] Note that, in the scope of parallel load balancing, it is furthermore distinguished between static and dynamic load balancing. In particular, static load balancing only exploits informations about the average behaviour of the system, whereas dynamic load balancing reacts to its current state and, therefore, in general, results in more complex strategies, see, e. g., Iqbal *et al.* [107] and Zhang *et al.* [213], but also in a better overall performance.

simulations, the load balancing is carried out using a domain decomposition strategy. Herein, the discrete solution domain Ω^h is decomposed into k subdomains, proceeding, for instance, from an overlapping method, such as the additive Schwarz method, or a non-overlapping procedure, such as *Balancing domain decomposition*. An overview on different decomposition procedures can be found in Toselli & Widlund [184] or Gropp *et al.* [88].

As an example, the domain decomposition following a non-overlapping method is illustrated in Figure 5.5.

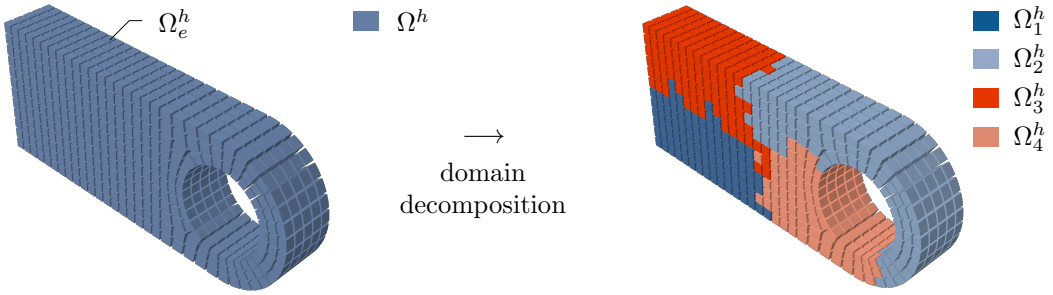

Figure 5.5: *Sketch of the load balancing via domain decomposition in a parallel simulation using four processes.*

Herein, the spatial-discrete solution domain $\Omega^h = \cup_e \Omega_e^h$ is decomposed into four non-overlapping domains, viz.

$$\Omega^h = \bigcup_k \Omega_k^h \qquad \text{with} \qquad k \in \{1, 2, 3, 4\}\,, \tag{5.4}$$

where k denotes the number of subdomains, which usually corresponds to the number of processes used in the parallel simulation. In this connection, the decomposition of the discrete domain is carried out at the beginning of a parallel FE simulation and the individual subdomains are then distributed to the individual threads and/or processes. However, when mesh refinement strategies are used, the decomposition and distribution have to be repeated at every refinement stage in order to obtain the best load balancing.

5.3 Abaqus-PANDAS co-simulation

The governing volume-coupled multi-field problems of interest exhibit, due to the various mutual intrinsic interacting components, a complex nature, especially, with respect to the numerical implementation, which requires significant efforts. In this connection, the underlying models have been, at first, implemented into the research code PANDAS and, subsequently, linked to the commercial finite-element package Abaqus[17]. The linkage is based on the user-defined-element subroutine (UEL) of Abaqus. On the one hand, it introduces all material models of PANDAS into an environment relevant for industrial applications and, on the other hand, provides, in comparison to the native UEL subroutine of Abaqus, a more user-friendly programming environment for user-defined material

[17] All remarks regarding Abaqus are related to version 6.14-2.

models with an arbitrary number of degrees of freedom. The coupling exhibits minimal-invasive properties with respect to the IBVP-definition process in Abaqus and allows for the parallel analysis of large-scale problems on high-performance computing clusters. The coupling can be divided into two modules. In particular, these are

- the **pre-processing module**, which is a Python script to alter the Abaqus input deck in a pre-processing step and
- the **runtime module**, which is embedded into PANDAS and wraps its functionality to match the requirements of the Abaqus UEL subroutine.

Herein, the pre-processing module automatically derives a suitable user-element definition from the topology, i. e. the nodal connectivity of the standard Abaqus elements, which have been created during the definition of the IBVP in Abaqus CAE[18], together with the knowledge of the material-model-dependent nodal degrees of freedom from the PANDAS element definition.

In what follows, the runtime module will be discussed in detail. However, as simulations incorporating user-defined elements require special efforts in order to allow for a convenient post-processing of the simulation results, a discussion of suitable user-element post-processing methods is put in front.

5.3.1 Post-processing of user-defined elements

The special treatment, necessary when carrying out UEL-based simulations, can be traced back to the fact that the ansatz functions and the method used to integrate the governing weak forms (e. g. via *Gauss*-point quadrature), which are also essential for the post-processing, are merely defined within the UEL subroutine and, therefore, not known to the post-processing module of Abaqus CAE. To cope with that, a suitable strategy is needed, on the one hand, to introduce shape functions for the node-to-node interpolation and, on the other hand, set to the values of the dependent variables, e. g. stresses, at the integration points of any individual element. In this connection, several methods have been proposed in the literature.

A naive approach initially stores the integration-point data in a temporary database, e. g. in a text file as was proposed in Schenke & Ehlers [172], or in the binary old results database[19] of Abaqus `.fil`, see Roth *et al.* [166], while the simulation is running. Subsequently, at the end of an analysis[20], the content of the database is merged into the results database of Abaqus (`.odb`). In a similar way, database formats of third-party tools, such as `Tecplot` or `Paraview`, might be exploited, which, however, have not been tested by the author. Another very prominent method introduces the so-called overlay (or dummy or ghost) elements, which solely serve as data container as they exhibit, in relation to the simulated process, neglectable material properties. Therein, an Abaqus

[18] Abaqus CAE is the graphical user interface (GUI) of Abaqus.

[19] In particular, the keyword `*EL FILE` requests the UEL storage container `SDV` to be written to the `.fil` file, thereby chosing the output format (binary or text), see Abaqus Documentation [49].

[20] A database merge after each successful time increment is not possible with the current implementation of Abaqus.

element, with a similar element topology, is connected in parallel to the user-defined element, thereby associating ansatz functions for the nodal interpolation and integrations points to hold the dependent variables. In order to transfer the integration-point data between the overlay and the corresponding user-defined element, a process-local memory is exploited as a temporary data container, from which the `CUVARM` subroutine retrieves the integration-point data and writes to the results database of Abaqus, see Figure 5.6. In this connection, it is important to note that in a process-based parallelisation, which incorporates a decomposition of the simulated domain and a distribution of the partial domains onto the individual processes, it may be necessary to transfer data between the processes (e. g. via MPI programming standard) as the domain-decomposition algorithm of Abaqus does not guarantee that the overlay and its corresponding user-defined element reside in the same process.

	post-processing method		
	overlay element	text-file database	binary-file database
ease of use	+	∘	∘
runtime performance	∘	+	+
post-processing performance	+	−	−
Abaqus/Standard	+	+	+
Abaqus/Explicit	∘	+	+

Table 5.1: Contrasting juxtaposition of common post-processing methods when using user-defined elements in Abaqus simulations.

An overview of common post-processing methods, in particular, the overlay-element method, and the procedures exploiting a text and a binary file as a temporary database are, with their advantages and drawbacks, summarised in Table 5.1. In particular, they are assessed in terms ease of use, their runtime and post-processing performance, and their applicability to Abaqus/Standard (implicit time-integration schemes) and Abaqus/Explicit (explicit time-integration schemes). In this regard, considering the usability, the overlay element is considered the best among the three, as it requires least user interaction, although it produces a significant computational overhead, see Section 5.3.3, during the runtime of a simulation through the evaluations of the actual neglectable overlay-element contributions. Moreover, as the underlying Abaqus release does not provide the whole set of utility subroutines of Abaqus/Standard in Abaqus/Explicit, the overlay-element post-processing method is not fully available in Abaqus/Explicit. In particular, the node-to-node interpolation is realised via the overlay elements, but the integration-point data cannot be visualised. On the contrary, the database-based methods suffer from the very time-intensive reading from the temporary database and data-merging into the Abaqus `.odb` at the end of an analysis, which is due to the extensive read and write processes from and to the hard-drive. In particular, although the access times of the binary file are, in comparison to the text file, significantly lower, the subsequent slow merging process into the `.odb` cancels its run-time performance advantage and, therefore, both procedures show a very bad overall performance, which gets especially pronounced when handling huge amounts of data from large-scale parallel simulation. Hence, according to the au-

thors opinion, the overlay-element method best serves the requirements, and, therefore, is the method of choice for the purpose of this monograph.

5.3.2 Coupling workflow

Proceeding from the overlay-element-based post-processing method, the underlying workflow of the software coupling is depicted in Figure 5.6. Therein, the `UEL` subroutine, written in FORTRAN programming language, solely acts as a dummy subroutine to bypass its callings to the C-coded `CUEL` subroutine of the Abaqus/PANDAS wrapper, thereby handing over the functionality of the `UEL` subroutine to PANDAS.

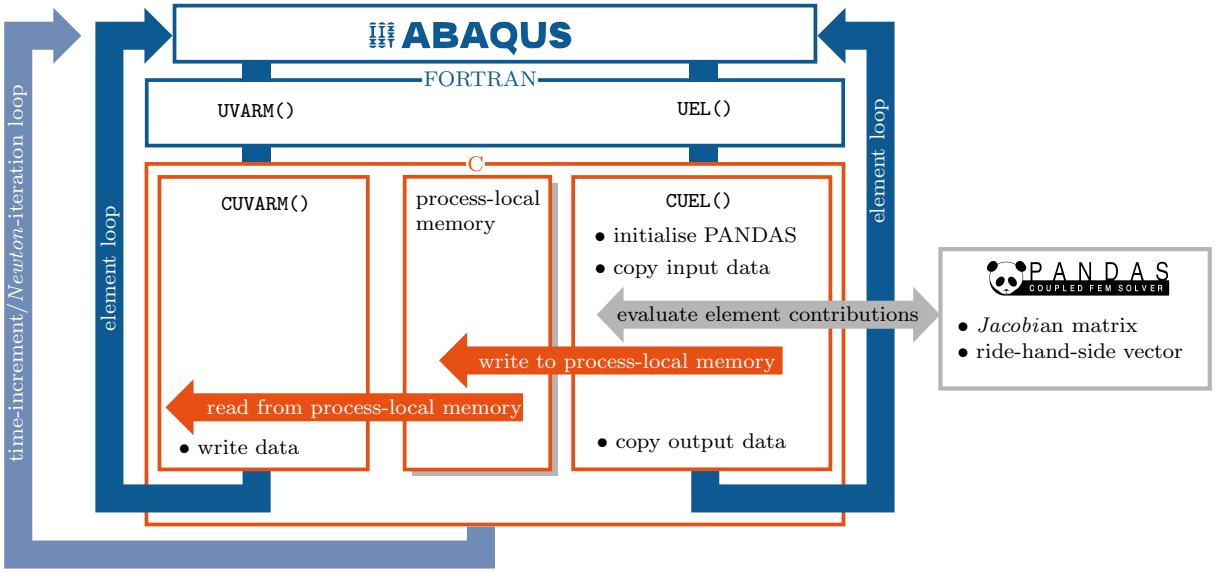

Figure 5.6: *Schematic sketch of the coupling workflow exploiting the overlay-element-based post-processing method.*

In this regard, at the first time the `CUEL` is called, `PandasInit` will set up the PANDAS infrastructure, in particular, a dummy mesh, which consists of a single dummy element. Subsequently, the input data provided by the `UEL` are converted to a PANDAS-matching format, thereby providing the geometric data of the actual element, from which PANDAS will evaluate the element-wise contributions to the overall right-hand-side vector[21] through `PhysResidual` and to the Jacobian (implicit procedure) or mass matrix (explicit procedure), respectively, through `PhysTangent`, which are then converted back to a `UEL`-conforming data format. Finally, the integration-point data will be stored to a hash-based[22,23] database residing in a process-local memory[24]. To complete the evaluation

[21] Note that the right-hand-side vector requested by the `CUEL` subroutine only comprises the internal element response based on the current values of the underlying degrees of freedom. The external load vector applied on the Neumann boundaries is added by Abaqus.

[22] A hash table is a look-up table, where each entry is associated with a hash key, which uniquely identifies its position. In this way, very fast look-up tables can be realised.

[23] Thanks to UTHASH from `http://troydhanson.github.io/uthash/`.

[24] Note that this procedure is thread-safe, as each element in the look-up table will always only be

of the element-wise contributions, the `CUVARM` subroutine, as part of the computations of the overlay-element contributions, is called by Abaqus in order to retrieve the integration-point data of the associated user-defined element. Finally, Abaqus will gradually assemble the overall system of equations, apply the boundary conditions and solve the system for the nodal unknowns in each time increment.

As the domain decomposition algorithm of Abaqus does not guarantee that the user-defined element and its corresponding overlay element reside on the same process, the integration-point data needs to be transferred between the individual processes via the MPI communication standard. In particular, as in a parallel process it is not predefined whether the `UEL` or the `UVARM` subroutine of the associated overlay-user-element pairing is called first, the inter-process communication is realised via the non-blocking send and receive operations, see Section 5.1.4, using `MPI_ISend` and `MPI_IRecieve`. Both operations merely open an inter-process-communication window, without the need to finish the transmission upon their calling (compare blocking operations in Section 5.1.4). The transmission will be completed once each send or receive is paired with the respective receive or send operation, where the user-element number is used as an transmission identifier to match the send-receive pairings.

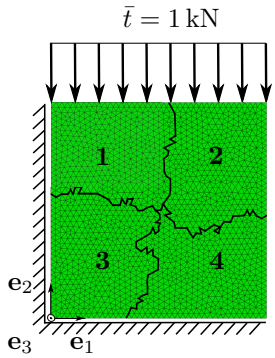

Figure 5.7: *Benchmark problem decomposed into four MPI domains.*

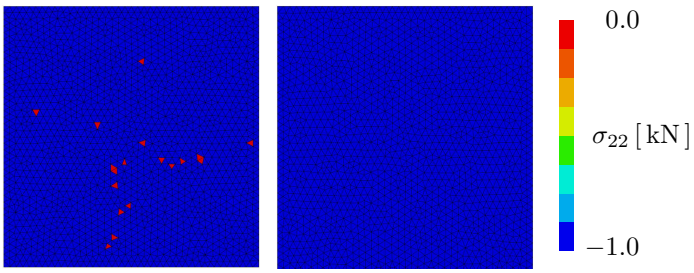

Figure 5.8: *Contour plot of σ_{22} for a simulation without (left) and with MPI-based communication (right) of integration point data.*

In order to verify the overlay-element-based post-processing method in a parallel analysis, a benchmark problem is investigated. Therein, a simple initial-boundary-value problem (IBVP) is realised, where the displacements at the right and bottom edges are constrained in normal direction, and the upper edge is loaded by the surface load $\bar{t} = 1\,\mathrm{kN/m}$, see Figure 5.7. The material behaviour is governed by a single-phasic (non-porous) linear-elastic material law. The analysis is carried out in parallel comprising a thread- and process-based parallelisation. In particular, the problem has been decomposed into four MPI domains, where each subdomain is split again in two threads, i. e. the benchmark problem runs in parallel on eight computing cores.

The resulting stress distribution is depicted in Figure 5.8. Therein, the previously mentioned non-matching processes assignment of the user-defined and its respective overlay

accessed from a specific thread, in particular, the thread in which the current element under consideration resides in.

element is clearly illustrated in Figure 5.8 (left) by the non-homogeneous stress distribution. In particular, it can be observed that some of the finite elements still depict a zero stress value, which was the initial value at the beginning of the analysis. In contrast, when incorporating an inter-process communication of the integration-point variables, i. e. of the stress values in this particular case, a homogeneous stress field is obtained, see Figure 5.8 (right).

5.3.3 Benchmarks

Next, different performance benchmarks are carried out. The first benchmark illustrates the computational overhead of the overlay-element post-processing method (post-processing-method benchmark) and the second benchmark (parallel-simulation benchmark) addresses the parallel scalability of the thread- and MPI-based parallelisation methods. In this regard, the underlying IBVP used in both benchmarks is depicted in Figure 5.9.

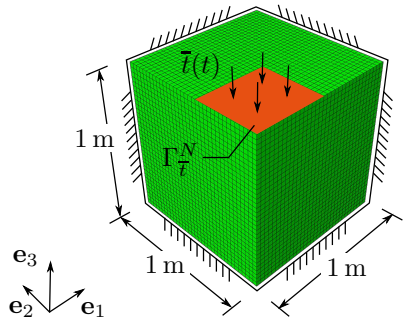

Figure 5.9: *Sketch of the initial-boundary-value problem of the benchmark test.*

	Abaqus	Abaqus/PANDAS	
		with OEM	without OEM
runtime (DS) [s]	7249	13 690	8 446
performance loss (DS) [%]	-	89	17
runtime (IS) [s]	15 992	20 111	10 695
performance loss (IS) [%]	-	25	-69

Figure 5.10: *Benchmark results in sequential execution for stand-alone Abaqus and Abaqus/PANDAS co-simulation.*

Therein, a cubic domain (length: 1 m, width: 1 m, height: 1 m), composed of a linear elastic ($\mu^S = 26\,923\,\mathrm{N/m^2}$, $k_0^S = 40\,385\,\mathrm{N/m^2}$, $k_1^S = 0\,\mathrm{N/m^2}$) single-phasic material, is subjected to a linearly increasing surface load,

$$\bar{t}(t) = \bar{t}_0\, t \qquad \text{with} \qquad \bar{t}_0 = 1\,\mathrm{N}\,,\ 0 \leq t \leq 1000\,\mathrm{s}\,, \tag{5.5}$$

acting on the Neumann boundary $\Gamma_{\bar{t}}^N$. The domain is spatially discretised with 38 184 elements using quadratic ansatz functions for the solid displacements $\mathbf{u}_S$. Hence, the degrees of freedom of the overall system sum up to 488 985. The time increment is fixed to $\Delta t = 10\,\mathrm{s}$ and, therefore, 100 time steps are necessary to simulate the process. The Benchmarks have been carried out on a compute node[25] of the LEAD HPC cluster[26].

[25] A compute node consists of two AMD Opteron™ Processor (model 6328) with 32 cores, each running at 3.2 GHz, and is equipped with 256 GB memory.

[26] The permission to use the HPC cluster of the LEAD (**L**ower **E**xtremity **A**mputee **D**ynamics) project, processed within the Continuum Biomechanics Group at the University of Stuttgart, is highly appreciated.

Post-processing-method benchmark

The first set of benchmarks is dedicated to the investigation of the computational overhead due to the overlay-element post-processing method (OEM). Herein, the simulation times of Abaqus in stand-alone mode using the built-in material model are compared to the simulations with and without OEM. All computations have been carried out using, on the one hand, the direct (DS) and, on the other hand, the iterative solver (IS) of Abaqus. The results are summarised in table 5.10. Herein, it can be seen that the performance loss is approximately 89 % and 17 % in case of the direct and the iterative solver, respectively.

The different performance losses can be explained as follows. The time needed to complete a time step, or a Newton increment in a non-linear analysis, is mainly composed of two tasks, which are, on the one hand, the evaluation of the element-wise contributions, which is, within the present co-simulation approach, composed of the contributions of both the overlay and the user-defined elements, and, on the other hand, the solution of the assembled system of equations. However, as the resulting system of equations of the underlying linear problem can be solved more efficiently using the direct solver[27] rather than the iterative solver. In consequence, the share in the total runtime of the element-wise evaluations of PANDAS is higher in comparison to the slice needed to solve the system of equations. In case of the iterative solver, a runtime comparison between the stand-alone Abaqus and the Abaqus/PANDAS co-simulation shows an awkward behaviour. In particular, exploiting the overlay-element method (OEM), a loss in performance of approximately 25 % can be observed. However, when the overlay elements are neglected (without OEM), a performance increase, illustrated by the negative performance loss, of approximately 69 % is observed. Without the knowledge of the particulars of the Abaqus implementation, an elaboration is beyond the scope of the author.

Parallel-simulation benchmark

The second set of benchmarks investigates the behaviour of the coupling workflow under parallel-execution conditions. The underlying IBVP is depicted in Figure 5.9 and will be analysed in parallel using either p parallel threads or MPI-processes, where $p \in \{2, 4, 8, 16, 32\}$. Moreover, the direct solver is used to solve the system of equations. The resulting runtime measurements are summarised in Table 5.2.

For a better illustration of the parallel scalability, the parallel speedup and the parallel efficiency factor for a MPI- and a thread-based parallelsisation are depicted in Figures 5.11 and 5.12, and Figures 5.13 and 5.14, respectively. Note that, herein, the ideal parallel speedup indicating the best achievable performance-enhancement multiplier, which is equal to the number of used parallel threads or processes, is illustrated by the gray line.

[27] It is assumed, but not verifiable by the author, that the LU-decomposition-based direct solver of Abaqus recognised the linearity of the problem, i. e. the constant Jacobi matrix, and, therefore optimises the solution procedure in such a way that the LU decomposition, see, e. g., Hoffman & Frankel [103], of the resulting system of equations is carried out only once. This assumption is further supported through the records of the time needed to solve the system of equations. Herein, at the first increment, the solution took approximately 3 838 s, whereas in each subsequent time increment the systems was solved in 3 s.

	number of threads/processes					
	p = 1	p = 2	p = 4	p = 8	p = 16	p = 32
thread-based parallelisation						
runtime (Abaqus) [s]	7 249	3 775	2 157	1 323	917	797
speedup S_p (Abaqus) [-]	1.00	1.92	3.36	5.44	7.84	8.96
efficiency E_p (Abaqus) [-]	1.00	0.96	0.84	0.68	0.49	0.28
runtime (Abaqus/PANDAS) [s]	13 690	7 502	4 209	2 498	1 739	1 703
speedup S_p (Abaqus/PANDAS) [-]	1.00	1.82	3.24	5.44	7.84	8.0
efficiency E_p (Abaqus/PANDAS) [-]	1.00	0.91	0.81	0.68	0.49	0.25
MPI-based parallelisation						
runtime (Abaqus) [s]	7 249	3 794	2 092	1 299	965	1 255
speedup S_p (Abaqus) [-]	1.00	1.92	3.44	5.36	7.52	5.76
efficiency E_p (Abaqus) [-]	1.00	0.96	0.86	0.67	0.47	0.18
runtime (Abaqus/PANDAS) [s]	13 690	7 523	4 594	2 811	1 685	7 642
speedup S_p (Abaqus/PANDAS) [-]	1.00	1.8	2.96	4.88	8.16	1.6
efficiency E_p (Abaqus/PANDAS) [-]	1.00	0.90	0.74	0.61	0.51	0.05

Table 5.2: *runtime comparison between thread- and MPI-based parallelisation for stand-alone Abaqus and Abaqus/*PANDAS *co-simulation.*

Addressing at first the investigation of the MPI-based parallelisation method, the parallel speedup and efficiency plots, depicted in Figure 5.11 and 5.12, respectively, show a controversial behaviour. In particular, up to 16 MPI processes, the parallel speedup factor increases monotonically and is in good agreement for stand-alone Abaqus and Abaqus/PANDAS co-simulation. However, from 16 processes onwards, the parallel speedup decreases, which illustrates the saturation of the parallel solution strategy. To be more

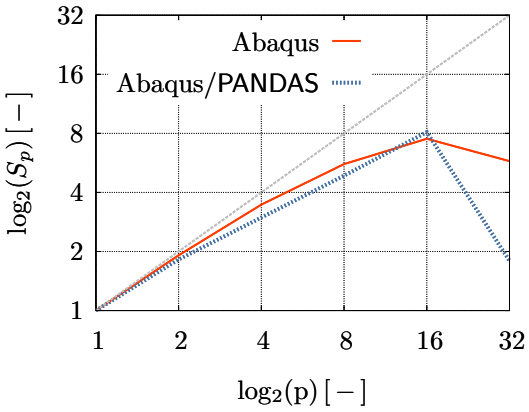

Figure 5.11: *Parallel speedup S_p comparison between Abaqus and Abaqus/*PANDAS *in a MPI-based parallelisation for different numbers* p *of parallel process.*

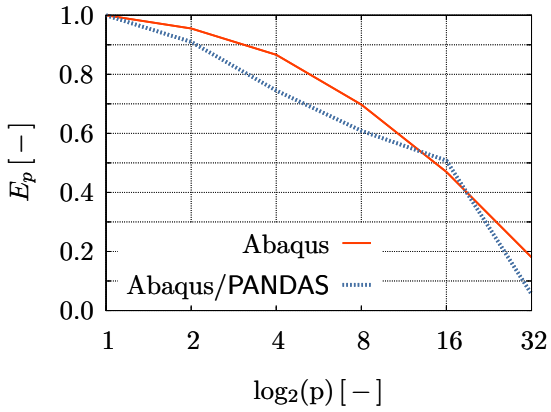

Figure 5.12: *Parallel efficiency E_p comparison between Abaqus and Abaqus/*PANDAS *in a MPI-based parallelisation for different numbers* p *of parallel processes.*

precise, this observation is owed to the increasing number of MPI subdomains and, therewith, the decreasing size of the MPI subdomains, which, in turn, emphasises the share in time in the overall solution time needed for the necessary process-to-process communication, e. g. the transfer of the nodal values at the subdomain interfaces. This behaviour is even more pronounced in case of the Abaqus/PANDAS co-simulation, where the transfer of the integration-point data causes an additional overhead and, therefore, a huge performance drop.

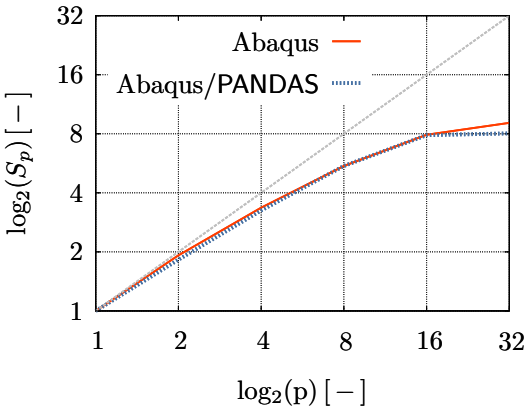

Figure 5.13: *Parallel speedup S_p comparison between Abaqus and Abaqus/PANDAS in a thread-based parallelisation for different numbers* p *of parallel threads.*

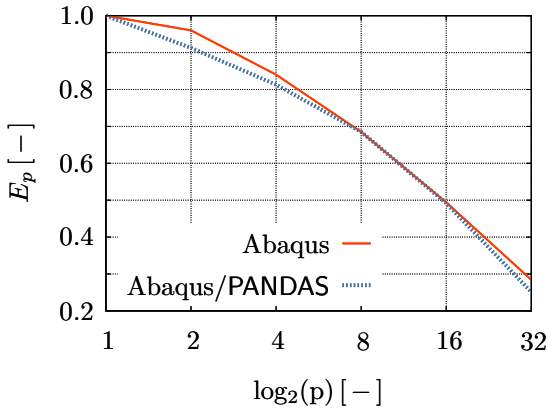

Figure 5.14: *Parallel efficiency E_p comparison between Abaqus and Abaqus/PANDAS in a thread-based parallelisation for different numbers* p *of parallel threads.*

Drawing the attention to the investigation of the parallel scalability in case of the thread-based parallelisation, the parallel speedup and efficiency factor, depicted in Figure 5.13 and 5.14, on the one hand, illustrates the agreement in the parallel-performance enhancement for stand-alone Abaqus and Abaqus/PANDAS. On the other hand, it indicates that the parallel saturation is reached beyond 32 parallel threads. Consequently, for an efficient parallel solution strategy on hybrid systems incorporating both parallelisation methods, it is strongly recommended to firstly increase the number of parallel threads within a MPI process before extending the number of parallel MPI-processes.

Chapter 6: Simulations

The present chapter is dedicated to the simulation of several volume-coupled multi-field problems, thereby illustrating the diverse application possibilities of the Abaqus/PANDAS co-simulation approach. Most simulations are carried out in parallel exploiting either a thread- or a hybrid (thread- and MPI-based) parallelisation method. To begin with, the efficient solution of dynamic problems in the scope of porous materials is addressed. For this purpose, parametric studies are carried out investigating, on the one hand, the parallel scalability of the co-simulation approach, thereby exploiting implicit and explicit time-integration schemes and, on the other hand, the eligibility of the presented unbound-domain treatment for the representation of semi-infinite domains. Subsequently, more realistic application scenarios concern the simulation of soil mechanical problems, in particular, the investigation of the soil stability under cyclic loading condition, and the simulation of multiphasic flow processes within textile fabrics.

6.1 Parametric studies in porous-media dynamics

In general, in a dynamic analysis the response of a mechanical system to impact or impulsive loadings is investigated. In particular, the rapidly changing loading conditions give rise to dynamic phenomena, such as waves dispersing through the spatial domain. In this regard, a sufficient accurate and efficient solution strategy requires, on the one hand, a fine temporal disretisation in order to resolve the dynamic phenomena and, on the other hand, with respect to the wave-propagation problem, the extension of the spatial domain towards infinity in order to suppress wave reflections. The present section starts with a contrasting juxtaposition of the implicit and explicit time-marching schemes with respect to their computational efficiency and their parallel scalability. Subsequently, the previously introduced unbound-domain treatment, comprising the infinite-element approximation and the viscous-damped boundaries, is studied numerically with respect to its wave-absorption capabilities.

6.1.1 Abaqus/Standard versus Abaqus/Explicit

The following simulations serve the investigation of the computational efficiency and the parallel scalability of the implicit and explicit time-marching schemes of Abaqus/Standard and Abaqus/Explicit, respectively, where both exploit the Abaqus/PANDAS co-simulation approach.

The underlying initial-boundary-value problem (IBVP) is depicted in Figure 6.1. Herein, an ellipsoidal halfspace (first and second minor axis: 20 m, third minor axis: 10 m) with a drained top surface ($\overline{p}^{FR} = 0$) is simplified to a one-fourth model by exploiting its symmetry and by introducing suitable boundary conditions at the symmetry planes.

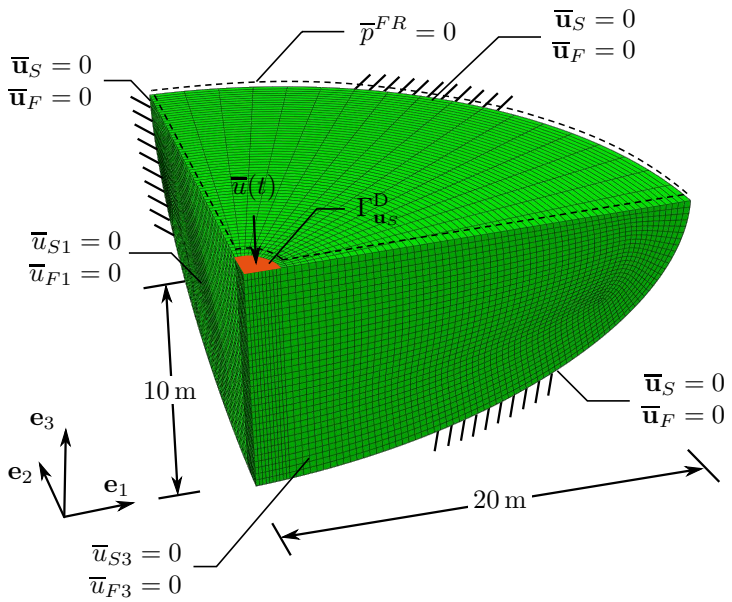

Figure 6.1: *IBVP of the benchmark problem serving the parametric study.*

Parameter	Value	Unit
n^S_{0S}	0.6	-
μ^S	$5.6 \cdot 10^6$	$\mathrm{N/m^2}$
k^S_1	$8.4 \cdot 10^6$	$\mathrm{N/m^2}$
k^S_2	0.0	$\mathrm{N/m^2}$
ρ^{SR}	2700	$\mathrm{kg/m^3}$
n^L_0	0.399	-
ρ^{LR}	1000	$\mathrm{kg/m^3}$
γ^{LR}	$1 \cdot 10^4$	$\mathrm{kg/m^3}$
μ^{LR}	$1 \cdot 10^{-3}$	$\mathrm{N\,s/m^2}$
n^G_0	0.001	-
θ_0	293	K
R^G	287	$\mathrm{J/(kg\,K)}$
μ^{GR}	$2 \cdot 10^{-5}$	$\mathrm{N\,s/m^2}$
K^S_{0S}	10^{-5}	$\mathrm{m^2}$

Figure 6.2: *Material parameters of the benchmark problem.*

A sinusoidal-shaped displacement impulse, given by

$$\begin{aligned} &\overline{u}(t) = \overline{u}_0 \sin(2\pi f t)[H(t) - H(t-\tau)] \\ &\text{with} \qquad \overline{u}_0 = 0.05\,\mathrm{m}\,,\ f = 10\,\mathrm{Hz}\,,\ \tau = 0.05\,\mathrm{s}\,,\ 0 \leq t \leq 0.5\,\mathrm{s} \end{aligned} \tag{6.1}$$

is applied at the Dirichlet boundary $\Gamma^{\mathrm{D}}_{\mathbf{u}_S}$. The material description follows the dynamic hybrid model, see Section 3.2.2, where the governing material parameters are summarised in Table 6.2. In this connection, note that material under consideration is highly permeable ($K^S_{0S} = 10^{-5}\,\mathrm{m^2}$) in order to the reduce the material-intrinsic damping and, in consequence, to allow for the triggered waves to propagate through the entire domain. The spatial domain is discretised by 38 295 elements. At this juncture, constraint by the requirement for a proper post-processing of the simulation results exploiting the OEM and the technical limitations of Abaqus/Explicit, linear ansatz functions for all nodal unknowns, i. e. $\mathbf{u}_S$, $\mathbf{u}_F$ and p^{FR}, are used. Note that, for this particular problem, the solution does not exhibit any instabilities although the LBB condition, see Section 4.1.2, is not satisfied. The resulting system exhibits 294 056 degrees of freedom. The benchmark problem, is simulated using, on the one hand, the implicit HHT method, see Section 4.3.1, of Abaqus/Standard and, on the other hand, the central-difference method together with the forward *Euler* method, see Section 4.3.2, of Abaqus/Explicit. The simulations have been carried out in parallel on a compute node[1] of the LEAD HPC cluster exploiting different numbers of parallel processes and threads, respectively, i. e. $\mathrm{p} \in \{2, 4, 8, 16, 32\}$. In particular, in case of Abaqus/Standard, a thread-based parallelisation and a direct solver[2] based

[1] A compute node consists of two AMD Opteron™ Processors (model 6328), each composed of 16 cores running at 3.2 GHz, and is equipped with 256 GB memory.

[2] Note that the for large-scale problems more suitable Krylov-subspace-based iterative solvers are not available for the imposed HHT time-integration scheme in Abaqus/Standard.

on a LU-decomposition method are utilised, whereas Abaqus/Explicit proceeds from a MPI-based parallelisation. Moreover, with respect to the Nyquist-Shannon sampling theorem, the time increments in Abaqus/Standard are fixed to $\Delta t_{\text{impl.}} = 5 \cdot 10^{-3}\,\text{s}$, whereas in Abaqus/Explicit the time step is set to $\Delta t_{\text{expl.}} = 5 \cdot 10^{-5}\,\text{s}$ to satisfy the CFL stability condition, see Courant *et al.* [45].

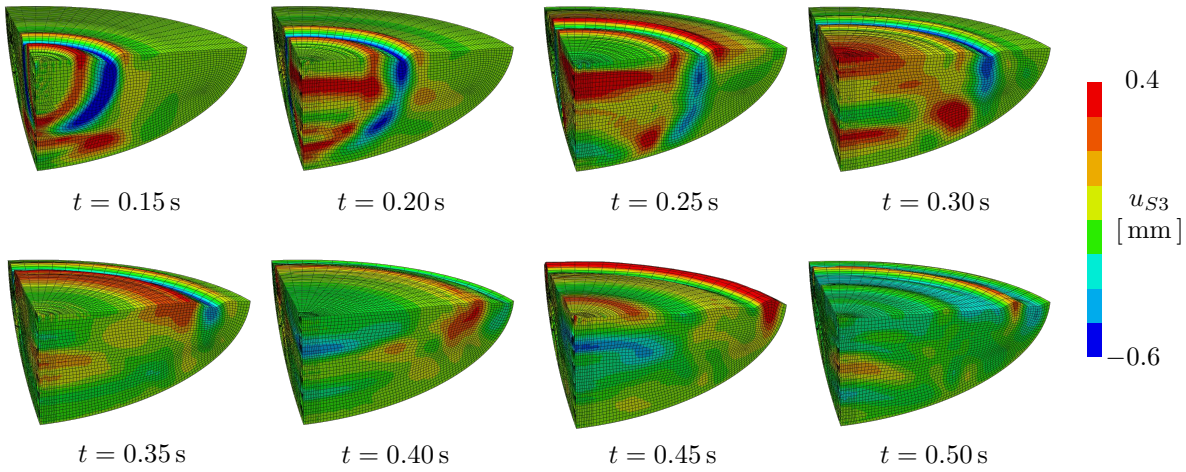

Figure 6.3: *Sequence of contour plots of the solid displacement u_{S3} in the vertical direction on the deformed mesh (scale factor: 2000).*

The simulation results are depicted in Figure 6.3. Therein, a sequence of contour plots of the solid displacement $\mathbf{u}_S$ in direction of $\mathbf{e}_3$, i. e. $u_{S3} = \mathbf{u}_S \cdot \mathbf{e}_3$, is given. The imposed loading impulse triggers two bulk-wave types, in particular, a compressional wave (p-wave) and a transverse shear wave (s-wave), which propagate through the domain and are reflected on the domain boundaries.

	number of threads/processes					
	p = 1	p = 2	p = 4	p = 8	p = 16	p = 32
Abaqus/Explicit						
runtime T_p [s]	31 923	15 757	8 449	4 382	2 612	1 087
speedup S_p [-]	1.00	1.92	3.77	7.28	12.22	30.28
efficiency E_p [-]	1.00	0.96	0.94	0.91	0.76	0.94
Abaqus/Standard						
runtime T_p [s]	851 966	446 056	247 604	137 444	79 393	44 114
speedup S_p [-]	1.00	1.91	3.44	6.19	10.73	19.31
efficiency E_p [-]	1.00	0.96	0.84	0.77	0.67	0.60

Table 6.1: Summarised runtimes T_p, and the related parallel speedups and efficiencies, S_p and E_p, of Abaqus/Standard and Abaqus/Explicit for a different number p of parallel threads and processes, respectively.

The measured runtimes, the related parallel speedups S_p and parallel efficiencies E_p of the benchmark problem are summarised in Table 6.1. Herein, it is clearly illustrated that

Abaqus/Explicit excels the implicit procedure of Abaqus/Standard, on the one hand, in terms of the computational costs and, on the other hand, with respect to the parallel scalability. In particular, a comparison of the simulation runtimes reveals that Abaqus/Explicit solves the given problem significantly faster even in sequential execution ($T_1 = 31\,923\,\mathrm{s}$) than Abaqus/Standard in parallel ($T_{32} = 44\,114\,\mathrm{s}$). Furthermore, Abaqus/Explicit exhibits a better parallel scalability with an increasing number of parallel threads or processes, respectively, which is illustrated by the higher parallel speedup and parallel efficiency factors, S_p and E_p. To examine this observation in more detail, the evolutions of S_p and E_p in relation to p are investigated, see Figures 6.4 and 6.5, respectively. In particular, Figure 6.4 illustrates the superior parallel behaviour of the explicit procedure through, on the one hand, the computed speedup being closer to the ideal speedup (gray line) and, on the other hand, the weaker speedup degradation with increasing number of threads/processes. The poor parallel scalability of Abaqus/Standard, or of implicit procedures in general, can be traced back to the inevitable inter-thread (or inter-process) communications while solving the system of equations. In particular, the share of the communication time in the overall problem runtime increases together with the rising number of threads, as, simultaneously, the number of subdomains and, consequently, the number of subdomain boundaries which require communication, advances accordingly. This effect will become even more pronounced with increasing model complexity, i. e. increasing number of degrees of freedom, as the number of floating-point operations necessary to solve a system of equations of size $n \times n$ using a LU-decomposition-based method is approximately $2/3\,n^3$, see Vandenberghe [191], which is a cubic relation in n. Note that the speedup and the efficiency of Abaqus/Explicit utilising $\mathrm{p} = 16$ processes is not in line with the others, i. e. $\mathrm{p} \in \{1, 2, 4, 8, 32\}$. However, the origin of this observation cannot be traced back by the author as the particulars of the algorithmic implementation are not known.

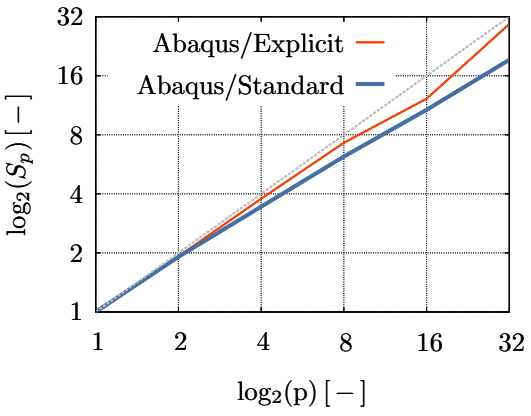

Figure 6.4: *Comparison of the parallel speedup S_p between Abaqus/Explicit and Abaqus/Standard for a different number* p *of parallel threads/processes.*

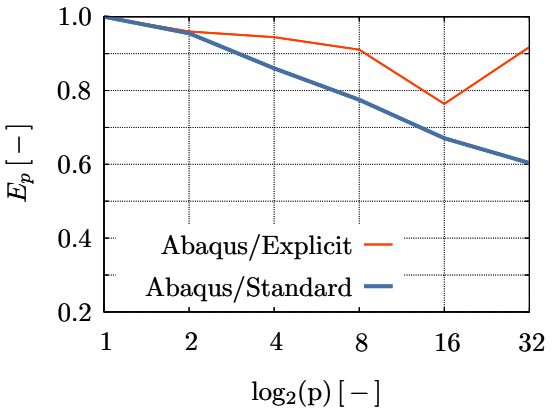

Figure 6.5: *Comparison of the parallel efficiency E_p between Abaqus/Explicit and Abaqus/Standard for a different number* p *of parallel threads/processes.*

6.1.2 Unbound-domain treatment

When investigating problems under rapidly changing loadings conditions, special attention needs to be paid to the approximation of the real problem by a suitable IBVP. In this regard, the semi-infinite half-space is split into a near-field, which is, in general, the domain of interest, and a far-field. However, truncating the semi-infinite half-space at the near field, which is often sufficient in quasi-static simulations, introduces artificial boundaries at which, in a dynamic analysis, the incoming waves are reflected back into the domain of interest.

The following simulations address a parametric study of the far-field treatment presented in Section 4.2. Herein, the finite-element (FE) discretisation of the near-field is extended towards infinity via infinite elements (IE), where, additionally, a viscous-damped boundary (VDB) is introduced at the FE-IE interface. The energy-absorbing behaviour is realised through dashpots at the interface layer. The damping coefficients of the dashpots and the residual stiffness of the IE are in the scope of the parametric study.

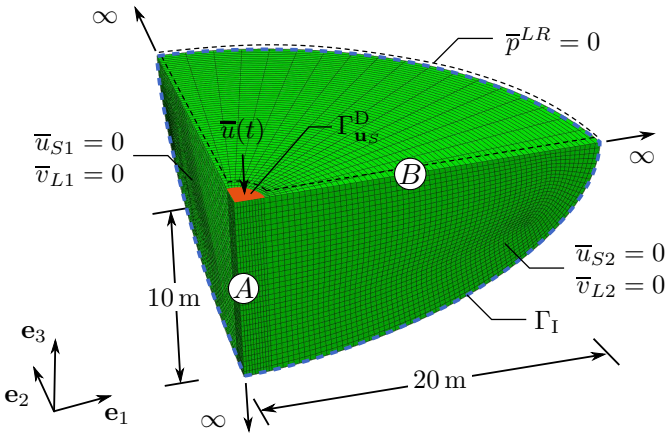

Figure 6.6: *IBVP of the parametric study to investigate the unbound-domain treatment.*

Parameter	Value	Unit
n^S_{0S}	0.6	-
μ^S	$2.6 \cdot 10^4$	$\mathrm{N/m^2}$
k^S_1	$4.0 \cdot 10^4$	$\mathrm{N/m^2}$
k^S_2	0.0	$\mathrm{N/m^2}$
ρ^{SR}	2700	$\mathrm{kg/m^3}$
ρ^{LR}	1000	$\mathrm{kg/m^3}$
γ^{LR}	$1 \cdot 10^4$	$\mathrm{kg/m^3}$
μ^{LR}	$1 \cdot 10^{-3}$	$\mathrm{N\,s/m^2}$
K^S_{0S}	10^{-5}	$\mathrm{m^2}$

Figure 6.7: *Material parameters of the parametric study of the unbound-domain treatment.*

The underlying IBVP of the parametric study is depicted in Figure 6.6. Therein, an ellipsoidal domain (first and second minor axis: 20 m, third minor axis: 10 m) is extended towards infinity by use of infinite elements[3], where the dashpots associated with the viscous-damped boundary (VDB) are attached at the FE-IE interface Γ_{I}. The material description follows the dynamic liquid-saturated model, see Section 4.1.1, where the material parameters are summarised in Table 6.7.

The semi-infinite halfspace is spatially discretised through 38 295 finite and 1 449 infinite elements. In the former, the underlying field variables, i. e. $\mathbf{u}_S$, $\mathbf{v}_L$ and p^{LR}, are approximated through quadratic ansatz ($\mathbf{u}_S$) and linear ansatz functions ($\mathbf{v}_L$ and p^{LR}), respectively, whereas in the latter, the ansatz functions account for the decaying and finally vanishing property of the fields $\mathbf{u}_S$ and $\mathbf{v}_L$, see Marques & Owen [139], and the

[3]Note that the infinite elements are not depicted in Figure 6.6.

non-vanishing characteristic of p^{LR} towards infinity. The resulting system exhibits 671 479 degrees of freedom.

In order to trigger waves propagating through the domain, a displacement impulse given by a sinusoidal half wave

$$\begin{aligned} &\overline{u}(t) = \overline{u}_0 \sin\left(2\,\pi\,f\,t\right)\left[H(t) - H(t-\tau)\right] \\ &\text{with} \quad \overline{u}_0 = 5 \cdot 10^{-3}\,\mathrm{m}\,, \quad f = 1\,\mathrm{Hz}\,, \quad \tau = 0.5\,\mathrm{s} \end{aligned} \tag{6.2}$$

is applied at the Dirichlet boundary $\Gamma^{\mathrm{D}}_{\mathbf{u}_S}$. The solid displacements and the pore-liquid velocities are zero normal to the symmetry planes, i. e. $u_{S1} = 0$, $v_{L1} = 0$, $u_{S2} = 0$ and $v_{L2} = 0$, and have to vanish at infinity, i. e. $\overline{\mathbf{u}}_{S,\infty} = \mathbf{0}$ and $\overline{\mathbf{v}}_{L,\infty} = \mathbf{0}$. In order to judge the energy-absorbing capability of the unbound-domain treatment, the vertical displacements of the solid skeleton at A (located at a depth of 5 m) and B (located 10 m from the vertical symmetry line) are evaluated.

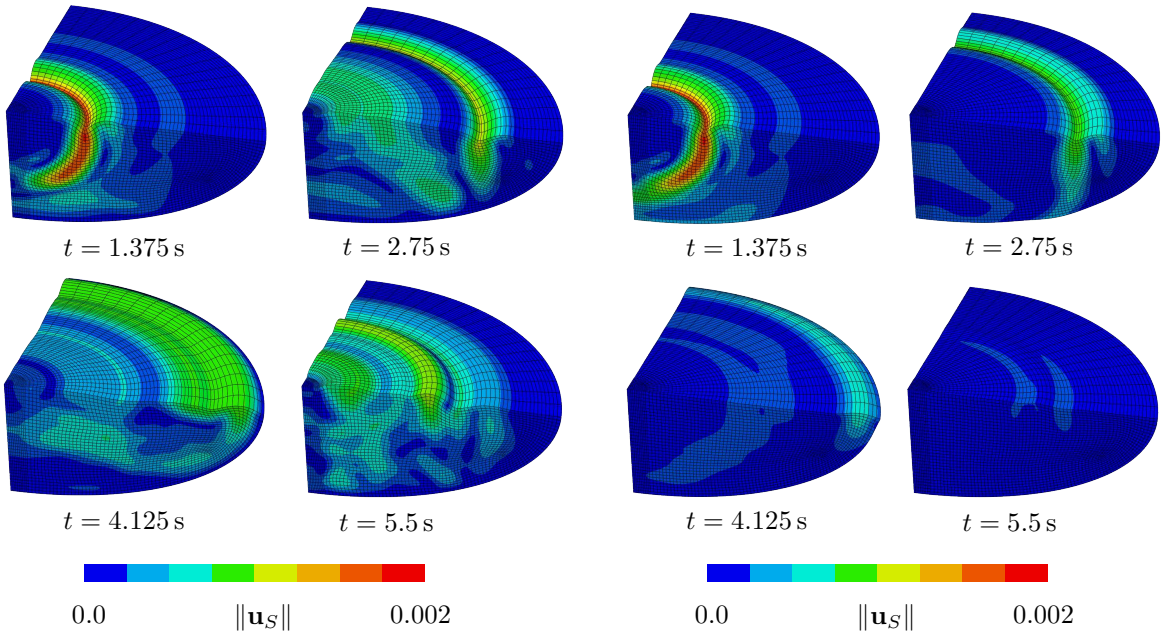

Figure 6.8: *Contour plot of the magnitude of the solid displacement $\|\mathbf{u}_S\|$ on the deformed geometry (scale factor: 500) of the truncated semi-infinite halfspace.*

Figure 6.9: *Contour plot of the magnitude of the solid displacement $\|\mathbf{u}_S\|$ on the deformed geometry (scale factor: 500) of the semi-infinite halfspace incorporating the VDB.*

Due to the size of the problem, the simulations have been carried out in parallel on 40 cores exploiting a thread-based parallelisation on a compute node[4] of the HPC cluster of the SRC SimTech[5]. The prescribed displacement impulse triggers, on the one hand, a compression wave propagating in negative direction of $\mathbf{e}_3$, and, on the other hand, a surface wave (*Rayleigh wave*) spreading in circles along the surface. In case of the

[4] A compute node consists of two Intel Xeon™ Processors (E5-2680 v2), where each is composed of 10 physical cores running at 2.8 GHz and supporting Intels Hyper-threading™ technology, and is equipped with 256 GB of memory.

[5] Stuttgart Research Centre for Simulation Technology

truncated domain both wave types are reflected at the artificial domain boundaries, see Figure 6.8, whereas the reflections are significantly attenuated, see Figure 6.9, when the unbound-domain treatment is utilised.

Influence of the damping coefficients

At first, the choice of the damping coefficients a and b of the dashpots at the FE-IE interface with respect to the energy-absorbing behaviour is elucidated[6]. In particular, the proposed values of Lysmer & Kuhlemeyer [133] (LK), viz. $a = b = 1$, which give the best energy absorption if the wave-propagation direction is normal to the FE-IE interface, is compared to the approach of White *et al.* [198] (W), which is based on the maximisation of the dissipated energy over different wave incidence angles. In the latter approach, the damping coefficients are computed via relation (4.21) and yield $a = 0.93$ and $b = 0.69$ with the material parameters provided in Table 6.7.

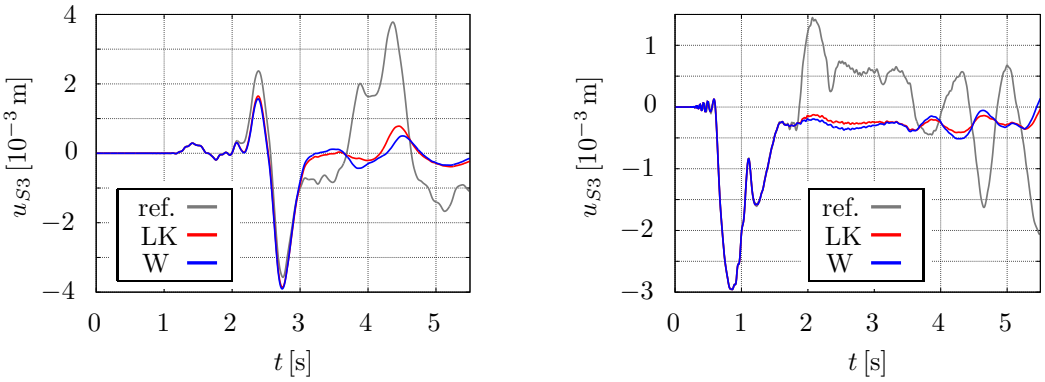

Figure 6.10: *Evolution of the vertical displacement of B (left) and A (right) for the damping parameters according to Lysmer & Kuhlemeyer [133] (LK) and White et al. [198] (W).*

The simulation results are depicted in Figure 6.10. Therein, the gray line is used as a reference (ref.) showing the result of the truncated domain without a particular far-field treatment. It can be seen that the approach of White *et al.* [198] (W) gives slightly better results compared to Lysmer & Kuhlemeyer [133] (LK). However, as the approach of White *et al.* [198] proceeds from the linear elastic Hookean law for the constitutive description of the solid in the near field, their proposal is tied to the first and second Lamé constants and, thus, may not be suitable for arbitrary solid material descriptions.

Influence of the quasi-static contribution

The subsequent study investigates the influence of the quasi-static contribution. Consequently, the damping parameters of the VDB are fixed to $a = b = 1$.

Comparing the records of the solid displacement at the points A and B, see Figure 6.11, it can be recognised that the negligence of the quasi-static contribution (NS) gives a better energy absorption in comparison to the case where the quasi-static contribution

[6]Herein, the quasi-static contribution of the IE formulation, see Section 4.2, has been neglected.

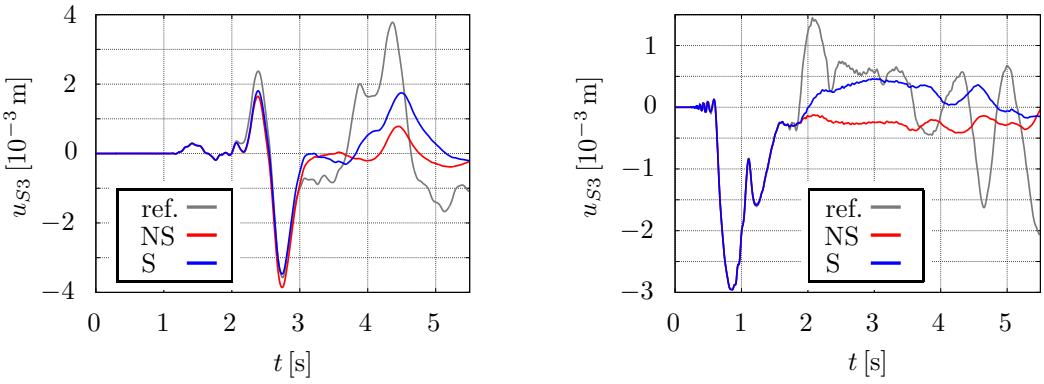

Figure 6.11: *Evolution of the vertical displacement of B (left) and A (right) in the case of a considered (S) or neglected quasi-static contribution (NS).*

(S) is considered. These findings are in agreement with Haeggblad & Nordgren [91], who, however, carried out simulations on singlephasic materials. Nevertheless, if a simulation contains quasi-static loading steps, for instance, if the transient load is preceded by a consolidation step in a geomechanical analysis, the quasi-static contribution has to be considered, as it provides the necessary residual stiffness to the far field.

6.2 Soil mechanics

The present section is dedicated to the simulation of soil-mechanical problems. In particular, the numerical investigations address liquefaction phenomena in fully saturated granular assemblies which are subjected to cyclic loading conditions as they occur, for instance, during earthquakes, geotechnical installations processes (e. g. installation of vibro-injection piles) or in the foundation of on-shore or off-shore wind power plants. In this connection, the dynamic liquid-saturated model, see Section 3.2.2, and the elasto-plastic description of the solid skeleton proceeding either from the pure isotropic hardening (IH) or the mixed isotropic-kinematic hardening (IKH) model.

At first, element tests are considered, where, on the one hand, the responses of IH and IKH model are contrasted both in comparison with the result of a quasi-static cyclic experiment applied on a dry soil specimen. On the other hand, the IHK model is used to mimic the vital phenomena during soil liquefaction, in particular, the gradual pore-pressure build-up under cyclic loading conditions, within a water-saturated soil specimen. Next, more realistic scenarios are considered, thereby addressing the simulation of specific soil liquefaction phenomena, in particular, flow liquefaction within a loose and cyclic mobility in a dense sand. In this regard, the governing material parameters of the dense sand, which is used within the research unit FOR 1136 *GeoTech*[7] have been identified using the procedure described in Ehlers & Avci [61]. A brief summary of the identification process and the resulting solid-skeleton parameters are given in Appendix B.

[7]The founding of the subproject *Partially saturated soils under dynamic loading conditions* (Eh107/18) within the research unit FOR 1136 *Holistic simulations of geotechnical installation processes (GeoTech)* by the German Research Foundation (DFG) is gratefully acknowledged by the author.

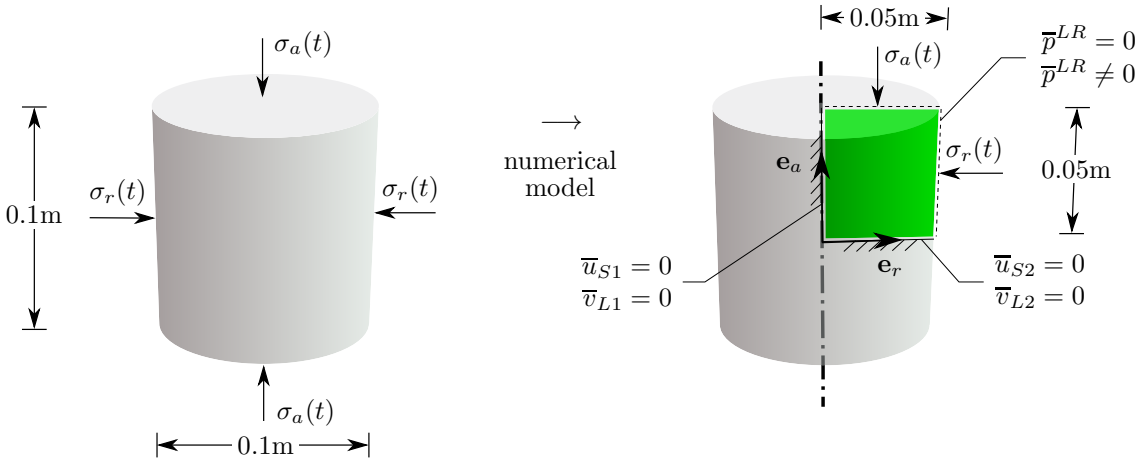

Figure 6.12: *Geometry and loading of the triaxial test (left) and the deduced IBVP (right).*

6.2.1 Element tests

The present section concerns element tests, thereby, on the one hand, contrasting the model responses of the IH and IKH model in comparison to the experimental results in case of a dry soil specimen, which will serve as a reference for the simulations. On the other hand, the IKH model will be used the describe soil liquefaction within a fluid-saturated specimen. The underlying referenced triaxial test and the deduced IBVP are depicted in Figure 6.12. In the numerical model, the axial symmetry of the problem is exploited, thereby simplifying the actual three-dimensional problem to a axial-symmetric two-dimensional FE model. The IBVP is composed of a single finite element, where the field variables, i. e. the solid displacement $\mathbf{u}_S$, pore-liquid velocity $\mathbf{v}_L$ and the pore-liquid pressure p^{LR}, are approximated through quadratic ($\mathbf{u}_S$) and linear shape functions ($\mathbf{v}_L$, p^{LR}), respectively. The solid displacements and fluid velocities normal to the symmetry lines are equal to zero, i. e. $\overline{u}_{S1} = \overline{u}_{S2} = \overline{v}_{L1} = \overline{v}_{L2} = 0$, whereas the free edges on the specimen surface are perfectly drained, i. e. $\overline{p}^{LR} = 0$, in case of the dry specimen but undrained, i. e. $\overline{p}^{LR} \neq 0$, in case of the fluid-saturated specimen. To be more precise in the latter, the undrained conditions only hold during the cyclic loading stage. The specimen is still perfectly drained at the free edges while the confining pressure is applied. The sample is subjected to cyclic loading conditions, through a prescription of the axial $\sigma_a(t)$ and the radial stresses $\sigma_r(t)$, which translate to the surface tractions $\overline{t}_a(t) = \sigma_a(t)$ and $\overline{t}_r(t) = \sigma_r(t)$ in the axial and radial direction, respectively, in the numerical model acting on the respective Neumann boundaries of the overall aggregate momentum balance. In the first step, the confining pressure, i. e. $\sigma_a(t) = \sigma_r(t) = 0.1\,\mathrm{MPa}$, is applied in the interval $t \in [\,0\,\mathrm{s}, 600\,\mathrm{s}\,]$. Subsequently, the radial stress is kept constant and the axial stress periodically increases and decreases with an amplitude of $\Delta\sigma_a = 0.05\,\mathrm{MPa}$, thereby utilising either a zigzag pattern in case of the dry specimen, see Figure 6.13, or an sinusoidal load, see Figure 6.14, via

$$\sigma_a(t) = \overline{\sigma}_0 \sin(\pi f t) \qquad \text{with} \qquad \overline{\sigma}_0 = -0.05\,\mathrm{MPa}\,,\ f = 1\,\mathrm{Hz}\,. \tag{6.3}$$

In any case, the simulations proceed from the dynamic liquid-saturated model, see Section 3.2.2, thereby, on the one hand, utilising the IH model, see (3.64) with the material

parameters of the FOR 1136 sand, see Appendix B. On the other hand, the mixed IKH model, see (3.63), with the parameters summarised in Appendix C is exploited. Note that the material constants of the IHK are not found through an identification procedure, instead they are adapted from the parameters of the IH model. Moreover, in case of the fluid-saturated specimen ,the realistic density and the specific weight of the pore water are $\rho^{LR} = 10^3\,\mathrm{kg/m^3}$ and $\gamma^{LR} = 10^4\,\mathrm{N/m^3}$, respectively. In order to allow for pore-pressure accumulation in the element test, the intrinsic permeability is $K_{0S}^S = 10^{-10}\,\mathrm{m^2}$, which corresponds to a soil with a low permeability. Note that, due to the simplicity of the underlying IBVP, the simulations are carried out sequentially on a single CPU core.

The evolution of the axial solid strain of the experiment and the computed responses of the IH and IKH model are depicted in Figure 6.15. At first, the elaboration of the experimental records is addressed. As illustrated by the evolution of the axial strain, the subsequent loading-unloading loops alter the granular configuration, thereby allowing for an axial settlement of the specimen. This finding is in agreement with the experimental

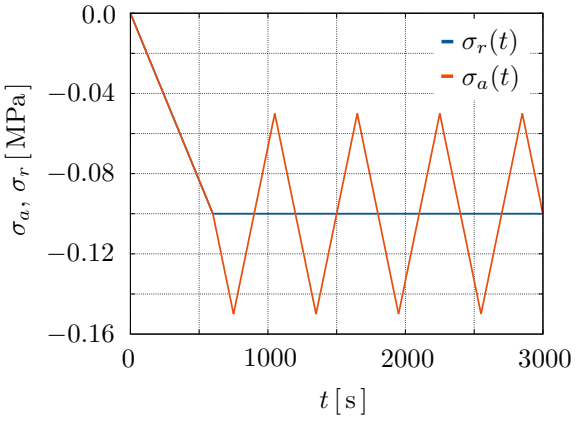

Figure 6.13: *Evolution of the axial $\sigma_a(t)$ and the radial stress $\sigma_r(t)$ applied on the dry soil specimen.*

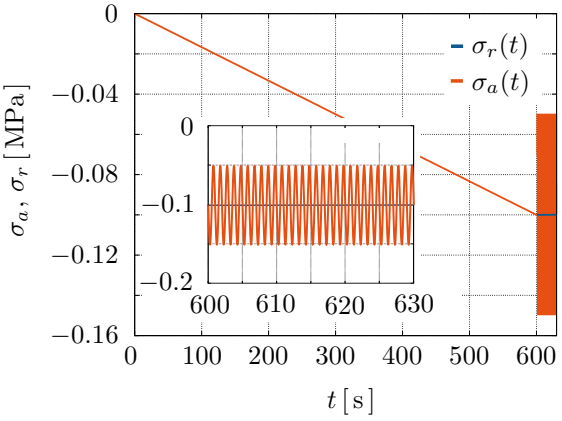

Figure 6.14: *Evolution of the axial $\sigma_a(t)$ and the radial stress $\sigma_r(t)$ applied on the fluid-saturated soil specimen.*

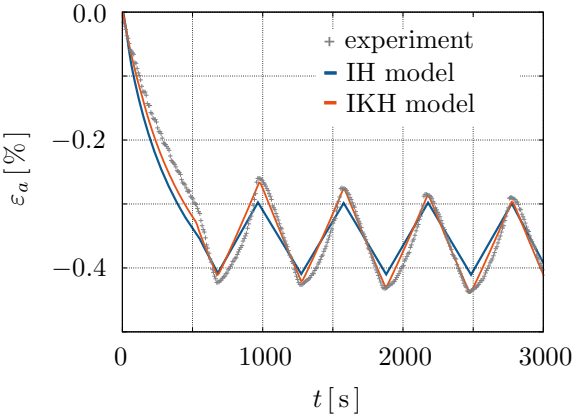

Figure 6.15: *Evolution of the total axial strain ε_a of the simulations and the experiments in case of the dry specimen.*

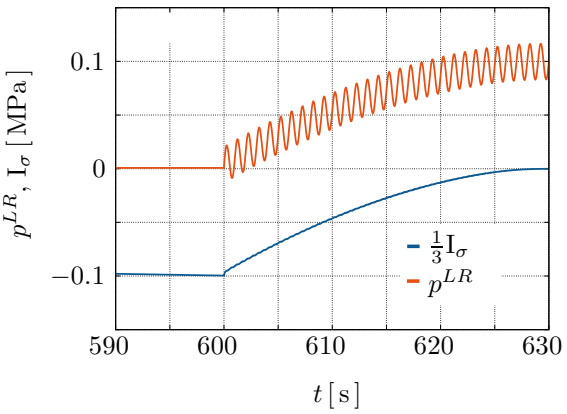

Figure 6.16: *Evolution of the of the pore pressure p^{LR} and the first stress invariant I_σ in case of the fluid-saturated specimen.*

observations of other authors, see, e. g., Wichtmann & Triantafyllidis [201] or Danne & Hettler [47]. Comparing the experimental observations with the model responses, it can be seen that only the IKH model is capable of predicting the axial settlement under the prescribed quasi-static loading conditions. The predictions of the IKH model are in very good agreement with the test result. However, it fails to mimic the curved shape of the zigzag pattern. In this regard, recall that the IHK model parameters are found through a manual procedure rather than an algorithmic tuning, for instance, via the prominent *Least-Squares* optimisation method, of the model parameters such that the error between simulation and experiment is minimised. Thus, it is impossible to judge whether the mismatch traces back to unsuitable constitutive relations or merely to an inappropriate set of material parameters, or a combination of both.

Next, the attention is drawn to the simulation results associated with the fluid-saturated specimen, see Figure 6.16. After the application of the confining pressure during perfectly drained conditions, the load is only carried by the solid skeleton, i. e. $p^{LR} = 0\,\mathrm{MPa}$ and $\mathrm{I}_\sigma = -0.1\,\mathrm{MPa}$. However, at the onset of the cyclic loading under the now undrained conditions, the pore-pressure accumulates due to the contractant tendency of the dry granular assembly. In consequence, the confining pressure is gradually transfered from the solid skeleton to the pore water finally leading to an entirely liquefied state at the end of the simulation, i. e. $p^{LR} = 0.1\,\mathrm{MPa}$ and $\mathrm{I}_\sigma = 0\,\mathrm{MPa}$.

6.2.2 Dynamic soil liquefaction

The next set of simulations is dedicated to the investigation of soils subjected to rapidly changing loading conditions. In particular, the simulation of flow liquefaction in a loose and cyclic mobility in a dense water-saturated sand are addressed.

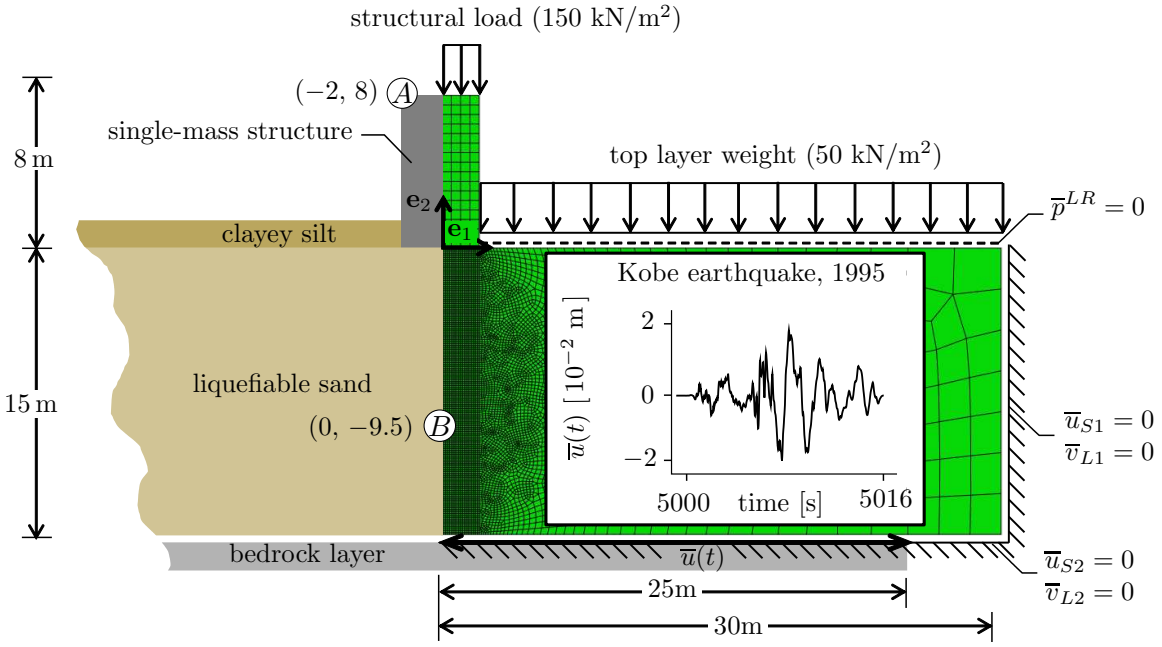

Figure 6.17: *Geometry (left) and deduced IBVP (right) of the liquefaction examples.*

The IBVP under consideration follows the idea of Heider *et al.* [98] and is inspired by the liquefaction-prone Wildlife Refuge area in the Imperial Valley in Southern California, where the layout of the domain of interest is as follows, see Figure 6.17 (left). From top to bottom, the soil layers are a clayey silt, a liquefiable sand and the bedrock layer. Based on that, a suitable numerical model is deduced, see Figure 6.17 (right), where the weight of the single-mass structure and the top layer are replaced by uniformly distributed loads of $150\,\mathrm{kN/m^2}$ and $50\,\mathrm{kN/m^2}$, respectively. Note that the replacement of the top layer by its corresponding load, avoids numerical difficulties as it ensures that the domain below is mostly under compression during the simulation. Below that is a layer of a liquefiable sand, which is described as an elasto-(visco)plastic material with isotropic hardening, see (3.64). The bedrock layer at the bottom of the domain under consideration is subjected to lateral displacements according to the records of the Kobe earthquake (Japan, 1995), which have been logged at the FUK station.

Note that the modelled semi-infinite halfspace has been truncated without the use of a particular far-field treatment, as, on the one hand, the prescribed bedrock-layer displacements mainly initiate shear waves and, on the other hand, the fluid-saturated soil exhibits significant damping properties with respect to compression waves, see Ehlers & Schenke [68]. Consequently, the size of the numerical problem, thereby the computational costs, have been reduced. Note that the finite-element mesh beneath the structure has been refined in order to account for the expected strain localisations. Moreover, tie constraints have been imposed at the interface between the structure and the foundation soil to ensure kinematic compatibility. The resulting numerical model consists of approximately 23 702 elements, which results by approximating the solid displacement $\mathbf{u}_S$ by quadratic, and the pore-liquid velocity and pressure, $\mathbf{v}_L$ and p^{LR}, through linear ansatz functions, in 107 822 degrees of freedom. In this connection, the simulations have been carried out in parallel exploiting a thread-based parallelisation method using 16 cores on the LEAD HPC compute cluster.

The loading history of the liquefaction problem can be split into two stages. At first, the structural and top layer weights are applied in an initialisation step, $t \in [\,0, 5000\,]\,\mathrm{s}$. Herein, the permeability is increased from $k^F = 10^{-5}$ m/s to $k^F = 10^{-3}$ m/s in order to speed up the consolidation process and to ensure a static equilibrium before proceeding with the second step, $t \in [\,5000, 5016\,]\,\mathrm{s}$, in which the displacement of the bedrock layer is prescribed according to the records of the Kobe earthquake.

	Parameter	Value	Unit
dense FOR 1136 sand (1)			
initial solid volume fraction	n^S_{0S}	0.61	-
plastic potential	ψ_1	1.3	-
plastic potential	ψ_2	0.53	-
loose sand (2)			
initial solid volume fraction	n^S_{0S}	0.4	-
plastic potential	ψ_1	0.4	-
plastic potential	ψ_2	0.1	-

Table 6.2: *Juxtaposition of the solid-skeleton material parameters of the dense FOR 1136 sand (set 1) to the adjusted parameters of the loose sand (set 2).*

The material parameters of the solid skeleton, i. e. the dense FOR 1136 sand, are given in Appendix B. Moreover, the realistic density and the specific weight of the pore water are $\rho^{LR} = 10^3\,\mathrm{kg/m^3}$ and $\gamma^{LR} = 10^4\,\mathrm{N/m^3}$, respectively. In order to trigger liquefaction phenomena with the available material parameters, following the approach of Heider [97], on the one hand, the prescribed solid displacements $\overline{u}(t)$ are scaled up by a factor of 15, and, on the other hand, selected material parameters of the dense FOR 1136 sand are adapted in order to mimic the typically behaviour of a loose sand, see Table 6.2. In particular, the initial solid volume fraction n^S_{0S} is decreased, which, in turn, increases the pore-liquid volume fraction and, therefore, allows for higher seepage velocities. Moreover, the adjustment of the plastic potential parameters, ψ_1 and ψ_2, alter the evolution of the volumetric solid strains under pure deviatoric loading, such that the granular assembly exhibits pure contractant properties for large deformations.

Flow liquefaction in a loose sand

The first example addresses the simulation of flow liquefaction in a loose, water-saturated sand. As elaborated before, the degradation of the soil strength can be traced back to a pore-pressure build-up due to the contractant tendency of the soil. In particular, the rise in pore pressure weakens the normal contact force between the soil grains, and, consequently, the intergranular frictional forces, which, in turn, results in a reduced load bearing capacity.

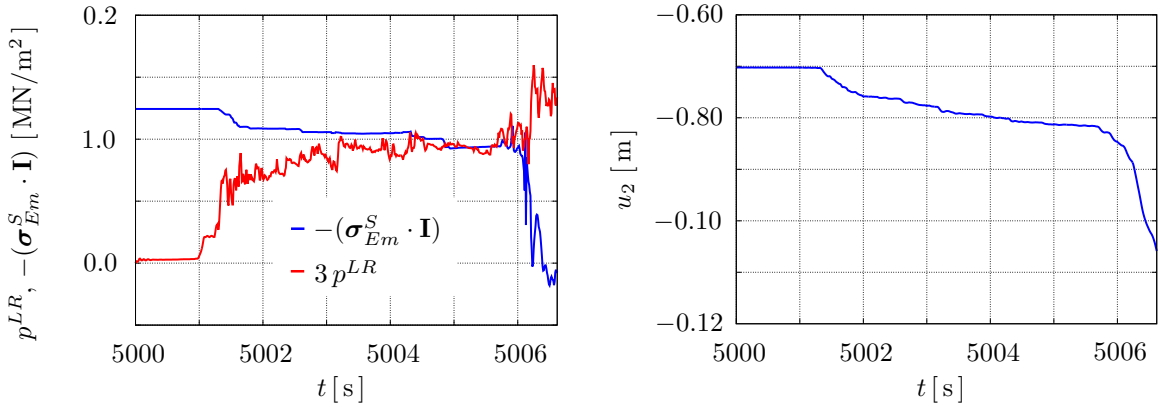

Figure 6.18: *Evolution of the pore pressure p and the effective volumetric solid stress $\boldsymbol{\sigma}^S_{Em} \cdot \mathbf{I}$ at point B (left) and the time history of the vertical displacement of point A (right) in the case of flow liquefaction.*

To make this interplay clearer, the evolution of the pore pressure p^{LR} (red line) and the effective volumetric solid stress $\boldsymbol{\sigma}^S_{Em} \cdot \mathbf{I}$ (blue line), which is associated with the intergranular normal contact forces, at point B are plotted in Figure 6.18 (left). With the onset of the cyclic motions, the contractant tendency of the loose soil gives rise to a pore-pressure build-up. In particular, after an initial surge, at about $t \approx 5001\,\mathrm{s}$, a steady rise can be observed, which, however, continues into a dramatic increase at approximately $t \approx 5006\,\mathrm{s}$. In consequence, the negative volumetric solid stress, which corresponds, according to the continuum-mechanical framework, to a decrease of the

intergranular normal forces[8], drops accordingly and, finally, vanishes. In consequence, the intergranular frictional forces vanish as well. As a result, the foundation soil liquefies and does not recover into a static equilibrium any more. This observation also illustrated in Figure 6.18 (right), where the vertical displacement of point A, which is located on top of the single-mass structure, is depicted. Therein, the collapse of the soil foundation is easily recognised by the rapidly increasing vertical displacement of the structure.

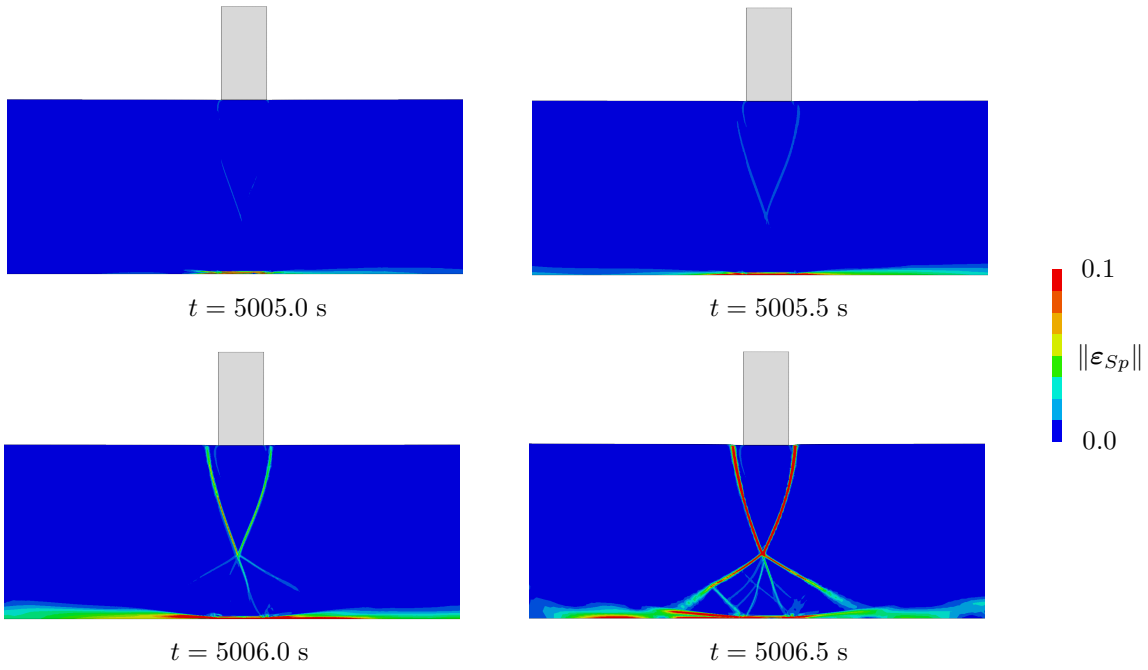

Figure 6.19: *Contour plots of the Euklidian norm of the accumulated plastic strain tensor* $\|\boldsymbol{\varepsilon}_{Sp}\|$ *on the deformed mesh (scale factor: 5) at different times illustrating flow liquefaction.*

A time sequence of contour plots of the Euklidian norm of the accumulated plastic strain tensor, i. e. $\|\boldsymbol{\varepsilon}_{Sp}\| = \sqrt{\boldsymbol{\varepsilon}_{Sp} \cdot \boldsymbol{\varepsilon}_{Sp}}$, on the deformed finite-element mesh is depicted in Figure 6.19. It clearly illustrates the failure of the loose foundation soil beneath the structure. This particular failure mode is known as punching shear failure, see Day [50]. The computation terminates at approximately $t \approx 5006.5\,\mathrm{s}$ due to extremely distorted finite elements located in the developing shear bands beneath the structure. Note that, herein, the formation of shear bands is hindered by the stiff bedrock layer.

Cyclic mobility in a dense sand

The second example is dedicated to the simulation of cyclic mobility. Herein, the liquefiable domain beneath the structure is described as a water-saturated dense sand, see also the parameters of the solid skeleton summarised in Appendix B. Similar to the case of flow liquefaction in a loose sand, the interplay between the pore pressure p^{LR} and the volumetric solid stress $\boldsymbol{\sigma}^{S}_{Em} \cdot \mathbf{I}$ is decisive, see Figure 6.20 (left).

[8]Note that the effective volumetric solid stress may take slight positive values, which is a non-physical property in the considered cohesionless sand. However, for the sake of a better convergence during the solution procedure, the parameters of the yield surface are chosen to allow for a slight amount of cohesion.

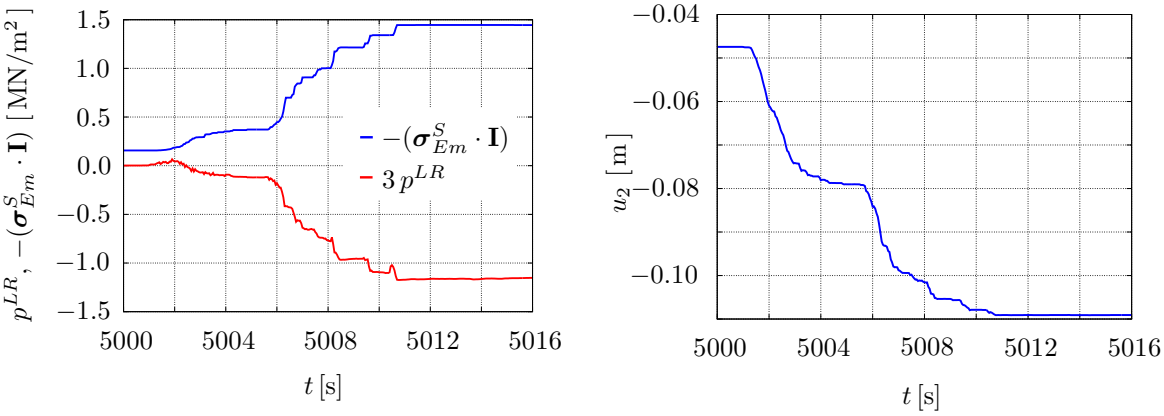

Figure 6.20: *Evolution of the pore pressure p^{LR} and the effective volumetric solid stress $\boldsymbol{\sigma}^S_{Em} \cdot \mathbf{I}$ at point B (left) and the time history of the vertical displacement of point A (right) in the case of cyclic mobility.*

In contrast to flow liquefaction, only a slight pore-pressure build-up is observed, as the contractant density of the dense granular assembly is only limited to very small strains, see the experimental results in Appendix B. Nevertheless, the small pore-pressure increase is sufficient to decrease the lead-bearing capacity of the foundation soil beneath the structure and, therefore, initiates the vertical settlement of the latter. With ongoing displacement, the dense soil changes its deformation behaviour from contractant to dilatant. Consequently, the developing underpressure increases the intergranular frictional forces, which initially slows down the vertical settlement and subsequently restablishes a

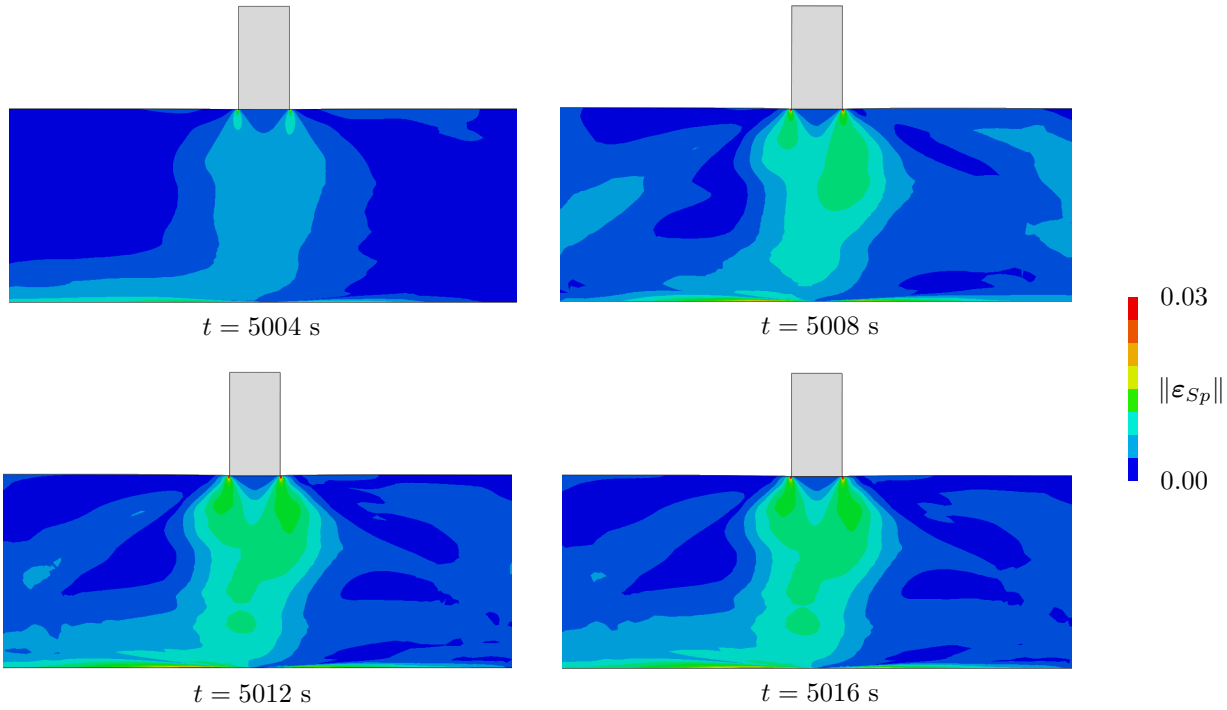

Figure 6.21: *Contour plots of the Euklidian norm of the accumulated plastic strain tensor $\|\boldsymbol{\varepsilon}_{Sp}\|$ on the deformed mesh (scale factor 5) at different times in the case of cyclic mobility.*

static equilibrium as illustrated by the evolution of the vertical displacement of point A in Figure 6.20 (right).

The sequence of contour plots showing the Euklidian norm of the accumulated plastic strains $\|\boldsymbol{\varepsilon}_{Sp}\|$ is depicted in Figure 6.21. It becomes apparent that, in contrast to flow liquefaction, only limited plastic deformation takes place. Thus, the overall stability of the soil foundation is maintained.

6.3 Vacuum-assisted resin transfer moulding

The following section concerns the simulation of the the resin impregnation of a dry fibre fabric through vacuum-assisted resin transfer moulding (VARTM), which is a step in the line of production when manufacturing structures made of fibre-reinforced plastics (FRP). In contrast to commonly used materials, such as metals or alloys, the compound material and structure are build at the same production step. In this regard, a reliable simulation of the line of actions helps, on the one hand, to predict the mechanical properties of the final part and, on the other hand, to reduce the manufacturing cost through, for instance, a minimisation of the production rejects. In the VARTM procedure, the dry (gas-saturated) fabric is placed in a single-pieced mould, sealed with vacuum-tight bag and the ambient air is evacuated from the setup. Subsequently, an open (exposed to the ambient pressure) resin reservoir is attached at the inlet from which the whole fabric is gradually impregnated with the resin.

The simulation of the infiltration process proceeds from the quasi-static triphasic model presented in Section 3.2.1, where the fibre network is assigned to the materially incompressible solid skeleton ($\alpha = S$), the resin is the materially incompressible pore liquid ($\alpha = L$), and the ambient air is described as a materially compressible pore gas ($\alpha = G$).

Choice of the primary variables

The underlying multiphasic modelling approach offers various possibilities to build the set of independent field variables. However, its collocation, on the one hand, is vital for the robustness and efficiency of the solution procedure, see, e. g., Wu & Forsyth [206] or Helmig [100], and, on the other hand, is constrained by the knowledge of the underlying initial and boundary conditions and, therefore, depends on the intended application scenario. Having the numerical simulation of the VARTM process in mind, it is convenient[9] to proceed from the solid displacement $\mathbf{u}_S$, and the pore-liquid saturation s^L and the pore-liquid pressure p^{LR} as the primary variables. This choice allows for a straightforward application of the initial and boundary conditions in the IBVP. In particular, the initial unsaturated state and the vacuum are prescribed through an initial pore-liquid saturation s_0^L and an initial pore-liquid pressure p_0^{LR}, respectively, whereas the injection prerequisites

[9] Proceeding from two pore pressures p^{LR} and p^{GR} as the governing field variables of the pore fluids, the prescription of the initial and boundary conditions, i. e. the initial saturation and the vacuum, is only possible in an implicit manner through the capillary-pressure-saturation relation $s^L = s^L(p^C)$, where $p^C = p^C(p^{LR}, p^{GR})$ is given as the pressure drop across the pore-liquid-pore-gas interface, see Section 3.1.3.

are applied via a rise of the pore-liquid saturation $\overline{s}^L$ and pore-liquid pressure $\overline{p}^{LR}$ both defined at the inlet on the domain boundaries.

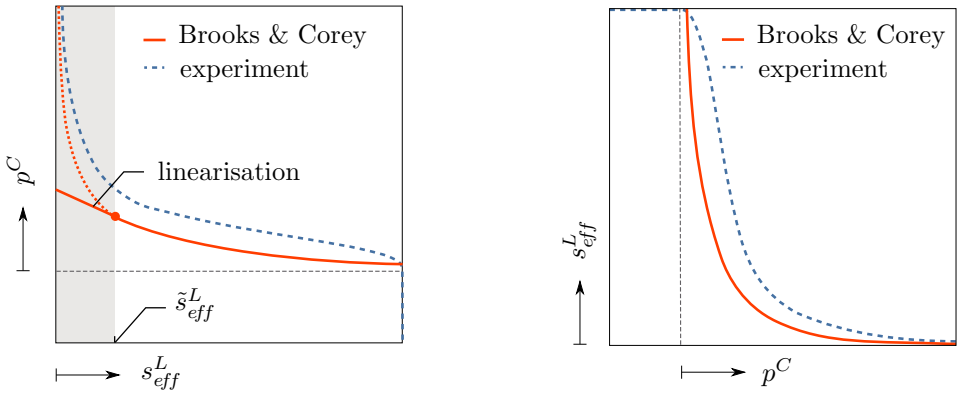

Figure 6.22: *Sketch of the capillary-pressure-saturation relations $s^L_{eff} = s^L_{eff}(p^C)$ (left) and $p^C = p^C(s^L_{eff})$ (right) and the linearisation of the latter.*

However, this choice leads to a unfavourable formulation from the numerical point of view. In particular, with the knowledge of the primary variable s^L, the capillary pressure p^C has to be evaluated from the capillary-pressure-saturation relation $p^C = p^C(s^L_{eff})$, see Figure 6.22 (left). Herein, as can be seen from the experimental result, the effective saturation s^L_{eff} tends to minus infinity for $s^L_{eff} \to 0$ and for $s^L_{eff} \to 1$, which is a numerical disadvantageous property. To cope with that, a linearisation of the capillary-pressure saturation relation is carried out, where, proceeding from the law of Brooks & Corey, a linearisation is only necessary for $s^L_{eff} \leq \tilde{s}^L_{eff}$. Herein, $\tilde{s}^L_{eff}$ denotes the linearisation threshold. In contrast, when proceeding from the pore pressures p^{LR} and p^{GR} as the primary variables, the relation $s^L_{eff} = s^L_{eff}(p^C)$ will be exploited, where for every capillary pressure p^C, the respective effective saturation s^L_{eff} can be computed, see Figure 6.22 (right).

Material parameters

Concerning the description of the multiphasic flow process, the description of the transition from the air-saturated to the resin-saturated state within the partially saturated zone and particularly the identification of the wetting and non-wetting pore fluids is vital for the shape of the flow front (sharp or diffuse). In this regard, Verrey *et al.* [193] performed infiltration experiments on non-crimp fabrics with different infiltrating liquids. They have experimentally shown that the decision whether the pore liquid or the pore gas is the wetting fluid is not only an *a priori* assumption depending on the material pairing, but is also strongly related to the arising flow conditions. These results are in agreement with the experimental observations of Coney & Masica [43], who recorded the evolution of the contact angle with a high-speed camera, and the microstructural simulations of Kunz *et al.* [119].

The flow conditions are characterised by the dimensionless capillary number Ca, where, with respect to the context of deformable porous materials, its initial definition, see, e. g.,

Saylor & Bounds [169], is adopted,

$$Ca = \frac{v_f\,\mu^{LR}}{\sigma^{LG}} \qquad \longrightarrow \qquad Ca = \frac{\mathbf{w}_L \cdot \mathbf{e}_f\,\mu^{LR}}{\sigma^{LG}}\,. \tag{6.4}$$

In the former, v_f denotes the propagation speed of the flow front, which is, with respect to the underlying multiphasic modelling framework, replaced by the contribution of the pore-liquid seepage velocity $\mathbf{w}_L$ in the propagation direction $\mathbf{e}_f$ of the flow front. Moreover, μ^{LR} is the dynamic viscosity of the resin and σ^{LG} is the surface tension in the resin at the resin-air (liquid-gas) interface under no-flow conditions.

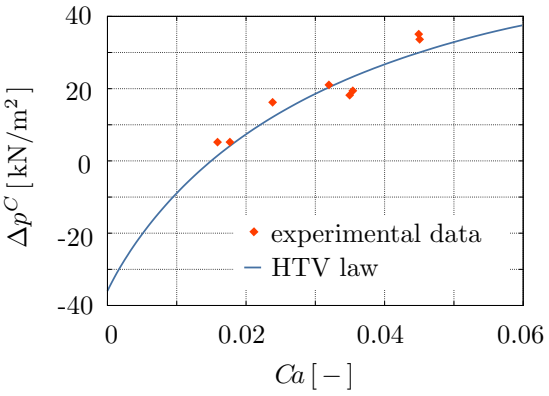

Figure 6.23: *Capillary-pressure drop Δp^C over the capillary number Ca for the experimental data and the parameter-optimised HTV relation according to Verrey et al. [193].*

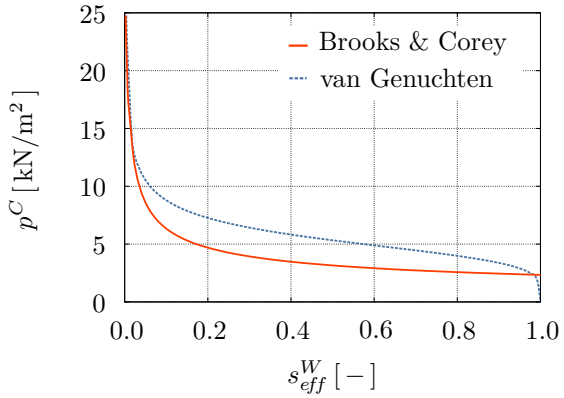

Figure 6.24: *Capillary pressure p^C over the effective saturation s^W_{eff} of the van Genuchten and the Brooks & Corey law based on the material parameters of Nordlund & Michaud [149].*

In the experiments of Verrey *et al.* [193], the injection pressure, which was applied on the epoxy resin[10], necessary to displace the ambient air within a glass-fibre fabric was measured. The results are summarised in Figure 6.23 (left). Therein, on the one hand, the dependency of the capillary-pressure drop Δp^C across the interface from resin to air over the capillary number Ca is illustrated. On the other hand, the parameter-optimised *Hoffmann-Tanner-Voinov* (HTV) relation, see, e. g., Kistler [113], is plotted. It can be seen that the capillary-pressure drop gradually increases from $\Delta p^C \approx -36\,\mathrm{kN/m^2}$ at $Ca = 0$ (no-flow condition) towards $\Delta p^C \approx 38\,\mathrm{kN/m^2}$ at $Ca = 0.06$. In particular, the former states that a spontaneous infiltration, also termed wicking, takes place, which indicates the epoxy to be the wetting fluid, whereas the latter defines the epoxy as the non-wetting fluid. In this regard, accounting for the infiltration conditions (temperature, injection pressure, resin and fibre-fabric material) described in Nordlund & Michaud [149], the capillary number is approximately 0.025. Consequently, the capillary-pressure drop is positive and the epoxy is defined to be the non-wetting liquid in the subsequent simulations. In extension, Nordlund & Michaud [149] also determined the parameters of the van Genuchten law, see van Genuchten [81], which, for the purpose of this monograph, have been adopted to the model of Brooks & Corey via the relation proposed by Lenhard *et al.* [127]. Moreover, further experiments have revealed that the dynamic viscosity of the resin μ^{LR} was approximately constant within the tested time range $t \in [\,0, 180\,]\,\mathrm{s}$.

[10] In particular, the Epikote 828 LV DGEBA epoxy from Shell has been used.

Parameter	Symbol	Value	Unit
initial volume fraction	n^S_{0S}	0.55	-
maximum volume fraction	$n^S_{\max}$	0.60	-
shear modulus	μ^S	$2 \cdot 10^6$	$\mathrm{N/m^2}$
bulk modulus 1	k^S_1	$4 \cdot 10^6$	$\mathrm{N/m^2}$
bulk modulus 2	k^S_2	$4 \cdot 10^6$	$\mathrm{N/m^2}$
effective solid density	ρ^{SR}	3000	$\mathrm{kg/m^3}$
effective liquid density	ρ^{LR}	1020	$\mathrm{kg/m^3}$
dynamic liquid viscosity	μ^{LR}	$7.5 \cdot 10^{-2}$	$\mathrm{N\,s/m^2}$
specific gas constant	R_{air}	287	$\mathrm{J/(mol\,K)}$
absolute temperature	θ	353	K
initial gas pressure	p^{GR}_0	10^5	$\mathrm{N/m^2}$
dynamic gas viscosity	μ^{GR}	$2 \cdot 10^{-5}$	$\mathrm{N\,s/m^2}$
residual liquid saturation	s^L_{res}	0.0	-
residual gas saturation	s^G_{res}	0.0	-
Brooks & Corey parameter 1	p^d	2342	$\mathrm{N/m^2}$
Brooks & Corey parameter 2	λ	2.318	-
initial intrinsic permeability	K^S_{0S}	$3.6 \cdot 10^{-10}$	$\mathrm{m^2}$
deformation dependent permeability	π	1.0	-

Table 6.3: Material parameters of the VARTM simulations for the solid (glass-fibre fabric), the pore liquid (epoxy) and the pore gas (ambient air).

Drawing the attention to the description of the solid skeleton, the mechanical behaviour of the entire textile is not only governed by properties of the individual yarns, but also strongly related by the fibre-to-fibre interaction, see Howell [105] or Kothari & Gangal [116]. Consequently, a suitable description of the frictional material textile is principally provided through the elasto-plastic framework discussed in Section 3.1.2. However, as the material parameters for the fabric are not available, the textile is treated as soft but purely elastic material in the subsequent simulations. Consequently, merely qualitative results regarding the fluid-fibre interactions are provided and discussed. The intrinsic permeability and the initial solid volume fraction, where the latter is a measurement of the fibre content per unit volume, are taken from Amico & Lekakou [5] and Nordlund & Michaud [149], respectively. The remaining material parameters, such as the specific gas constant and the ambient pressure, are taken from the physics text book by Gerthsen & Meschede [82]. The governing material parameters are summarised in Table 6.3.

Multiphasic flow process

The resin-infiltration process is driven by simultaneously active convective and diffusive processes, see Appendix D for their identifications, where generally one of both is dominating. In particular, a diffusion-dominated flow is characterised by a gentle rise in the pore-liquid saturation resulting in a wide partially saturated zone, whereas a convection-

driven flow is identified by a steep saturation gradient at the flow front and, therefore, by a narrow partially saturated domain. Consequently, in order to avoid spurious oscillations in the solution of the pore-liquid saturation, an adequate fine spatial discretisation is necessary in the latter.

In this connection, the so-called Péclet number Pe is introduced in the related literature, see, e. g., Helmig [100] or Graf [85], as an indicator whether the solution will exhibit instabilities, or in other words, the flow is diffusion- or convection-dominated. The Péclet number is defined as:

$$Pe = \frac{\|\mathbf{c}\|_2 \, l}{d} \qquad \begin{cases} 0 \leq Pe \leq 1 & \text{(diffusion-dominated flow)} \\ Pe > 1 & \text{(convection-dominated flow)} \end{cases} . \tag{6.5}$$

Therein, $\|\mathbf{c}\| = \sqrt{\mathbf{c} \cdot \mathbf{c}}$ denotes the Euklidian norm of the convection-velocity vector $\mathbf{c}$, d is the diffusion coefficient and l is the characteristic length[11]. Addressing the spurious oscillations in a convection-dominated flow, several methods have been proposed, see, e. g., Donea & Huerta [51], John & Knobloch [110] or Kuzmin [120] for an overview. They basically proceed from the idea to degrade the convective parts through an artificially applied diffusion. In this connection, the term spurious oscillations at layers diminishing (SOLD) methods has been proposed by John & Knobloch [110] in order to summarise these methods dealing with the steep gradients in convection-dominated convection-diffusion problems. However, note that for the purpose of this monograph, instead of applying a suitable stabilisation method, an adequate fine spatial discretisation ensures the stability of the solution process.

6.3.1 Laboratory-inspired element test

The present simulation targets a comprehensive survey of the quasi-static triphasic model subjected to a common infiltration scenario. The underlying simulation example illustrates the resin impregnation process of an initially gas-saturated glass-fibre fabric.

The governing IBVP is depicted in Figure 6.25. Therein, the initially dry glass-fibre fabric (length 1 m, width 0.6 m, thickness 0.01 m) is discretised by one element in the direction of $\mathbf{e}_2$ and $\mathbf{e}_3$, respectively, and via 1000 elements in the direction of $\mathbf{e}_1$, thereby providing necessary spatial resolution along the flow-front propagation direction in order to resolve the resulting steep saturation gradient. The independent field variables are approximated through quadratic ($\mathbf{u}_S$) and linear ansatz functions (s^L, p^{LR}), respectively, resulting in 22032 degrees of freedom. The rigid mould is modelled by constraining the solid displacements normal to the surface on all surfaces except of the top one, which is free to move. Note that, in the following, all pressures are given as an excess (positive) or as an under pressure (negative) relative to the ambient pressure.

[11] The choice of the characteristic length is related to the underlying numerical solution scheme. For instance, proceeding from the *finite-differences method* usually resulting in a structured grid, the characteristic length corresponds to the grid size in the different spatial dimensions. However, for unstructured meshes, as they usually appear in the FEM, the radius of a sphere with a volume equivalent to the volume of the finite element under consideration is commonly used instead, see, e. g., Kuzmin [120].

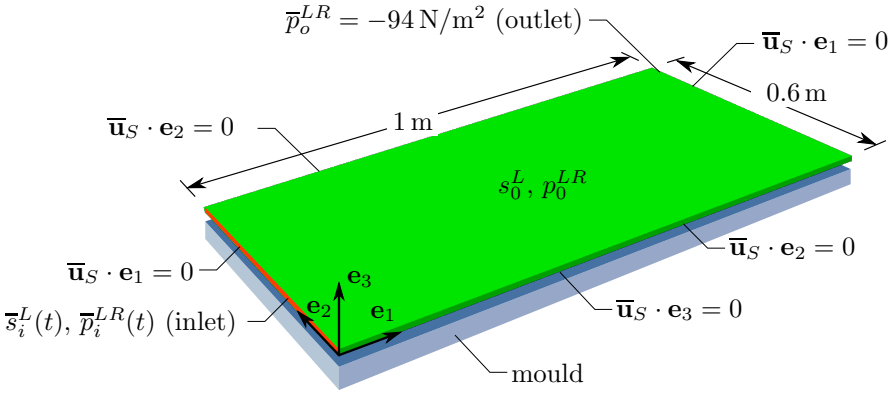

Figure 6.25: *IBVP of the laboratory-inspired impregnation simulation.*

Before the resin injection takes place, the pore gas is evacuated from the initially fully gas-saturated ($\overline{s}_0^L = 0$) fabric yielding an initial pore-liquid pressure of $p_0^{LR} = -94 \cdot 10^3\,\mathrm{N/m^2}$, which, consequently, compacts the textile. Herein, the intrinsic permeability is increased to $K^S = 10^{-6}\,\mathrm{m^2}$ in order to ensure an equilibrium state before the injection of the resin takes place. Subsequently, at $t = 0\,\mathrm{s}$, the resin reservoir, which is exposed to the ambient pressure, is attached to the inlet, i. e. $\overline{s}_i^L = 1.0$ and $\overline{p}_i^{LR} = 0\,\mathrm{N/m^2}$, whereas the liquid pressure at the outlet is constant and fixed to $\overline{p}_o^{LR} = -94\,\mathrm{N/m^2}$. In order to allow for a better convergence, both the liquid saturation and the pore-liquid pressure are not applied instantaneously. Instead, they are applied within the time interval $t \in [\,0, 5\,]\,\mathrm{s}$, see Figure 6.26 (left), and $t \in [\,5, 15\,]\,\mathrm{s}$, see Figure 6.26 (right). The threshold $\tilde{s}_{eff}^L$ for the linearisation of the capillary-pressure-saturation relation is set to $\tilde{s}_{eff}^L = 10^{-5}$.

The simulation has been carried out in parallel exploiting 4 MPI processes, where each process is split into two concurrent threads. Consequently, the simulation is executed on 8 cores. The resulting impregnation process is illustrated by a sequence of contour plots depicted in Figure 6.27. Therein, the upper row illustrates the movement of the resin flow front through the evolution of the liquid saturation s^L, which exhibits a steep saturation gradient within the partially saturated zone due to the convection-dominated flow process. The second row depicts the evolution of the spatial distribution of the pore-

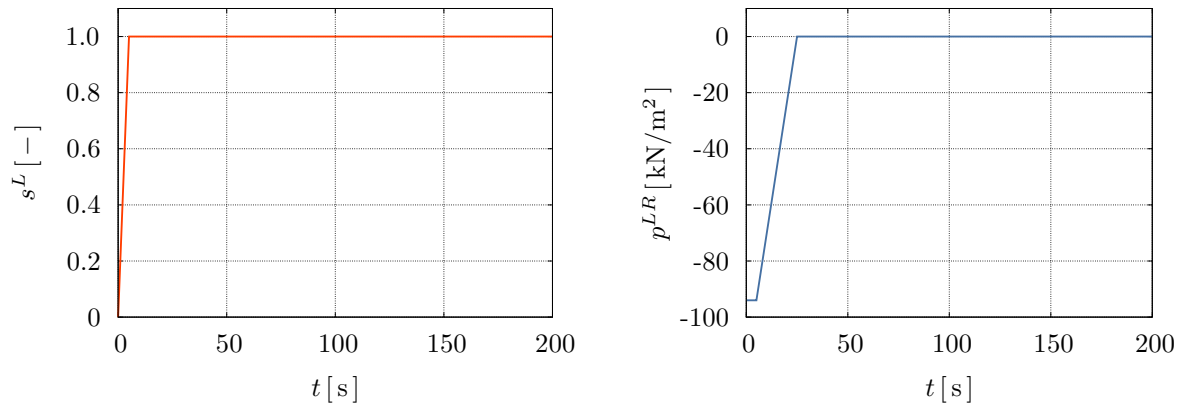

Figure 6.26: *Evolution of the prescribed pore-liquid saturation $\overline{s}_i^L(t)$ (left) and the prescribed pore-liquid pressure $\overline{p}_i^{LR}(t)$ (right) on the domain boundaries.*

fluid-mixture pressure p^{FR}. According to Dalton's law, p^{FR} is additively composed of the partial pressures of the pore-liquid and the pore gas, i. e. $p^{FR} = s^L p^{LR} + s^G p^{GR}$, and is, therefore, directly related to the evolution of the saturations and effective pressures of the respective pore fluids. In particular, as the resin moves, i. e. the liquid saturation s^L evolves, the spatial distribution of the effective liquid pressure p^{LR} and, therewith the pressure p^{FR} of the pore-fluid mixture develops accordingly, as p^{LR} is only spatially distributed for $s^L \neq 0$. As the flow front moves, the pressure gradient in the pore liquid between the inlet and the flow front depletes. In consequence, the convective part within the flow process is attenuated, which, in turn, on the one hand, pronounces the diffusive contribution resulting in a wider partially saturated zone and, on the other hand, slows down the propagation velocity of the flow front. Next, the investigation of the fluid-solid interaction is addressed. The increase of p^{FR} counteracts the initial compaction due to the applied vacuum, and decreases the solid volume fraction n^S, see Figure 6.27 (third row). In consequence, the fibre content per unit volume in the fully impregnated plate is degraded in comparison to the fibre volume content after applying the vacuum. The plate is fully saturated after approximately $t = 187\,\mathrm{s}$. Note that the simulation fails to converge when the flow front reaches the outlet. This fact can be traced back to the non matching values of the pore-liquid pressure prescribed at the outlet through $\overline{p}_o^{LR}$ and due to its evolution within the plate. Consequently, the Newton-Raphson procedure fails to converge once the flow front reaches the outlet. To allow for a complete saturation of the whole plate before the simulation fails to converge, the outlet is slightly shifted outside the domain of interest and the discrete domain is extended accordingly.

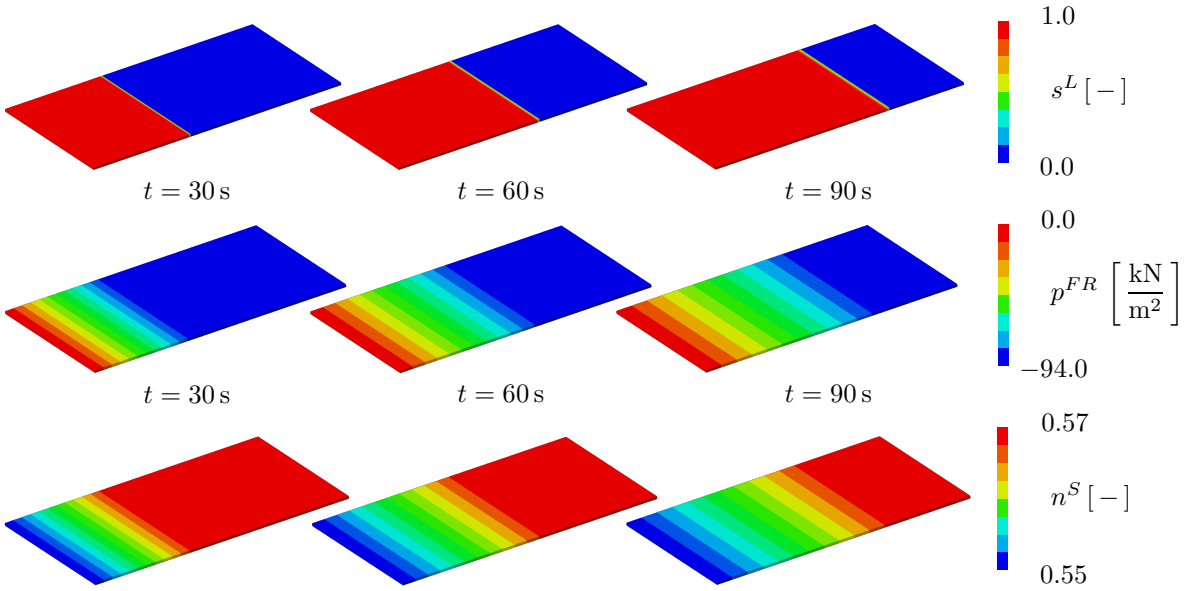

Figure 6.27: *Illustration of the evolution of the resin saturation s^L, the pressure p^{FR} of the pore-fluid mixture and the solid volume fraction n^S (from top to bottom).*

To elaborate the previous findings in more detail, Figure 6.28 depicts the spatial distribution along the plate of the pore-liquid saturation s^L (upper left), the pore-fluid-mixture pressure p^{FR} (upper right), the solid volume fraction n^S (lower left), and of the solid displacements u_{S1} and u_{S3} (lower right). All snapshots have been taken 30 s after the

resin has been injected. Therein, the steep gradient in s^L and the resulting nearly linear distribution of p^{FR} between the inlet and the flow front are clearly illustrated. To be more precise, as p^{FR} is given by the sum of the partial pressures of the respective pore fluids, i. e. $p^{FR} = s^L p^{LR} + s^G p^{GR}$, its spatial distribution near the flow front is nonlinear due to the steep rise of s^L, but continuous into a linear increasing distribution towards the inlet. As the flow front moves, the rise of p^{FR} gradually counteracts the initial compaction of the fibre fabric, which was found after applying the vacuum. This results in a decrease of the solid volume fraction and, therefore, in a reduction of the fibre content per unit volume of the overall fibre-resin compound. Furthermore, on the one hand, an increase of the thickness of the overall compound through the solid-displacement component u_{S3} in the direction $\mathbf{e}_3$ (along thickness) and, on the other hand, the drag of the fibres in the direction $\mathbf{e}_1$ (along the plate) via u_{S1} can be observed. In this connection, it is important to recall that the fabric is described as a purely elastic material and, therefore, does not allow for the evaluation of the remaining fabric distortions once the whole textile has been fully saturated.

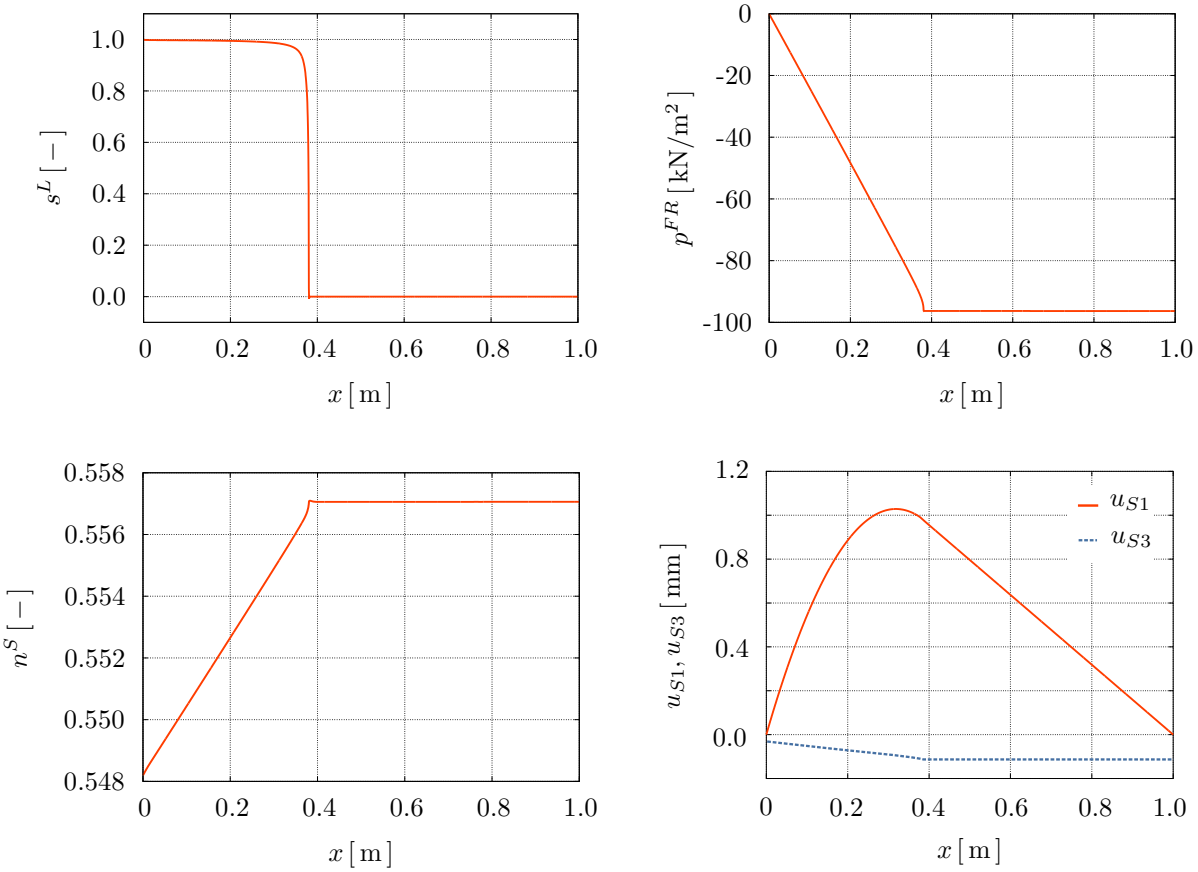

Figure 6.28: *Spatial distribution in the* $\mathbf{e}_1$*-direction along the plate at time* $t = 30\,\mathrm{s}$ *of the pore-liquid saturation* s^L *(upper left), of the pore-fluid mixture* p^{FR} *(upper right), of the solid volume fraction* n^S *(lower left), and of the solid displacements* u_{S1} *and* u_{S3} *(lower right) in the directions* $\mathbf{e}_2$ *and* $\mathbf{e}_3$*, respectively.*

6.3.2 Impregnation of a race-car seat

The present simulation addresses a more realistic simulation scenario as it may occur within an industrial application. Herein, the resin-impregnation process of a race-car seat is investigated numerically. Theses parts are commonly made of carbon-fibre reinforced plastic (CFRP). However, due to a lack of material parameters, the simulation proceeds from of a glass-fibre fabric instead. Consequently, the governing material parameters are the same as in the previous example, see Table 6.3. The underlying geometry, and boundary and initial conditions are depicted in Figure 6.29. As before, the dry glass-fibre fabric, which is assumed to exhibit homogeneous material properties[12] is placed in a rigid mould, which will be, in contrast to the previously example, modelled by constraining the solid displacements in all directions at the outer surface, i. e. $\mathbf{u}_S = \mathbf{0}$. Exploiting the symmetry of the configuration, only half of the problem will be considered in the simulation. In this connection, the overall IBVP will be cut at the symmetry plane, thereby introducing suitable boundary conditions, i. e. $\overline{u}_{S2} = 0$. Subsequently, one half of the geometry will be approximated by 111 418 brick elements, where the field variables are approximated by quadratic ($\mathbf{u}_S$) and linear ansatz functions (s^L, p^{LR}) resulting in a system composed of 2 801 841 degrees of freedom.

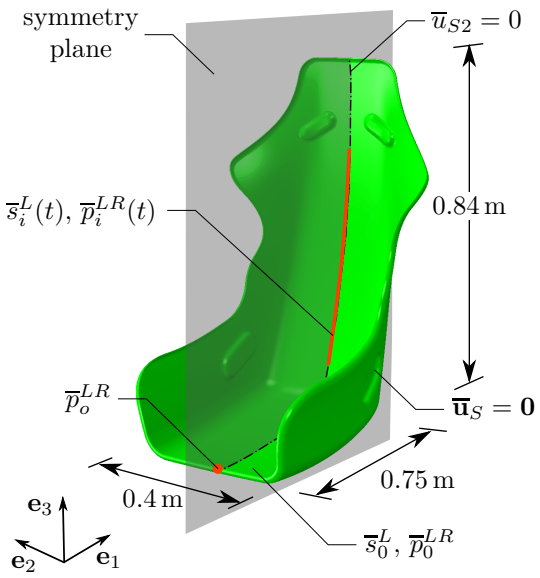

Figure 6.29: *Geometry and boundary conditions of the resin-imbibition simulation of the race-car seat.*

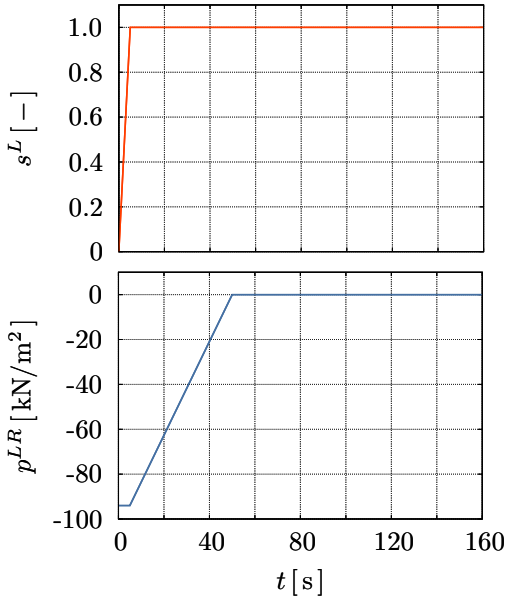

Figure 6.30: *Evolution (top) of the prescribed pore-liquid saturation $\overline{s}_i^L(t)$ and of the prescribed pore-liquid pressure $\overline{p}_i^{LR}(t)$ (bottom) on the domain boundaries.*

As before, the pore gas is evacuated from the initial gas-saturated ($\overline{s}_0^L = 0$) fabric in a preceding load step, thereby creating a underpressure of $p_0^{LR} = -94 \cdot 10^3\,\mathrm{N/m^2}$. Sub-

[12] Note that the compound is generally not homogeneous as the fibre direction and stacking sequence are governed by the load directions and distributions, yielding non-homogeneous material properties. Note that a simulation proceeding from non-homogeneously distributed permeabilities, thereby exploiting the Abaqus/PANDAS co-simulation approach, has been carried out by Schenke & Ehlers [173].

sequently, at $t = 0\,\mathrm{s}$, the resin reservoir, which is exposed to the ambient pressure, is attached to the inlet. In particular, in order to avoid strong oscillations in the solution, the pore-liquid saturation is increased within the interval $t \in [\,0, 5\,]\,\mathrm{s}$, see Figure 6.30 (top), whereas the injection pressure is applied within the interval $t \in [\,5, 50\,]\,\mathrm{s}$, see Figure 6.30 (bottom). The pore-liquid pressure at the outlet is fixed to $\overline{p}_o^{LR} = -94\,\mathrm{N/m^2}$. Note that, as elaborated in the previous example, the analysed domain is slightly extended at the outlet. To allow for a complete simulation of the impregnation process. In this example, the threshold $\tilde{s}_{eff}^{L}$ for the linearisation of the capillary-pressure saturation relation is set to $\tilde{s}_{eff}^{L} = 10^{-1}$.

The simulation is carried out on 160 cores of the HPC cluster of the SRC SimTech, where the computations have been distributed to four compute nodes. In particular, although it is from a parallel efficiency point of view favourable to proceed from a thread-based parallelisation on a computed node, see Section 5.3.3, the overall simulation is scattered into 40 MPI processes, where each process is further split into four concurrent threads. This load balancing is motivated by the fact that the underlying Abaqus analysis type, viz. `*Coupled temperature-displacement`, does not allow for a thread-based parallel evaluation of the the element-wise contributions. In particular, preliminary performance tests[13] have revealed that the present scattering gives best load balance for the underlying problem. The simulation was completed after approximately 109 hours.

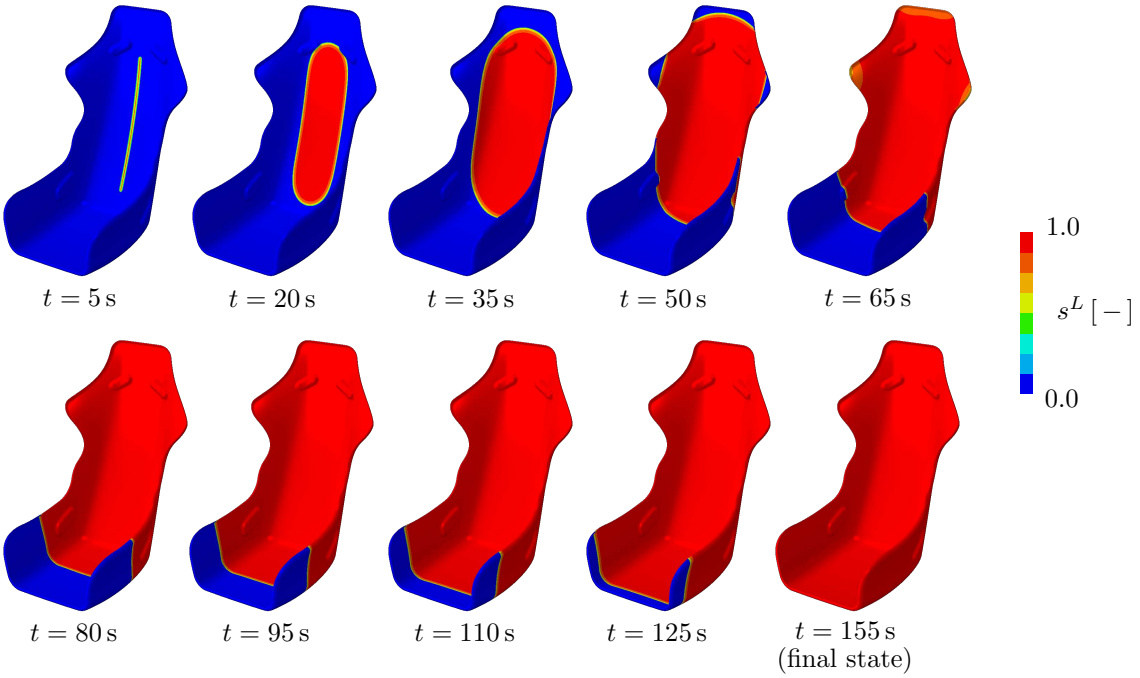

Figure 6.31: *Sequence of contour plots illustrating the evolution of the resin saturation* s^L.

A sequence of contour plots illustrating the evolution of the pore-liquid saturation is de-

[13] Herein, the time to compute a single time increment has been measured, from which, with the knowledge of the necessary number of *Newton* iterations, the time for the assembly and the solution of the overall system of equations is determined in a subsequent step. For the given problem the assembly and the solution took about $t = 160\,\mathrm{s}$ on the available hardware.

picted in Figure 6.31, where, the resin flow is illustrated through snapshots in constant time steps of $\Delta t = 15\,\mathrm{s}$ in the interval $t \in [\,5, 125\,]\,\mathrm{s}$ and the fully saturated state after approximately $t = 155\,\mathrm{s}$ is given. The sequence clearly illustrates the diminishing propagation velocity of the resin, which is, as elaborated in the previous example, attributed to the decreasing pressure gradient in the pore liquid.

Chapter 7:
Summary and future aspects

7.1 Summary

The present monograph concerned the simulation of volume-coupled multi-field problems, which arose from the macroscopic TPM as a suitable modelling framework. Herein, a parallel solution strategy based on an Abaqus-PANDAS co-simulation approach has been utilised to solve soil mechanical problems and multiphasic flow processes as showcases.

Addressing the simulation of materials with an irregular and complex microstructure, such as soils or fibre textiles, the TPM has been elected as the appropriate modelling framework. At first, a more general dynamic triphasic model composed of a solid skeleton, a pore liquid and a pore gas has been set up. The description of the solid scaffold follows an elasto-plastic approach, thereby incorporating either a pure isotropic or a mixed isotropic-kinematic hardening model. Subsequently, the general formulation has been condensed to yield simplified material models, which are, however, tailored to specific application scenarios. In particular, on the one hand, these are the dynamic biphasic models, where the pore space is either filled with a compressible pore-fluid mixture composed of pore gas and pore liquid (dynamic hybrid model), or merely by an incompressible pore liquid (dynamic liquid-saturated model). In the latter, the solid-skeleton description follows the elasto-plastic approach. On the other hand, a quasi-static triphasic model with a linear-elastic solid was deduced.

Next, the spatial and temporal discretisation and the respective solution schemes have been addressed. The spatial discretisation of the semi-infinite halfspace was carried out via finite elements (FE) (near-field approximation) and infinite elements (IE) (extension towards infinity), where, to attenuate the wave reflections at the FE-IE interface, an energy-absorbing layer has been introduced. In order to efficiently solve the given problem, the different implicit and explicit temporal discretisation schemes of Abaqus/Standard and Abaqus/Explicit were utilised. In particular, addressing the simulation of rapid processes explicit time-marching schemes are generally preferred, although small time increments are necessary due to their only conditional stability. In this regard, it was illustrated that the explicit procedure was merely applicable to the dynamic hybrid model, as the incompressibility of the pore liquid would lead in the case of the liquid-saturated model to an algebraic side constraint and, therefore, to a non-invertible matrix. Following the explicit method, the coupled system of PDE was decomposed following the block-Jacobian procedure into subsystems being of first and second order in time. The former subsystem was discretised using the explicit Euler method, whereas the latter utilised the central-difference scheme. Moreover, in order to achieve an efficient solution procedure with a good parallel-scalability, the row-sum matrix lumping procedure has been used.

The dynamic liquid-saturated model exploited the implicit Hilber-Hughes-Taylor (HHT) method of Abaqus/Standard. The quasi-static systems, i. e. the quasi-static triphasic

model and the elasto-plastic description of the solid scaffold, were advanced in time via the implicit Euler method.

Subsequently, the parallel solution strategy was addressed, where an Abaqus/PANDAS co-simulation approach was utilised. The coupling has been realised via the user-defined element (UEL) subroutine of Abaqus, where Abaqus provided the FE-based solution framework and PANDAS contributed the material response. The post-processing of the user-element results was realised via the overlay-element method. Herein, a standard element of Abaqus is connected in parallel to the user-defined element, thereby introducing, on the one hand, ansatz functions for the nodal interpolations and, on the other hand, a data container to hold the dependent variables, such as stresses, seepage velocities or internal-state variables, for the post-processing step. It was demonstrated that this post-processing method is suitable for thread- and MPI-based parallelisations, however, it suffers from a significant computational overhead, which, in the worst case, nearly doubles the necessary computation time. The bad performance was traced back to the computation of the overlay element. Consequently, when a comprehensive post processing of the simulation results is not necessary, the performance loss of the co-simulation approach decreases to approximately 20 %. Subsequently, the parallel scalability has been elaborated for thread- and MPI-based parallelisation methods. It turned out that the co-simulation procedure shows, in comparison to stand-alone Abaqus, a quite similar parallel speedup factor for a thread-based parallelisation, whereas in case of MPI the speedup rapidly degrades for a higher number of parallel processes.

In order to judge the efficiency of the implicit and explicit time-integration schemes in terms of problem runtime and parallel scalability, a dynamic benchmark problem has been computed via Abaqus/Standard and Abaqus/Explicit. It has been observed that the extensive but necessary inter-process communication significantly degrades the parallel speedup in Abaqus/Standard, whereas Abaqus/Explicit shows a good parallel efficiency. Moreover, a parametric study concerning the unbound-domain treatment has been carried out, where the wave-absorbing capabilities of the FE-IE layer was of particular interest. It was concluded that a negligence of the quasi-static contribution in the far-field formulation gives much better wave imbibing behaviour, whereas an adjustment of the damping coefficients shows only a slight impact. Addressing the simulation of soil mechanical problems, the responses of the isotropic and the mixed isotropic-kinematic hardening model have been compared to experimental data, which have been obtained from quasi-static cyclic triaxial tests applied to a dry specimen. It has been shown that the pure isotropic hardening model fails to mimic the gradual axial settlement of the granular assembly under slow cyclic loading conditions. In contrast, the mixed isotropic-kinematic hardening model was able to reproduce the experimental observations in quite a good agreement. Additionally, it was illustrated that the mixed isotropic-kinematic hardening model resembles the gradual pore-pressure accumulation in an undrained element test. Subsequently, the biphasic fluid-saturated soil model has been used to simulate soil failures induced by dynamic loading conditions. In particular, the capability of the dynamic liquid-saturated model to mimic the principle physical behaviour during flow liquefaction and cyclic mobility has been shown. Finally, the simulation of vacuum-assisted resin transfer moulding has been carried out. Herein, attention was especially paid to interaction between the

pore fluids, i. e. resin and ambient air, and their interplay with the soil skeleton, i. e. the fibre textile. It has been shown that the presented modelling approach adds significant advances to the field of the VARTM-process simulation by qualitatively reproducing the fibre displacements and, consequently, the reduction of the fibre content per unit volume of the overall fibre-resin compound due to the injection pressure. The impregnation simulation of a race-car seat reveals the applicability of the Abaqus/PANDAS co-simulation approach for modelling and solution within a productive environment.

7.2 Future aspects

The proposed Abaqus/PANDAS co-simulation approach has been successfully applied to the solution of ubiquitous volume-coupled multi-field problems, thereby exploiting Abaqus as the parallel-capable FE framework and PANDAS as the material-model library. Nevertheless, the present monograph motivates plenty of enhancement possibilities concerning, for instance, the underlying material models and the co-simulation approach.

Addressing the simulation of soils, or granular assemblies in general, which are subjected to cyclic loading conditions, it has been shown that the incorporation of the mixed isotropic-kinematic-hardening model in the solid-skeleton description qualitatively recovers the observed axial settlement during the quasi-static cyclic loading of the soil specimen. However, it was also illustrated that the proposed model does not reproduce the exact characteristics of the axial-strain evolution, i. e., the curvature in the zigzag pattern. To trace back the origin of the mismatch, further experimental investigations are necessary to optimise the governing material parameters, on the one hand, and to identify further physical processes, which might be essential for the mimicking of the experimental observations, on the other hand.

The proposed unbound-domain treatment already significantly suppresses the wave reflections at the transition from the near-field to the far-field formulation when simulating problems residing in an semi-infinite halfspace. However, a comparison between the presented procedure to the other methods proposed in the literature is still pending. In this regard, according to the author's opinion, the method of perfectly matching layers (PML) seems to be another promising ansatz.

Concerning the description of the vacuum-assisted resin transfer moulding, the proposed model can be improved by additionally accounting for the temperature-dependent and the curing-level-dependent resin viscosity. The former, i. e. the heat-transport problem, can to be considered by extending the set of governing PDE by the energy balances of the individual constituents or, if proven to be sufficient, the energy balance associated with the overall aggregate. The dependency of the curing-level in the resin viscosity can be accounted through an incorporation of a description of the reaction kinetics. The numerical efficiency of the underlying multiphasic flow model can be significantly enhanced, on the one hand, by implementing an analytical formulation rather than a numerical approximation of the Jacobian tangent and, on the other hand, through a suitable stabilisation strategy to smear the steep-saturation gradient at the flow front, thereby allowing for a coarser FE discretisation. In the author's opinion, promising approaches are provided by

the spurious oscillations at layers diminishing (SOLD) methods or the phase-field modelling procedure. Moreover, concerning in particular the simulation of the VARTM procedure, the constraint to thin-walled structures motivates the utilisation of shell elements rather than the exploited volume elements.

Although the proposed Abaqus/PANDAS co-simulation strategy represents a matured state in its current implementation, it still offers several enhancement possibilities, especially concerning the post-processing of the simulation results. In particular, in order to reduce the computational overhead in Abaqus/Standard and to enable a complete post-processing in Abaqus/Explicit at all, a good strategy was the alteration of the Abaqus results database not at the end of the analysis, but after each successful temporal increment. However, this procedure is currently not supported by Abaqus. Any attempt will lead to an abnormal termination of the simulation. However, due to the gradual progression of the Abaqus FEA package, this possibilities may arise with upcoming releases.

Appendix A:
Material time derivatives of the pore-fluid volume fractions

The evaluation of the material time derivatives of the pore-fluid volume fractions with respect to the solid skeleton of the constituent φ^α with $\alpha = \beta$, proceeds from the mass balance $(2.28)_2$:

$$\begin{aligned} 0 &= \underbrace{(n^\beta \rho^{\beta R})'_S + \operatorname{grad}\,(n^\beta \rho^{\beta R}) \cdot \mathbf{w}_\beta}_{(n^\beta \rho^{\beta R})'_\beta} + (n^\beta \rho^{\beta R}) \operatorname{div}\,\mathbf{v}_\beta = \\ &= (n^\beta)'_S\, \rho^{\beta R} + n^\beta (\rho^{\beta R})'_S + \operatorname{grad}\,(n^\beta \rho^{\beta R}) \cdot \mathbf{w}_\beta + (n^\beta \rho^{\beta R}) \operatorname{div}\,\mathbf{v}_\beta\,. \end{aligned} \tag{A.1}$$

Herein, the underbraced term denotes the material time derivative with respect to the pore fluid φ^β. Sticking to the general case of a materially compressible pore fluid, i. e. $(\rho^{\beta R})'_S \neq 0$, the solution of (A.1) for $(n^\beta)'_S$ gives

$$\begin{aligned} (n^\beta)'_S &= -\frac{1}{\rho^{\beta R}} [\underbrace{n^\beta (\rho^{\beta R})'_S + n^\beta \operatorname{grad}\,\rho^{\beta R}}_{= n^\beta (\rho^{\beta R})'_\beta} + \rho^{\beta R} \operatorname{grad}\, n^\beta \cdot \mathbf{w}_\beta + (n^\beta \rho^{\beta R}) \operatorname{div}\,\mathbf{v}_\beta] = \\ &= -\left[\frac{n^\beta}{\rho^{\beta R}} (\rho^{\beta R})'_\beta + \operatorname{grad}\, n^\beta \cdot \mathbf{w}_\beta + n^\beta \operatorname{div}\,\mathbf{v}_\beta \right]. \end{aligned} \tag{A.2}$$

Note that, herein, the product rule has been used. Finally, the material time derivatives of the pore-gas and pore-liquid volume fractions with respect to the solid motion, $(n^G)'_S$ and $(n^L)'_S$, can be given. In particular, after exploiting the material incompressibility of the latter, i. e. $(\rho^{LR})'_L = 0$, they read,

$$\begin{aligned} (n^G)'_S &= -\left[\frac{n^G}{\rho^{GR}} (\rho^{GR})'_G + \operatorname{grad}\, n^G \cdot \mathbf{w}_G + n^G \operatorname{div}\,\mathbf{v}_G \right], \\ (n^L)'_S &= -\left[\operatorname{grad}\, n^L \cdot \mathbf{w}_L + n^L \operatorname{div}\,\mathbf{v}_L \right]. \end{aligned} \tag{A.3}$$

Appendix B:
Material parameters of the IH model

Following the DIN 18196 of the German Institute for Standardisation, the underlying granular material, in particular, the sand[1] of the research unit FOR 1136 "GeoTech", can be classified as closely graded sand with an average grain diameter of $d_{50} = 0.55\,\mathrm{mm}$, see Figure B.1. The density of an individual soil grain, which corresponds to the realistic solid density of the overall aggregate, is $\rho^{SR} = 2\,650\,\mathrm{kg/m^2}$.

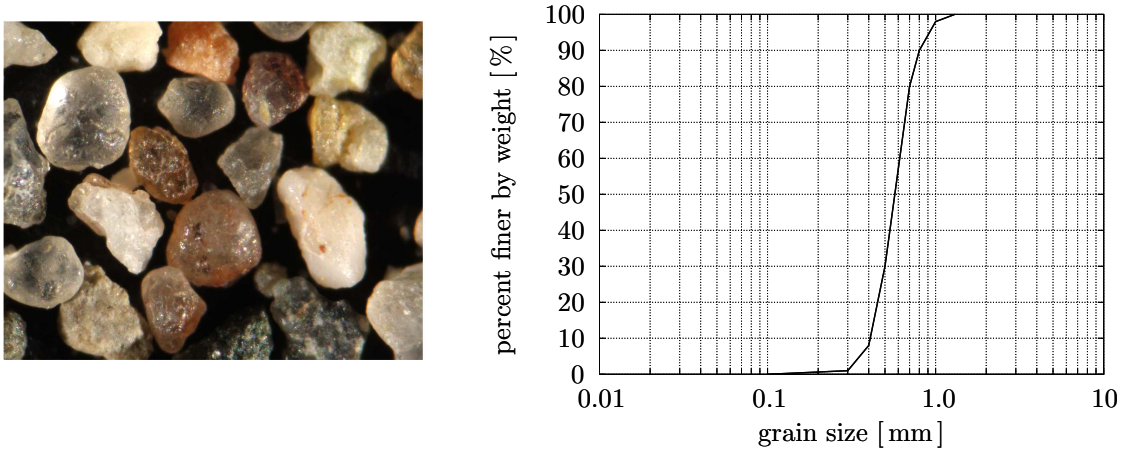

Figure B.1: *Microscopic picture of the soil grains (left) and grain size distribution (right) of the sand of the research unit FOR 1136.*

In order to identify the solid-skeleton material parameters associated with the FOR 1136 sand, the course of actions as described in Ehlers & Avci [61] is followed. Herein, initially several triaxial tests on cylindrical sand specimens (height: 0.1 m, diameter: 0.1 m) have been carried out, from which, subsequently, the material parameters are identified through a staggered identification scheme. In particular, at first, the elastic shear modulus μ^S is determined straightforward from triaxial loading-unloading loops and the compression-extension-ratio parameter $\overset{*}{\gamma}$ of the failure surface is found from compression and extension experiments at different confining pressures. Subsequently, several triaxial tests at different confining pressure, in particular, $\sigma_{c,1} = 0.1\,\mathrm{MPa}$, $\sigma_{c,2} = 0.2\,\mathrm{MPa}$ and $\sigma_{c,3} = 0.3\,\mathrm{MPa}$, have been carried out, where the axial σ_a and radial stresses σ_r, the axial strain ε_a, and the volumetric strain ε^V have been recorded. The material parameters are then found through a minimisation of the squared error between simulation and experiment, which is known as *Least-Squares* optimisation method. In particular, a gradient-based constrained optimisation is used, in which the Hessean matrix is approximated through the BGFS (Broyden, Fletcher, Goldfarb, Shannon) procedure, see, e. g., Spellucci [181],

[1]The sand samples have been provided by the Institute of soil and rock mechanics (Institut für Boden- und Felsmechanik, IBF) of the Karlsruher Institute of Technology (KIT).

Parameter	Symbol	Value	Unit
elastic parameters and solidity			
initial volume fraction	n^S_{0S}	0.6	-
maximum volume fraction	$n^S_{\max}$	0.623	-
shear modulus	μ^S	190	$\mathrm{MN/m^2}$
bulk modulus 1	k^S_1	20	$\mathrm{MN/m^2}$
bulk modulus 2	k^S_2	47	$\mathrm{MN/m^2}$
yield-surface parameters			
yield-surface parameter	α	0.01	$\mathrm{m^2/MN}$
yield-surface parameter	κ	0.0001	$\mathrm{m^2/MN}$
yield-surface parameter	m	$0.\overline{54}$	-
initial yield surface			
yield-surface parameter	δ_0	0.0009	$\mathrm{m^2/MN}$
yield-surface parameter	ϵ_0	0.1	$\mathrm{m^2/MN}$
yield-surface parameter	β_0	0.05	-
yield-surface parameter	γ_0	0.0	-
failure surface			
yield-surface parameter	$\overset{*}{\delta}$	0.09	$\mathrm{m^2/MN}$
yield-surface parameter	$\overset{*}{\epsilon}_0$	0.01	$\mathrm{m^2/MN}$
yield-surface parameter	$\overset{*}{\beta}$	0.255	-
yield-surface parameter	$\overset{*}{\gamma}$	1.75	-
failure-surface constant	$\overset{*}{C}_\epsilon$	0.4	$\mathrm{m^2/MN}$
iso. hard. evolution constants			
volumetric constant	C^V_δ	-93	$\mathrm{m^2/MN}$
volumetric constant	C^V_ϵ	-150	$\mathrm{m^2/MN}$
volumetric constant	C^V_β	-250	-
volumetric constant	C^V_γ	-0	-
deviatoric constant	C^D_δ	23	$\mathrm{m^2/MN}$
deviatoric constant	C^D_ϵ	200	$\mathrm{m^2/MN}$
deviatoric constant	C^D_β	180	-
deviatoric constant	C^D_γ	20	-
plastic potential			
parameter 1	ψ_1	1.3	-
parameter 2	ψ_2	0.53	-
viscoplasticity			
reference stress 1	σ_0	0.0001	$\mathrm{MN/m^2}$
relaxation time	η	0.001	s
viscoplastic exponent	r	0.001	s

Table B.1: Material parameters of the solid skeleton of the sand of the research unit FOR 1136.

and the parameter constraints are considered via the sequential-quadratic-programming (SQP) technique, see Spellucci [182].

The identified solid-skeleton material parameters of the research-unit sand FOR 1136 are summarised in the Table B.1. A comparison between the simulation and the experiments for the triaxial experiments at different confining pressures and for the isotropic compres-

sion test are depicted in Figure B.2. As can been seen, the model responses are in a quite good agreement with the experimental observations.

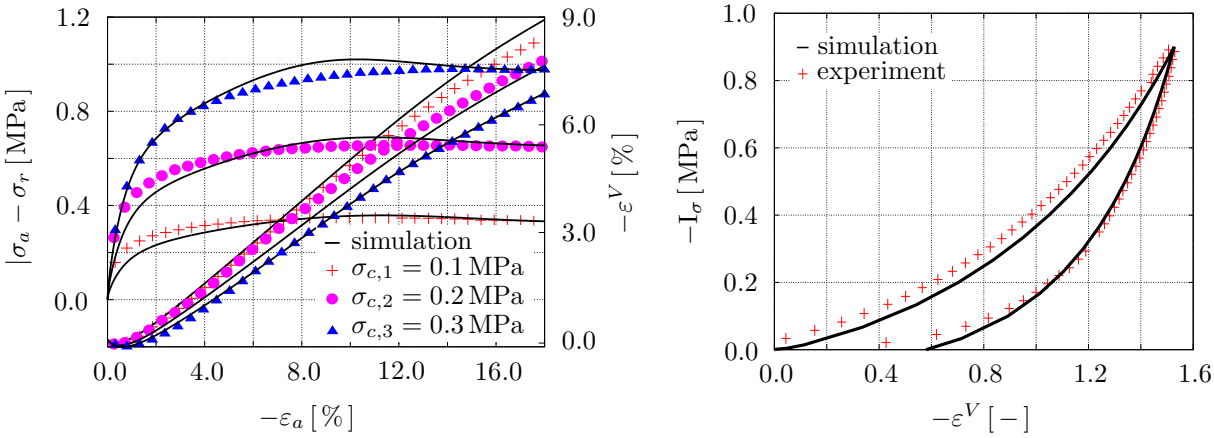

Figure B.2: *Comparison of the experimental data with the simulation results of the triaxial tests at different confining pressures (left) and of the isotropic loading-unloading loop (right).*

Appendix C:
Material parameters of the IKH model

Proceeding from the material constants of the pure isotropic hardening (IH) model, see Table B.1, the governing parameters of the mixed isotropic-kinematic hardening (IKH) model are guessed and the adjustments according to Table C.1 are made.

Parameter	Symbol	Value (IH)	→	Value (IKH)	Unit
elastic parameters					
shear modulus	μ^S	190		100	MN/m^2
bulk modulus 1	k_1^S	20		5	MN/m^2
bulk modulus 2	k_2^S	47		7	MN/m^2
yield-surface parameters					
yield-surface parameter	α	0.01		10^{-5}	m^2/MN
yield-surface parameter	κ	0.0001		10^{-6}	m^2/MN
initial yield surface					
yield-surface parameter	δ_0	0.5		10^{-5}	m^2/MN
yield-surface parameter	ϵ_0	0.01		0.1	m^2/MN
yield-surface parameter	β_0	0.003		0.05	-
failure surface					
yield-surface parameter	$\overset{*}{\delta}$	0.09		0.0005	m^2/MN
yield-surface parameter	$\overset{*}{\epsilon}_0$	0.01		10^{-6}	m^2/MN
yield-surface parameter	$\overset{*}{\beta}$	0.255		0.003	-
iso. hard. evolution constants					
volumetric constant	C_δ^V	-93		-2500	m^2/MN
volumetric constant	C_ϵ^V	-150		-2500	m^2/MN
volumetric constant	C_β^V	-250		-10	-
deviatoric constant	C_δ^D	23		-2500	m^2/MN
deviatoric constant	C_ϵ^D	200		-2500	m^2/MN
deviatoric constant	C_β^D	180		10	-
deviatoric constant	C_γ^D	20		10	-
kin. hard. evolution constants					
volumetric constant	C_0^V	-		0	m^2/MN
volumetric constant	C_1^V	-		0	m^2/MN
deviatoric constant	C_0^D	-		400	m^2/MN
deviatoric constant	C_1^D	-		50	m^2/MN
plastic potential					
parameter	ψ_1	1.3		0.001	-
parameter	ψ_2	0.53		1.0	-

Table C.1: Material-parameter adjustments of the solid skeleton for the mixed isotropic-kinematic hardening (IKH) model.

Appendix D:
Driving contributions in multiphasic flow processes

As described in Section 6.3, the multiphasic flow process within deformable porous media can be governed by the independent field variables solid displacement $\mathbf{u}_S$, pore-liquid saturation s^L and effective pore-liquid pressure p^{LR}. Within the partially saturated zone, the pore gas can be identified as the wetting fluid, i. e. $W = G$, and the pore liquid as the non-wetting fluid, i. e. $NW = L$, according to the findings of Verrey *et al.* [193] for the given material pairings.

In order to identify the convective and diffusive contributions in the underlying multiphasic flow problem, the mass balance of the pore gas needs to be expressed in terms of the independent field variables and recast to take the form

$$(s^L)'_S + \mathbf{c}^L \cdot \operatorname{grad} s^L - \operatorname{div}(\mathbf{D}^L \operatorname{grad} s^L) + f(\mathbf{u}_S, (\mathbf{u}_S)'_S, s^L, p^{LR}, (p^{LR})'_S) = 0\,. \tag{D.1}$$

Therein, $\mathbf{c}^L$ and $\mathbf{D}$ denote the convection velocity and the diffusion-coefficient tensor, respectively, of the pore liquid, and f is a scalar-valued function collecting the remaining contribution. Moreover, $\operatorname{grad}(\cdot) = \partial(\cdot)\partial x$ and $\operatorname{div}(\cdot) = \operatorname{grad}(\cdot) \cdot \mathbf{I}$ denote the gradient and the divergence operator, respectively, with $\mathbf{I}$ being the identity tensor.

To begin with, recall the mass balance of the pore gas, see $(3.83)_3$, viz.:

$$0 = (n^G \rho^{GR})'_S + n^G \rho^{GR} \operatorname{div}(\mathbf{u}_S)'_S + \operatorname{div}(n^G \rho^{GR} \mathbf{w}_G)\,. \tag{D.2}$$

Therein, $n^G \mathbf{w}_G$ denotes the filter velocity of the pore gas, which is given by, see $(3.69)_2$,

$$n^G \mathbf{w}_G = \underbrace{\kappa_r^G \left(-\frac{\mu^{GR}}{\gamma^{GR}} \mathbf{K}_{0S}^S\right)}_{:= \mathbf{A}} \Big[\operatorname{grad} p^{GR} - \rho^{GR} \mathbf{g}\Big]\,. \tag{D.3}$$

Herein, p^{GR} denotes the effective pressure of the pore gas. In what follows, p^{GR} will be replaced by an expression obtained from the definition of the capillary pressure, which is, within the current setting, given by the difference between the effective pressures of the non-wetting pore liquid and the wetting pore gas, p^{LR} and p^{GR}, i. e.

$$p^C = p^{LR} - p^{GR} \qquad \longrightarrow \qquad p^{GR} = p^{LR} - p^C\,. \tag{D.4}$$

Consequently, (3.77) can be exploited:

$$\rho^{GR} = \frac{p^{LR} - p^C}{R^G \theta} \qquad \longrightarrow \qquad \begin{aligned} \operatorname{grad} \rho^{GR} &= \frac{1}{R^G \theta}\Big[\operatorname{grad} p^{LR} - \operatorname{grad} p^C\Big]\,, \\ (\rho^{GR})'_S &= \frac{1}{R^G \theta}\Big[(p^{LR})'_S + (p^C)'_S\Big]\,. \end{aligned} \tag{D.5}$$

In a next step, by incorporating (D.4) into (D.3), the mass balance (D.2) is recast to read

$$(n^G\rho^{GR})'_S + n^G\rho^{GR}\,\mathrm{div}\,(\mathbf{u}_S)'_S + \mathrm{div}\,\Big[\rho^{GR}\kappa_r^G\mathbf{A}\,(\mathrm{grad}\,p^{LR} - \mathrm{grad}\,p^C - \rho^{GR}\,\mathbf{g})\Big] = 0\,, \tag{D.6}$$

which can be reformulated using the product rule[1] to yield

$$\begin{aligned}
&(n^F)'_S\,s^G\rho^{GR} + n^F(s^G)'_S\,\rho^{GR} + n^F s^G(\rho^{GR})'_S + \mathrm{div}\,\Big[\rho^{GR}\kappa_r^G\mathbf{A}\,(-\mathrm{grad}\,p^C)\Big] + \\
&\quad + \mathbf{A}\,(\mathrm{grad}\,p^{LR} - \rho^{GR}\mathbf{g})\cdot(\kappa_r^G\,\mathrm{grad}\,\rho^{GR} + \rho^{GR}\,\mathrm{grad}\,\kappa_r^G) - \\
&\quad - \rho^{GR}\kappa_r^G\Big[\,(\mathbf{A}\,\mathbf{g})\cdot\mathrm{grad}\,\rho^{GR} + \rho^{GR}\,\mathrm{div}\,(\mathbf{A}\,\mathbf{g})\Big] + \\
&\quad + \rho^{GR}\kappa_r^G\Big[\,\mathbf{A}\,\mathrm{grad}\,p^{LR}\Big] = 0\,.
\end{aligned} \tag{D.7}$$

Subsequently, the dependencies $p^C = p^C(s^G)$ and $\kappa_r^G = \kappa_r^G(s^G)$ are exploited, viz.

$$\mathrm{grad}\;p^C(s^G) = \underbrace{\frac{\partial p^C}{\partial s^G_{eff}}\frac{\partial s^G_{eff}}{\partial s^G}}_{=\,\dfrac{\partial p^C}{\partial s^G}}\mathrm{grad}\;s^G \qquad \text{and} \qquad \mathrm{grad}\;\kappa_r^G(s^G) = \underbrace{\frac{\partial \kappa_r^G}{\partial s^G_{eff}}\frac{\partial s^G_{eff}}{\partial s^G}}_{=\,\dfrac{\partial \kappa_R^G}{\partial s^G}}\mathrm{grad}\;s^G\,, \tag{D.8}$$

which are, together with the expressions $s^G = 1 - s^L$, $\mathrm{grad}\,s^G = -\mathrm{grad}\,s^L$ and $(s^G)'_S = -(s^L)'_S$ as a result of saturation condition $(2.1)_2$, viz. $s^L + s^G = 1$, as well as $(\mathrm{D}.5)_2$ and $(\mathrm{D}.5)_3$ are inserted into the mass balance (D.7) to obtain

$$\begin{aligned}
&-(n^F)'_S\,(1-s^L)\rho^{GR} + n^F(1 - \frac{1}{R^G\theta}\frac{\partial p^C}{\partial s^G})(s^L)'_S\,\rho^{GR} - n^F(1-s^L)(p^{LR})'_S - \\
&\quad - n^F(1-s^L)\rho^{GR}\,\mathrm{div}\,(\mathbf{u}_S)'_S - \mathrm{div}\,\Big[\,\overbrace{\rho^{GR}\kappa_r^G\frac{\partial p^C}{\partial s^G}\mathbf{A}}^{=\,\mathbf{D}^L}\,(\mathrm{grad}\,s^L)\Big] - \\
&\quad - \Big[\,\frac{\kappa_r^G}{R^G\theta}\mathbf{A}\,(\mathrm{grad}\,p^{LR} - \rho^{GR}\mathbf{g}) - \frac{\rho^{GR}\kappa_r^G}{R^G\theta}\mathbf{A}\mathbf{g}\Big]\cdot\mathrm{grad}\,p^{LR} + \\
&\quad - \rho^{GR}\kappa_r^G\,\mathrm{div}\,(\mathbf{A}\,\mathrm{grad}\,p^{LR}) + (\rho^{GR})^2\kappa_r^G\,\mathrm{div}\,(\mathbf{A}\mathbf{g}) + \\
&\quad + \Big[\,\underbrace{(\rho^{GR}\frac{\partial\kappa_r^G}{\partial s^G} - \frac{\kappa_r^G}{R^G\theta}\frac{\partial p^C}{\partial s^G})\mathbf{A}\,(\mathrm{grad}\,p^{LR} - \rho^{GR}\mathbf{g}) - \frac{\kappa_r^G\rho^{GR}}{R^G\theta}\frac{\partial p^C}{\partial s^G}\mathbf{A}\mathbf{g}}_{=\,\mathbf{c}^L}\Big]\cdot\mathrm{grad}\,s^L = 0\,.
\end{aligned} \tag{D.9}$$

With the reformulated mass balance at hand, the convection-velocity vector $\mathbf{c}^L$ and the

[1] In particular, the relations $\mathrm{div}\,(\phi\mathbf{v}) = \mathbf{v}\cdot\mathrm{grad}\,\phi + \phi\,\mathrm{div}\,\mathbf{v}$ and $\mathrm{grad}\,(\alpha\beta) = \beta\,\mathrm{grad}\,\alpha + \alpha\,\mathrm{grad}\,\beta$, see Ehlers [57], are utilised.

diffusion-coefficient tensor $\mathbf{D}^L$ can be identified:

$$\begin{aligned}
\mathbf{D}^L &= -\rho^{GR}\kappa_r^G \frac{\partial p^C}{\partial s^G}\frac{\mu^{GR}}{\gamma^{GR}}\,\mathbf{K}_{0S}^S\,,\\
\mathbf{c}^L &= -(\rho^{GR}\frac{\partial \kappa_r^G}{\partial s^G} - \frac{\kappa_r^G}{R^G\theta}\frac{\partial p^C}{\partial s^G})\,\frac{\mu^{GR}}{\gamma^{GR}}\mathbf{K}_{0S}^S\,(\operatorname{grad} p^{LR} - \rho^{GR}\mathbf{g}) + \frac{\kappa_r^G\rho^{GR}}{R^G\theta}\frac{\partial p^C}{\partial s^G}\frac{\mu^{GR}}{\gamma^{GR}}\,\mathbf{K}_{0S}^S\,\mathbf{g}\,,\\
&\text{where} \qquad \partial p^C/\partial s^G < 0 \qquad \text{and} \qquad \partial \kappa_r^G/\partial s^G > 0\,.
\end{aligned} \tag{D.10}$$

Note that, herein, the expression of the constant coefficient tensor $\mathbf{A}$, see (D.3), has been inserted. Following this, in agreement with Allen *et al.* [2], a dependency of the diffusion-coefficient tensor $\mathbf{D}^L$ on the slope in the capillary-pressure-saturation relation can be identified. Moreover, it can be observed the convection velocity $\mathbf{c}^L$ of the pore liquid is given by an expression similar to the filter velocity, see (D.3).

Bibliography

[1] Acartürk, A.: *Simulation of Charged Hydrated Porous Media*. Dissertation Thesis, Report No. II-18 of the Institute of Applied Mechanics (CE), University of Stuttgart 2009.

[2] Allen, M. B.; Behie, G. A. & Trangenstein, J. A.: *Multiphase flow in porous media: mechanics, mathematics, and numerics*. Springer-Verlag, New York, Berlin, Heidelberg 1988.

[3] Ambati, M.; Gerasimov, T. & de Lorenzis, L.: A review on phase-field models of brittle fracture and a new fast hybrid formulation. *Computational Mechanics* **55** (2014), 383–405.

[4] Amdahl, G. M.: Validity of the single processor approach to achieving large scale computing capabilities. In *AFIPS Conference Proceedings*. ACM, New-York 1967, pp. 483–485.

[5] Amico, S. & Lekakou, C.: An experimental study of the permeability and capillary pressure in resin-transfer moulding. *Composites Science and Technology* **61** (2001), 1945–1959.

[6] Ammann, M.: *Parallel finite element simulations of localization phenomena in porous media*. Dissertation Thesis, Report No. II-11 of the Institute of Applied Mechanics (CE), University of Stuttgart 2005.

[7] Aneiros, A. P.: *Some contributions in time-harmonic dissipative problems*. Dissertation thesis, University of Santiago de Compostela 2007.

[8] Armstrong, P. J. & Frederick, C. O.: *A Mathematical Representation of the Multiaxial Bauschinger Effect*. Report No. RD/B/N 731, Central Electricity Generating Board and Berkeley Nuclear Laboratories (CEGB) 1966.

[9] Arslan, U. M.: *Zur Frage des elastoplastischen Verformungsverhaltens von Sand*. Mitteilungen der Versuchsanstalt für Bodenmechanik und Grundbau 23, TH Darmstadt 1980.

[10] Avci, O.: *Coupled Deformation and Flow Processes of partially staurated soils: experiments, model validation and numerical Investigation*. Dissertation Thesis, Report No. II-26 of the Institute of Applied Mechanics (CE), University of Stuttgart 2013.

[11] Babuška, I. & Elman, H.: Some aspects of parallel implementation of the finite-element method on message passing architectures. *Journal of Computational and Applied Mathematics* **27** (1989), 157–187.

[12] Bastian, P.; Droske, M.; Engwer, C.; Klöfkorn, R.; Neubauer, T.; Ohlberger, M. & Rumpf, M.: Towards a unified framework for scientific computing. In Barth, T. J.; Griebel, M.; Keyes, D. E.; Nieminen, R. M.; Roose, D.; Schlick, T.; Kornhuber, R.; Hoppe, R.; Périaux, J.; Pironneau, O.; Widlund, O. & Xu, J. (eds.): *Domain Decomposition Methods in Science and Engineering*. Springer-Verlag, Berlin, Heidelberg 2005, Vol. 40 of Lecture Notes in Computational Science and Engineering, pp. 167–174.

[13] Basu, U.: Explicit finite element perfectly matched layers for transient three-dimensional elastic waves. *Computer Methods in Applied Mechanics and Engineering* **77** (2009), 151–176.

[14] Basu, U. & Chopra, A. K.: Perfectly matched layers for time-harmonic elastodynamics of unbounded domains: theory and finite-element implementation. *Computer Methods in Applied Mechanics and Engineering* **192** (2003), 1337–1375.

[15] Bathe, K. J.: *Finite-Elemente-Methoden*. Springer-Verlag, Berlin 1990.

[16] Bauschinger, J.: *Über die Veränderung der Elastizitätsgrenze und die Festigkeit des Eisens und Stahls durch Strecken und Quetschen, durch Erwärmen und Abkühlen und durch oftmals wiederholte Beanspruchungen*. Mitteilungen aus dem mechanisch-technischem Laboratorium 13, Königlich Bayerische Technische Hochschule München 1886.

[17] Bear, J.: *Hydraulics of groundwater*. McGraw-Hill, New York 1979.

[18] Biot, M. A.: Theory of propagation of elastic waves in a fluid-saturated porous solid. *Journal of the Acoustical Society of America* **28** (1956), 168–178.

[19] Black, S.: Inside analysis: Simulating VARTM for better infusion. *High-performance composites* **1** (2008), URL `http://www.compositesworld.com/articles/`, accessed October 2016.

[20] Bluhm, J.; Bloßfeld, W. M. & Ricken, T.: Energetic effects during phase transition under freezing-thawing load in porous media – a continuum multiphase description and fe-simulation. *Journal of Applied Mathematics and Mechanics* **94** (2014), 586–608.

[21] de Boer, R.: *Theory of Porous Media.* Springer-Verlag, Berlin 2000.

[22] de Boer, R. & Brauns, W.: Kinematic hardening of granular materials. *Ingenieur-Archiv* **60** (1990), 463–480.

[23] de Boer, R. & Ehlers, W.: *Theorie der Mehrkomponentenkontinua mit Anwendung auf bodenmechanische Probleme*. Forschungsberichte aus dem Fachbereich Bauwesen, Heft 40, Universität-GH-Essen 1986.

[24] Bowen, R. M.: Theory of mixtures. In Eringen, A. C. (ed.): *Continuum Physics*. Academic Press, New York 1976, Vol. III, pp. 1–127.

[25] Bowen, R. M.: Incompressible porous media models by use of the theory of mixtures. *International Journal of Engineering Science* **18** (1980), 1129–1148.

[26] Bowen, R. M.: Compressible porous media models by use of the theory of mixtures. *International Journal of Engineering Science* **20** (1982), 697–735.

[27] Boyd, S. P. & Vandenberghe, L.: *Convex Optimization*. Cambridge University Press, Cambridge 2004.

[28] Braess, D.: *Finite Elements: Theory, Fast Solvers, and Applications in Solid Mechanics*. Cambridge University Press, Cambridge 2007, 3rd edn.

[29] Brawer, S.: *Introduction to Parallel Programming*. Academic Press Inc., London 2014.

[30] Brezzi, F. & Fortin, M.: *Mixed and Hybrid Finite Element Methods*. Springer-Verlag, New York 1991.

[31] Brooks, R. & Corey, A. T.: Hydraulic properties of porous media. In *Hydrology Papers*. Colorado State University 1964.

[32] Bruschke, M. V. & Advani, S. G.: A finite element/control volume approach to mold filling in anisotropic porous media. *Polymer Composites* **11** (1990), 398–405.

[33] Butenhof, D.: *Programming with POSIX threads*. Addison-Wesley, Reading 1997.

[34] Buttlar, D.; Farrell, J. & Nichols, B.: *Pthreads Programming: A POSIX Standard for Better Multiprocessing (A Nutshell handbook)*. O'Reilly Media, Sebastopol 1996.

[35] Casagrande, D. R.: Characteristics of cohesionless soils affecting the stability of slopes and earth fills. *Journal of the Boston Society of Civil Engineers* **23** (1936), 13–32.

[36] Castro, G.: On the behavior of soils during earthquakes, liquefaction. In Cakmak, A. S. (ed.): *Soil Dynamics and Liquefaction*. Elsevier, New York 1987, pp. 229–250.

[37] Castro, G. & Poulos, S. J.: Factors affecting liquefaction and cyclic mobility. *ASCE: Journal of the Geotechnical Engineering Division* **103** (1977), 501–506.

[38] Chaboche, J. L.: Constitutive equations for cyclic plasticity and cyclic viscoplasticity. *International Journal of Plasticity* **5** (1989), 247–302.

[39] Chaboche, J. L.: On some modifications of kinematic hardening to improve the description of ratcheting effects. *International Journal of Plasticity* **7** (1991), 661–678.

[40] Chandra, R.; Menon, R.; Dagum, L.; Kohr, D.; Maydan, D. & McDonald, J.: *Parallel programming in OpenMP*. Morgan Kaufmann Publishers, San Francisco 2001.

[41] Chapman, B.; Jost, G. & van der Pas, R.: *Using OpenMP: Portable shared memory parallel programming*. The MIT Press, Cambridge 2007.

[42] Coleman, B. D. & Noll, W.: The thermodynamics of elastic materials with heat conduction and viscosity. *Archive for Rational Mechanics and Analysis* **13** (1963), 167–178.

[43] Coney, T. A. & Masica, W. J.: *Effect of flow rate on the dynamic contact angle for wetting liquids*. Report No. NASA TN D-5115, Lewis Research Center 1969.

[44] Cook, R. D.: *Concepts and applications of finite element analysis*. John Wiley & Sons, New York 2002, 4th edn.

[45] Courant, R.; Friedrichs, K. O. & Lewy, H.: Über die partiellen Differenzengleichungen der mathematischen Physik. *Mathematische Annalen* **100** (1928), 32–74.

[46] Cybenko, G.: Dynamic load balancing for distributed memory multiprocessors. *Journal of parallel and distributed computing* **7** (1989), 279–301.

[47] Danne, S. & Hettler, A.: Experimental strain response envelopes of granular materials for monotonous and low-cycle loading processes. In Triantafyllidis, T. (ed.): *Holistic simulation of geotechnical installation processes: Numerical and physical modelling*. Springer International Publishing, Switzerland 2015, pp. 229–250.

[48] Darcy, H.: *Les Fontaines Publiques de la Ville de Dijon*. Dalmont, Paris 1856.

[49] Dassault Systèmes: Abaqus 6.14 online documentation (2014), URL `http://caedoc.hlrs.de/abaqus/Documentation/docs/v6.14`.

[50] Day, R. W.: *Geotechnical Earthquake Engineering Handbook*. McGraw-Hill, New-York 2002.

[51] Donea, J. & Huerta, A.: *Finite element methods for flow problems*. John Wiley & Sons, Weinheim 2003.

[52] Drucker, D. C. & Prager, W.: Soil mechanics and plastic analysis for limit design. *Quarterly of Applied Mathematics* **10** (1952), 157–165.

[53] Ehlers, W.: On the thermodynamics of elasto-plastic porous media. *Archive of Mechanics* **41** (1989), 73–93.

[54] Ehlers, W.: *Poröse Medien – ein kontinuumsmechanisches Modell auf der Basis der Mischungstheorie*. Habilitation Thesis, Forschungsberichte aus dem Fachbereich Bauwesen, Heft 47, Universität-GH-Essen 1989.

[55] Ehlers, W.: Constitutive equations for granular materials in geomechanical context. In Hutter, K. (ed.): *Continuum Mechanics in Environmental Sciences and Geophysics*. Springer Vienna 1993, vol. 337 of *International Centre for Mechanical Sciences*, pp. 313–402.

[56] Ehlers, W.: A single-surface yield function. *Archive of Applied Mechanics* **65** (1995), 246–259.

[57] Ehlers, W.: *Vector and Tensor Calculus: An Introduction*. Lecture notes, Institute of Applied Mechanics (Chair of Continuum Mechanics), University of Stuttgart 1995–2009, URL `http://www.mechbau.uni-stuttgart.de/ls2`.

[58] Ehlers, W.: Grundlegende Konzepte in der Theorie Poröser Medien. *Technische Mechanik* **16** (1996), 63–76.

[59] Ehlers, W.: Foundations of multiphasic and porous materials. In Ehlers, W. & Bluhm, J. (eds.): *Porous Media: Theory, Experiments and Numerical Applications*. Springer-Verlag, Berlin 2002, pp. 3–86.

[60] Ehlers, W.: Challanges of porous media models in geo- and biomechanical engineering including electro-chemically active polymers and gels. *International Journal of Advances in Engineering Sciences and Applied Mathematics* **1** (2009), 1–24.

[61] Ehlers, W. & Avci, O.: Stress-dependent hardening and failure surfaces of dry sand. *International Journal for Numerical and Analytical Methods in Geomechanics* **37** (2013), 787–809.

[62] Ehlers, W.; Avci, O. & Markert, B.: Computation of slope movements initiated by rain-induced shear bands in small-scale tests and in situ. *Vadose Zone Journal* **10** (2011), 512–525.

[63] Ehlers, W. & Ellsiepen, P.: PANDAS: Ein FE-System zur Simulation von Sonderproblemen der Bodenmechanik. In Wriggers, P.; Meiner, U.; Stein, E. & Wunderlich, W. (eds.): *Finite Elemente in der Baupraxis FEM 1998*. Ernst & Sohn, Berlin 1998, pp. 391–400.

[64] Ehlers, W.; Ellsiepen, P.; Blome, P.; Mahnkopf, D. & Markert, B.: *Theoretische und numerische Studien zur Lösung von Rand- und Anfangswertproblemen in der Theorie Poröser Medien, Abschlußbericht zum DFG-Forschungsvorhaben Eh 107/6-2*. Report No. 99-II-1 of the Institute of Applied Mechanics (CE), University of Stuttgart 1999.

[65] Ehlers, W.; Graf, T. & Ammann, M.: Deformation and localization analysis of partially saturated soil. *Computer Methods in Applied Mechanics and Engineering* **193** (2004), 2885–2910.

[66] Ehlers, W.; Karajan, N. & Wieners, C.: Parallel 3-d simulation of a biphasic porous media model in spine mechanics. In Ehlers, W. & Karajan, N. (eds.): *Proceedings of the 2nd GAMM Seminar on Continuum Biomechanics*. Report No. II-16 of the Institute of Applied Mechanics (CE), University of Stuttgart 2007, pp. 11–20.

[67] Ehlers, W. & Schenke, M.: Simulation of soils under rapid cyclic loading conditions. In Triantafyllidis, T. (ed.): *Holistic Simulation of Geotechnical Installation*

Processes: Numerical and Physical Modelling. Springer International Publishing, Switzerland 2015, pp. 207–228.

[68] Ehlers, W. & Schenke, M.: Towards the holisitic simulation of geotechnical installation processes using vibro-injection piles. In Triantafyllidis, T. (ed.): *Holistic Simulation of Geotechnical Installation Processes: Benchmarks and Simulations*. Springer International Publishing, Switzerland 2016, pp. 163–185.

[69] Ehlers, W. & Scholz, B.: An inverse algorithm for the identification and the sensitivity analysis of the parameters governing micropolar elasto-plastic granular material. *Archive of Applied Mechanics* **77** (2007), 911–931.

[70] Ellsiepen, P.: *Zeit- und ortsadaptive Verfahren angewandt auf Mehrphasenprobleme pröser Medien*. Dissertation Thesis, Report No. II-3 of the Institute of Applied Mechanics (CE), University of Stuttgart 1999.

[71] von Estorff, O. & Firuziaan, M.: Coupled BEM/FEM approach for nonlinear soil/structure interaction. *Engineering Analysis with Boundary Elements* **24** (2000), 715–725.

[72] Evans, G.; Blackledge, J. & Yardley, P.: *Numerical Methods for Partial Differential Equations*. Springer Undergraduate Mathematics Series, Springer-Verlag London 2000.

[73] Ferrari, A.; Laloui, L. & Bonnard, C.: Geomechanical modelling of a natural slope affected by a multiple slip surface failure mechanism. In *Proceedings of the 1st International Symposium Com-Geo (Computational Methods in Geomechanics)*, 2009.

[74] Ferreira, A. & Rolim, J.: *Parallel Algorithms for Irregularly Structured Problems: Second International Workshop, IRREGULAR '95, Lyon, France, September 4 - 6, 1995. Proceedings*. Springer-Verlag, Berlin 1995.

[75] Finlayson, B. A.: *The Method of Weighted Residuals and Variational Principles: With Application in Fluid Mechanics, Heat and Mass Transfer*. Educational Psychology, Academic Press, Cambridge 1972.

[76] Fischer, P. & Hofer, P.: *Lexikon der Informatik*. Springer-Verlag, Berlin, Heidelberg 2008, 13 edn.

[77] Flynn, M. J.: Some computer organizations and their effectiveness. *IEEE Transactions on Computers* **21** (1972), 948–960.

[78] Fredlund, D. G. & Rahardjo, H.: *Soil Mechanics for Unsaturated Soils*. John Wiley & Sons, New York 1993.

[79] Fried, I. & Malkus, D. S.: Finite element mass matrix lumping by numerical integration with no convergence rate loss. *International Journal of Solids and Structures* **11** (1975), 461–466.

[80] Gebali, F.: *Algorithms and Parallel Computing*. John Wiley & Sons, New York 2011.

[81] van Genuchten, M. T.: A closed-form equation for predicting the hydraulic conductivity of unsaturated soils. *Soil Science Society of America Journal* **44** (1980), 892–898.

[82] Gerthsen, C. & Meschede, D.: *Gerthsen Physik*. Springer-Verlag, Berlin 2003.

[83] Göddeke, D.: *Fast and Accurate Finite-Element Multigrid Solvers for PDE Simulations on GPU Clusters*. Dissertation thesis, Technical University of Dortmund 2011.

[84] Godfrey, M. D. & Hendry, D. F.: The computer as von Neumann planned it. *IEEE Annals of the History of Computing* **15** (1993), 11–21.

[85] Graf, T.: *Multiphasic Flow Processes in Deformable Porous Media under Consideration of Fluid Phase Transitions*. Dissertation Thesis Report No. II-17 of the Institute of Applied Mechanics (CE), University of Stuttgart 2008.

[86] Grama, A.; Gupta, A.; Karypis, G. & Kumar, V.: *Introduction to Parallel Computing*. Pearson Education, Addison-Wesley 2003, 2 edn.

[87] Green, A. E. & Naghdi, P. M.: A general theory of an elastic-plastic continuum. *Archive for Rational Mechanics and Analysis* **18** (1965), 251–281.

[88] Gropp, W.; Bjørstad, P. & Smith, B. F.: *Domain Decomposition: Parallel Multilevel Methods for Elliptic Partial Differential Equations*. Cambridge University Press, Cambridge 2008.

[89] Gropp, W.; Lusk, E. & Skjellum, A.: *Using MPI : portable parallel programming with the Message-Passing-Interface*. The MIT Press, Cambridge 2014.

[90] Hadamard, J.: *Lectures on Cauchy's Problem in Linear Partial Differential Equations*. Dover Publications, Dover 2003.

[91] Haeggblad, B. & Nordgren, G.: Modelling nonlinear soil-structure interaction using interface elements, elastic-plastic soil elements and absorbing infinite elements. *Computers & Structures* **26** (1987), 307–324.

[92] Hager, G. & Wellein, G.: *Introduction to High Performance Computing for Scientists and Engineers*. CRC Press, Boca Raton 2010.

[93] Hairer, E.; Nørsett, S. P. & Wanner, G.: *Solving Ordinary Differential Equations I – Nonstiff Problems*. Springer-Verlag, Berlin 1993, 2nd edn.

[94] Hairer, E. & Wanner, G.: *Solving Ordinary Differential Equations II – Stiff and Differential-Algebraic Problems*. Springer-Verlag, Berlin 1991.

[95] Hassanizadeh, S. M. & Gray, W. G.: General conservation equations for multi-phase systems: 1. averaging procedure. *Advances in Water Resources* **2** (1979), 131–144.

[96] Haupt, P.: On the concept of an intermediate configuration and its application to a representation of viscoelastic-plastic material behavior. *International Journal of Plasticity* **1** (1985), 303–316.

[97] Heider, Y.: *Saturated Porous Media Dynamics with Application to Earthquake Engineering*. Dissertation Thesis Report No. II-25 of the Institute of Applied Mechanics (CE), University of Stuttgart 2012.

[98] Heider, Y.; Avci, O.; Markert, B. & Ehlers, W.: The dynamic response of fluid-saturated porous materials with application to seismically induced soil liquefaction. *Soil Dynamics and Earthquake Engineering* **63** (2014), 120–137.

[99] Heider, Y.; Markert, B. & Ehlers, W.: Dynamic wave propagation in infinite saturated porous media halfspaces. *Computational Mechanics* **49** (2012), 319–336.

[100] Helmig, R.: *Multiphase Flow and Transport Processes in the Subsurface: A Contribution to the Modeling of Hydrosystems*. Springer-Verlag, Berlin, Heidelberg 1997.

[101] Hilber, H. M.; Hughes, T. J. R. & Taylor, R. L.: Improved numerical dissipation for time integration algorithms in structural dynamics. *Earthquake Engineering and Structural Dynamics* **5** (1977), 283–292.

[102] Hinton, E.; Rock, T. & Zienkiewicz, O. C.: A note on mass lumping and related processes in the finite element method. *Earthquake Engineering and Structural Dynamics* **4** (1976), 245–249.

[103] Hoffman, J. D. & Frankel, S.: *Numerical Methods for Engineers and Scientists*. CRC Press, Boca Raton 2001.

[104] Holzapfel, G. A.: *Nonlinear Solid Mechanics. A Continuum Approach for Engineering*. John Wiley & Sons, Chichester 2000.

[105] Howell, H. G.: Inter-fibre friction. *Journal of the Textile Institute Transactions* **42** (1951), 521–533.

[106] Huebner, K. H.; Thornton, E. A. & Byrom, T. G.: *The finite element method for engineers*. John Wiley & Sons, New York, New York 2001, 4 edn.

[107] Iqbal, M.; Shahidh, B. & Saltz, J.: A comparative analysis of static and dynamic load balancing strategies. *International Conference on Parallel Processing* (1986).

[108] Iwan, W. D.: On a class of models for the yielding behavior of continuous and composite systems. *ASME Journal of Applied Mechanics* **34** (1967), 612–617.

[109] Jirásek, M. & Bažant, Z. P.: *Inelastic Analysis of Structures*. John Wiley & Sons, New York 2002.

[110] John, V. & Knobloch, P.: On spurious oscillations at layers diminishing (sold) methods for convection-diffusion equation: Part I - a review. *Computer Methods in Applied Mechanics and Engineering* **196** (2007), 2197–2215.

[111] Karajan, N.: *An extended biphasic description of the inhomogeneous and anisotropic intervertebral disc*. Dissertation Thesis, Report No. II-19 of the Institute of Applied Mechanics (CE), University of Stuttgart 2009.

[112] Khalili, N.; Yazdchi, M. & Valliappen, S.: Wave propagation analysis of two-phase saturated porous media using coupled finite-infinite element method. *Soil Dynamics and Earthquake Engineering* **18** (1999), 533–553.

[113] Kistler, S. F.: Hydrodynamics of wetting. In Berg, J. C. (ed.): *Wettability*. Marcel Dekker, New York 1993, 1st edn., pp. 311–249.

[114] Klunker, F.; Elsenhans, C.; Aranda, S.; Surjoseputro, W.; Wu, W.; Behnke, H. & Ziegmann, G.: Modelling the resin infusion process, part I: Flow modelling and numerical investigation for constant geometries. *Journal of Plastics Technology* **7** (2011), 179–205.

[115] Ko, H. & Scott, R. F.: Deformation of sand in shear. *Journal of the Soil Mechanics and Foundations Division* **93** (1967), 283–310.

[116] Kothari, V. K. & Gangal, M. K.: Assessment of frictional properties of some woven fabrics. *Indian Journal of Fibre & Textile Research* **19** (1994), 151–155.

[117] Krause, R. F.: *Growth, Modelling and Remodelling of Biological Tissue*. Dissertation Thesis, Report No. II-29 of the Institute of Applied Mechanics (CE), University of Stuttgart 2014.

[118] Kuhl, D.: *Modellierung und Simulation von Mehrfeldproblemen der Strukturmechanik*. Habilitation Thesis, Ruhr University of Bochum 2004.

[119] Kunz, P.; Zarikos, I. M.; Karadimitriou, N. K.; Huber, M.; Nieken, U. & Hassanizadeh, S. M.: Study of multi-phase flow in porous media: Comparison of sph simulations with micro-model experiments. *Transport in Porous Media* (2015), 1–20.

[120] Kuzmin, D.: *A Guide to Numerical Methods for Transport Equations*. Friedrich-Alexander-Universität, Erlangen-Nürnberg 2010.

[121] Lade, P. V.: Elastoplastic stress-strain theory for cohesionless soil with curved yield surfaces. *International Journal for Solids and Structures* **13** (1977), 1019–1035.

[122] Lade, P. V.: Experimental observations of stability, instability, and shear planes in granular materials. *Archive of Applied Mechanics* **59** (1989), 114–123.

[123] Lade, P. V. & Duncan, J. M.: Cubical triaxial tests on cohesionless soil. *ASCE: Journal of Soil Mechanics and Foundations Division* **99** (1973), 793–812.

[124] Lade, P. V. & Inel, S.: Rotational kinematic hardening model for sand. part i concept of rotating yield and plastic potential surfaces. *Computers and Geotechnics* **21** (1997), 183–216.

[125] Larsson, S. & Thomée, V.: *Partial Differential Equations with Numerical Methods*. Texts in Applied Mathematics, Springer-Verlag, Berlin 2003.

[126] Lee, E. H.: Elastic-plastic deformation at finite strains. *Journal of Applied Mechanics* **36** (1969), 1–6.

[127] Lenhard, R.; Parker, J. & Mishra, S.: On the correspondence between Brooks-Corey and van Genuchten models. *Journal of Irrigation and Drainage Engineering* **115** (1989), 744–751.

[128] Lewis, R. W. & Schrefler, B. A.: *The Finite Element Method in the Static and Dynamic Deformation and Consolidation of Porous Media*. Wiley-Blackwell 1998, 2nd edn.

[129] de l'Hôspital, G.: Analyse des infiniment petits pour l'intelligence des lignes courbes. In *L'imprimerie Royale*. Paris 1696.

[130] Li, X.: Finite element analysis of slope stability using a nonlinear failure criterion. *Computers and Geotechnics* **34** (2007), 127–136.

[131] Li, X.: Pml absorbing boundary condition for seismic numerical modeling by convolutional differentiator in fluid-saturated porous media. *Journal of Earth Science* **22** (2011), 377–385.

[132] Lin, C.-H. & Borja, R.: *Dynamic Theory of Mixtures and Its Finite Element Implementation for Nonlinear Analysis of Ground Motion Induced by Seismic Shaking*. Report No. 137 of the John A. Blume Earthquake Engineering Center, University of Stanford 2000.

[133] Lysmer, J. & Kuhlemeyer, R. L.: Finite dynamic model for infinite media. *ASCE: Journal of the Engineering Mechanics Division* **95** (1969), 859–877.

[134] Mahnkopf, D.: *Lokalisierung fluidgesättigter poröser Festkörper bei finiten elastoplastischen Deformationen*. Dissertation Thesis, Report No. II-5 of the Institute of Applied Mechanics (CE), University of Stuttgart 2000.

[135] Manzari, M. T. & Dafalias, Y. F.: A critical state two-surface plasticity model for sands. *Geotechnique* **47** (1997), 255–272.

[136] Markert, B.: *Porous media viscoelasticity with application to polymeric foams*. Dissertation Thesis, Report No. II-12 of the Institute of Applied Mechanics (CE), University of Stuttgart 2005.

[137] Markert, B.: *Weak or Strong - On Coupled Problems in Continuum Mechanics*. Habilitation Thesis, Report No. II-20 of the Institute of Applied Mechanics (CE), University of Stuttgart 2010.

[138] Markert, B.; Heider, Y. & Ehlers, W.: Comparision of monolithic and splitting solutions schemes for dynamic for dynamic porous media problems. *International Journal of Numerical Methods Engineering* **82** (2010), 1341–1383.

[139] Marques, M. M. C. & Owen, D. R. J.: Infinite elements in quasi-static materially nonlinear problems. *Computers & Structures* (1984), 729–751.

[140] Matthies, H. G.; Niekamp, R. & Steindorf, J.: Algorithms for strong coupling procedures. *Computer Methods in Applied Mechanics and Engineering* **195** (2006), 2028–2049.

[141] Matthies, H. G. & Steindorf, J.: Strong coupling methods. In Wendland, W. L. & Efendiev, M. (eds.): *Analysis and Simulation of Multifield Problems*. Springer-Verlag, Berlin 2003, pp. 13–36.

[142] Meggiolaro, M. A.; Castro, J. T. P. & Wu, H.: On the applicability of multi-surface, two-surface and non-linear kinematic hardening models in multiaxial fatigue. *Frattura ed Integritá Struttura* **33** (2015), 357–367.

[143] Message Passing Interface Forum: *MPI: A Message-Passing Interface Standard Version 3.0*. High Performance Computing Center Stuttgart (HLRS) 2012.

[144] Mills, N.: Incompressible mixture of Newtonian fluids. *International Journal of Engineering Science* **4** (1966), 97–112.

[145] Mróz, Z.: On the description of anisotropic workhardening. *Journal of the Mechanics and Physics of Solids* **15** (1967), 163–175.

[146] Mróz, Z.: An attempt to describe the behavior of metals under cyclic loads using a more general workhardening model. *Acta Mechanica* **7** (1969), 199–212.

[147] Newmark, N. M.: A method of computation for structural dynamics. *Journal of the Engineering Mechanics Division, ASCE* (1959), 67–94.

[148] Noll, W.: A mathematical theory of the mechanical behavior of continous media. *Archive for Rational Mechanics and Analysis* **2** (1958), 197–226.

[149] Nordlund, M. & Michaud, V.: Dynamic saturation curve measurement for resin flow in glass fibre reinforcement. *Composites Part A: Applied Science and Manufacturing* **43** (2012), 333–343.

[150] Ohno, N. & Wang, J. D.: Kinematic hardening rules with critical state dynamic recovery, Part II – Application to experiments of ratcheting behavior. *International Journal of Plasticity* **9** (1991), 391–403.

[151] Oka, F.; Higo, Y. & Kimoto, S.: Effect of dilatancy on the strain localisation of water-saturated elasto- viscoplastic soil. *International Journal of Solids and Structures* **39** (2000), 3625–3647.

[152] Oskooi, A. F.; Zhang, L.; Avniel, Y. & Johnson, S. G.: The failure of perfectly matched layers, and towards their redemption by adiabatic absorbers. *Optics Express* **16** (2008), 11376–11392.

[153] Pacheco, P.: *Parallel programming with MPI*. Morgan Kaufmann Publishers, San Francisco 1997.

[154] Patra, A. K.; Long, J. & Laszloffy, A.: Efficient parallel adaptive finite element methods using self-scheduling data and computations. In Banerjee, P.; Prasanna, V. K. & Sinha, B. P. (eds.): *High Performance Computing – HiPC'99: 6th International Conference, Calcutta, India, December 17-20, 1999*. Springer-Verlag, New York 1999, pp. 359–363.

[155] Perzyna, P.: Fundamental problems in viscoplasticity. *Advances in Applied Mechanics* **9** (1966), 243–377.

[156] Popescu, R.; Prévost, J. H.; Deodatis, G. & Chakrabortty, P.: Dynamics of nonlinear porous media with applications to soil liquefaction. *Soil Dynamics and Earthquake Engineering* **26** (2006), 648–665.

[157] Prévost, J. H.: Nonlinear transient phenomena in soil media. *Mechanics of Engineering Materials* **30** (1982), 3–18.

[158] Provatas, N. & Elder, K.: *Phase-Field Methods in Materials Science and Engineering*. John Wiley & Sons, New York 2010.

[159] Rauber, T. & Rünger, G.: *Parallel Programming*. Springer-Verlag, Heidelberg, New York, Dordrecht, London 2012.

[160] Rauch, A. F.: *EPOLLS: An Empirical Method for Prediciting Surface Displacements Due to Liquefaction-Induced Lateral Spreading in Earthquakes*. Dissertation Thesis, Report No.: etd-219182249741411, Virginia Polytechnic Institute and State University 1997.

[161] Rempler, H.-U.: *Damage in multi-phasic materials computed with the extented finite-element method*. Dissertation Thesis, Report No. II-23 of the Institute of Applied Mechanics (CE), University of Stuttgart 2012.

[162] Richards, L. A.: Capillary conduction of liquids through porous mediums. *Physics* **1** (1931), 318–333.

[163] Ricken, T.; Werner, D.; Holzhütter, H.; König, M.; Dahmen, U. & Dirsch, O.: Modeling function–perfusion behavior in liver lobules including tissue, blood, glucose, lactate and glycogen by use of a coupled two-scale PDE–ODE approach. *Biomechanics and modeling in mechanobiology* **14** (2015), 515–536.

[164] Robertson, P. K.: Design considerations for liquefaction. *Proceedings of the 13th International Conference on Soil Mechanics and Foundation Engineering* **5** (1994), 185–188.

[165] Roscoe, K. H. & Burland, J. B.: On the generalized stress-strain behaviour of wet clay. In Heyman, J. & Leckie, F. A. (eds.): *Engineering Plasticity*. Cambridge University Press, Cambridge 1968, pp. 535–609.

[166] Roth, S.; Hütter, G.; Mühlich, U.; Nassauer, B.; Zybel, L. & Kuna, M.: Visualisation of user defined finite elements with Abaqus/Viewer. *GACM Report Summer 2012* (2012), 7–14.

[167] Santamarina, J.; Klein, K. A. & Fam, M. A.: *Soils and waves*. John Wiley & Sons, Chichester 2001.

[168] Sasikumar, M.; Shikhare, D. & Prakash, R. P.: *Introduction to parallel processing*. PHI Learning 2014.

[169] Saylor, J. R. & Bounds, G. D.: Experimental study of the role of the Weber and capillary numbers on Mesler entrainment. *AIChE Journal* **58** (2012), 3841–3851.

[170] Schad, H.: *Nichtlineare Stoffgleichungen für Böden und ihre Anwendung bei der numerischen Analyse von Baugrundaufgaben*. Disseration Thesis, 10, University of Stuttgart 1979.

[171] Schanz, M.: *Wave Propagation in viscoelastic and poroelastic continua*. Springer-Verlag, Berlin 2001.

[172] Schenke, M. & Ehlers, W.: On the analysis of soils using an abaqus-pandas interface. *Proceedings in Applied Mathematics and Mechanics* **11** (2011), 431–432.

[173] Schenke, M. & Ehlers, W.: Parallel solution of volume-coupled multi-field problems using an abaqus-pandas software interface. *Proceedings in Applied Mathematics and Mechanics* **15** (2015), 419–420.

[174] Schofield, A. N. & Wroth, C. P.: *Critical State Soil Mechanics*. McGraw-Hill, New York 1968.

[175] Shannon, C. E.: Communication in the presence of noise. *Proceedings of the Institute of Radio Engineers* **37** (1949), 10–21.

[176] Sheppard, W. F.: Central-difference formulæ. *Proceedings of the London Mathematical Society* **1** (1899), 449–488.

[177] Simo, J. C. & Hughes, T. J. R.: *Computational Inelasticity*. Interdisciplinary Applied Mathematics, Springer, New York 2000.

[178] Simo, J. C. & Taylor, R. L.: Consistent tangent operators for rate-independent elastoplasticity. *Computer Methods in Applied Mechanics and Engineering* **48** (1985), 101–118.

[179] Simo, J. C. & Taylor, R. L.: A return mapping algorithm for plane stress elastoplasticity. *International Journal for Numerical Methods in Engineering* **22** (1986), 649–670.

[180] Song, X.: *Vacuum-assisted resin transfer molding (VARTM): Model development and verification*. Phd thesis, Virginia Polytechnic Institute and State University 2003.

[181] Spellucci, P.: *Numerische Verfahren der nichtlinearen Optimierung*. Birkhäuser, Basel 1993.

[182] Spellucci, P.: A new technique for inconsistent qp problems in the sqp-method. *Mathematical Methods of Operations Research* **47** (1998), 335–400.

[183] Tian, J.; Li, G.; Fei, W. & Zeng, G.: An efficient gpu acceleration format for finite element analysis. *Journal of Electronics* **30** (2013), 599–608.

[184] Toselli, A. & Widlund, O.: *Domain Decomposition Methods – Algorithms and Theory*. Springer-Verlag, Berlin, Heidelberg 2005.

[185] Tracy, F. T.: An accuracy analysis of mass matrix lumping for three-dimensional, unsaturated flow, finite element, porous media computations using analytical solutions **7** (2007), 2020025–2020026.

[186] Trochu, F.; Gauvin, R. & Gao, D. M.: Numerical analysis of the resin transfer molding process by the finite element method. *Advances in Polymer Technology* **12** (1993), 392–342.

[187] Truesdell, C.: Thermodynamics of diffusion. In Truesdell, C. (ed.): *Rational Thermodynamics*. Springer-Verlag, New-York 1984, 2nd edn., pp. 219–236.

[188] Truesdell, C. & Noll, W.: *The Nonlinear Field Theories of Mechanics*. Band III/3., Springer-Verlag, Berlin 1965.

[189] Truesdell, C. & Toupin, R. A.: The classical field theories. In Flügge, S. (ed.): *Handbuch der Physik*. Springer-Verlag, Berlin 1960, Band III/1.

[190] Tucker, A. B. & Noonan, R.: *Programming languages: principles and paradigms*. McGraw-Hill 2002.

[191] Vandenberghe, L.: *Lecture notes on applied numerical computing*. University of California, Los Angeles 2015.

[192] Vermeer, P. A.: A double hardening model for sand. *Géotechnique* **28** (1978), 413–433.

[193] Verrey, J.; Michaud, V. & Månson, J.-A. E.: Dynamic capillary effects in liquid composite moulding with non-crimp fabrics. *Composites Part A: Applied Science and Manufacturing* **37** (2006), 92–102.

[194] von Neuman, J.: *First Draft of a Report on the EDVAC*. Moore School of Electrical Engineering, University of Pennsylvania 1945.

[195] Vrh, M.; Halilovič, M. & Štok, B.: Improved explicit integration in plasticity. *International Journal for Numerical Methods in Engineering* **81** (2010), 910–938.

[196] Wagner, A.: *Extented Modelling of the Multiphasic Hiuman Brain Tissue With Application to the Drug-Infusion Processes*. Dissertation Thesis, Report No. II-27 of the Institute of Applied Mechanics (CE), University of Stuttgart 2014.

[197] Walshaw, C.; Cross, M. & Everett, M.: Parallel dynamic graph partitioning for adaptive unstructured meshes. *Journal of Parallel and Distributed Computing* **47** (1997), 102 – 108.

[198] White, W.; Vallianppan, S. & Lee, I. K.: Unified boundary for finite dynamic models. *ASCE: Journal of the Engineering Division* **103** (1977), 949–964.

[199] Whitman, R. V.: On liquefaction. *Proceedings of the 11th International Conference on Soil Mechanics and Foundation Engineering* **4** (1985), 1923–1926.

[200] Wichtmann, T.; Niemunis, A. & Triantafyllidis, T.: Strain accumulation in sand due to cyclic loading: drained triaxial tests. *Soil Dynamics and Earthquake Engineering* **25** (2005), 967–979.

[201] Wichtmann, T. & Triantafyllidis, T.: Behaviour of granular soils under environmental induced cyclic loads. In di Prisco, C. G. & Wood, D. M. (eds.): *Mechanical Behaviour of Soils Under Environmentally-Induced Cyclic Loads*. Springer-Verlag, Wien 2012.

[202] Wieners, C.: M++. URL `http://www.mathematik.uni-karlsruhe.de/~wieners`.

[203] Wieners, C.: Distributed point objects. A new concept for parallel finite elements. In Kornhuber, R.; Hoppe, R.; Périaux, J.; Pironneau, O.; Widlund, O. & Xu, J. (eds.): *Domain Decomposition Methods in Science and Engineering*. Springer-Verlag, Berlin 2004, pp. 175–183.

[204] Wolf, H.; Knig, D. & Triantafyllidis, T.: Experimental investigation of shear band patterns in granular material. *Journal of Structural Geology* **25** (2003), 1229–1240.

[205] Wriggers, P.: *Konsistente Linearisierung in der Kontinuumsmechanik und ihre Anwendung auf die Finite-Elemente-Methode*. Habilitation Thesis, Report No. F 88/4, Forschungs und Seminarberichte aus dem Bereich der Mechanik der Universität Hannover 1988.

[206] Wu, Y.-S. & Forsyth, P. A.: On the selection of primary variables in numerical formulation for modeling multiphase flow in porous media. *Journal of Contaminant Hydrology* **48** (2001), 277–304.

[207] Wunderlich, W.; Schäpertöns, B. & Temme, C.: Dynamic stability of non-linear shells of revolution under consideration of the fluid-soil-structure interaction. *International Journal for Numerical Methods in Engineering* **37** (1994), 2679–2697.

[208] Xavier, C. & Iyengar, S. S.: *Introduction to Parallel Algorithms*. John Wiley & Sons, Chichester 1998.

[209] Xu, C. & Lau, F. C.: *Load Balancing in Parallel Computers: Theory and Practice*. Kluwer Academic Publishers, Norwell 1997.

[210] Yamada, Y. & Ishihara, K.: Anisotropic deformation charateristics of sand under three dimensional stress conditions. *Soils and Foundation* **19** (1979), 79–94.

[211] Yazdchi, M.; Khalili, N. & Valliappan, S.: Dynamic soil-structure interaction analysis via coupled finite-element-boundary-element method. *Earthquake Engineering & Structural Dynamics* **18** (1999), 499–517.

[212] Young, T.: An essay on the cohesion of fluids. *Philosophical Transactions of the Royal Society of London* **95** (1805), 65–87.

[213] Zhang, Y.; Kameda, H. & Hung, S. L.: Comparison of dynamic and static load-balancing strategies in heterogeneous distributed systems. *Computers and Digital Techniques, IEE Proceedings* **144** (1997), 100–106.

[214] Zienkiewicz, O. C. & Bettes, P.: *Soil Mechanics - Transient and Cyclic Loads*. John Wiley & Sons Ltd., Chichester 1982.

[215] Zienkiewicz, O. C.; Chan, A. H. C.; Pastor, M.; Schrefler, B. A. & Shiomi, T.: *Computational Geomechanics with Special Reference to Earthquake*. John Wiley & Sons, Chichester 2001.

[216] Zienkiewicz, O. C.; Chang, C. T. & Hinton, E.: Non-linear seismic response and liquefaction. *International Journal for Numerical and Analytical Methods in Geomechanics* **2** (1978), 381–404.

[217] Zienkiewicz, O. C. & Taylor, R. L.: *The Finite Element Method for Solid and Structural Mechanics, Vol. 2*. Butterworth-Heinemann, Oxford 2005, 6th edn.

[218] Zienkiewicz, O. C. & Taylor, R. L.: *The Finite Element Method. The Basis, Vol. 1*. Butterworth-Heinemann, Oxford 2005, 6th edn.

[219] Zienkiewicz, O. C.; Taylor, R. L. & Zhu, J. Z.: *The Finite Element Method: Its Basis and Fundamentals*. Elsevier Science 2005.

[220] Zinatbakhsh, S.: *Coupled Problems in the Mechanics of Multi-Physics and Multi-Phase Materials*. Dissertation Thesis, Report No. II-30 of the Institute of Applied Mechanics (CE), University of Stuttgart 2015.

Curriculum Vitae

Personal Data:

Name:	Maik Schenke
Parents:	Reinhard and Claudia Schenke
Date of birth:	Mai 13, 1980
Place of birth:	Gera, Germany
Nationality:	German

Education and Professional Occupation:

09/1986 – 07/1992	POS Gera (formerly Karl-Marx-Oberschule Gera)
09/1992 – 07/1995	Hauptschule Saarbrückener Straße Nürnberg
09/1995 – 07/1996	Hauptschule Hummelsteiner Weg Nürnberg
09/1997 – 07/1999	Fachoberschule Rollnerstraße Nürnberg degree: Fachgebundene Hochschulreife (Technik) (subject-linked high school diploma, natural science)
09/1999 – 6/2000	military service in Klosterlechfeld (Bavaria)
09/2000 – 9/2005	studies in aerospace engineering at the Fachhochschule Aachen (incl. studies at the ESTACA Paris, 2/2004 to 7/2004) degree: Dipl.-Ing. (FH)
10/2005 – 11/2006	stress engineer at Airbus Stade (vertical tail plance A380)
12/2006 – 12/2008	studies of COMMAS at the Universität Stuttgart degree: M. Sc.
since 1/2009	research associate at the Institute of Applied Mechanics (civil engineering) at the Universität Stuttgart, research-project title: *Dynamic Loading of Partially Saturated Soils:* *an investigation in the framework of numerical mechanic* *of strongly coupled problems* funded by the German Research Foundation (DFG) within the project "GeoTech" (FOR1136)

Released Report Series

II-1 Gernot Eipper: *Theorie und Numerik finiter elastischer Deformationen in fluidgesättigten porösen Festkörpern*, 1998.

II-2 Wolfram Volk: *Untersuchung des Lokalisierungsverhaltens mikropolarer poröser Medien mit Hilfe der Cosserat-Theorie*, 1999.

II-3 Peter Ellsiepen: *Zeit- und ortsadaptive Verfahren angewandt auf Mehrphasenprobleme poröser Medien*, 1999.

II-4 Stefan Diebels: *Mikropolare Zweiphasenmodelle: Formulierung auf der Basis der Theorie Poröser Medien*, 2000.

II-5 Dirk Mahnkopf: *Lokalisierung fluidgesättigter poröser Festkörper bei finiten elastoplastischen Deformationen*, 2000.

II-6 Heiner Müllerschön: *Spannungs-Verformungsverhalten granularer Materialien am Beispiel von Berliner Sand*, 2000.

II-7 Stefan Diebels (Ed.): *Zur Beschreibung komplexen Materialverhaltens: Beiträge anläßlich des 50. Geburtstages von Herrn Prof. Dr.-Ing. Wolfgang Ehlers*, 2001.

II-8 Jack Widjajakusuma: *Quantitative Prediction of Effective Material Parameters of Heterogeneous Materials*, 2002.

II-9 Alexander Droste: *Beschreibung und Anwendung eines elastisch-plastischen Materialmodells mit Schädigung für hochporöse Metallschäume*, 2002.

II-10 Peter Blome: *Ein Mehrphasen-Stoffmodell für Böden mit Übergang auf Interface-Gesetze*, 2003.

II-11 Martin Ammann: *Parallel Finite Element Simulations of Localization Phenomena in Porous Media*, 2005.

II-12 Bernd Markert: *Porous Media Viscoelasticity with Application to Polymeric Foams*, 2005.

II-13 Saeed Reza Ghadiani: *A Multiphasic Continuum Mechanical Model for Design Investigations of an Effusion-Cooled Rocket Thrust Chamber*, 2005.

II-14 Wolfgang Ehlers & Bernd Markert (Eds.): *Proceedings of the 1st GAMM Seminar on Continuum Biomechanics*, 2005.

II-15 Bernd Scholz: *Application of a Micropolar Model to the Localization Phenomena in Granular Materials: General Model, Sensitivity Analysis and Parameter Optimization*, 2007.

II-16 Wolfgang Ehlers & Nils Karajan (Eds.): *Proceedings of the 2nd GAMM Seminar on Continuum Biomechanics*, 2007.

II-17 Tobias Graf: *Multiphasic Flow Processes in Deformable Porous Media under Consideration of Fluid Phase Transitions*, 2008.

II-18 Ayhan Acartürk: *Simulation of Charged Hydrated Porous Materials*, 2009.

II-19 Nils Karajan: *An Extended Biphasic Description of the Inhomogeneous and Anisotropic Intervertebral Disc*, 2009.

II-20 Bernd Markert: *Weak or Strong – On Coupled Problems In Continuum Mechanics*, 2010.

II-21 Wolfgang Ehlers & Bernd Markert (Eds.): *Proceedings of the 3rd GAMM Seminar on Continuum Biomechanics*, 2012.

II-22 Wolfgang Ehlers: *Poröse Medien – ein kontinuumsmechanisches Modell auf der Basis der Mischungstheorie*, 2012. Nachdruck der Habilitationsschrift aus dem Jahr 1989 (Forschungsberichte aus dem Fachbereich Bauwesen der Universität-GH-Essen **47**, Essen 1989).

II-23 Hans-Uwe Rempler: *Damage in multi-phasic Materials Computed with the Extended Finite-Element Method*, 2012.

II-24 Irina Komarova: *Carbon-Dioxide Storage in the Subsurface: A Fully Coupled Analysis of Transport Phenomena and Solid Deformation*, 2012.

II-25 Yousef Heider: *Saturated Porous Media Dynamics with Application to Earthquake Engineering*, 2012.

II-26 Okan Avci: *Coupled Deformation and Flow Processes of Partial Saturated Soil: Experiments, Model Validation and Numerical Investigations*, 2013.

II-27 Arndt Wagner: *Extended Modelling of the Multiphasic Human Brain Tissue with Application to Drug-Infusion Processes*, 2014.

II-28 Joffrey Mabuma: *Multi-Field Modelling and Simulation of the Human Hip Joint*, 2014.

II-29 Robert Krause: *Growth, Modelling and Remodelling of Biological Tissue*, 2014.

II-30 Seyedmohammad Zinatbakhsh: *Coupled Problems in the Mechanics of Multi-Physics and Multi-Phase Materials*, 2015.

II-31 David Koch: *Thermomechanical Modelling of Non-isothermal Porous Materials with Application to Enhanced Geothermal Systems*, 2016.

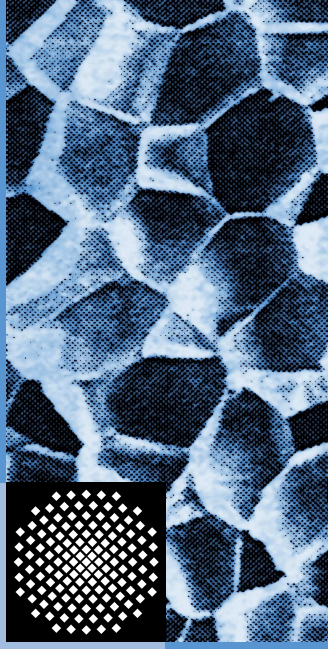

ISBN 978-3-937399-32-4
(D 93 – Dissertation, Universität Stuttgart)